Diffusion, Nucleation and Recombination in Confined Geometries

Inauguraldissertation
zur Erlangung des Doktorgrades der
Mathematisch-Naturwissenschaftlichen Fakultät
der Universität zu Köln

vorgelegt von

Ingo Lohmar
aus Köln

Köln 2009

Berichterstatter: Prof. Dr. Joachim Krug
Prof. Dr. Thomas Nattermann
Prof. Dr. Ofer Biham
(The Hebrew University, Jerusalem, Israel)

Tag der letzten mündlichen Prüfung: 28.04.2009

Zusammenfassung

In dieser Arbeit werden mehrere Probleme der Oberflächenphysik bearbeitet, die auf Diffusion als Transportmechanismus beruhen. Wesentliche Teile behandeln Systeme, in denen Teilchen durch Reaktion oder Keimbildung bei einem Zusammentreffen wechselwirken.

Für das astrophysikalische Problem der Wasserstoffrekombination auf interstellarem Staub wird die bisherige analytische Behandlung wesentlich verbessert: Der für die Reaktion entscheidende Parameter wird konsistent definiert, und bei seiner Berechnung wird die Natur zweidimensionaler Diffusion berücksichtigt. Im Rahmen mehrerer Modelle, die miteinander verglichen werden, kommt man zu expliziten Resultaten, die durch Monte-Carlo-Simulationen exzellent bestätigt werden. Ein besonderes Augenmerk gilt dabei dem Einfluss der eingeschränkten Geometrie, die anhand eines Minimalmodells analytisch untersucht und verstanden werden kann. Auch Fragen zum Einfluss von Unordnung in der Oberflächenstruktur werden behandelt. Ein weiterer Abschnitt betrachtet das eng verwandte Problem der Keimbildung am Inselrand bei epitaxialem Kristallwachstum, das sich aber bereits unter moderaten Annahmen als analytisch nicht mehr behandelbar erweist.

Das Stufenwachstum unter Einfluss von kodeponierten Verunreinigungen ist ein technologisch wichtiger Prozess, der in einem eindimensionalen Random-Walk-Modell untersucht wird. Anhand mikroskopischer Modelle der so entstehenden Unordnung der Oberfläche lassen sich interessante und ebenfalls für Simulationen relevante Aussagen treffen. Diese betreffen sowohl den allgemeinen Einfluss auf die Geschwindigkeit und Stabilität des Stufenwachstums als auch die Natur der Randbedingungen im entsprechenden Kontinuumsmodell.

Im letzten Teil wird ein Modell ausführlich analytisch untersucht, das Diffusionsfelder in Desorptionsexperimenten beschreibt, welche man durch Echtzeitbeobachtung auf großem Maßstab direkt sichtbar machen kann. Das Modell beschreibt experimentelle Daten sehr gut und stellt einen wichtigen Schritt im Verständnis der zugrundeliegenden Prozesse dar. Aufgrund dieses Verständnisses lassen sich aus der Beobachtung einer Oberfläche mit komplexer Morphologie direkte Rückschlüsse auf ihre mikroskopischen Eigenschaften ziehen.

Abstract

In this work we address several problems of surface physics which are all based on the transport mechanism of diffusion. Essential parts consider systems in which particles interact upon meeting, either by reaction or by nucleation.

For the astrophysical problem of hydrogen recombination on interstellar dust, the previous analytical treatment is substantially improved upon: The parameter responsible for reaction is defined consistently, and in its calculation, we account for the nature of two-dimensional diffusion. Within several models that are also compared with each other, one obtains explicit results that excellently agree with Monte Carlo simulations. Special attention is given to the influence of the confined geometry, which is analytically examined and explained for a minimal model. We also deal with the role of disorder in the surface structure. A further section presents the closely related problem of nucleation at island edges, which, however, proves to be no longer tractable analytically even under moderate assumptions.

Step growth under the effect of codeposited impurities is a technologically relevant process, which is examined in a one-dimensional random walk model. Using microscopic models for the resulting disorder on the surface, one finds interesting results that also bear implications for simulations. Those results concern the general influence on the speed and stability of step growth as well as the nature of boundary conditions in the corresponding continuum model.

In the last part we thoroughly analyze a model to describe the diffusion field in desorption experiments, which can be made directly visible on a large scale and with real time resolution. The model agrees well with experimental data and hence constitutes an important step in understanding the fundamental processes involved. Based on this understanding, one can draw direct conclusions from the observation of a surface of complex morphology on its microscopic properties.

Contents

Chapter 1

General Introduction

One can hardly imagine a more general physical mechanism than *diffusion*. All phenomena that involve *transport* yet are of *stochastic* (as opposed to deterministic) character, are based on diffusion: Mixing of heterogeneous gases or liquids, osmotic transport in biological cells, moving atoms or whole clusters in crystal growth, as well as the role of exciton transport in the mechanism of photosynthesis or in semiconductors — this variety shows that stochastic systems have come a long way from the original single-particle BROWNian motion ingenuously explained by Einstein [1]. Moreover, many processes that are not genuinely diffusive in the obvious microscopic sense of the word are still described by the same mathematics as if they were, e.g., heat conduction in solids, certain traffic models or the spreading of an epidemic disease.

To specialize a bit more, we will not deal with diffusion in the bulk, but rather on surfaces [2]. The importance of this aspect is due to several factors. First, the surface of a system is the interface to its environment. In many processes this is the only region where reactants can enter or leave the system, where experimental probing and manipulation are easiest, and where equilibration phenomena with the surroundings take place. Second, for the systems and regimes considered herein, the surface is the only part of the system where particles are truly mobile (for steric or energetic reasons), or where their mobility furnishes effects qualitatively different from the bulk case (as in island edge diffusion, cf. Chapter 6). These characteristics of surface diffusion render it the key mechanism behind thin film growth and the build-up of nanostructures at surfaces.

For quite a long time, people were mostly interested in the long-time / long-distance behavior of diffusion, i.e., in rather general transport properties, such as the (asymptotic) mean-square displacement once a disordered environment is considered [3, 4]. In principle, the isozone problem discussed in this thesis (Part III) belongs to this sort of problems, in that they feature non-interacting particles. The random walk (RW) here was considered mostly a model system that, under certain very general conditions, exhibits a diffusive behavior in a proper continuum limit.

Starting in the early 1970s however, this has changed considerably, as *reaction-diffusion* systems have received a lot of attention. In such systems, diffusion is the mechanism that transports particles, but those particles are considered interacting (typically on contact) by pair annihilation, particle creation, forming

another species, forming an immobile nucleus etc. Clearly, systems of that type suggest completely different questions: How often do particles meet? How long does it take for the first (or any later) encounter to occur (depending on the initial separation of a pair)? What distance has been traveled before the meeting takes place? What is the asymptotic behavior of the concentration of a given species? All these quantities can be desired for a fixed initial condition or as an average over an appropriate ensemble.

The processes discussed herein are recombination [e.g., 5, for a recent review in our context], where a reaction to another species takes place upon meeting, and nucleation [2], where meeting particles form a stable immobile nucleus. It should be obvious that many of the questions we have raised above are of a *first-passage* type [6]: They are not concerned with the final fate of the system, but with the time until an event (such as meeting a partner) happens for the first time, or with the probability for the individual particle to have a certain destiny, such as having an encounter or leaving the system altogether.

The following systems will be discussed in this thesis (in this order):

Hydrogen recombination on interstellar dust grains: This forms the major part of this work and is based on the publications Lohmar and Krug [7, 8], with further unpublished efforts (e.g., on the disordered situation) included. Our contribution to the vast astrophysical literature on this subject is an important conceptual clarification, an assessment of the influence of the global geometry, and the analysis of different modeling approaches, necessary to enable accurate comparison with experimental and numerical data. Together this forms an entirely analytic theory of the process that agrees with kinetic Monte Carlo simulations.

Island edge nucleation in homoepitaxial crystal growth: This is an 'offspring' problem with some intricate relations to the main matter of the first part. We basically lay out a general approach that, unfortunately, has not lead to many hard results.

Impurity-induced step growth instabilities: This presents a small analytically tractable model that may be of importance for the understanding of experimental features.

Isozone theory: Here we develop a theory to interpret recent large-scale real-time observations of diffusion fields on metal surfaces. The model presented in Roos *et al.* [9] is extended, and we explain in some detail what features of the striking experimental observations it can explain.

The first and the third system are prototypical as they exhibit all crucial features mentioned already in the title of this thesis: Diffusion or random walks in confined geometries (i.e., with non-open boundary conditions and for a certain spatial dimension) and reaction upon meeting of particles, in the presence of disorder. The questions asked here always are of the first-passage type as mentioned above. The latter feature also holds true for island edge nucleation, but here, (spatially quenched) disorder does not occur. Obviously, these systems are far from equilibrium, and including reaction processes, they share a non-linear time evolution.

The last item (isozone theory) is linked to the rest rather on the level of the physical system than on such more fundamental similarities. It is, however,

still a surface diffusion problem, but to the extent discussed herein, it is neither strongly dependent on geometry, nor does it incorporate disorder. Moreover, it will become clear that our treatment there is not always limited to a steady-state situation; where it is, "steady-state" has a different meaning than, e.g., for the hydrogen recombination system.

The methods to treat our problems are as follows:

- Analytical treatment of (mostly stationary) diffusion equations. Those are solvable for many geometries and boundary conditions. Solutions can be expanded asymptotically to gain insight into the system's properties.
- Exact random walk theory using generating functions, FOURIER (and possibly LAPLACE) transforms, TAUBERian theorems, recursion relations, and again asymptotic expansions. Similar techniques may be applied to many relevant master equations.
- Kinetic Monte Carlo simulation of the detailed microscopic processes nowadays always allows the treatment of the full problem including possible disorder.

These techniques may lead to a very simple solution of certain problems, but may become virtually useless for others. One finds that the spatial dimension has a crucial impact: One dimension often leads to relatively easy problems, while two dimensions are often most difficult, as this is the upper critical dimension of many diffusion-mediated systems, and for $d \geq 3$ dimensions, a simple mean-field-like treatment may give good results again. A difficulty at least as fundamental is the introduction of any disorder (in transition rates). If one wants to retain a detailed description (not annealing the disorder), a very restricted one-dimensional class of models (described in Part II) is, to the best of our knowledge, the only fully analytically tractable case (cf. Section 7.2.1, however). Finally, for problems of first-passage nature (as opposed to transport properties), we are not aware of reasonably general effective theories. The real-space renormalization group (RSRG) technique [10] is a powerful method, but, alas, it relies on a self-similarity feature of the potential landscape to renormalize.

The relation between the different parts and possible ramifications to other work as well as the cause and effect of the aforementioned difficulties will always be highlighted in more detail in the corresponding parts of this thesis. Obviously, very similar systems come in many guises, and on the other hand, slight alterations introduced to the model may completely change its behavior and the appropriate means to understand it. As it stands, this might even be considered a typical feature of reaction-diffusion systems [11].

Part I

Hydrogen Recombination on Interstellar Dust Grains

Chapter 2

Motivation, Related Questions, and Outline

Hydrogen is the most common element in our universe, and its molecular form is the most common molecule, yet formation of the latter from the former is a puzzle not completely resolved to this day. This simplest of chemical reactions, $H + H \longrightarrow H_2$, is part of the complex network of processes that occur in interstellar clouds of gas and dust, taking place both in the gas phase and on the surfaces of dust grains. It has long been known that this particular reaction is very inefficient in the gas phase, to the extent that one cannot reconcile the mechanism with observed cloud temperatures and hydrogen abundances [12]. Instead, it is the most important *surface reaction* [13], the underlying scenario being as follows: Atoms impinge onto the dust grain surface and stick to it. They diffuse as random walkers, possibly reacting and forming a molecule if they meet each other before desorbing again [12, 14, 15]. Note that for more complex reactions, chemistry is believed to often take place "in the matrix", i.e., in the solid phase of ice mixture mantles around the dust grain core.

The theory of such processes has been constantly refined over the last 40 years, see Vidali *et al.* [5] for a recent review. From an astrophysical point of view, the paramount aim is to be able to efficiently and accurately determine production rates, depending on all parameters including grain and gas phase temperature, grain size distribution and reactant concentrations, and to incorporate them into models of the gas phase reaction network. To achieve this, the most basic approach employs chemical rate equations (RE), which characterize the state of the single grain by continuous concentration variables. The production rate of any species is taken proportional to the product of the concentrations of the reactants.

Because of these features, rate equations are inappropriate as soon as (temporal or spatial) fluctuations in the reactant number on a dust grain become of the order of their mean values, a condition easily satisfied for small grains subject to low fluxes of reactants. One then has to account for the full probability distribution $P(N)$ of the number of reactants N on a grain. This can be achieved in stochastic Monte Carlo (MC) simulations [16–18] or by solving the master equation (ME) governing the time evolution of $P(N)$ [19–22].

From a theoretical point of view, surface reactions as described above are

interesting as an example of a reaction-diffusion system in a *confined geometry*. All the aforementioned frameworks are similar in that they neglect any spatial structure (including this confinement) of the system as well as the microscopic processes responsible for transport and reaction on the surface. These aspects are instead solely represented by the *sweeping rate* A, which is typically defined as the inverse of the time a single atom would require to visit all S adsorption sites. Moreover, it is conventionally taken to be of the form [17]

$$A = a/S \tag{2.1}$$

with a denoting the rate of hops between neighboring sites. The latter approximation neglects *back-diffusion*, i.e., the re-visiting of sites that cannot be neglected for the two-dimensional random walk, and that slows down exploration. The former definition suffers from the more fundamental shortcoming that it takes a single-atom point of view and focuses on the exploration of the surface; however, the actual problem is the *joint* diffusion of two reactants, terminated either by desorption or meeting, and hence a *first-passage problem* in nature.

Obviously, kinetic (sometimes termed 'microscopic') Monte Carlo simulation can easily account for these details [23, 24], but apart from the general interest in analytical results, it poses a computational challenge to reliably learn about the long-time behavior of possibly complex reaction networks.

As is typical for reaction-diffusion systems, it is very easy to add features of experimental relevance to a perfectly understood model that immediately render it virtually impossible to solve analytically. For hydrogen recombination on dust grains, important extensions include a complicated, possible fractal structure of the network of adsorption sites, porosity of the grain (both geometric factors), and most importantly, a wide distribution of binding and transition energies that implies disordered rates of hopping and desorption. Under such circumstances, microscopic Monte Carlo simulations are currently the only means to examine the full system. In fact, despite the extensive literature on disordered media [e.g., 3, 4, 11, 25], to the best of our knowledge this even holds true already for the fundamental two-particle first-passage problem once we account for a confined (two-dimensional) geometry and possible desorption.

It will still be important to examine simple homogeneous models, both to establish a reference point to validate Monte Carlo simulations against, and to further progress of analytical exploration. Herein, we will mostly be considered with such homogeneous settings, and successively determine the importance (or lack thereof) of factors such as using different shapes and types of the lattice of adsorption sites.

2.1 Experimental and Observational Status

Quantitative predictions for production rates and abundances of certain reaction products obviously depend on an array of "microscopic" parameters. Among these are reactant concentrations in the gas phase and its temperature (governing the impingement flux onto the dust grains), and a multitude of characteristics of the dust grains: Their temperature (possibly subject to stochastic heating, cf. Cuppen *et al.* [26]), the size distribution (see Mathis *et al.* [27], Weingartner and Draine [28] and Lipshtat and Biham [29] for the importance for hydrogen

$E_{\mathrm{H}}^{\mathrm{diff}}$/meV	$E_{\mathrm{H}}^{\mathrm{des}}$/meV	$E_{\mathrm{HD}}^{\mathrm{des}}$/meV	Surface	Ref.
		25.5 ± 0.6	polycryst. olivine	[32]
24.7	32.1	27.1	polycryst. olivine	[34]
44.0	56.7	46.7	amorphous carbon	[34]
44.5	52.3	46.5, 52.8, 61.2	por. water ice, low dens.	[36]
55	62	68.7	por. water ice, high dens.	[36]
35	44	35, 53	amorphous olivine	[37]
35	44	35, 53, 75	amorphous olivine	[38]

Table 2.1: List of activation energy barriers for diffusion and desorption of reactants and products.

formation rates), the grain geometry (i.e., the lattice structure formed by adsorption sites and maybe its fractal nature, as well as the overall shape), and possible porosity (the influence of which is examined in Perets and Biham [30]).

While we mentioned observations of interstellar clouds of gas and dust that lead to the intricate models of combined gas-phase grain-surface chemistry, one always has to make further far-reaching assumptions on the nature of the grains: What material(s) are they made of (and for a mixture: are the various ingredients clustered or spatially uncorrelated in occurrence?)? Do they have layers of ice on top and made up of what substance(s)? What is the roughness of the surface? What are the typical binding and transition-state energies of the adsorption sites, and what is their distribution?

It is only a relatively recent development that one tries to find answers to some of those questions in laboratory experiments. Let us describe an exemplary setup employed to examine conditions which can, as is expected, be reasonably extrapolated to astrophysically relevant conditions: One picks a surface of a given composition, and maybe of specified roughness, which is placed in an ultra-high vacuum (UHV) chamber cooled by a He cryostat. In the first phase ("irradiation") the probe is held at constant low temperature of the range $5 \ldots 30\,\mathrm{K}$. By distinct atom beams, H and D atoms are deposited onto the surface. In the second phase called "temperature-programmed desorption" (TPD), the surface slab is heated up linearly with time to let adsorbed atoms desorb on time scales amenable to laboratory experiments. The desorbed species yield is then detected by quadrupole mass spectroscopy. The TPD curves thus obtained can be used to find the overall production rate of HD as well as the activation energy barriers for diffusion and desorption of hydrogen atoms as well as molecules.

Such experiments have been performed for several surfaces which are believed to be of astrophysical relevance. Among these are olivine (a silicate rich in Fe, Mg, Si and oxygen), amorphous and crystalline carbonaceous solids, as well as (possibly porous) water ice layers [31–38]. We give a non-exhaustive list of activation energies thus obtained in Table 2.1. We will return to discuss the limited knowledge on surface roughness, porosity and (maybe corresponding to these factors) the distributions of activation energies in Section 5.1.

2.2 Related Problems

As specific as the above setting may seem, the fundamental theoretical problems that arise are intimately connected to very remote fields. This is basically due to the ubiquity of the random walk and stochastic reaction-diffusion models in physics. We shall briefly highlight two such connections.

One problem that will only indirectly appear elsewhere in this thesis (Section 6.3.1) is that of second-layer nucleation in epitaxial crystal growth [2]. Consider a crystal surface onto which further atoms impinge and afterwards diffuse. There exists a kinetic regime in which the *critical* cluster size is unity, i.e., dimers that form upon meeting of two atoms become stable and immobile. Crystal growth will then proceed to form *islands* on the surface, and atoms impinging after such islands have been nucleated may land on the second layer, i.e., on top of an island. It is an important question fundamental to the theory of surface morphology with what probability nucleation occurs *on top* of an island, hence in the second or even higher layers.

If atoms could cross the step edges between the underlying atomic layer and the island layer without any additional energetic barrier, nucleation properties on top of the island would obviously be homogeneous throughout the system (apart from possible steric effects). However, the Ehrlich-Schwoebel (ES) effect [39] is precisely such an additional energy barrier of inter-layer transport (compared to intra-layer diffusion), its strength depending on the probe temperature and the material(s) involved. This confines atoms to the top of the island, and can greatly affect the nucleation rate and the spatial distribution of nucleation events. Under certain experimental conditions, an effectively infinite ES barrier is realized, such that atoms are forever confined to the top of the island, and are certain to participate in a nucleation event sooner or later.

The basic similarity of second-layer nucleation and surface reactions is that reactants impinge onto a *finite* region, either with boundaries or closed, and may leave it prior to a reaction event by stepping down the terrace or by desorption from any adsorption site, respectively. In second-layer nucleation, the *first* event is the important one, for surface reactions, steady-state situations are of most interest. Despite those differences, there is a common feature of utmost importance: the confined geometry, which has been identified as the reason that mean-field-like rate equation analysis to determine the reaction / nucleation rate fails in both problems [40].

Another very similar problem is the diffusion and nucleation of atoms *along the edge* of islands as described above. This topic will be discussed in Chapter 6 of this thesis.

There are more remote fields that provide interesting applications, such as the chemical kinetics in aerosol droplets [41], and biological problems like exciton trapping on photosynthetic units [42] as well as several search, transport and binding processes of or along DNA strands [43, 44]. For the latter ones, the homogeneous situation is only a first step to relevant results, and the crucial two-dimensionality of our problem does not necessarily apply either. However, other biological mechanisms such as protein diffusion and reaction on biomembranes raise questions very similar to ours and can take place on a two-dimensional surface [45].

For the discussion of the relation of our efforts to a variety of theoretical

works the reader is referred to Chapter 7.

2.3 Outline

In this Part of the present thesis we tackle the following problems. We will first introduce the basic approaches to analytically determine the reaction rate / efficiency, explaining why a naïve rate equation treatment fails in the relevant regimes, and what renders the master equation framework superior. A central part of our work is the consistent definition of the important parameter common to both approaches, the sweeping rate A hitherto roughly approximated, and we establish the relation to the encounter probability p of a pair of reactants. The latter will afterwards be calculated using different models: First, a continuum diffusion model, second, a discrete random walk analysis. We obtain asymptotic expressions in two limiting regimes of experimental relevance. The different models to find the encounter probability are compared and we explain the considerable discrepancy for realistic system sizes and parameters, which is of crucial importance for comparison to simulations. The random walk case also allows a study of the effect of a distorted aspect ratio as a toy model of the effect of the global grain geometry. We demonstrate that this reduces the encounter probability by several mechanisms, and can give rise to a crossover to one-dimensional behavior, both of which features we explain. Afterwards, we determine the effect that the proper definition has on the sweeping rate compared to earlier approximations. We proceed to discuss in some detail the behavior of the master equation results, and examine the observationally relevant effects that the revised set of parameters implies. We also supply results of extensive kinetic Monte Carlo simulations for the encounter probability, and show that for those, only the random walk analysis provides a full quantitative understanding. Finally, we discuss some efforts to understand the role of rate disorder in the system, and we explain the related problem of island edge nucleation that turns out surprisingly (i.e., too) hard to solve.

For simplicity, we will speak of reactants, particles, and hydrogen atoms interchangeably throughout; we expect results to be relevant for general networks of diffusion-mediated reactions.

Chapter 3

Analytical Results

3.1 Sweeping Rate and Encounter Probability

Let us first describe more precisely the system at hand, cf. Figure 3.1. Consider a dust grain onto which H atoms impinge homogeneously at a total flux F (number per unit time),[1] and they can desorb again at a rate W. If two atoms meet, they are assumed to react to form molecular hydrogen which immediately desorbs, or which at least does not affect diffusion and reaction of H atoms. One may then set up a standard rate equation for the mean number $\langle N\rangle$ of H atoms on a single grain [46],

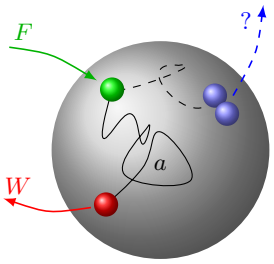

Figure 3.1: The basic setup for hydrogen recombination.

$$\frac{\mathrm{d}\langle N\rangle}{\mathrm{d}t} = F - W\langle N\rangle - 2A\langle N\rangle^2. \tag{3.1}$$

The last term shows the fundamental assumption of the rate equation treatment, namely that the reaction rate is proportional to the mean number of all reactants involved, thus neglecting both the discreteness and fluctuations of the particle number. Here, we have a production / reaction rate of

$$R_{\mathrm{RE}} = A\langle N\rangle^2, \tag{3.2}$$

as two atoms are used to form one molecule. The factor of proportionality is the *sweeping rate* A.

The above expression for the reaction rate is substituted in the master equation treatment, where [19–21]

$$R_{\mathrm{ME}} = A\langle N(N-1)\rangle. \tag{3.3}$$

As it should, the rate is now proportional to the mean number of *pairs* of atoms on the grain, and in particular it vanishes for $N = 1$. Both expressions agree if and only if $\langle N^2\rangle - \langle N\rangle^2 = \langle N\rangle$. This equality of the variance and the mean of

[1] Up to (and including) Chapter 5, F will denote a surface-integrated flux, deviating from the notation commonly used in transport phenomena, and the term *flux* will be used loosely.

the distribution of the reactant number on the grain, $P(N)$, defines the POISSON distribution and is independent of the magnitude of $\langle N \rangle$.

Comparison of both equations shows that the failure of the rate equation prediction with respect to the master equation reaction rate is not an implication of a small mean number of particles $\langle N \rangle \ll 1$ [47]. In fact, as long as POISSON statistics of N are preserved by atoms that may freely enter and leave the system, the rate equation treatment is exact for arbitrary $\langle N \rangle$. It fails on small grains because of the *confinement* of reactants to the surface, thus strongly increasing the probability for atoms simultaneously present to meet each other. Consequently, it is then much less probable to find such a pair of reactants on the grain surface than it would have been with a POISSON distribution, and the master equation reaction rate is smaller than the rate equation result. We will shortly recur to this point with a quantitative result in Section 3.1.1. The closely related failure of rate equations to describe second-layer nucleation is reviewed in Section 6.3.1; it corresponds to treating particles as non-interacting.

Equation (3.3) suggests a clear interpretation for the sweeping rate A. There are $N(N-1)/2$ pairs of reactants on the grain, hence $2A$ is the rate at which *pairs of atoms are removed by the reaction.* This is one channel for a pair to exit the system, the other being the desorption of one of the particles, with a total rate $2W$. Therefore, the probability that the given pair of atoms meets before one partner has desorbed is the *encounter probability*

$$p = \frac{2A}{2A + 2W} = \frac{A}{A + W}. \tag{3.4}$$

(Throughout, subscripts will denote certain models and / or simulations from which it is obtained, as well as further specializations.) This formulation clearly expresses the first-passage problem nature. It also provides us with the sweeping rate in terms of the encounter probability,

$$A = \frac{Wp}{1 - p}. \tag{3.5}$$

Before we investigate several ways to calculate p and also examine the implications for the sweeping rate A, we derive an alternative interpretation of the encounter probability.

For numerical simulations, especially for the inclusion in large networks of both surface and gas phase reactions, modified rate equation treatments have been proposed [17, 48]. The basic idea was to replace the coefficient A by another parameter if it exceeds F and W. The methodology is briefly reviewed in Biham and Lipshtat [21], where it amounts to replacing A by W as soon as $F/W < 1$ *and* $W/A < 1$. This procedure can be made plausible for both relevant kinetic regimes, that we will later identify as 'small-' and 'large-grain' regimes. While it quantitatively improves upon the standard rate equation results, it is still an ad hoc procedure. More importantly, it still neglects discreteness of the reactants, and the fact that the kinetics is fluctuation-dominated on small grains.

In a recent development, Garrod [49] proposes a novel modification scheme of the rate equation, not restricted to replacing coefficients, but rather changing the entire functional form of the production rate under certain conditions. The prescription (we specialize to single-species reactions) is that if the average

number of reactants $\langle N\rangle \ll 1$, the RE production rate is modified to read

$$R_{\mathrm{RE,mod}} = C_{\mathrm{mod}} \cdot F\langle N\rangle, \qquad \text{where} \quad C_{\mathrm{mod}} = \frac{k}{k+2W}.$$

C_{mod} is dubbed an "efficiency factor" that quantifies the competition between reaction and desorption, and is introduced to the production rate in a (well-motivated) ad hoc step. Therein, k is the conventional approximation for the reaction rate that should read $2A$ in our notation. With this identification, the efficiency factor obviously coincides precisely with our encounter probability p of (3.4). It is mentioned in Garrod [49] that the rate *for* $C_{\mathrm{mod}} = 1$ can be obtained from the master equation treatment, in the regime of small grains on which additionally, reaction outshines desorption. We may now add that in fact, the production rate $R_{\mathrm{RE,mod}}$ perfectly agrees with the small-grain approximation of the ME result (3.29) *for any* $C_{\mathrm{mod}} \equiv p$. Here we have supplied a genuine derivation for its appearance (earlier in this Section and by deriving (3.29)).

3.1.1 Non-Poissonian statistics

We now establish a simple quantitative relation between the encounter probability p and the deviation of $P(N)$ from a Poisson distribution, in the limit where the mean number of reactants on the grain is small ($\langle N\rangle \ll 1$). One may then truncate the distribution $P(N)$ at $N = 2$, so that $\langle N\rangle \approx P(1) + 2P(2)$ and $\langle N^2\rangle \approx P(1) + 4P(2)$. Therefore, the recombination rate (3.3) reads

$$R_{\mathrm{ME}} \approx 2AP(2). \tag{3.6}$$

On the other hand, R_{ME} can be determined for $\langle N\rangle \ll 1$ with the following simple statistical argument [40, 50]: An atom that lands on the grain will be involved in a reaction if, first, there is another atom already present (true with probability $P(1)$) and, second, if both encounter each other (true with probability p). Thence we have

$$R_{\mathrm{ME}} \approx FP(1)p \approx WP(1)^2 p, \tag{3.7}$$

where the second step uses that, to leading order for $\langle N\rangle \to 0$, $\langle N\rangle \approx F/W \approx P(1)$ (cf. Section 3.8). Combining (3.6), (3.7) and (3.5) we obtain the central relation

$$P(2) \approx \frac{1}{2}(1-p)P(1)^2. \tag{3.8}$$

The Poisson distribution has $P(2) = P(1)^2/2$ for $\langle N\rangle \to 0$. Hence the factor $1-p$ quantifies the deviation of $P(N)$ from the Poisson distribution, corresponding to the depletion of the probability to find pairs, and caused by the recombination reaction.

The relation (3.8) furnishes a simple expression for the discrepancy of the rate equation recombination rate (3.2) compared to the true rate (3.3). For $\langle N\rangle \to 0$ the ratio of the two reads

$$\frac{R_{\mathrm{ME}}}{R_{\mathrm{RE}}} \approx 2P(2)/P(1)^2 \approx 1-p,$$

showing that the confined grain geometry is crucial for the breakdown of the rate equation description.

3.2 Diffusion Model for p

Let us start with a continuum diffusion model to find the encounter probability. We choose the simplest closed two-dimensional surface, a sphere of radius R, on which there is an equidistant lattice of S adsorption sites. This geometry has the important feature that all adsorption sites are equivalent. (We will briefly discuss an example where this is not the case in Section 3.2.4.)

We have to consider a pair of atoms, each of which hops between adjacent sites at a rate a and desorbs at a rate W. Using the translational invariance to our advantage, the situation may equally be described as a single particle moving and desorbing at twice the rates, $2a$ and $2W$, respectively, while the other atom has become an immobile target present throughout. Since we are only concerned with the probability, not the time of the meeting or desorption, this constant common factor of 2 does not influence the result at all — we may thus use the original rates a and W and ask with what probability a particle meets a fixed non-desorbing target.

3.2.1 Stationary Diffusion Problem

Analogously to Krug [40] we now pass to a continuum limit where the occupation probability $n(\mathbf{x})$ of the moving atom obeys a stationary diffusion equation. For the spherical grain of radius R, we model the fixed 'target atom' as a circular area of radius r at the north pole of the sphere. We will always assume the grain large enough to host at least a few hundred adsorption sites, whence $r \ll R$. In the discrete setting the surface is tiled by adsorption sites forming some regular lattice, so that the radius r of the target atom implies a distance of $2r$ between adjacent adsorption sites. It is then easy to show for some common lattice structures that the number of adsorption sites is given by

$$S = g(2R/r)^2,$$

where the factor $g = \mathcal{O}(1)$ reflects the lattice geometry (see Appendix A.1).

For an undirected (total) hopping rate a between adjacent adsorption sites, the diffusion constant of the two-dimensional random walk on the lattice formed by the sites reads $D = a(\delta x)^2/4$; since the length of a single step is $\delta x = 2r$, we have $D = ar^2$ [2]. We thus obtain the stationary diffusion equation

$$D\nabla^2 n + \frac{F}{4\pi R^2} - Wn = 0, \tag{3.9}$$

governing the occupation probability n of the moving atom in the steady state of impingement, desorption and reaction. To employ the azimuthal symmetry of the problem we transform into spherical polar coordinates, where the Laplace operator becomes

$$\nabla^2 = \frac{1}{R^2 \sin\theta} \frac{\partial}{\partial\theta} \sin\theta \, \frac{\partial}{\partial\theta}.$$

We account for the reaction that removes the pair of atoms by prescribing an absorbing boundary condition at the boundary of the fixed atom,

$$n(\theta = r/R) = 0. \tag{3.10}$$

3.2.2 Exact Solution

There exists a unique non-negative solution of (3.9), (3.10) that remains finite at the south pole $\theta = \pi$. It is most easily found after transforming to the new variable $z = \cos\theta$, and is given in terms of Legendre functions of the first kind $P_\nu(z)$ by[2]

$$n(\theta) = \frac{F}{4\pi R^2 W}\left[1 - \frac{P_\nu(-\cos\theta)}{P_\nu(-\cos(r/R))}\right],$$

with the index

$$\nu = -\frac{1}{2} + \sqrt{\frac{1}{4} - \left(\frac{R}{\ell_D}\right)^2}, \tag{3.11}$$

and the *diffusion length*

$$\ell_D = \sqrt{D/W}.$$

The latter is the typical distance that an atom on an unbounded surface would diffuse before it desorbs.

There are now two contributions to the encounter probability of the pair of atoms (already averaged over all possible starting points). First, a certain fraction of all impinging atoms reaches the target by diffusion, namely the fraction of the impingement flux F that enters the target as a diffusion flux:

$$p_{\text{flux}} = 2\pi R \sin(r/R) \times \frac{D}{R}\left.\frac{\partial n}{\partial\theta}\right|_{\theta=r/R} \times \frac{1}{F}.$$

Using a standard identity [51, 8.752, 1.] this yields

$$p_{\text{flux}} = \frac{\sin(r/R)}{2(R/\ell_D)^2}\frac{P_\nu^1(-\cos(r/R))}{P_\nu(-\cos(r/R))}, \tag{3.12}$$

where $P_\nu^1 = -(1-z^2)^{1/2}\,\mathrm{d}P_\nu/\mathrm{d}z$. Second, a (small) fraction of atoms impinges directly on top of the target area. This gives rise to an additional contribution to the encounter probability, namely the (purely geometrical) ratio $u \equiv (1 - \cos(r/R))/2$ of the target versus the total surface area.[3]

Together, the total encounter probability of a pair of atoms becomes

$$p_{\text{diff}} = \frac{\sin(r/R)}{2(R/\ell_D)^2}\frac{P_\nu^1(-\cos(r/R))}{P_\nu(-\cos(r/R))} + \frac{1-\cos(r/R)}{2}. \tag{3.13}$$

Equation (3.13) is the central result of this Section. We emphasize that the encounter probability does not depend on the impingement flux because it only contains information about two atoms that are already assumed to be present on the grain. The following Section will discuss the behavior of the encounter probability in the regimes of physical interest.

[2] Mathematical details can be found in Gradshteyn and Ryzhik [51], Sections 8.7f., especially 8.706f., 8.823 and 8.840 to 8.842. Although the index ν can become complex, all physical expressions are real.

[3] Although this term is of the order of $(r/R)^2 \ll 1$, we found it must be accounted for in certain situations. The essential reason for this is that, while $u \ll p_{\text{flux}} < p_{\text{diff}}$ is valid in *all* regimes of interest, we will also be concerned with the complementary quantity $1 - p$ appearing in (3.5). This however can become arbitrarily small, and particularly of the order of u or smaller. Appendix A.2 will show that inclusion of u even *simplifies* further analysis.

3.2.3 Limiting Behavior

The different asymptotic regimes of interest are defined by the ordering of the three length scales, r, R and ℓ_D. As mentioned before, $r \ll R$ is mandatory such that the dust grain can host a reasonable number of adsorption sites. Clearly, $r \ll \ell_D$ as well, because otherwise the adatom hardly performs any hops before it desorbs again. We first derive the approximate behavior based on these assumptions, and hence common to all relevant regimes. In terms of the parameters of (3.13) the common feature is that $r/R \ll 1$, thus being the appropriate quantity in which to expand first.

The actual calculation involves some subtleties, whence we relegate most of this to Appendix A.2. To leading order in r/R, one obtains[4]

$$p_{\text{diff}}^{-1} \approx \left(\frac{R}{\ell_D}\right)^2 \left[\ln\left(\frac{2R}{r}\right)^2 - 2\gamma - 2\psi(\nu+1) - \pi\cot(\nu\pi)\right]. \tag{3.14}$$

Here $\psi(z) \equiv \mathrm{d}(\ln\Gamma)/\mathrm{d}z$, with $\Gamma(z)$ the Γ-function, and $\gamma = -\psi(1) \approx 0.577215665$ is Euler's constant. To better understand the behavior of the encounter probability we examine the two remaining regimes in which r is the smallest length scale of the problem. The relation between the grain radius R and the diffusion length ℓ_D then defines 'small' and 'large' grains.

3.2.3.1 Small Grains

This regime is defined by $r \ll R \ll \ell_D$, and hence $|\nu| \ll 1$. A first-order expansion of p_{diff} about $\nu \to 0-$ yields $p_{\text{diff}} \approx 1 + \nu[\ln(2R/r)^2 - 1]$, so that with $\nu \approx -(R/\ell_D)^2$ we have[5]

$$p_{\text{diff}} \approx 1 - \left(\frac{R}{\ell_D}\right)^2 \left[\ln\left(\frac{2R}{r}\right)^2 - 1\right] \to 1.$$

With a small desorption rate each atom spends enough time on the grain to fully explore it many times. For low fluxes, the recombination efficiency is then limited by the rare event that two atoms are simultaneously present on the grain. If this situation arises however, they almost surely meet. This is the regime where the failure of the rate equation approach is most pronounced, see Section 3.1.1.

3.2.3.2 Large Grains

Here on the other hand, $r \ll \ell_D \ll R$ and $\nu = -1/2 + i\lambda$ with $\lambda \approx R/\ell_D \gg 1$. Owed to the form of ν, the cotangent in (3.14) is purely imaginary and cancels the imaginary part of $\psi(\nu+1)$ (cf. Footnote 4). The Γ-function behavior implies $\psi(z) \approx \ln z + \mathcal{O}(z^{-1})$ for arguments of large modulus, which leads to $\operatorname{Re}\psi(\nu+1) \approx \ln(R/\ell_D)$ for the remaining real part of ψ. Together this yields

$$p_{\text{diff}} \approx \left(\frac{\ell_D}{R}\right)^2 \frac{1}{\ln(2\ell_D/r)^2 - 2\gamma} \ll 1. \tag{3.15}$$

[4] This approximation does not invalidate the reality of p for values of ν of the form (3.11).

[5] We will treat logarithms of large quantities as being of the order of unity throughout, consequently retaining coequal numerical constants in sums, although the logarithms are usually significantly larger. This might slightly blur the fundamental functional relation, but it is numerically adequate in many realistic situations.

Here, low fluxes imply a low recombination efficiency due to fast desorption, which does not allow the atoms to spend sufficient time on the grain to react. In contrast to the small-grain regime, the confinement of the atoms to the grain surface is not felt, and hence the rate equation continues to apply even for small numbers of reactants. This is the *second order* regime of Biham and Lipshtat [21] and Krug [40].

3.2.3.3 Translation to Discrete Parameters

For consistency and easy comparison with later results we translate our results back to the original language of the discrete picture: This is done via the relations $(2R/r)^2 = S/g$, $\ell_D/r = \sqrt{(D/r^2)/W} = \sqrt{a/W}$, and accordingly $R/\ell_D = \sqrt{SW/(4ga)}$. Figure 3.2 shows the encounter probability p_{diff} as a function of the (logarithmic) grain size for three representative values of the ratio $W/a \ll 1$.

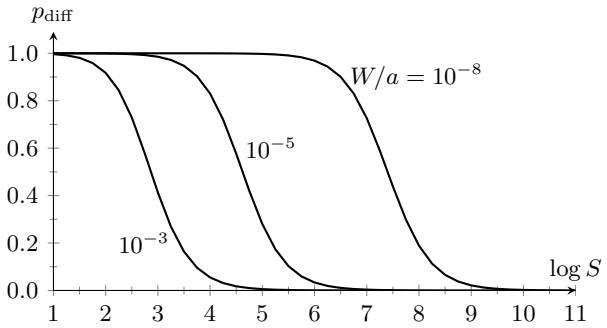

Figure 3.2: Encounter probability p_{diff} as a function of the grain size S (on a logarithmic scale to the basis of 10). The grain size discriminating between small and large grains is given by a/W. Starting at unity and monotonically decreasing, one can see the gentle roll-off of the encounter probability to take place around this critical size, yet of very similar shape in all three cases.

In the small-grain regime, now characterized by $SW/a \ll 1$, we have the encounter probability

$$p_{\mathrm{diff}} \approx 1 - \frac{SW}{4ga}\left[\ln(S/g) - 1\right], \tag{3.16}$$

while for large grains, given by $W/a \ll 1 \ll SW/a$, we obtain

$$p_{\mathrm{diff}} \approx \frac{4ga}{SW}\frac{1}{\ln(4a/W) - 2\gamma}. \tag{3.17}$$

3.2.4 Disc Geometry

The idea to obtain the encounter probability from a stationary diffusion equation was demonstrated in Krug [40] for the simpler case of a flat disc geometry. The outer boundary (at the radius R) is taken to be reflecting, and the fixed absorbing target atom area is a small disc of radius r in its center.

The asymptotic results obtained *ibid.* assume logarithms of large arguments to be generally large as well (dominating possible numerical constants of the order of unity). For better comparison (and foreseeing later important consequences) we re-derived the asymptotics including such numerical (pre-)factors, see Appendix A.3 for details. Moreover, we included the contribution for encounters "by deposition". One may easily translate the results to the discrete parameter set analogously to the spherical case. This shows that, first, in both regimes the functional form as well as the pre-factors coincide.

In the "large-disc" regime the asymptotic behavior precisely agrees with the sphere result (3.17), even *including the logarithmic factor* (or coequal $\mathcal{O}(1)$ terms). However, there is a slight difference in the "small-disc" regime, where

$$p_{\mathrm{diff,disc}} \approx 1 - \frac{SW}{4ga} \left[\ln(S/g) - 3/2\right],$$

with the lattice factor g defined before, compared to (3.16) with a constant 1 instead of 3/2. Numerical evaluation shows that under realistic assumptions on the parameters, there is only a small (of the order of a few per cent) difference of both geometries in between these limiting cases.

We regard this as strong evidence supporting our conviction that curvature effects do not matter with $S \gg 1$: The underlying reason is that the radius of curvature (in terms of the lattice spacing) is always of the same order as the (linear) system size. In the large-grain regime, the random walk typically does not travel long enough to feel the radius of curvature, as $\ell_D \ll \sqrt{S}$, so that obviously, curvature remains meaningless. But as soon as $\ell_D \sim \sqrt{S}$, essentially the whole lattice is explored anyway, and the small fraction of unvisited sites depends on the failure of *locally* dense sweeping, not on curvature.

3.3 Random Walk Theory

There are several reasons to strive for an alternative model that allows calculation of the encounter probability. First, as we are basically considering a reaction-diffusion system here, the 'atomistic' point of view of the random walk is clearly more natural than a continuum theory as described above. Second, we will see that the random walk picture can be generalized to a lattice with distorted aspect ratio without substantial complications. It is therefore possible to study, on a fundamental quantitative level, the influence of a change in the confining geometry which was already found to be of great importance, cf. Section 3.1.1.

3.3.1 Our Model

We start our treatment with a homogeneous lattice of adsorption sites, i.e., all sites are equivalent, and the lattice extends to L_j lattice sites in the jth of d dimensions, with periodic boundary conditions. Two walkers are randomly placed on two (not necessarily different) sites of the lattice. Then they move between nearest-neighbor sites with an undirected hopping rate a (corresponding to diffusion of the atoms on the grain surface), and may desorb at a constant rate $W \ll a$, ending the random walk realization. In the language of random walk theory, the latter property is described as a *mortal* random walk. In our

case, the survival probability per step reads

$$\xi = 1 - \frac{W}{a+W} = \frac{a}{a+W} = \frac{1}{1+W/a} \lesssim 1 \tag{3.18}$$

(obviously, only the ratio of the rates W/a can enter the treatment as long as we consider the discrete-time two-particle problem). When the two walkers meet by one hopping onto the site the other one occupies, they react and this random walk realization has ended successfully. The probability for this to happen is the encounter probability p defined in Section 3.1.

Although the physical picture might rather suggest a continuous-time random walk (CTRW) version with an appropriate waiting time distribution, we will only consider the discrete-time variant herein. This keeps the analytical treatment as easy as possible, and we will later argue and numerically prove (cf. Section 4) that it accurately describes our situation. Homogeneity of the lattice implies that the problem reduces to that of a single (mortal) walker to meet a target site, cf. Appendix A.4.

3.3.2 Exact Results

Using only well-known facts from the theory of random walks, we refer the reader to Appendix A.4 for details of the calculation. For the encounter probability on a lattice as described above, one obtains an expression already found, e.g., in den Hollander and Kasteleyn [52], viz.

$$p_{\mathrm{rw}}^{-1} = (1-\xi)SP^*(\mathbf{0};\xi) = \sum_{\mathbf{m}\in\Omega} \frac{1-\xi}{1-\xi\lambda(2\pi\mathbf{L}^{-1}\mathbf{m})}. \tag{3.19}$$

Here, $S = \prod_{j=1}^{d} L_j$ is the total number of sites and $P^*(\mathbf{0};\xi)$ is the number of times a mortal walker on a periodic homogeneous lattice returns to the origin. Ω denotes the lattice, $\mathbf{m}$ is a 'lattice vector' of d integer components $0 \le m_j \le L_j - 1$ with $j = 1,\ldots,d$, and $\mathbf{L} = \mathrm{diag}(L_1,\ldots,L_d)$. The type of lattice is represented by the *structure function* λ (basically a discrete FOURIER transform of the normalized transition probability) of the walk. We specify to $d = 2$ at this point, where it reads $\lambda(\mathbf{k}) = (\cos k_1 + \cos k_2)/2$ for an isotropic walk on a square lattice that we will further on refer to as 'type (a)', and $\lambda(\mathbf{k}) = [\cos k_1 + \cos k_2 + \cos(k_1 + k_2)]/3$ for the isotropic walk on a triangular lattice (coordination number 6), now designated as 'type (b)'.

As suggested by the applications we have in mind, we focus on the two-dimensional case where both $L_{1,2} \gg 1$, and with 'long survival' as defined by $1 - \xi \ll 1$. Under these conditions, (3.19) affords several regimes which are defined by comparison of all dimensionless 'lengths'. Introducing the typical single-atom random walk length

$$\ell = \sqrt{a/W} \gg 1,$$

we distinguish 'large' lattices for which $1 \ll \ell \ll L_{1,2}$ and 'small' lattices with $1 \ll L_{1,2} \ll \ell$. We will later return to the intermediate regime in which one lattice length is smaller, yet the other one larger than the random walk length.

The aforementioned cases (a) and (b) belong to a fairly general class of walks for which one summation in equation (3.19) can be carried out explicitly [42]. We

generalized the result to the case $L_1 \neq L_2$, and present it in Appendix A.5. The single-sum expression thus obtained is used whenever we want to numerically evaluate p_{rw}, and we have implemented this evaluation in a small and straightforward `GNU Octave` script.

Note that the encounter probability given in (3.19) includes walkers starting on the same site, counted as encounters on the zeroth step. For comparisons we will sometimes need the encounter probability $\tilde{p}_{\mathrm{rw}}$ calculated such that it does *not* allow this special initial condition, but only counts meetings by hopping. Both quantities are related by

$$p_{\mathrm{rw}} = \frac{1}{S} + \left(1 - \frac{1}{S}\right) \tilde{p}_{\mathrm{rw}},$$

as one can see by splitting up p_{rw} according to the starting site of the second walker, i.e., either on the same site as the first one (with probability $1/S$), or on any other site (with probability $1 - 1/S$). This leads to the expression

$$\tilde{p}_{\mathrm{rw}} = \frac{S p_{\mathrm{rw}} - 1}{S - 1}$$

in terms of p_{rw}. Similarly, $\tilde{p}$ with other subscripts will henceforth denote probabilities p that are obtained from other models using the corresponding analogous convention, i.e., excluding an encounter due to coinciding initial positions. In the context of hydrogen recombination on dust grain surfaces, this convention is realized by the mechanism of 'Langmuir-Hinshelwood rejection' of atoms that impinge on top of another [53, and references therein].

3.3.3 Large-Lattice Approximation

Formally, large lattices are characterized by $S \gg a/W \gg 1$ or, more precisely, by $1 \ll \ell \ll L_{1,2}$, but one may also define this regime by the fact that boundary conditions and (apart from the initial placement) the total number of adsorption sites no longer matter. Even if those boundaries were not periodic, but really affected the random walker, e.g., by reflection, the walk might *either* come close to the target *or* experience boundary effects due to the finiteness of the lattice, but not in the same walk realization. One may then send $L_{1,2} \to \infty$ in (3.19), and the sum becomes an area integral. After some manipulations detailed in Appendix A.6, one obtains[6]

$$p_{\mathrm{rw}} \approx \frac{a}{SW} \begin{cases} \pi \frac{1}{\ln[8a/W]} & \text{square lattice,} \\ \frac{2\pi}{\sqrt{3}} \frac{1}{\ln[12a/W]} & \text{triangular lattice,} \end{cases} \tag{3.20}$$

with relative errors of $\mathcal{O}(1 - \xi)$.

3.3.4 Small-Lattice Approximation

In this regime, $1 \ll L_{1,2} \ll \ell$ or $a/W \gg S \gg 1$, and again we use results for $P^*(\mathbf{0}; \xi)$ from the random walk literature.

[6] For approximations here and in the following we will treat $1 - \xi$ and $(1 - \xi)/\xi = W/a$ synonymously due to $\xi \lesssim 1$, and will no longer mention this when it only introduces higher-order errors compared to the desired accuracy. Moreover, we will consider logarithms as being of the order of unity, which can render some expressions more cumbersome but is numerically adequate.

We first restrict ourselves to the quadratic lattice, i.e., $L_1 = L_2 = \sqrt{S}$. Note that the result is later generalized to $L_1 \neq L_2$, whence we refer the reader to Section 3.4.4 for details of the calculation. Generally, the expansion for $1 - \xi \ll S^{-1} \ll 1$ reads

$$P^*(\mathbf{0};\xi) = \frac{1}{S(1-\xi)} + c_1 \ln(cS) + \mathcal{O}\left(S^{-1}, S(1-\xi), \sqrt{1-\xi}\right),$$

with real constants c and c_1. This is shown in Montroll [42], which gives the first calculations providing the important pre-factor inside the logarithm (for square and triangular lattices), later extended and subject to minor corrections in den Hollander and Kasteleyn [52]. The earlier and easily accessible derivation in Montroll and Weiss [54] does not deliver this pre-factor, unfortunately. For the encounter probability this yields

$$p_{\mathrm{rw}} \approx 1 - \frac{SW}{a} c_1 \ln(cS). \tag{3.21}$$

Note that the original expansion is valid only for $(1-\xi)S\pi^{-1}\ln(cS) \ll 1$, or equivalently, as long as $1 - p_{\mathrm{rw}} \ll 1$. This would thus make a more precise definition of a 'small lattice'.

The constant c_1 takes the value $1/\pi$ for the square lattice case (a), and $c_1 = \sqrt{3}/(2\pi)$ for the triangular lattice (b), respectively. The crucial factor c *inside* the logarithm appears in the different guise c_2 in Montroll [42], which is related to ours by $c_2/c_1 = \ln c$. For the square lattice this ratio reads

$$\begin{aligned}\ln c &= \frac{\pi}{3} + 2\left(\gamma - \ln\pi + \frac{1}{2}\ln 2\right) + 4\left[\mathrm{e}^{-2\pi} + \frac{3}{2}\mathrm{e}^{-4\pi} + \frac{4}{3}\mathrm{e}^{-6\pi} + \ldots\right] \\ &\approx 0.612807020,\end{aligned}$$

whereas for the triangular lattice one obtains

$$\begin{aligned}\ln c &= \frac{\pi}{2\sqrt{3}} + 2\left(\gamma - \ln\pi + \frac{1}{2}\ln 3\right) - 4\left[\mathrm{e}^{-\sqrt{3}\pi} - \frac{3}{2}\mathrm{e}^{-2\sqrt{3}\pi} + \frac{4}{3}\mathrm{e}^{-3\sqrt{3}\pi} - \ldots\right] \\ &\approx 0.853262084.\end{aligned}$$

We used standard rounding and checked the consistency of the numerical evaluation against, first, the original figures and, when available, the improved ones from den Hollander and Kasteleyn [52].

The proper continuum limit of these results will be analyzed in Section 3.5, not only because it is of genuine theoretical interest, but also to compare with results of the diffusion approach.

3.3.5 A Heuristic Derivation

This Section describes an argument that originally was presented in Lohmar and Krug [7] to re-cover the results of the diffusion model on the sphere. It is given here as it is based on random walk considerations; the fact that it may serve as an explanation for continuum models as well will be briefly returned to in Section 3.5.

All asymptotic results obtained so far have a characteristic logarithmic factor. Its argument is of the order of the number of sites that the random walk of

the moving atom has seen (we still consider the first H atom fixed and present throughout, as explained at the beginning of Sections 3.2 and 3.3.2): For the two-dimensional random walk, a well-studied quantity is the number of *distinct* sites the walker has visited in $n \gg 1$ steps. It is asymptotically given by

$$N_{\mathrm{dis}} \approx \frac{\pi n}{C \ln(Bn)},$$

where C and B are constants depending on the lattice type, viz. $C = 1$ and $B = 8$ for the square, and $C = \sqrt{3}/2$ and $B = 12$ for a triangular lattice, respectively (Montroll and Weiss [54], or Hughes [55] as a textbook reference). Note that the above N_{dis} is the leading term of an asymptotic expansion, and thence a poor estimate for moderate values of n. We relate the number of steps to the time passed by $n = at$, which is a good approximation for $n \gg 1$.

Our reasoning is complemented by the effective residence time t_{res} of the moving atom in the two limiting regimes. For the encounter probability very small (large grains / lattices), only a small portion of the grain is explored, and (to first order in $a/(SW)$) the residence time is governed by desorption, $t_{\mathrm{res}} \approx 1/W$. The atom has thence performed $n = a/W$ hops and visited $N_{\mathrm{dis}} \approx (\pi/C)(a/W)/\ln(Ba/W)$ distinct sites. Since the encounter probability averages over all spatial initial conditions, it is simply given by the ratio N_{dis}/S, such that

$$p_{\mathrm{rw,heur}} \approx \frac{\pi a}{CSW} \frac{1}{\ln(Ba/W)}.$$

Comparison with (3.20) shows that both expressions agree *exactly* including the pre-factor inside the logarithm.

On the other hand, for an encounter probability near unity (small grains / lattices), the stay of the atom is almost always ended by recombination, hence the residence time reads $t_{\mathrm{res}} \approx 1/A$. By this time, the entire grain has been explored, and the number of distinct sites visited has saturated at $N_{\mathrm{dis}}(n = at_{\mathrm{res}}) \approx S$. Inversion (again to first order) yields $t_{\mathrm{res}} \approx S \ln[BC/\pi \cdot S] \cdot C/(\pi a)$. The atom desorbs prior to any reaction with probability $1 - p$, or alternatively in this regime with a probability given by the desorption rate W times the residence time $1/A$. This gives

$$p_{\mathrm{rw,heur}} \approx 1 - \frac{CSW}{\pi a} \ln[BC/\pi \cdot S].$$

We have to compare to p_{rw} as of (3.21), wherein a factor c_1 occurs. It can be read off to satisfy $c_1 = C/\pi$ for the types of lattice considered here, so that again, pre-factors and functional dependence of both results agree. The pre-factor *inside* the logarithm has to be evaluated numerically, which yields $\ln BC/\pi$ values of $0.934711656\ldots$ and $1.196335728\ldots$ for type (a) and (b) lattices, respectively, to be compared with the values of $\ln c$ given in Section 3.3.4. This is not a good agreement, but understandably so: Not even accounting for the nature of the N_{dis} expansion, the ensuing *heuristic* derivation assumes the walker does not die until it has visited all S sites, and is based on the inversion of the transcendental equation $N_{\mathrm{dis}}(at) = S$, which is approximated by one iteration. It is the very pre-factor just mentioned that suffers from this approximation.

3.4 The Distorted Lattice

3.4.1 Motivation and Basic Definitions

On the one hand we have seen that changes in the model to calculate p, which one might have suspected to be of great importance, only leave a rather minute imprint on the result: See, e.g., the comparison of the disc geometry with reflecting boundary, compared to the closed surface of the sphere, Section 3.2.4. We will find the same phenomenon in the overall comparison of the continuum to the random walk models (Section 3.5) — all the time, the only difference in asymptotic results for both regimes occurs solely in the pre-factor inside the logarithm.

The corresponding discrepancies show in the same order of magnitude in both cases, although in the first case (sphere versus disc), topology and boundary conditions fundamentally differ, in contrast to the latter comparison. With hindsight, this is strong quantitative evidence that curvature and connectivity effects are not responsible for the difference between diffusion and random walk model results, as we had considered at some point.

On the other hand one cannot deny that boundary conditions and the general shape of the lattice should have *some* effect on random walk properties, at least in certain regimes, and quite likely, on the encounter probability. Questions concerning the influence of confined geometries, albeit without desorption and hence focusing on mean first-passage times rather than on probabilities, have been detailedly analyzed in a recent remarkable series of papers [56–58]. We have experienced the peculiarity of spatial dimension two for the random walk and the encounter probability — one question that naturally arises is what happens for a large distortion such that the lattice becomes *effectively* one-dimensional?

To examine such effects, the random walk model suggests itself, i.e., we continue to examine periodic torus lattices with lengths L_1 and L_2 now generally different. The case $L_1 \neq L_2$ will be referred to as *rectangular*, while $L_1 = L_2$ is called *quadratic*. Note that we use the term *square* exclusively to label the lattice type (internal structure) as opposed to its shape or geometry. We still assume all lengths $L_{1,2}$, $\ell \gg 1$ in view of the applications, and without loss of generality set $L_2 \leq L_1$, which might further be specialized to $L_2 \ll L_1$. Ordering lengths, we then have the following three (instead of the former two) refined asymptotic regimes:

- The earlier large-lattice regime $1 \ll \ell \ll L_2 \leq L_1$.
- The intermediate regime $1 \ll L_2 \ll \ell \ll L_1$. This is a new situation for rectangular lattices, where the walk easily sweeps one dimension but is typically short compared to the other.
- The known small-lattice regime $1 \ll L_2 \leq L_1 \ll \ell$.

We define the *aspect ratio* as $\mu := L_2/L_1 \in (0, 1]$.

The large-lattice regime will not be of much interest for the remainder of this Section. As there, the walker does not feel boundaries, the double integral limit of (3.19) appropriately yields a result merely depending on the *total* number of sites S, not on the lattice lengths, cf. Section 3.3.3. Any analytical refinement for the rectangular situation can only provide very limited insight, viz. regarding the

nature and direction of subordinate corrections (depending on the aspect ratio L_2/L_1) to the small encounter probability. These corrections are rooted in the rare events when a random walker actually experiences the periodic boundary *and* comes close to the target during one walk.

3.4.2 Plots of p_{rw}

We show the encounter probability p_{rw} on a type (a) square lattice as a function of (the logarithm of) the aspect ratio μ, while keeping S and ξ constant inside each graph (we checked that the type (b) lattice shows no qualitative difference). Figure 3.3 starts in the small-lattice regime for the quadratic case (rightmost in the plot), Figure 3.4 shows the results starting in the large-lattice regime, and in both cases, we present one absolutely small ($S = 4 \times 10^2$) and one absolutely large lattice ($S = 4 \times 10^6$).

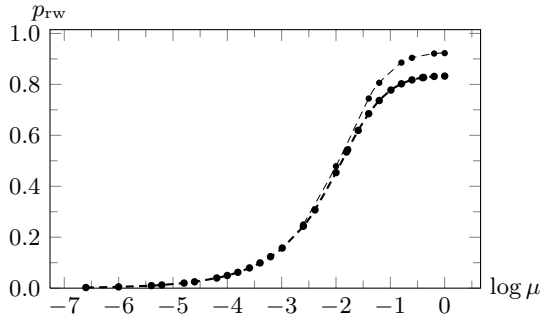

Figure 3.3: Encounter probability (on a square lattice) as a function of $\log \mu$, for fixed sizes $S = 4 \times 10^6$ (thick) and $S = 4 \times 10^2$ (thin), respectively, and $SW/(4a) = 10^{-2}$ in both cases.

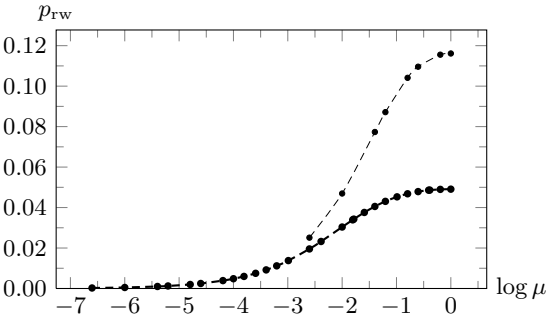

Figure 3.4: As Figure 3.3 with $SW/(4a) = 1$.

In each instance the encounter probability exhibits a stark monotonic decline upon distortion (i.e., moving left in the Figures), although for the absolutely small lattice, the shape is less pronounced and the curve ends at a fair fraction of its peak value. First, we analyze separately several aspects of this behavior, and finally we will put our findings together in a qualitative explanation.

3.4.3 Extreme Distortion

The simplest situation arises if we use the two-dimensional p_{rw} result on a type (a) lattice, but let one dimension shrink to a single lattice unit ($S = L_1 L_2 = L \cdot 1$). From (3.19) we then obtain

$$p_{\mathrm{rw}}^{-1} = \sum_{m=0}^{S-1} \frac{1-\xi}{1-(\xi/2)\left(\cos(2\pi m/S)+1\right)}.$$

Second, we directly employ a truly one-dimensional lattice, where the sum for an unbiased walk (different structure function!) reads

$$p_{\mathrm{rw,\,1d}}^{-1} = \sum_{m=0}^{S-1} \frac{1-\xi}{1-\xi\cos(2\pi m/S)},$$

different from the former limit. Obviously, $p_{\mathrm{rw,\,1d}} > p_{\mathrm{rw}}$ for a given number of adsorption sites S and equal ξ.

Explaining this result for the "extremely distorted" situation will point out one factor in the general problem. As the two-dimensional lattice is periodic, it has now become a torus in which the one-lattice-unit direction is completely "wrapped up", and the walker still performs steps in this direction. Quite differently, the genuinely one-dimensional walk only performs steps in the extended direction. The net effect is that the two-dimensional walker wastes on average half of the steps it takes, moving in the 'wrong' dimension and not coming any closer to the target site. Indeed, this suffices to re-gain one result from the other heuristically: The 2d-walk then corresponds to a 1d-walk with the same desorption rate W, but with the undirected hopping rate effectively halved by the useless waiting steps, $a \to a/2$. This implies $(1-\xi)/\xi \to 2(1-\xi)/\xi$, and minimal manipulation of the two expressions given above yields that this casts the 1d-walk result into that for the two-dimensional walk. A related phenomenon for an immortal walker in the presence of an absorbing boundary has been explained comparing the structure functions and equating wasted steps to a sojourn probability by Montroll and Scher [59].

3.4.4 Generalization of the RW Result

The small-lattice asymptotics of Section 3.3.4 can be generalized to the case $L_1 \neq L_2$. The calculations are shown in some detail in Appendix A.7.

With some re-ordering we obtain the following generalization of $P^*(\mathbf{0};\xi)$ for a distorted lattice:[7]

$$\begin{aligned} P^*(\mathbf{0};\xi) = {} & \frac{1}{L_1 L_2 (1-\xi)} + \frac{\ln L_1}{r\pi(1-2q_0)} \\ & + \frac{\frac{L_2}{3L_1} + \frac{1}{r\pi}\left[2\gamma + 2\ln(2/\pi) - \ln(1+\eta)\right] + S_3^{(0)}/r}{2(1-2q_0)} \\ & + \frac{-\frac{1}{3} + \frac{(3\eta-1)\pi}{36r}\frac{L_2}{L_1} + S_3^{(1)}/r}{2(1-2q_0)L_1 L_2} + \mathcal{O}(L^{-4}) + \mathcal{O}(1-\xi)^{1/2}, \end{aligned} \tag{3.22}$$

[7] To stay close to the notation in Montroll [42], we re-use the notation r and η only for the remainder of this Section and in the associated Appendix A.7; these quantities are unrelated to any radial coordinate or efficiency elsewhere in this Part.

where, first of all, terms are arranged in orders of $\sqrt{1-\xi}$, as this is the smallest quantity, and, inside, according to orders of $L_{1,2}$. q_0 is the probability for a step into a lattice unit direction (cf. Appendix A.5), and r and η are defined in Appendix A.7. Here it suffices to say that they take the values $r = 1 = \eta$ for the square lattice case (a), and $r = \sqrt{3}/2$, $\eta = 1/3$ for the triangular lattice case (b), respectively. The sum contributions $S_3^{(0,1)}$ have to be evaluated for the lattice type at hand; we could easily do this only for the square lattice, for which they read ($r = 1 = \eta$ and $q_0 = 1/4$ inserted)

$$\begin{aligned} S_3^{(0)} &= \frac{4}{\pi}\Big(\mathrm{e}^{-2\pi\mu} + \frac{3}{2}\,\mathrm{e}^{-4\pi\mu} + \frac{4}{3}\,\mathrm{e}^{-6\pi\mu} + \dots\Big), \\ S_3^{(1)} &= -\frac{4\pi}{3}\mu\Big(\mathrm{e}^{-2\pi\mu} + 3\,\mathrm{e}^{-4\pi\mu} + 4\,\mathrm{e}^{-6\pi\mu} + \dots\Big) \\ &\quad + \frac{8\pi^2}{3}\mu^2\Big(\mathrm{e}^{-2\pi\mu} + 6\,\mathrm{e}^{-4\pi\mu} + 12\,\mathrm{e}^{-6\pi\mu} + \dots\Big), \end{aligned} \tag{3.23}$$

Note however that also for the triangular lattice, S_3 can be expected to be a small correction (in the vicinity of the quadratic lattice) to the other terms in $P^*(\mathbf{0};\xi)$.

The expansion is asymmetric in the lattice lengths, since they enter different approximations: In the given form, L_2 is the limit of the sum which is exactly and explicitly evaluated (see Appendix A.5), whereas L_1 is the limit in several Euler-MacLaurin formulas. Clearly, one expects the expansion to fit best for $L_2 \leq L_1$, and this is the ordering we will assume consistently.

We collect the assumptions entering the result: We need $L_1 L_2(1-\xi) \ll 1$, since otherwise, the overall form of the expansion is meaningless., cf. Eq. B35 of Montroll [42]. Further it is crucial that the evaluated sum limit is small, $L_2 \ll \ell = \sqrt{\xi/(1-\xi)} \approx 1/\sqrt{1-\xi}$, for the first summand's expansion to converge (*ibid.* Eqs. B11f.), and the other large for the Euler-MacLaurin formula, $L_1 \gg 1$. Finally, the aspect ratio L_2/L_1 must not be too small as to allow convergence in Eqs. B28ff. *ibid.*, also see (3.23). These conditions are satisfied in the small-lattice regime whenever L_2/L_1 does not become too small, and for the intermediate regime provided that *additionally*, $L_1 L_2(1-\xi) \ll 1$.

Obviously one could exchange the roles of the lengths $L_2 < L_1$ in the derivation, the sum evaluated in the 1-direction instead. Therefore, the results above will remain valid upon swapping L_1 against L_2 as long as the corresponding conditions remain satisfied; we call this the 'swapped-lengths' version. Owed to $L_1 \ll \ell$ we are restricted to the small-lattice regime, and detailed inspection of the B28 derivation of Montroll [42] shows the remaining condition to read $L_1/L_2^3 \ll 1$.

Checking for consistency between the two expressions has to take place in the small-lattice regime and has to account for the changing orders of several terms. A numerical comparison between both approximation versions and the exact p_{rw} showed that in fact, the swapped-lengths version better reproduces the exact result, not bothered by the aforementioned convergence issues. This is a minute problem, and both versions agree with each other and the exact result (for a square lattice) over a certain range of distortions. We tested $\mu = L_2/L_1 = 1/4 \dots 1$ for the small-lattice regime with $S = 4 \cdot 10^6$, $a/W = 10^8$, where the swapped-lengths version agrees with the exact result farther down to $\mu \sim 1/10$.

3.4.5 Small Distortion

With the result of Section 3.4.4 we can complement our earlier study of extreme distortion by an analysis of the effect of a small deformation of the quadratic lattice. What are the effects of the global change of geometry on the random walk if we start to distort a quadratic lattice of $S = L^2$ sites, keeping W/a and S fixed. The latter requirement is crucial since (as can be seen from previous results) changing S would dominate more subtle effects, hindering us from distorting to "nearby" integer lengths as $(L-1)(L+1) = S-1$.

Instead, we will treat p_{rw} as a function of μ, S and ξ, where we keep the latter two arguments constant and assume μ to vary continuously. The local behavior around the quadratic shape value μ^* is meaningful provided higher-order terms do not restrict its validity to an interval too small. We do not feel this is a restriction, essentially since we cannot conceive of a mechanism that could render $p_{\mathrm{rw}}|_{S,\,\xi=\mathrm{const},\,\mu\leq\mu^*}$ non-monotonic.

Here we focus on the small-lattice regime for two reasons: First, one expects aspect ratio effects to be most prominent there, second, we there know the general asymptotic behavior from Section 3.4.4. Intermediate lattices are out of reach starting from a square lattice, and large lattices were argued before to be rather insusceptible to distortion.

We have $\mathrm{d}^2p/\mathrm{d}\mu^2 = [S(1-\xi)]^{-1}\frac{\mathrm{d}^2(P^*(\mathbf{0};\xi))^{-1}}{\mathrm{d}\mu^2}$, and at the extremal point, $\frac{\mathrm{d}^2(P^*(\mathbf{0};\xi))^{-1}}{\mathrm{d}\mu^2} = -(P^*(\mathbf{0};\xi))^{-2}\frac{\mathrm{d}^2P^*(\mathbf{0};\xi)}{\mathrm{d}\mu^2}$, since the first derivative $\mathrm{d}p/\mathrm{d}\mu|_{\mu=\mu^*}$ vanishes due to $L_1 \leftrightarrow L_2$ symmetry of p. All we need to know here is the sign of the second $P^*(\mathbf{0};\xi)$ derivative. We employ the approximation of Section 3.4.4 and suppose that the dominant contributions to $P^*(\mathbf{0};\xi)$ also dominate the sign of the second derivative. The mere μ dependence of the expression (in terms of S and μ instead of any lengths) then reads

$$\begin{aligned} P^*(\mathbf{0};\xi) = \mathrm{const} + \frac{\ln\sqrt{S/\mu}}{r\pi(1-2q_0)} + \frac{\mu/3 + S_3^{(0)}/r}{2(1-2q_0)} \\ + \frac{\frac{(3\eta-1)\pi}{36r}\mu + S_3^{(1)}/r}{2(1-2q_0)S} + \mathcal{O}\left(L^{-4}, (1-\xi)^{1/2}\right), \end{aligned}$$

whence in the second derivative, only the S_3 contributions and those from the square root term survive, viz.

$$\frac{\mathrm{d}^2P^*(\mathbf{0};\xi)}{\mathrm{d}\mu^2} \approx \frac{\frac{1}{\pi}\mu^{-2} + \mathrm{d}^2(S_3^{(0)} + S_3^{(1)}/S)/\mathrm{d}\mu^2}{2r(1-2q_0)}.$$

The $S_3^{(1)}$ contribution is irrelevant due to the S^{-1} factor, and

$$\frac{\mathrm{d}^2S_3^{(0)}}{\mathrm{d}\mu^2} = 16\pi\left(\mathrm{e}^{-2\pi\mu} + 6\,\mathrm{e}^{-4\pi\mu} + 12\,\mathrm{e}^{-6\pi\mu} + \dots\right),$$

where (as before), we only treat case (a) with $r = 1 = \eta$. We numerically evaluate this at $\mu = 1$ and obtain an approximate figure of 0.095. Thence, $\frac{\mathrm{d}^2P^*(\mathbf{0};\xi)}{\mathrm{d}\mu^2} > 0$, and consequently, $\mathrm{d}^2p/\mathrm{d}\mu^2 < 0$: The encounter probability of the random walk in the small-lattice regime has a maximum for the quadratic lattice, and it decreases with any distortion from this shape.[8] This is the quantitative basis for the heuristic arguments in Section 3.4.7.

[8] We checked by numerical evaluation that $P^*(\mathbf{0};\xi)$ is monotonic, or equivalently, that the

3.4.6 The Quasi-One-Dimensional Limit

Between the quadratic and the extremely distorted cases we want to clarify the nature of the transition to one-dimensionality. We will examine a lattice whose macroscopic structure approaches one-dimensionality as the aspect ratio goes to zero.

To this end we first establish a relation between the regimes of the one-dimensional and the distorted two-dimensional lattice. The 2d-large-lattice regime is characterized by ℓ being the smallest length scale, which does not sensibly correspond to any one-dimensional regime. This obviously implies that the large-lattice regime of a one-dimensional lattice (length $L \gg \ell_{1\mathrm{d}}$) is the analogue of the 2d-intermediate lattice given by $1 \ll L_2 \ll \ell \ll L_1$: In both cases, exactly one lattice dimension is much larger than the typical random walk length. The analogy is intuitive, as a 2d-intermediate lattice, with an ℓ circle around the fixed target, looks just like a one-dimensional large lattice when viewed "from afar". Similarly, the 2d-small lattice ($1 \ll L_2 \ll L_1 \ll \ell$) corresponds to the 1d-small lattice $1 \ll L \ll \ell$, both defined by the diffusion length that easily extends over the lattice size.

Next we have to determine the proper scaling limit of all lengths in the 2d-small-lattice regime that enables us to apply (3.22) of Section 3.4.4. We let the largest length ℓ approach to infinity and express $L_{1,2}$ in powers of ℓ. To allow for $\mu = L_2/L_1 \to 0$, we opt for the swapped-lengths version. Let $L_1 \sim \ell$ and $L_2 \sim \ell^{1/2}$ (for the latter, any exponent in $[1/3, 1)$ works, the lower bound presumably an artefact of the details of the involved approximations only). Then $L_1/L_2^3 \sim \ell^{-1/2} \to 0$, which satisfies a central assumption for the approximations, while $L_1/L_2 \sim \ell^{1/2} \to \infty$, so that the $S_3^{(0),(1)}$ terms also vanish. Further, $L_1 L_2(1-\xi) \sim \ell^{-1/2} \to 0$ and $L_1/L_2 \cdot L_1 L_2(1-\xi) \to \text{const}$. This scaling describes a situation where all lengths diverge, but the larger lattice dimension proportional to the random walk length, while the smaller length increases more slowly, hence distorting the lattice to vanishing aspect ratio L_2/L_1.

If we combine these results we get that

$$p_{\mathrm{rw}}^{-1} \approx 1 + L_1 L_2 (1-\xi) \left\{ \frac{\ln L_2}{r\pi(1-2q_0)} + \frac{L_1/L_2}{6(1-2q_0)} \right\}, \tag{3.24}$$

where we omitted higher-order terms in the brackets. In this form, logarithmic correction terms (and coequal $\mathcal{O}(1)$ terms in $P^*(\mathbf{0};\xi)$) can be seen to extinct, but the second correction term actually approaches a constant. Neglecting all higher-order terms thence yields

$$p_{\mathrm{rw}} \approx 1 - \frac{L_1^2(1-\xi)}{6(1-2q_0)} = 1 - \frac{(L_1/\ell)^2}{3},$$

where in the second step we naturally chose a square lattice ($q_0 = 1/4$) and used $1-\xi \approx \ell^{-2}$ to leading order. The corresponding outcome of the one-dimensional

first derivative of $P^*(\mathbf{0};\xi)$ indeed does not change its sign from $\mu = 1$ to $\mu = 1/4$, corresponding to the distortion $L_1 \to 2L_1$, $L_2 \to \frac{1}{2}L_2$ from a quadratic lattice with even lengths $L = L_1 = L_2$. Again we used the swapped-lengths version of (3.22) to avoid convergence issues and improve agreement with the exact result, for details cf. Section 3.4.4; the conditions for this to be allowed are easily satisfied.

small-lattice regime (A.9) implies (cf. Appendix A.8)

$$p_{\mathrm{rw,\,1d}} \approx 1 - \frac{(L/\ell_{\mathrm{1d}})^2}{6}.$$

The proper scaling limit thus produces a crossover from logarithmic correction terms in the full two-dimensional small-lattice regime to the squared length ratio correction we found for the corresponding genuinely one-dimensional small-lattice regime. The result only depends on the larger length (scaling as the random walk length), while the smaller one has disappeared. As it should be, with the appropriate rescaling of the random walk length, $\ell_{\mathrm{1d}} \to \ell/\sqrt{2}$ (which respects that the number of steps is split up between the two dimensions, as explained in Section 3.4.3 and in Appendix A.8) we recover the precise numerical pre-factor of the leading correction term.

We finally remark that the crossover behavior also holds for lattice type (b), due to the fact that the (swapped-lengths version) S_3 terms still vanish for $L_1/L_2 \to \infty$, as can easily be seen from the details of the derivation (not shown). This vanishing is forced, because the eventual 1d-limit on the level of the (symmetric) structure function only admits a freedom of choice in the (effective) sojourn probability, irrelevant for the encounter probability.

3.4.7 Discussion of Figures 3.3 and 3.4

It is now appropriate to put the piecewise explanation of the previous Sections together for a thorough understanding of how the behavior of Figures 3.4 and 3.3 arises. S and ξ are kept constant 'inside one plot'.

The cumulative effect of full distortion from the quadratic shape to a $S \cdot 1$ lattice strongly depends on the absolute lattice size: For an absolutely large lattice, the minimum probability drops to less than 0.5% of that in the quadratic case peak of p_{rw} (henceforth in this Section p for brevity), while 1/6 of the peak value is left on the absolutely small lattice. For the quadratic case, either $p \sim 1$ or $p \sim (a/W)/S$, but invariably, lattices end in their 1d-large-lattice regime (with halved hopping rate), where $p_{\mathrm{1d}} \sim \sqrt{a/W}/S$, see Appendix A.8. For given quadratic lattice regime SW/a but allowing S to vary, p is unaffected, whence $p/p_{\mathrm{1d}} \propto S\sqrt{W/a} = \sqrt{SW/a}\sqrt{S} \propto \sqrt{S}$ holds *in both regimes*. The two-dimensional walk misses many sites with increasing length,[9] yet still sweeps an *area* $\sim \ell^2$ in the large-lattice limit; there, the one-dimensionality of the extremely distorted case (in the 1d-large-lattice regime) changes the ℓ power to the unfavorable. In contrast, starting from a quadratic 2d-small lattice, distortion could only yield minute corrections to near-perfect encounter probability.

The shape of the p_{rw} decline is governed by two cooperating effects both *decreasing* the encounter probability on distortion, related to the *dynamics* and the *initial conditions* of our problem.

As for the dynamics, 'wasted steps' (described in Section 3.4.3) in the smaller lattice dimension have an impact on the exploration of the surface. There surely are no steps wasted close to quadratic shape, but even close to maximal distortion, where the effect is strongest, it only halves the hopping rate, or equivalently modifies the random walk length by an $\mathcal{O}(1)$-factor. This hardly

[9] van Wijland *et al.* [60] give a detailed analysis of the support of the two-dimensional simple random walk with some far-reaching intriguing results.

shows on our logarithmic scale, since we only expect power-law behavior of p in the lengths. Once $L_2 \ll \ell$, motion in the 2-direction is indeed 'wasteful', as more steps or further reduction of L_2 no longer facilitate reaching the target: The walker's residence probability is already spread out in this direction, and uncharted waters can only be explored by stepping out in the other dimension. But whenever this significantly worsens the chances to reach the target on distortion, it is a result of increasing the larger lattice length exclusively. If we introduced two different random walk length scaling with lattice dimensions (e.g., by an anisotropic hoping rate), nothing would change at all. The dynamic effect amounts to distortion changing the ratios $L_{1,2}/\ell$, which may switch the (refined) regimes and enter asymptotic expressions (they determine how fast the lattice is swept in one direction, or how much of it is swept at all).

The 'static' effect is independent of the dynamics and solely depends on initial conditions. Throughout, deposition of the walker is taken as homogeneous. Even when, in the small-lattice regime, the largest parts of the lattice will be explored by most walks, it is still an obstacle for the *individual* walk if it starts further away from the target. A simple sketch then suffices to see that as soon as the lattice becomes distorted, the whole distribution of initial distance to the target (in particular its average) is shifted to larger distances. In the large-lattice regime, a 'sharp' region of radius ℓ around the target is not directly affected, but the spatial probability distribution of an immortal walker is then essentially a Gaussian spreading with time: Moving sites slightly further away strongly reduces the chance of a walker to reach the target from there in a given number of steps. Therefore, rare long and successful walks are additionally suppressed by shifting the initial distance distribution. The effect is amplified only further by the exponential distribution of the number of steps taken during the walker's lifetime.

Depending on the absolute lattice size, the regimes, and the aspect ratio of the lattice, it is not easy to quantify the relative impact of both effects. We will analyze the different regimes of $L_{1,2}$ and ℓ to explain their influence; any numerical $\mathcal{O}(1)$ factors in the comparisons will be omitted.

In the large-lattice regime $\ell \ll L_{1,2}$, the walk is always two-dimensional in nature. We earlier argued that different lengths of the lattice hardly have any effect here, and the encounter probability reads $p \sim \ell^2/S \ll 1$, independent of the aspect ratio. This region is seen in the small peak plateau at the right of Figure 3.4. Only the static effect might be important here.

The small-lattice regime $L_{1,2} \ll \ell$ has $p \lesssim 1$. A small fraction of walks do *not* lead to recombination, but in this regime, *avoiding* the target does not become much easier when the lattice is distorted. The aspect ratio then determines whether the random walk behaves essentially one- or two-dimensional. From (3.24) of Section 3.4.6 we expect a crossover between these regions at an aspect ratio of roughly $\mu = 1/\ln L_2$ below which (small-lattice) one-dimensional behavior prevails, namely $p \approx 1 - (L_1/\ell)^2/3$. Though, apart from the absence of logarithmic corrections, this is very different from the two-dimensional behavior in that only the larger length enters, we cannot spot it in the plots, since the respective term has to be small anyway for the expression to be applicable. This implies that again, there is but a minute effect of distortion, cf. the peak plateaus in Figure 3.3. Actually, those plateaus are more pronounced here compared to the corresponding large-lattice plots, since even the static effect has no more significant influence — basically the whole lattice is swept anyway.

The intermediate case $L_2 \ll \ell \leq L_1$ is more complicated, since it is unclear whether dying or meeting the target dominates the residence time of the walker and the magnitude of p. Again, the aspect ratio decides whether we deal with a genuinely two-dimensional lattice, or rather one so elongated it is of one-dimensional nature.

For $\mu = L_2/L_1 \ll 1$ extremely small, the system is effectively one-dimensional in its 1d-large-lattice regime. Homogenization in the L_2-direction is much faster than the spreading in the L_1-direction then, and the probability to reach the target becomes that of reaching the *projection* of the target position onto the L_1-dimension. This roughly coincides with the probability for the walker to start within a reach ℓ of the projected position which reads $p \sim \ell/L_1$. Appendix A.8 justifies this reasoning for an effectively one-dimensional intermediate lattice.

However, for aspect ratios not small enough, the nature of the two-dimensional random walk wins: spreading without densely visiting the swept area, but with increasing 'sponginess' of the set of visited sites, the specialty of spatial dimension two. We are led to expect a dependence on S/ℓ^2 with characteristic logarithmic corrections similar to the quadratic case. For moderately small L_2/L_1 we employ the result of Section 3.4.4 provided that $(L_1/\ell)(L_2/\ell) \ll 1$, which leads to $p \approx 1 - (S/\ell^2)c_1(\text{const.} + \ln L_1)$, a functional dependence similar to the small-grain quadratic lattice expansion. We could not determine the crossover aspect ratio between these behaviors, because in this regime, the expansion breaks on the way to the one-dimensional asymptotics. For the quadratic periodic lattice, the logarithmic correction emerges from integration of the slowly decaying return probability of long walks. With a distorted lattice, the dominant bounding contribution stems from the larger length only, as is most easily seen by rescaling the approximate integral expression, Appendix A.6.

We have described in detail the intermediate regime because it is responsible for all the behavior of the plots in Figures 3.3 and 3.4 outside the plateau around the quadratic shape. Invariably, once the larger (smaller) length of $L_{1,2}$ becomes of the order of ℓ, depending on whether we started in the small- (large-)lattice regime, we observe the onset of a linear decline on a $\log \mu$ scale ($\sim -\ln L_1 \propto \frac{1}{2} \log \mu$ with S constant) — this is precisely the condition to enter the intermediate regime along with its predicted two-dimensional behavior.

In the leftmost (most distorted) part of the Figures, the absolute lattice size becomes crucial. On absolutely large lattices (thick lines in the Figures), the linear decline ends in an exponential shape close to full distortion, as we end up with effective 1d-large-lattice behavior $p \sim \ell/L_1$ as argued above. The crossover aspect ratio is read off to be roughly between $1/400$ and $1/1000$. It is no longer sensible to separate a dynamic from a static effect here: The latter one considers the number of sites in reach ℓ of the target, reading $2L_2\ell$ to leading order, whence for constant S we also obtain $p \sim L_2\ell/S \sim \ell/L_1$.

Quite the contrary, the absolutely small lattices (thin lines in the Figures) nowhere clearly deviate from the 2d-intermediate-regime decline down to full distortion. First, the overall decline is now less extreme, as explained before. In fact, the exponential tail on the absolutely large lattices provides precisely the decrease of the remaining $\sim 15\%$ of the peak value that are still present for fully distorted absolutely small lattices. Second, we are still in the 1d-limit for full distortion. But leaving $\mu = 1/S$, two-dimensional effects and the corresponding logarithmic terms (linear on our scale) immediately dominate the p behavior, because the aspect ratio is far less extreme than for the absolutely large lattices

— consistently, the crossover aspect ratio determined there is not reached here.

3.5 Model Comparison and Convergence

So far, we have examined two models to obtain the encounter probability, which differ in their basic nature: Continuum diffusion versus a lattice model. For the diffusion model, we already compared the sphere to the flat disc, and despite other boundary conditions and curvature, found good agreement in the asymptotic results. In the random walk analysis, we checked against a heuristic derivation from long-known random walk results and find a similar agreement. It is now mandatory to compare the continuum with the discrete approaches, and this will provide important information for the comparison between analytical theory and simulations (Chapter 4).

We first determine the proper scaling of the discrete random walk parameters to perform the continuum limit. We have to stay in the same regime of the system, hence we need to keep both ratios L_j/ℓ, and consequently SW/a, fixed. Further, the aspect ratio has to be conserved, whence L_2/L_1 is kept constant as well (this point is moot as long as we use quadratic lattices, i.e., $L_1 \equiv L_2$ anyhow). Subject to these constraints, we then let the number of lattice sites become very large, $S \to \infty$. This joint limit preserves all quantities of our expressions depending only on the 'regime parameter' $\sim S(1-\xi)$, hence we can analyze separately the asymptotic results obtained for the two regimes of the quadratic lattice.

Throughout, we allow for walkers to meet by coinciding initial positions, and corresponding terms in the diffusion models will be incorporated as well; that is, we always use p and not $\tilde{p}$.

3.5.1 Large Grains

Translating the diffusion model result (3.15) via the relations given in Section 3.7, one has

$$p_{\text{diff}} \approx \frac{4ga}{SW} \frac{1}{\ln(4a/W) - 2\gamma},$$

with $g = \pi/4$ for the square lattice, and $g = \pi/(2\sqrt{3})$ for the triangular lattice, respectively. The corresponding random walk result is (3.20),

$$p_{\text{rw}} \approx \frac{\pi a}{CSW} \frac{1}{\ln(Ba/W)},$$

with B, C as found in Section 3.3.3 and explicitly defined in Section 3.3.5. Comparison of the factors g and C immediately shows that for our cases $4g = \pi/C$, therefore not only the functional dependence, but also the numerical pre-factors of p_{diff} and p_{rw} coincide once again.

The pre-factor *inside* the logarithm however clearly differs, which only becomes irrelevant in the true limit $S \to \infty$. Note specifically that in the diffusion result, there is no longer any imprint of the lattice type, as opposed to the discrete result. We should emphasize that (e.g., in Section 3.2.3) care was taken that in the given form of the asymptotic expressions, all omitted terms are of higher order, particularly in the denominator expression, where further terms are of 'polynomially' smaller order than unity.

With this, we calculate the relative error of p_{diff} with respect to the random walk expression,

$$\Delta = \frac{\ln B - 2(\ln 2 - \gamma)}{\ln(a/W) + 2(\ln 2 - \gamma)}.$$

With $2(\ln 2 - \gamma) \approx 0.23$ and taking into account the values of B this implies that in the large-lattice regime, the diffusion model result for the encounter probability systematically exceeds that given by the random walk. Although the discrepancy vanishes in the continuum limit $S \to \infty$, it does so only very slowly, like $1/\ln(a/W)$ or as $1/\ln S$ (since $SW/a = \text{const.}$).

3.5.2 Small Grains

The earlier asymptotic results for small lattices read

$$p_{\text{diff}} \approx 1 - \frac{SW}{4ga}\left[\ln(S/g) - 1\right],$$

with the lattice factor g as before, while the random walk derivation yielded (3.21),

$$p_{\text{rw}} \approx 1 - \frac{SW}{a} c_1 \ln(cS).$$

We observe that pre-factors satisfy $c_1 = 1/(4g)$, and once more, the pre-factors as well as the functional dependence of both expressions agree.

For the pre-factor *inside* the logarithm, we have, on the one hand, the numerical values of $\ln c$ as given in Section 3.3.4. The analogous factor in the diffusion model result reads $-\ln g - 1$, and numerical evaluation provides $-0.758435525\ldots$ and $-0.902276561\ldots$ for types (a) and (b), respectively, both completely off. The discrepancy here is much stronger than in the comparison of the exact random walk asymptotics to the heuristically derived, although the latter was flawed by several approximations, cf. Section 3.3.5.

For $S \to \infty$ with $SW/a = \text{const.}$ we will eventually still leave the small-lattice regime as p drifts away from unity, cf. the remark in Section 3.3.4 regarding the used expansion. Therefore, here the discrepancy between the models is more appropriately measured by the relative deviation of the complements $1 - p$,

$$\Delta' = -\frac{\ln(cg\,\mathrm{e})}{\ln(cS)} < 0$$

for the diffusion model outcome relative to that of the random walk. Again the diffusion model encounter probability systematically *exceeds* that obtained from the random walk model, and again, this discrepancy vanishes only logarithmically slowly as the system size $S \to \infty$.

3.5.3 Results

We have established that the asymptotics of the random walk encounter probability p_{rw} differ from its diffusion model analogon p_{diff} in logarithmic terms. In the true continuum limit $S \to \infty$, $W/a \to \infty$ with $SW/a = \text{const.}$, this difference eventually vanishes, however, it does so only logarithmically in the system size S: This slow convergence is inevitable, and a direct consequence of the marginality of spatial dimension two for the random walk and diffusion. Note that, especially

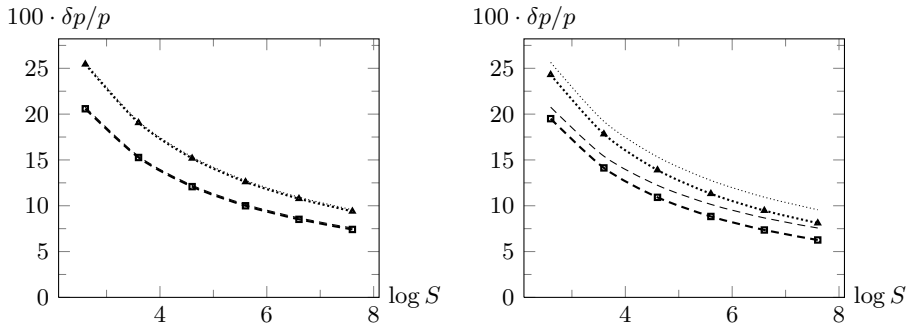

(a) $SW/(4a) = 10^{-3}$ **(b)** $SW/(4a) = 10^{-2}$ (still a *small* lattice)

Figure 3.5: Relative difference (per cent) of $1 - p_{\text{diff}}$ w.r.t. $1 - p_{\text{rw}}$, type (a) (dashed / squares), type (b) (dotted / triangles); thinner lines the prediction $-\Delta'$.

for the comparison of discrete-space simulations to analytic results, this might be a crucial point.

To illustrate the magnitude of the effect, we thence plot the relative discrepancy of the *exact* result of the diffusion model p_{diff} w.r.t. that of the random walk p_{rw} per cent, i.e., $100 \cdot (p_{\text{diff}} - p_{\text{rw}})/p_{\text{rw}}$ for the large lattice regime; for the small-lattice plots, this is substituted by the relative difference of the complements $(1 - p)$. For each plot, lattice sizes are chosen such that the lengths $L_1 = L_2 = L$ are integers most closely yielding $S = 4 \cdot 10^2, 4 \cdot 10^3 \ldots$, viz. $L = 20, 63, 200, 632, 2000, 6325$. At the same time, $\log(a/W) = 2, 3 \ldots$ increases with the lattice size, whence the 'regime' parameter $SW/(4a)$ stays nearly constant and we properly approach the continuum limit. We also show the error estimates Δ and Δ' as appropriate for the given regime.

We find that the error predictions nicely agree with the discrepancy of the exact results in both regimes, and with increasing precision the further we delve into a certain regime. This also verifies that the different asymptotic results (used to derive the estimates) are inherent in the respective models, not due to any relevant terms erroneously omitted. The discrepancy shows the expected slow logarithmic decrease in the system size throughout, and it is obviously considerable even for the largest lattices, where still, the error increases the further we enter one regime.

While we have not examined the hexagonal lattice in the full random walk result, it is known that in the N_{dis} expression used in the heuristic derivation of Section 3.3.5, one has $C = 3\sqrt{3}/4$ [55]. Hence the identification $C = \frac{\pi}{4g}$ still holds in this case (cf. Appendix A.1), and the agreement of the *leading-order* behavior between diffusion model and the heuristic random walk result extends to the hexagonal lattice.

3.6 On Lattice Type Effects

Chang *et al.* [23] performed kinetic Monte Carlo simulations of the hydrogen recombination system, on the basis of which they argued that the lattice type (e.g., simple square or triangular) substantially affects recombination efficiency.

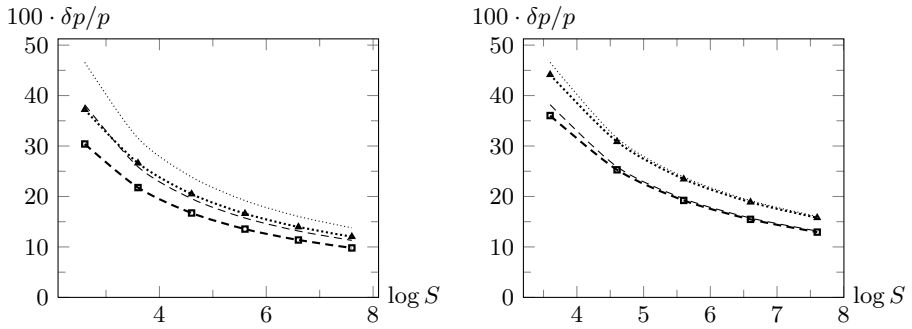

(a) $SW/(4a) = 10^0$ (already a *large* lattice) **(b)** $SW/(4a) = 10^1$

Figure 3.6: Relative difference (per cent) of p_{diff} w.r.t. p_{rw}, type (a) (dashed / squares), type (b) (dotted / triangles); thinner lines the prediction Δ.

This was suspected a result of supposedly higher encounter probability on lattices with higher coordination number due to less back-diffusion.

From the standpoint of the diffusion model that preceded the random walk analysis in our work, such claims do not appear entirely unreasonable: We have to rule out the possibility that the continuum approximation is fundamentally flawed in this respect. Although the transition from a lattice walk to continuum diffusion obliterates the basic differences of lattice types, most properties of a random walk are immune to this limiting process. The effect of different types of lattice on the encounter probability obtained in the diffusion model is carried by the lattice factor g occurring in the expressions of Section 3.2.3.3, and is owed to back-diffusion (for the effect of the latter cf. also Section 3.7.2). On the other hand, the effect of back-diffusion is most easily quantified in terms of N_{dis}, the number of distinct visited sites, as explained in Section 3.3.5. From the comparison of models in Section 3.5 it then follows that the diffusion model accurately represents lattice type effects on this fundamental level, and at least to leading order in the asymptotic expressions.

To explain our findings contrary to the above claim, note that back-diffusion is *not* a local effect. Typically, a two-dimensional random walker does *not* return to the site he currently occupies by stepping out and then reversing this step, which would occur with a probability equal to the inverse coordination number. In fact, the major contribution to the return probability stems from paths of long intermediate excursions before eventually coming back. This does not contradict the observation that qualitatively, the sweeping rate indeed obeys the behavior implied by the 'immediate-return' assumption, as it scales with g (for large grains), which increases with the coordination number (cf. Section A.1).

Our result is strengthened by the agreement of all ways, including the rigorous random walk analysis, to derive the asymptotic behavior of p. They differ only in sub-leading terms, but predict identical functional form and a coinciding leading-order dependence on the lattice type, namely as a mere factor close to unity. Section 3.9.1 will show that the difference in p due to the lattice type (square, triangular, or hexagonal) has an equally minute effect when used in the master equation recombination efficiency (asymptotically in both regimes). There we offer an explanation for the discrepancy with Chang *et al.* [23] as well.

3.7 Effect on Sweeping Rate

The encounter probability p was originally introduced as an auxiliary quantity to find the recombination rate [40] or the true sweeping rate A [7], respectively. Therefore we shall now examine the sweeping rate inasmuch as it is changed from the conventional approximation $A \approx a/S$.

3.7.1 Asymptotic Behavior

Using the results of Section 3.3.4, for the small-grain regime $SW/a \ll 1$ we obtain the sweeping rate (3.5)

$$A \approx \frac{W}{1-p_{\mathrm{rw}}} \approx \frac{a/S}{c_1 \ln(cS)}, \tag{3.25}$$

where c_1 is an explicit and $c \sim \mathcal{O}(1)$ a numerical constant depending on the lattice type, see Section 3.3.4. For large grains we have $W/a \ll 1 \ll SW/a$, leading (Section 3.3.3) to a sweeping rate of

$$A \approx W p_{\mathrm{rw}} \approx \frac{\pi}{C} \frac{a/S}{\ln(Ba/W)}, \tag{3.26}$$

where the lattice-dependent constants B and C are as defined in Section 3.3.5. Compared to the conventional approximation (2.1), we see that in both limits, the sweeping rate is reduced by a logarithmic factor.

3.7.2 Comparison with the Conventional Approximation

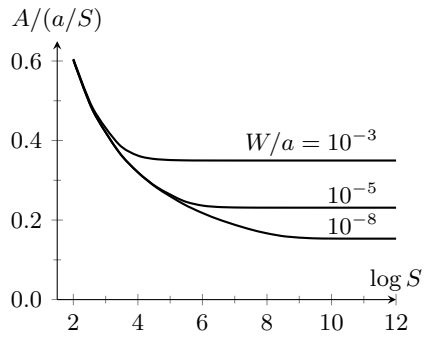

Figure 3.7: Reduction factor of the true sweeping rate w.r.t. the conventional approximation, for three different values of the ratio $W/a \ll 1$.

We now compare the true sweeping rate as obtained from (3.19) and (3.5) with the conventional approximation a/S, measured by the reduction factor

$$\frac{A}{a/S} = \frac{SW}{a} \frac{p_{\mathrm{rw}}}{1-p_{\mathrm{rw}}}.$$

The lattice structure will not concern us in this Section, thence we restrict ourselves to the square lattice case.

To illustrate the behavior derived in Section 3.7.1, Figure 3.7 shows the reduction factor $A/(a/S)$ plotted versus the (logarithmic) grain size for three values of W/a. For (absolutely) small grains, all graphs converge, as once the small-grain regime is entered, the reduction is no longer affected by W/a, cf. (3.25). On the other hand for large grain sizes, the reduction approaches an asymptotic value depending on W/a.

Obviously, the sweeping rate is considerably reduced throughout, but it may be a bit surprising that it is most pronounced for *large* grains. This can be understood as follows: The crucial effect in the reduction of A compared to the

conventional approximation is back-diffusion — the fact that a random walker revisits sites already seen. On small grains, however, this is not effective, as in most cases, the whole grain is swept anyway; also, different values of $W/a \ll 1$ do not change the reduction factor since recombination (not desorption) limits the residence time. With increasing grain size, desorption increasingly competes with recombination as the limiting factor, and hence back-diffusion becomes more effective. In the large-grain regime, this effect saturates (as a function of the grain size), as basically all walks are ended by desorption, and increasing S does not affect the single walk anymore.

In contrast to the effect of back-diffusion, we have seen in Section 3.1.1 that the change from the rate equation to the master equation description (for $\langle N\rangle \ll 1$) is *only* important (and reduces the reaction rate) for small grains. This is because it is due to another mechanism: The spatial confinement induces a large encounter probability on such grains, which deforms the distribution $P(N)$ from its Poisson shape.

3.8 Master Equation Results

We have by now extensively discussed the encounter probability of two particles, measuring the first-passage competition between reaction and desorption, and the resulting sweeping rate. Ultimately, however, we want to know the reaction rate or efficiency; moreover, this is the quantity that is most directly observable for experimental systems like the interstellar cloud dust grains. As we have explained in Section 3.1.1, only the master equation framework appropriately accounts for fluctuations in the particle number on the grain by governing the time evolution of the full distribution $P(N)$. The zero-dimensional master equation reads

$$\begin{aligned}\frac{\mathrm{d}P(N)}{\mathrm{d}t} &= F\left[P(N-1)-P(N)\right] + W\left[(N+1)P(N+1)-NP(N)\right] \\ &\quad + A\left[(N+2)(N+1)P(N+2)-N(N-1)P(N)\right]\end{aligned}$$

(with minor modifications for $N = 0,\ 1$). For the stationary situation $\mathrm{d}P/\mathrm{d}t \equiv 0$, the main analytical results of this approach are [19, 21]

$$\langle N\rangle = \sqrt{\frac{F}{2A}}\frac{I_{W/A}(2\sqrt{2F/A})}{I_{W/A-1}(2\sqrt{2F/A})}, \tag{3.27}$$

$$\eta = \frac{2R_{\mathrm{ME}}}{F} = \frac{2A}{F}\langle N(N-1)\rangle = \frac{I_{W/A+1}(2\sqrt{2F/A})}{I_{W/A-1}(2\sqrt{2F/A})}, \tag{3.28}$$

where $F = fS$ is the total flux of reactants, and $I_\nu(z)$ are modified Bessel functions (see Appendix B.1). The definition of η is normalized to account for the fact that it takes *two* atoms to form one molecule. The physically meaningful set of parameters in these expressions consists in S, F/W, and W/A.

One should note that the ME does not include Langmuir-Hinshelwood (LH) rejection, i.e., there is no repulsion of any impinging atoms due to a site already being occupied. Such a rejection would imply a modification of the impingement term in the master equation, namely $F\left[P(N-1)-P(N)\right] \to F\left[\left(1-\frac{N-1}{S}\right)P(N-1)-\left(1-\frac{N}{S}\right)P(N)\right]$, and using $\tilde{p}$ instead of p in calculating the sweeping rate A, thus only accounting for reactions triggered by hopping

of already present adatoms. While the modification in the second half of the impingement term could be absorbed in the (appropriately modified) corresponding desorption rate term, one cannot do the same for the first half, and consequently, the modified ME would differ significantly. Here we thence neglect LH rejection, and appropriately we will use p as well for the numerical evaluation in Section 3.9.

In Appendix A.9, we detailedly examine the analytical behavior of (3.27) and (3.28). Here we only mention that in the regime of small mean particle number on the grain, $\langle N \rangle \ll 1$, one obtains

$$\eta \lessapprox \frac{2F}{W} \frac{1}{W/A+1} \ll 1.$$

Since $p = 1/(W/A+1)$ according to (3.4),

$$\eta \approx \frac{2F}{W} p, \tag{3.29}$$

which coincides with the result found in Krug [40], Eq. 8 for small particle number. On large enough grains, $W/A \gg 1$ and $\eta = 2AF/W^2$ [see also 21]. For $W/A \ll 1$ on the other hand (small enough grains), $\eta \approx 2F/W$; since the meeting rate becomes very large, all atoms that impinge during the fraction of time $F/W \ll 1$ when a possible partner is already present on the grain *do* recombine (the factor 2 is the number of atoms involved in a reaction). This is perfectly reasonable for a small mean particle number on the grain.

3.9 Experimentally Relevant Efficiency Behavior

Here we will examine the effect of an altered sweeping rate on the master equation efficiency, under relevant experimental conditions for interstellar dust clouds. To facilitate comparison to previous work, we consider the following standard scenario: Desorption and hopping are assumed to be thermally activated by the grain temperature T, i.e.,

$$W = \nu \exp\left(-\frac{E_W}{k_\mathrm{B}T}\right), \qquad a = \nu \exp\left(-\frac{E_a}{k_\mathrm{B}T}\right), \tag{3.30}$$

where $\nu = 10^{12}\,\mathrm{s}^{-1}$ is a uniform attempt frequency for the processes. From the experimental results listed in Table 2.1, we choose the set Katz *et al.* [34] which is commonly used [20, 21, e.g.]: For an olivine surface, analysis of temperature-programmed desorption experiments yielded activation energies $E_a/k_\mathrm{B} = 287\,\mathrm{K}$ and $E_W/k_\mathrm{B} = 373\,\mathrm{K}$ (in more suitable units). The flux of H atoms is obtained as $F = n_\mathrm{H} v_\mathrm{H} \pi R^2$, where n_H is the number density of hydrogen atoms in the gas phase, $v_\mathrm{H} = \sqrt{8k_\mathrm{B}T_\mathrm{gas}/(\pi m_\mathrm{H})}$ the thermal velocity of hydrogen atoms of mass $m_\mathrm{H} = 1.67 \times 10^{-24}\,\mathrm{g}$ and temperature T_gas, and πR^2 arises as the cross section of spherical grains of radius R (we assume the perfect sticking of H atoms onto the grain surface throughout). Finally, with the area density s of adsorption sites we have $f = F/(4\pi R^2 s) = n_\mathrm{H} v_\mathrm{H}/(4s)$.

We adopt typical parameters for an interstellar gas cloud from Biham *et al.* [20], with a density $n_\mathrm{H} = 10\,\mathrm{cm}^{-3}$ of H atoms in the gas phase at a temperature

of 100 K. Their estimate $s \approx 2 \times 10^{14}\,\mathrm{cm}^{-2}$ for the site density on an olivine surface, also derived from laboratory experiments, leads to an effective flux of $f = 1.8 \times 10^{-9}\,\mathrm{s}^{-1}$. Altogether the physical parameters are hence given as

$$\frac{W}{a} = \exp\left(-\frac{86\,\mathrm{K}}{T}\right), \quad \frac{f}{W} = \exp\left(\frac{373\,\mathrm{K}}{T} - 47.665\right). \tag{3.31}$$

Our results are always obtained for a single grain of fixed size S. The more commonly used production rate per unit volume $\mathcal{R}_{\mathrm{H}_2}$ is recovered by an average over the grain size distribution according to

$$\mathcal{R}_{\mathrm{H}_2} = \sum_S R_{\mathrm{ME}}(S) n_{\mathrm{g}}(S) = \sum_S \frac{1}{2} f S \eta(S) n_{\mathrm{g}}(S),$$

where $n_{\mathrm{g}}(S)$ denotes the number density of dust grains with S adsorption sites. The general expectation is a broad distribution of grain sizes with many small grains dominating the total surface area [27, 28]. The influence of such a size distribution on $\mathcal{R}_{\mathrm{H}_2}$ has been examined by Lipshtat and Biham [29]. Typically, the total number density of dust grains is taken to be of the order of $10^{-12} n_{\mathrm{H}}$ [13].

3.9.1 Size Dependence

Here, we keep the grain temperature fixed at $T = 10\,\mathrm{K}$ and focus on the size effect on the recombination efficiency η. For the remainder of this chapter, the true sweeping rate is evaluated using the random walk encounter probability p_{rw}. Figure 3.8 shows that the reduced true sweeping rate (as compared to the conventional approximation) also decreases the efficiency. The quick decline in efficiency as one passes from the large- into the small-grain regime is shifted to the left however, such that small grains have gained in importance relative to the total efficiency. It is illustrative to compare to the outcome η_{RE} of using the rate equation results consistently, i.e., employing the production rate (3.2) with the mean particle number obtained as the stationary solution of (3.1). The choice of the conventional approximation $A \approx a/S$ then eliminates any dependence of η_{RE} on the grain size: $2A/F$ scales like S^{-2}, and (3.1) implies that $\langle N \rangle$ scales with S, so that powers of S cancel *due to the special form* of a/S. Both scaling relations obviously break down using the true sweeping rate, which introduces a far more complicated S dependence. Against intuition, this would even render small grains more efficient than larger ones, the reason being that for the RE result, the only size dependence arises because of the reduction factor $A/(a/S)$, see Figure 3.7. This is another illustration for a fact we already mentioned (Section 3.7), namely that the substitution of the conventional a/S by the true sweeping rate accounts for a different aspect of the problem and most strongly affects a different regime than the replacement of the rate equation by the superseding master equation framework.

Microscopic Monte Carlo simulations for the efficiency have been performed in Chang *et al.* [23] using a continuous-time random walk algorithm. While we find good agreement with their square lattice results and agree with the identification of back-diffusion as the prime factor undermining the efficiency, our results show only a minute increase in efficiency on the triangular lattice, in stark contrast to the considerable improvement found *ibid.*

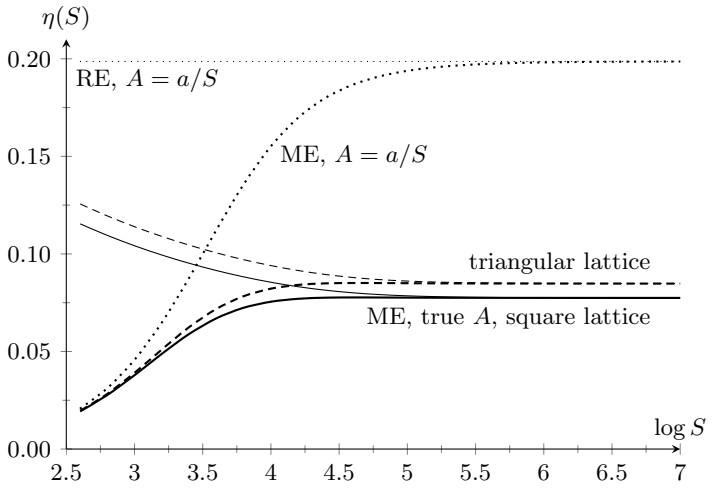

Figure 3.8: Recombination efficiency η as a function of the grain size S on a 10 K olivine grain in the standard scenario. The thick lines show $\eta(S)$ as computed with the master equation and the true sweeping rate (as found via the random walk model), the continuous line standing for a square, the dashed one for a triangular lattice. The thick dotted graph was plotted using a/S as in Biham *et al.* [20]. The corresponding thin lines show the predictions of the rate equation treatment for the respective choice of sweeping rate.

We have already argued in Section 3.6 that the lattice type (as far as investigated herein) has a very weak effect on the level of the encounter probability, *independent* of the model used to calculate p. We supplement this by an argument that there is no pronounced effect on the recombination efficiency as well: As argued in Sections 3.3.5 and 3.7.1, for large grains we have $A \approx WN_{\mathrm{dis}}/S$. Consequently, the asymptotic large-grain value of A for the triangular lattice exceeds that for a square lattice by a factor of $2/\sqrt{3} \approx 1.15$, the ratio of the respective values of g or C^{-1}. On the other hand, we have $\eta \approx 2AF/W^2$ from the large-grain behavior of the master equation result, and the aforementioned ratio should reappear in the efficiencies, which is in good agreement with Figure 3.8.

Commenting on the discrepancy to Chang *et al.* [23], we believe it is most likely due to a different scaling of rates: While we kept the *undirected* hopping rate a fixed in the comparison of square and triangular lattices, according to (3.30), it appears to us that in Chang *et al.* [23], the *directed* hopping rate was held constant. This entails an undirected rate a larger by a factor of 3/2 for the triangular lattice, which is of the correct order of magnitude to explain the change in η found *ibid.*, judging by the above approximations.

We cannot, however, completely rule out that lattice effects could be more pronounced in a many-particle situation, for which the zero-dimensional master equation formalism neglects all correlations.

3.9.2 Temperature Dependence

From an astrophysical point of view, the whole puzzle of hydrogen recombination in interstellar dust clouds is about the temperature window in which this process

is efficient; hence the temperature dependence is a most interesting aspect of the recombination efficiency. The temperature window arises from two factors: At the upper temperature bound, desorption has become so fast compared to hopping that the encounter probability of two atoms is virtually zero. At the lower bound however, desorption is suppressed so much that the grain coverage becomes of the order of unity. Once this happens, LH rejection becomes important: Atoms that impinge on adsorption sites already occupied are repelled, therefore the fraction of impinging atoms that participates in recombination events becomes very small.

Simulations of the system in Chang *et al.* [23] show results close to the analytical results of Biham *et al.* [20] in the efficiency peak, and somewhat smaller for still higher temperatures, both facts as expected in our model, compare, e.g., the fixed-temperature plot in Figure 3.8.

We focus on the effect of the sweeping rate here. Note first that we do *not* include LH rejection, as there is no feasible way to incorporate it in the master-equation framework. Therefore, we may only examine the high-temperature breakdown starting from the peak efficiency, where LH rejection should already be negligible [20]. Using (3.31) we obtain a rough estimate for the temperature at which our results fail: The mean coverage of H atoms on the grain is of the order of f/W. A temperature where this coverage becomes of the order of unity surely is beyond the validity of our assumptions, and this temperature is given by $T_{\mathrm{LH}} \approx 7.8\,\mathrm{K}$.

For fixed grain size (hence total impingement flux), the recombination efficiency is governed, first, by the relation between (fixed) S and the temperature-dependent W/a which determines the regime, and second, by the average number of reactants on the grain, smaller than but of the order of F/W. For increasing temperature, W/a increases and F/W decreases. This means we approach the large-grain regime with its small encounter probability, while the mean number of H atoms drops down, and both effects prohibit efficient recombination. Lowering the temperature, we enter the small-grain regime with almost certain encounters and an increasing mean coverage, both enhancing the recombination process. Without LH rejection, the reaction will become perfect as $T \to 0$: While diffusion of the atoms is heavily suppressed, desorption is so even more, and the steady-state point of view does not reveal that the eventually successful reaction process becomes extremely slow.

Consider first an absolutely small grain of 1000 adsorption sites, then even with the increased resolution, differences among the efficiency predictions are hardly visible in Figure 3.9a. As explained before, the breakdown of η for $T > 8\,\mathrm{K}$ is expected to apply to an analogous model including LH rejection as well. For a large grain of 10^6 adsorption sites (Figure 3.9b), the true sweeping rate results in a lower upper temperature bound for efficient recombination, the lattice type difference still nearly imperceptible. The impact of using the proper A is only visible for large grains, as the back-diffusion reducing A (with respect to a/S) is most effective there. (We refer to Figure 3.8 again to illustrate how η is affected once the temperature exceeds that at the efficiency peak.) The limiting efficiency behavior for low and high temperatures is independent of the choice of sweeping rate however: The argument given above only relies on the limits the encounter probability approaches in these cases; using the approximation $A \approx a/S$ in (3.4), instead of the true p we obtain the quantity $1/(1 + SW/a)$, which has the same limits. The Figures suggest that the size of the grain hardly matters for the

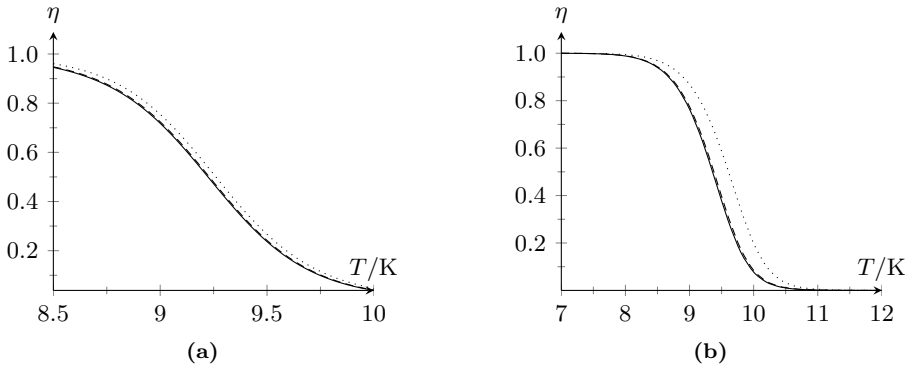

Figure 3.9: Left: Recombination efficiency as a function of the temperature T, for a grain of $S = 10^3$ sites. Again, the continuous line shows the master equation result with the true sweeping rate and a square lattice, the dashed line represents the result for a triangular lattice, and the dotted line uses the conventional approximation. Note that this plot is horizontally stretched to uncover the small differences. The regime of large grains only starts at higher temperatures outside the plotted region. Right: The same plot, now for a grain of size $S = 10^6$ sites. This size is 'large' for practically all shown temperatures.

upper temperature bound on effective recombination — a vast change in the number of adsorption sites results in only a minute change of the temperature bound.

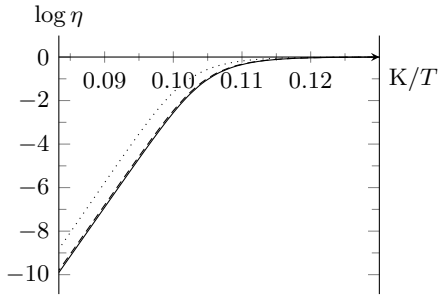

Figure 3.10: An ARRHENIUS plot of the recombination efficiency under the previous conditions.

Let us finally recast the last plot in the ARRHENIUS fashion, i.e., as $\ln \eta(1/T)$, shown in Figure 3.10. Temperature increases to the left of the plot, which shows thermally activated behavior with an effective energy read off to be $E_{\mathrm{act}}/k_{\mathrm{B}} \approx -440\,\mathrm{K}$. The large-grain result $\eta \approx 2AF/W^2$ and the A asymptotics (3.26) would imply an activation energy $E_a - 2E_W$, which evaluated for the parameters (3.30) yields $-459\,\mathrm{K}$, in good accordance with the plot.

We summarize the astrophysically relevant effect of employing the true sweeping rate (3.5) instead of (2.1) as follows: For given temperature, large grains are more affected by back-diffusion, whence small grains gain in importance compared to the reduced overall efficiency. For a fixed grain size, only (absolutely) large grains are subject to a correction, but the upper temperature bound for efficient recombination is not affected considerably. Since this bound seems instead to be very sensitive to a more refined modeling of the complex surface structure [23, 30], our findings strengthen the claim that such factors are crucial for hydrogen recombination.

Chapter 4

Kinetic Monte Carlo Simulations

In this Chapter, we will quantitatively compare our findings for the encounter probability to simulation results. The motivation is two-fold: First, one may consider it generally appropriate to validate theoretical findings by a direct simulation. Second, and more importantly, the simulation itself needs an established point of reference if we want to extend it to an inhomogeneous disordered environment (most likely for the 'full' efficiency simulation). The latter motivation indeed was our driving force here.

Algorithm. It is not difficult to simulate both the stochastic two-particle system employed in the definition of p and also the complete diffusion-reaction model of a dust grain, which includes ongoing stochastic deposition of random walkers and provides the recombination efficiency of the process.

Our simulation is based on a standard kinetic Monte Carlo (KMC) algorithm (described in detail in, e.g., Gödecke [61]) that tracks individual atoms deposited onto, hopping around on and desorbing from the lattice. Exactly as in the random walk model of Section 3.3 and as close as possible to the diffusion model, we use a homogeneous lattice with periodic boundaries. Waiting times are drawn from an exponential distribution with the mean given by the inverse of the total rate of all processes. This is the simplest implementation of the continuous-time random walk (CTRW) introduced in Montroll and Weiss [54].

Below we present a rough pseudo-code of the algorithm. For brevity, we only show a simplified main program for the efficiency simulation of a given grain realization, and leave out all details, subroutines, intermediate output and counting (this is where the bulk of the work lies). Notation of the main text is re-used whenever this appears unambiguous. The specialization to the two-particle case for finding the encounter probability should be obvious: The stochastic impingement is substituted by a random initial deposition of exactly two particles, and the large **repeat** loop becomes a **for** loop over the desired number of trials.

We have a few additional remarks: For the homogeneous situation that we have considered in the preceding Chapters, we devised simplified algorithms providing a substantial speedup. In the form presented here, the algorithm is

Algorithm 1 KMC simulation of the dust grain.

general initialization
set (disordered) process rates
populate grain with atoms $k = 1 \ldots N$ at positions $\mathbf{r}_k$

repeat
  increase time according to total rate of processes
  draw random $x \in [0, \text{total rate})$
  if $x < F$ **then** {a new atom shall impinge}
    draw random position; count the impingement
    if it position is empty **then**
      increment N; count a deposition
      update atom list / occupancy array / total rate
    else
      count a rejection
    end if
  else
    set sum $X = F$
    repeat
      increment k; add $X \leftarrow X+$ rate sum at $\mathbf{r}_k$
    until $x < X$ {kth atom to move}
    use x to determine its move (directed hop or desorption) analogously
    if atom desorbs **then**
      decrement N; count a desorption
      update atom list / occupancy array / total rate
    else {it hops to a target site}
      if target site is empty **then** {just hop there}
        update atom list / occupancy array / total rate
      else {a recombination!}
        decrement N by 2; count a recombination
        update atom list / occupancy array / total rate
      end if
    end if
  end if
until wanted number of atoms have impinged

print Statistics
print $\eta_{\mathrm{MC}} = \#\text{recombinations}/(\#\text{impingements}/2)$
print $N_{\mathrm{MC}} = \text{time-average}\, N$

fully suited to deal with *arbitrarily* inhomogeneous rates (for nearest-neighbor transitions) however, and we will use it again when we examine the influence of disorder in Chapter 5. Second, we only count simulation data from the stationary state of the system. To decide when this state is entered, we sub-divide the simulation into passes of a certain number of impingements, and generate per-pass statistics. Only if the efficiency has not changed too much (as judged by the pass length and its absolute value) between to consecutive passes, we assume the stationary state is reached and start counting for the final result.

With respect to the fully general standard KMC algorithm [61], we have made some small adjustments, benefiting from the special system at hand: Every atom always has a fixed number of possible moves (coordination number +1), and the corresponding rates *only* depend on its current position, hence we can store partial sums of rates per site once and for all. Moreover, the list of possible processes is naturally partitioned by the atoms, which facilitates finding the process to carry out, without the need to employ a full tree of comparisons. Lastly, we only need to keep a compact list of atom positions, completely specifying the simulation state at any time; for speed purposes however, we additionally entertain a complementary quantity — an array storing the number of the atom (if any) sitting at a given site of the lattice.

Technicalities. We chose `Fortran 95` to implement the algorithm. This language is straightforward, highly portable, has a well-defined specification,[1] and a huge re-usable code-base (e.g., for the pseudo-random-number generator we employed). It offers lots of features (such as fully standards-compliant and user-controlled numerical precision specification, single-bit manipulation, vectorized matrix calculations, and easy dynamical memory management, all as part of the language core) tailored to tackle numerical problems and to foster quick development, all without sacrificing the ultimate goal of sheer execution speed. The simulations have been carried out on the IBM high-performance computing cluster of the Institute for Theoretical Physics of the University of Cologne. We used parallel computing in the most primitive sense, i.e., by letting simulations for different parameter sets run simultaneously on up to roughly 20 computing nodes.

Relations to earlier work. If we consider a single moving and possibly desorbing random walker to meet an immobile and immortal target site in a homogeneous environment, this clearly eliminates any effect of continuous time and may be treated in terms of *steps* exclusively, a situation fully equivalent to the one we used to derive $\tilde{p}_{\mathrm{rw}}$. A flawless microscopic Monte Carlo simulation of such a system will eventually converge to the theoretic prediction if we sample more and more trials. Such simulations (without desorption, however) have been performed by Hatlee and Kozak [62], confirming the predictions of Montroll [42] and also analyzing alternative boundary conditions of the finite lattice.

In our simulations, both reactants are mobile and may desorb, and a continuous-time algorithm guarantees an ordering of all events. For the diffusion model, the equivalence of the one- and two-walker scenarios regarding the encounter probability was obvious, owed to the continuum picture, the stationarity (no time), and the fact that the concentration is effectively an average

[1] http://j3-fortran.org/doc/standing/archive/007/97-007r2/pdf/97-007r2.pdf

over all random walk realizations. But now, in the single CTRW instance in a homogeneous environment, we could still keep one walker fixed: If it were to make a move, we could simply re-label lattice sites and let the other walker hop appropriately instead, and if it were to desorb, the trial ends as if the other had desorbed. An equivalent description thus is that of a single walker to meet a fixed immobile target, and moving or desorbing at twice the original rates, with waiting times still exponentially distributed: The survival probability per step, and hence the encounter probability, remains unchanged. Note also that the description in terms of steps is completely justified; although the number of steps that occur in a given time interval is a stochastic quantity for the CTRW (in contrast to the discrete-time random walk, the relation for a huge class of waiting-time distributions investigated in, e.g., Bedeaux *et al.* [63]), the time passed is irrelevant for the encounter probability.

LH rejection. In Section 3.3.2 we have already mentioned LH rejection. Our simulations respect this rejection mechanism, i.e., the repulsion of atoms impinging on top of occupied sites for the full system, and the restriction that atoms start on distinct sites for the two-particle case. It is hence appropriate to refer to $\tilde{p}_{\mathrm{rw}}$ for all comparisons to theory.

Data analysis. A repeated sampling of N_{runs} independent Bernoulli trials with an (unknown) success probability p (recombination in our context) has a result with absolute standard deviation $\sigma = \sqrt{p(1-p)/N_{\mathrm{runs}}}$. Hence we expect a *relative* standard deviation $\tilde{\sigma} = \sigma/p$, evaluated using the (known) values of $\tilde{p}_{\mathrm{rw}}$, for the simulation average. Note that $\tilde{\sigma}$ can become rather large for small p, i.e., in the large-lattice regime. Furthermore, the binomial distribution for the number of recombinations for fixed success probability p of the single trials and the number of trials $N_{\mathrm{runs}} \to \infty$ approaches a Gaussian distribution. The mean value of $\tilde{p}_{\mathrm{mc}}$ (one data point) is thence drawn from a normal distribution with the above standard deviation. This implies that, plotting relative deviations from the theoretical prediction, we expect roughly a third of the (independent) data points to lie outside a corridor of half width $\tilde{\sigma}$.

4.1 Quadratic Lattices

For quadratic lattices we tested a wide range of parameters S and W/a, and for both types of lattices. We performed $N_{\mathrm{runs}} = 10^6$ individual trials for each data point, apart from the largest lattice $S \approx 4 \times 10^7$ with $\ell \geq 10^8$, where time constraints led to $N_{\mathrm{runs}} = 10^5$.

Figures 4.1a–4.1g show the relative error (per cent) $100 \cdot (\tilde{p}_{\mathrm{mc}} - \tilde{p}_{\mathrm{rw}})/\tilde{p}_{\mathrm{rw}}$ as a function of the lattice size S on a logarithmic scale. The lattice sizes and rate ratios a/W are chosen as described in Section 3.5.3, so that one plot roughly describes a fixed regime and about constant p, cf. the approximate expressions, to keep the standard deviation of the same order of magnitude. Outside the shown parameter ranges, nothing interesting happens; in the large-lattice regime, the leftmost data points are omitted as they no longer satisfy $a/W \gg 1$. We have also plotted a corridor of half width $\tilde{\sigma}$ around perfect coincidence.

As expected after the above considerations, we find excellent agreement between the analytic random walk result $\tilde{p}_{\mathrm{rw}}$ and $\tilde{p}_{\mathrm{mc}}$ obtained from Monte

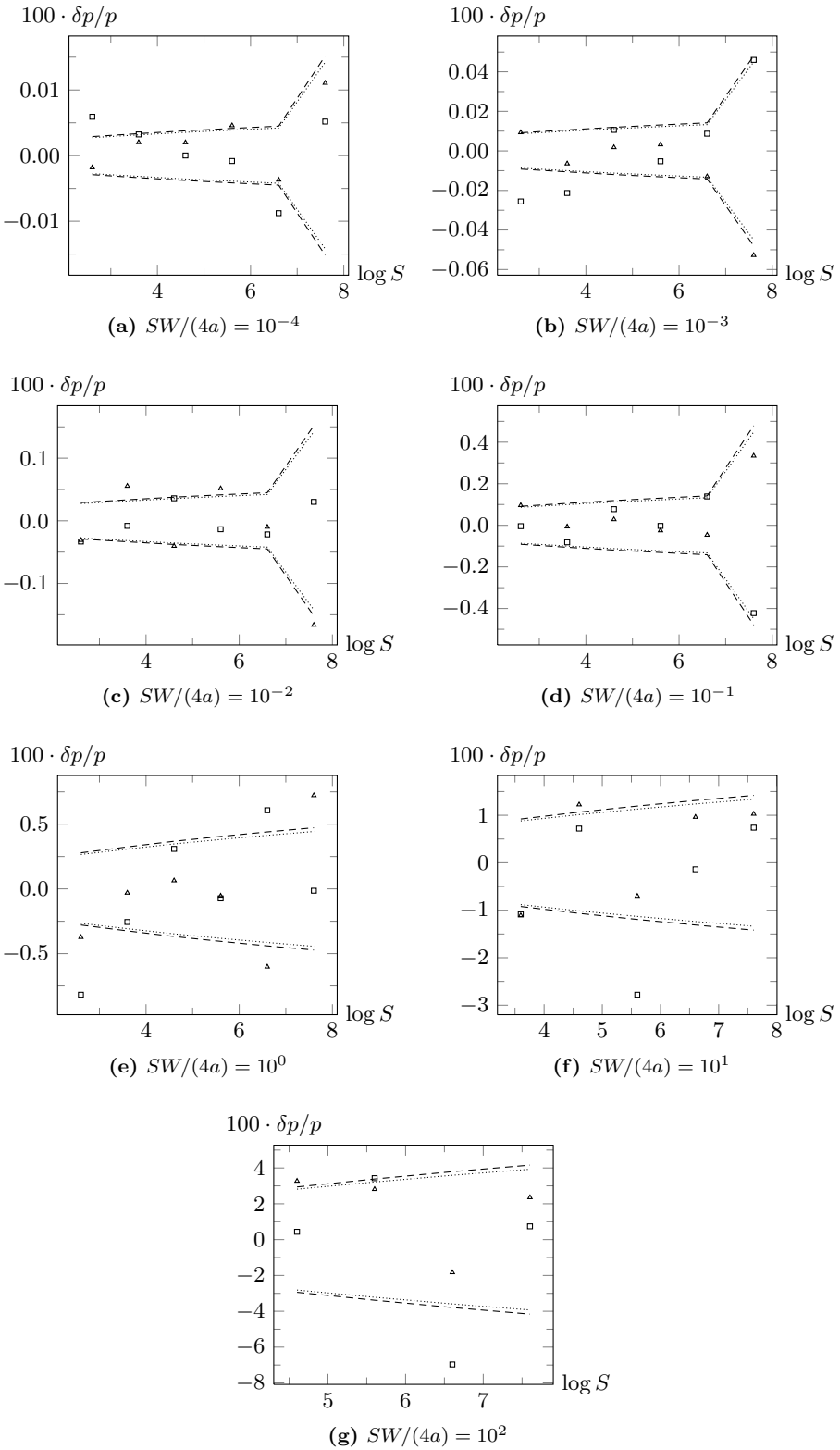

(a) $SW/(4a) = 10^{-4}$ **(b)** $SW/(4a) = 10^{-3}$

(c) $SW/(4a) = 10^{-2}$ **(d)** $SW/(4a) = 10^{-1}$

(e) $SW/(4a) = 10^{0}$ **(f)** $SW/(4a) = 10^{1}$

(g) $SW/(4a) = 10^{2}$

Figure 4.1: Relative difference of $\tilde{p}_{\mathrm{mc}}$ w.r.t. $\tilde{p}_{\mathrm{rw}}$ for various regimes $SW/(4a)$, type (a) (dashed / squares), type (b) (dotted / triangles). The lines form a corridor with a width given by the expected relative standard deviation.

Carlo simulations, verifying the analytical results as well as our simulation method. In fact, counted over all simulations we find precisely 26/78 values outside the $\tilde{\sigma}$ range; the largest deviations from $\tilde{p}_{\mathrm{rw}}$ are of the order of less than $3\tilde{\sigma}$, and less than 7%, and there is no systematic over- or underestimate of our theory. The simple random walk result describes the continuous-time simulations to excellent accuracy. As an aside, this also shows that the diffusion model results would completely fail as a quantitative description, most pronounced in the large-lattice regime: While we may properly simulate the largest realistic grain sizes and large diffusion lengths within reasonable time, we are still in a regime where, due to the slow logarithmic convergence of the continuum limit, only the random walk result agrees with KMC simulations, cf. Section 3.5.

4.2 Varying Aspect Ratio

We also checked that the discrete-time random walk picture is accurate for the distorted lattice with $L_1 \neq L_2$. $N_{\mathrm{runs}} = 10^6$ trials were sampled for each data point, except for the case of absolutely large lattices ($S = 4 \times 10^6$) still in the small-lattice regime ($a/W = 10^8$), where we used at least $N_{\mathrm{runs}} = 10^5$.

Here we keep S constant for one plot, while varying the individual lengths $L_{1,2}$. Conforming to plots in Section 3.4.2, we only present the results for $S = 400$ and $S = 4 \times 10^6$ as examples of absolutely small and large lattices, respectively. Also, we keep the "regime" (in the original sense introduced for quadratic lattices) constant as well: for $S = 400$, we choose $a/W = 10^2$ or $a/W = 10^4$, for $S = 4 \times 10^6$ we test with $a/W = 10^6$ and $a/W = 10^8$ (the latter figures belonging to the small-lattice regime), but recall that the refined regimes for $L_1 \neq L_2$ actually change when distorting the lattice. Values are chosen so that the larger length L_1 exceeds the random walk length ℓ in the large-lattice regime throughout, and that it is much smaller than this length in the small-lattice regime for the quadratic case, but finally becoming much larger than it when distorting the lattice. Again, we show the relative error of simulations with respect to the random walk result in per cent, and plot a (relative) standard deviation (as obtained from $\tilde{p}_{\mathrm{rw}}$) corridor for comparison, Figure 4.2.

We find that in fact, the agreement of Monte Carlo simulations with $\tilde{p}_{\mathrm{rw}}$ is again very good. The statistical insignificance of fluctuations (24 of 64 data points outside the plotted corridor of standard deviation) is slightly less obvious than for the quadratic case. However, combined with the largest errors of the order of $3\tilde{\sigma}$, all deviations at $< 11\%$, and no systematic error to be seen, we conclude that simulations agree with the simple random walk prediction here as well.

This completes our proof of full equivalence of the fixed-time-step random walk prediction and Monte Carlo CTRW simulation for all practical purposes. In retrospect, this justifies the exclusive use of analytic random walk results as far as the encounter probability is concerned. For the modeling and parameter extraction from experiments, the relevance of our findings is that we have illustrated that standard approximations like using a continuum instead of a spatially discrete model may have far-reaching consequences on the accuracy of comparisons.

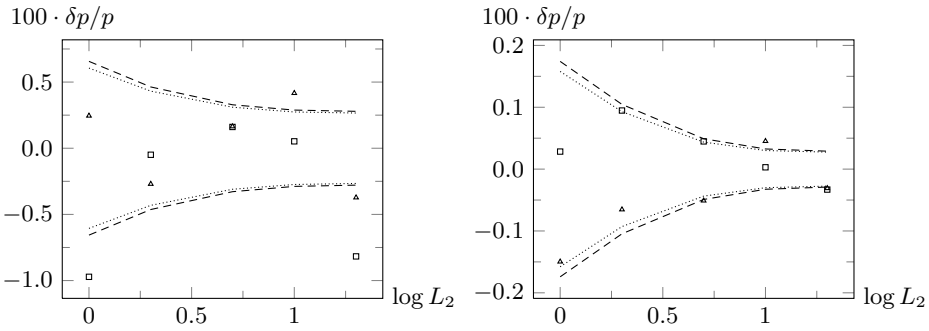

(a) $S = 4 \times 10^2$, $W/a = 10^{-2}$. **(b)** $S = 4 \times 10^2$, $W/a = 10^{-4}$.

(c) $S = 4 \times 10^6$, $W/a = 10^{-6}$. **(d)** $S = 4 \times 10^6$, $W/a = 10^{-8}$.

Figure 4.2: Relative difference of $\tilde{p}_{\mathrm{mc}}$ w.r.t. $\tilde{p}_{\mathrm{rw}}$ for two lattice sizes in both regimes, type (a) (dashed / squares), type (b) (dotted / triangles). Lines mark the expected relative standard deviation.

Chapter 5

Rate Disorder

It has been suggested very early [15] that a disordered grain surface, in the sense that binding energies and diffusion barriers are inhomogeneous over the grain, is crucial for the explanation of observed abundances of molecular hydrogen. This concept is by now generally accepted in the astrochemical community [64]. The reasoning is that even a few strong adsorption sites can greatly enhance the recombination efficiency: They will bind atoms for an unusually long time, such that other adatoms quickly scanning the surface by hopping between the 'shallower' sites can find them and react. The basic mechanism hence is best viewed as resulting in an increase of the average number of adatoms on the grain surface, while for the most intuitive kind of rate disorder, the encounter probability of two given atoms on the grain is *not changed*, cf. Section 5.3.1.

A full analytic theory of this reaction-diffusion problem with quenched disorder is beyond reach, owed to its two-dimensionality, confined geometry, included desorption, and the underlying first-passage nature. This Chapter contains modest efforts to understand and quantify the effect of disorder on hydrogen recombination on dust grain surfaces.

5.1 Observations and Experiments

If disorder is that important then one also expects it is crucial to have a reasonable model for the distribution of energies. From the astrophysical side, *systematical* experiments to determine binding energies and diffusion barriers are a fairly recent development altogether. Typically using TPD experiments, even then, the distributions of these energies can hardly be determined reliably. Buch and Czerminski [65], Hixson *et al.* [66] describe experiments and calculations of the eigenstates and energies of hydrogen, deuterium and H_2 on an amorphous ice cluster. Though not their focus, one can see [65, Figure 2] that the distribution of the binding energy in potential minima as well as of the energy barrier for diffusion is reasonably approximated by a Gaussian distribution, but the width they find is not easily transferred to our system. Cazaux and Tielens [67] is widely cited, since it accounts for diverse processes of hydrogen formation on dust grains; for our purposes however, the distinction between physisorption and chemisorption binding sites basically describes a model with two distinct binding energies. Perets *et al.* [36] find a discrete number of adsorption site types with

different mean binding energy to properly fit TPD experiments (for the produced H_2 only). The energy distribution is assumed to be GAUSSian, however, neither are more specific reasons given for that, nor is the width of the distribution. A similar fit to distributions around few different energies corresponding to distinct adsorption site types is found in Perets *et al.* [37], Vidali *et al.* [38] for a TPD analysis of HD molecules on amorphous olivine. Amiaud *et al.* [68, 69] study TPD experiments of D_2 on amorphous (non-)porous water ice. They find a binding energy distribution of polynomial form, $\rho(E) = c_1(E_0 - E)^{c_2}$, which, combined with an attempt frequency in the ARRHENIUS law, provides four fitting parameters. It is not clear to us how sensitive these findings are to details of the analyzed surfaces, and whether such a distribution may reproduce experimental results significantly better than, e.g., an exponential one.

Generally speaking, the distribution of binding energies and their effective mean value is always associated with the surface morphology: Porosity automatically provides a broader distribution of binding energies, e.g., for low-density ice one finds a broader distribution than for high-density ice [36]. Likewise, amorphous materials have significantly higher effective binding energies than their polycrystalline counterparts, as is pointed out, e.g., in Perets *et al.* [37], due to the inherently increased surface roughness. The latter correspondence is made quantitative in the KMC simulations of Cuppen and Herbst [24].

Little seems to be known about the activation energy distribution on the surfaces of interest. In the lack of more detailed results, it is reasonable to assume a GAUSSian distribution, if only because the central limit theorem suggests it for the sum of the many different random contributions to the activation energies at a given site. The width of the distribution remains unknown at this point. Therefore we can model the effect of disorder, but have a large uncertainty in comparison to experiments.

5.2 General Theoretical Remarks

Fundamentally, quenched disorder in the rates emerges from disordered activation energies for desorption and hopping, and we will always assume thermal activation of the rates with the form $\nu \exp(-\beta E)$, with inverse temperature $\beta = 1/(k_B T)$. Here, the attempt frequency ν is taken to be a single overall constant, and the activation energy E is a random variable that is drawn once and for all times.

We further imagine a potential energy landscape for the adatom which has constant saddle-point energies, but 'traps' of varying depths (binding energies). Obviously, the activation energies for hopping and desorption should then be correlated: The harder it is for an atom to hop to an adjacent adsorption site, the harder it is to desorb completely, and vice versa; however, the exact nature of this correlation is not as clear. There is also still a great freedom of choice for the dependence of rates on the energies.

We first restrict ourselves to *nearest-neighbor* transitions (for hopping) and rates which are all defined *at sites*, not on bonds; for hopping rates, this shall imply isotropy *from* a given site to all its nearest neighbors. Let us call this choice 'ultra-locality' of rates. For thermally activated rates this amounts to choosing one activation energy per site for hopping and one for desorption.[1]

[1] Spatially uncorrelated and isotropic hopping rates can always be described as only depending on an activation energy at the initial site, irrespective of the microscopic model for

One can then derive a relation between the rates a_s for hopping (with directed hopping rate a_s/z for coordination number z) and W_s for desorption at an adsorption site s. We balance desorption by an impingement flux f per site, and consider the stationary state. The stationary gain-loss equation for the adatom probability p_s at a site s with these contributions reads

$$p_s(a_s + W_s) = f + \sum_{\text{n.n.of}\, s} p_{s'} \frac{a_{s'}}{z}.$$

We now impose *detailed balance* to hold, i.e., there must not be any net flux between any two sites in the stationary state, $p_{s'}a_{s'}/z = p_s a_s/z$ for any two nearest neighbors. Inserting this yields the obvious $p_s = f/W_s$ (hopping does not affect the stationary state of only flux and desorption), and re-inserting this into the detailed balance condition implies that W_s/a_s is the same for neighboring sites. Hence on a dynamically connected lattice, we have $W_s/a_s = \text{const.}$ as a result merely of ultra-local rates and detailed balance.

The thermal form of rates now trivially implies that the activation energies only differ by a constant offset energy (so each site is independently assigned *one* energy drawn from a distribution, which then fixes both rates). This is a very natural choice suggested by the energy landscape picture, and such a correlation is also consistent with certain experimental findings for the systems discussed in Section 5.1 [36].

Chang *et al.* [23] also assume ultra-local thermally activated rates for their KMC simulations, but in contrast to our reasoning (and without a microscopic argument), they employ activation energies that are correlated by a constant *ratio* instead. We will not follow this route, not least for ease of calculation: In this case, W/a still strongly depends on the disordered activation energy at a given site, cf. the end of Section 5.4. More fundamentally however, we have shown above that this treatment is inconsistent with detailed balance.

In the following, we will therefore assume that all over the grain, $W/a = \text{const.}$, and there is a uniform extra activation energy needed for desorption compared to hopping. This model for activation energies and the associated rates is the natural generalization of the *random-trap* model [3, Chapter 7]; in its original form, this model prescribes site-dependent isotropic nearest-neighbor hopping, but does not include desorption.

5.3 A Simplistic Model: Effective Parameters

We start from the well-understood ME framework, and stick to a finite regular lattice with periodic boundary conditions. We will try to incorporate a distribution of the activation energies for hopping and desorption merely by using *effective* parameters for W/A, f/W and S. These parameters are easily defined for a homogeneous grain, where only the sweeping rate A involved some effort, as demonstrated in Section 3.1. Obviously, the total number of adsorption sites S cannot be changed. We now turn to the other parameters.

those rates.

5.3.1 Encounter Probability

In the continuum model for the encounter probability (Section 3.2), homogeneity is lost in each realization of disorder, and it cannot be regained by a local rescaling in the stationary diffusion equation, since the flux term is present. We argue in the random walk picture that this two-particle quantity nevertheless is *unaffected* by disorder: W/a is a constant all over the surface, hence the survival probability (per step) $\xi = \frac{a}{a+W} = \text{const.}$ as well. Again, as far as the encounter probability is concerned, one can then describe the walk in terms of steps (instead of a continuous time), independent of the disorder realization. Since the latter is seen to play no role, the reasoning holds true for specific initial and target sites and specific paths as well as for all averages.

For the homogeneous system, we found the sweeping rate (3.5) in terms of the encounter probability. The averages implicit in the latter quantity p are first, an average over initial positions, and second, over random walk paths. These averages are unaffected by disorder, as we argued above.

To give meaning to an effective parameter W/A in the disordered system, one has to include a third average over the disorder. This W/A is then understood to be the average ratio of the single adatom desorption rate and its meeting rate with a given partner atom. For a given pair of atoms on a disordered grain with several pairs, the relation between W/A and p seems less obvious than before, but the argument which leads to (3.4) still holds when we include the disorder average.

5.3.2 Flux vs. Desorption

Therefore disorder can only affect the effective value of the flux-parameter f/W.

The flux is still assumed to be homogeneous. For a homogeneous grain, one can interpret the parameter f/W as the mean coverage in the absence of recombination (in the stationary state). This interpretation can indeed serve as a definition of the parameter, since summing the original master equation without the recombination term, one obtains $\mathrm{d}(\langle N\rangle/S)/\mathrm{d}t = f - W(\langle N\rangle/S)$. Since the ME is unchanged, and only rates have to take some effective values, f/W_{eff} must still be given by the stationary mean coverage in the absence of recombination. The mean occupation probability of a site s is then given by f/W_s, and averaging over the grain leads to the mean coverage

$$\frac{f}{W_{\text{eff}}} = \frac{1}{S}\sum_s \frac{f}{W_s} = f\overline{W^{-1}}.$$

Here we introduce the overbar to denote the spatial average over all sites and in a given quenched disorder realization, whereas angles will always denote a full disorder average irrespective of any quenched realization. From this, the effective rate itself reads $W_{\text{eff}} = 1/\overline{W^{-1}}$. In the limit of large grains, $S \to \infty$, this spatial average converges with the one over the disorder distribution, since rates at different sites are independent identically distributed variables, and we shall first naïvely identify both averages (cf. Section 5.3.3 however). To quantify the difference, we note the well-known fact that the variance of a sum of independent random variables is the sum of their respective variances (given they all exist). Consequently, the sum of our identically distributed variables has a standard

deviation of $\sqrt{S}\sigma$, and the spatial average has the standard deviation $\sigma/\sqrt{S}$, where σ is the standard deviation of the distribution of the single-site quantity.

Microscopic argument. Why do we have to average the waiting times W^{-1} as opposed to the rates W? We only note that this average coincides with the one found appropriate in a related problem: Haus and Kehr [3] show straightforwardly that the random-trap model (without desorption) exhibits diffusive behavior at all times if one starts from the stationary distribution, with a diffusion coefficient corresponding to an effective hopping rate $1/\overline{a^{-1}}$. Similarly, the average residence time of the single atom on the grain reads (recall (3.18))

$$t_{\mathrm{res}} := \overline{a^{-1}} \cdot (1 + \xi + \xi^2 + \dots) = \overline{a^{-1}} \frac{a+W}{W} = \frac{a}{W} \overline{a^{-1}} (1 + W/a),$$

and the last factor is approximately unity, so that with $W/a = \text{const.}$ we have an effective desorption rate $t_{\mathrm{res}}^{-1} = 1/\overline{W^{-1}}$.

This inverted waiting time average (for hopping or for desorption) coincides with an average of the rates that is weighted with the stationary distribution (of non-interacting walkers). The reason is that on the one hand, we can consider a single random walk stepwise. Then we deal with the waiting times at individual sites (as above), and the average over these uncorrelated quantities need not be weighted. On the other hand, we can look at an ensemble of random walkers in a single time step and then deal with their rates as distributed *spatially*. Here, one has to take into account the appropriate distribution of the walker ensemble onto the sites, which brings into play the stationary distribution. The two averaging procedures thus correspond to the (self-averaging) single walk vs. the walk ensemble point of view.

Exemplary distributions. We consider the effect of simple distributions in systems large enough to identify the spatial and the disorder average.

Say we have a fraction $q \in [0,1]$ of randomly distributed traps with an enhanced binding energy E_+ for desorption, and balance this by sites with lowered binding energy E_-. (In the following, we typically omit the subscript "W" for brevity.) Given q, the mean energy $\langle E \rangle = qE_+ + (1-q)E_-$, and the energy spread $\Delta E = E_+ - E_-$, the binding energies read $E_+ = \langle E \rangle + (1-q)\Delta E$ and $E_- = \langle E \rangle - q\Delta E$. This yields an effective desorption rate

$$W_{\mathrm{eff}} = \frac{1}{\langle W^{-1} \rangle} = W(\langle E \rangle) \frac{\mathrm{e}^{q\beta\Delta E}}{(1-q) + q\,\mathrm{e}^{\beta\Delta E}}.$$

A more interesting case is that of a continuous distribution of activation energies, the most natural being a Gaussian or an offset exponential distribution,

$$\rho_{\mathrm{G}}(E) = \frac{1}{\sqrt{2\pi\sigma^2}} \exp\left[-\frac{(E - \langle E \rangle)^2}{2\sigma^2}\right], \quad \text{or}$$
$$\rho_{\mathrm{P}}(E) = \frac{1}{\sigma} \exp\left[\frac{-(E - E_{\min})}{\sigma}\right] \quad (E \geq E_{\min}, \quad \langle E \rangle = E_{\min} + \sigma).$$

Here σ is the standard deviation of the energy distribution.

In the Gaussian case (with $W \propto \exp(-\beta E)$) one obtains the effective rate

by a simple integration,

$$\langle W^{-1}\rangle^{-1} = W(\langle E\rangle)\exp\left(-\beta^2\sigma^2/2\right).$$

This effect is *not* a mere additional activation energy, but introduces a rather strong reduction of the effective desorption rate especially for σ/k_B larger than the temperature. For cold grains at $T = 10\,\mathrm{K}$ and a small standard deviation of $\sigma/k_\mathrm{B} = 20\,\mathrm{K}$, the suppressing factor already becomes $\mathrm{e}^{-2} \lesssim 1/7$.

Using the exponential distribution has an even more profound effect. For the energy $E \geq E_\mathrm{min}$ the yet unaveraged inverse rate W^{-1} picks up an additional factor $\phi := \exp[\beta(E - \langle E\rangle)] \geq \exp[\beta(-\sigma)]$ compared to the value at the average activation energy. The distribution of ϕ can be obtained via $\rho_\mathrm{P}(E)\mathrm{d}E = \tilde{\rho}(\phi)\,\mathrm{d}\phi = \tilde{\rho}(\phi)\beta\phi\,\mathrm{d}E$ as $\tilde{\rho}(\phi) = \frac{1}{\beta\sigma}\,\mathrm{e}^{-1}\,\phi^{-1-1/(\beta\sigma)}$. Now as long as $\sigma < 1/\beta$, i.e., for high temperatures or small variance, ϕ has a finite average of $\exp(-\beta\sigma)/(1-\beta\sigma)$. For lower temperatures or large variance however, $\beta\sigma \geq 1$, and the ϕ average becomes infinite. Consequently we have (continuous in $\beta\sigma$)

$$\langle W^{-1}\rangle^{-1} = \begin{cases} W(\langle E\rangle)\exp(\beta\sigma)(1-\beta\sigma) & \text{for } \beta\sigma < 1, \\ 0 & \text{for } \beta\sigma \geq 1. \end{cases}$$

In the latter regime, the single atom desorbs after a finite time, but for any given time no matter how late, there is too large a fraction of cases in which the atom is still present. We note that the above seemingly innocent example $T = 10\,\mathrm{K}$ and $\sigma/k_\mathrm{B} = 20\,\mathrm{K}$ lies well inside this regime.

Clearly, a diverging reaction-free coverage is inconsistent with the (forced) neglect of LH rejection. It is also unphysical since the *individual* atom has a finite lifetime on the grain, and hence, a non-zero chance to desorb before it recombines. However, the recombination efficiency η with diverging reaction-free coverage is the same as that of an infinite flux, keeping W/a and S fixed. Consequently, in the ME efficiency given by (3.28) we only have to send the argument $2\sqrt{2F/A} \propto \sqrt{S\cdot W/A\cdot f/W}$ to infinity. From Appendix B.1 we then get $\eta \to 1 + \mathcal{O}(z^{-1})$ for $z \to \infty$, contrary to the physical argument. This illustrates the implications of lacking any dependence on the disorder realization and the individual random walk.

5.3.3 Finite Size Effects

For exponentially distributed binding energies, a disorder average like the reaction-free coverage $f\langle 1/W\rangle$ can diverge, although for a finite number S of adsorption sites on the grain it must clearly be finite. We now discuss how to account for finite S as this effect is of general importance. A typical way to prevent divergences is to introduce a cutoff at a finite upper energy bound, and often one chooses the expectation value of the maximum binding energy of the S adsorption sites (and renormalizes accordingly).

Assuming the probability distribution function (PDF) ρ of the single random variable 'binding energy' to include necessary cutoffs (like $\Theta(E - E_\mathrm{min})$ for the exponential distribution), the PDF for the maximum of S independent identically

distributed (i.i.d.) random variables to be E is given by

$$\rho_{\max}(E) = \frac{\mathrm{d}}{\mathrm{d}E}\left\{\left[\int_{-\infty}^{E}\rho(E')\,\mathrm{d}E'\right]^{S}\right\} = S\rho(E)\left[\int_{-\infty}^{E}\rho(E')\,\mathrm{d}E'\right]^{S-1}.$$

In the first form, the curly brackets are the probability for S independent energies to be less than or equal to E, so the derivative is the PDF of being equal to E. The second form shows as factors that we have S possible ways to choose the site which has maximal binding energy E, the probability that this energy is realized on that site, and the probability for all other sites' energies to be lower or equal. The expectation value of the maximum thus reads

$$\langle E_{\max}\rangle = \int_{-\infty}^{\infty}\mathrm{d}E\,E\,\frac{\mathrm{d}}{\mathrm{d}E}\left\{\left[\int_{-\infty}^{E}\rho(E')\,\mathrm{d}E'\right]^{S}\right\}.$$

Note that the tempting integration by parts generally leads to convergence trouble here. We consider distributions with finite mean $\langle E\rangle$ and variance σ^2, and the new variable $\tilde{E} = (E - \langle E\rangle)/\sigma$ (with PDF $\tilde{\rho}(\tilde{E}) = \sigma\rho(E)$) consequently has zero mean and unit variance. Rewriting the above expression in $\tilde{E}$, we obtain (using the normalization of $\rho_{\max}(E)$ and omitting the tilde in the end)

$$\langle E_{\max}\rangle = \langle E\rangle + \sigma\int_{-\infty}^{\infty}\mathrm{d}E\,E\,\frac{\mathrm{d}}{\mathrm{d}E}\left\{\left[\int_{-\infty}^{E}\tilde{\rho}(E')\,\mathrm{d}E'\right]^{S}\right\},$$

and the derivative will be noted $\tilde{\rho}_{\max}(E)$ accordingly.

Exponential distribution. For the exponential distribution (which raised the issue and makes explicit calculations feasible) this can be evaluated in a nearly closed form. We have $\tilde{\rho}(E) = \Theta(E+1)\exp[-(E+1)]$, so $\tilde{\rho}_{\max}(E) = S\Theta(E+1)\exp[-(E+1)]\,\{1-\exp[-(E+1)]\}^{S-1}$ and

$$\begin{aligned}\int_{-\infty}^{\infty}\mathrm{d}E\,E\tilde{\rho}_{\max}(E) &= \int_{0}^{\infty}\mathrm{d}E\,(E-1)\tilde{\rho}_{\max}(E-1)\\ &= -1 + S\int_{0}^{\infty}\mathrm{d}E\,E\sum_{k=0}^{S-1}\binom{S-1}{k}(-)^k\exp[-E(k+1)]\\ &= -1 + S\sum_{k=0}^{S-1}\binom{S-1}{k}\frac{(-)^k}{(k+1)^2} =: -1 + X_S\,.\end{aligned}$$

Dragging one $(k+1)$ into the binomial, we get $X_S = \sum_{k=0}^{S-1}\binom{S}{k+1}\frac{(-)^k}{k+1}$. We split the binomial into $\binom{S-1}{k}+\binom{S-1}{k+1}$. The first sum can be evaluated by again dragging in a factor $(k+1)$ to yield $(1/S)\sum_{k=0}^{S-1}\binom{S}{k+1}(-)^k = -(1/S)\sum_{k=1}^{S}\binom{S}{k}(-)^k = -(1/S)[(1-1)^S - 1] = 1/S$. The second sum reads $\sum_{k=0}^{S-2}\binom{S-1}{k+1}\frac{(-)^k}{k+1} = X_{S-1}$, since the $k = S-1$ term vanishes. Thus $X_S = X_{S-1} + 1/S$, and with $X_1 = 1$

we have $X_S = \sum_{k=1}^{S}(1/k)$. Hence for the exponential distribution,

$$\langle E_{\max}\rangle = \langle E\rangle + \sigma\left(-1 + \sum_{k=1}^{S}\frac{1}{k}\right) = E_{\min} + \sigma\sum_{k=1}^{S}\frac{1}{k}.$$

The sum approaches the logarithm and can (by EULER-MACLAURIN summation) be approximated as $\ln S + \gamma + 1/(2S)$ with an absolute error of less than about 2×10^{-3} for $S > 400$, and obviously, the order of magnitude of the error is not changed by omitting the $1/(2S)$ term. $\gamma = 0.577\ldots$ is Euler's constant.

We now calculate the disorder average $\langle W^{-1}\rangle_S$ that one obtains from an energy distribution cut off at $\langle E_{\max}\rangle$ (for S sites) and renormalized, so that

$$\langle W^{-1}\rangle_S = \nu^{-1}\int_{-\infty}^{\langle E_{\max}\rangle} \mathrm{d}E\,\exp(\beta E)\frac{\rho(E)}{\mathcal{N}},$$

where $\mathcal{N} = \int_{-\infty}^{\langle E_{\max}\rangle}\mathrm{d}E\,\rho(E)$ is the normalization. Using the approximation $\sum_{k=1}^{S}(1/k) \approx \ln S + \gamma$, this gives

$$\mathcal{N} \approx \int_{0}^{\ln S+\gamma} \mathrm{e}^{-x}\,\mathrm{d}x = 1 - \frac{1}{\mathrm{e}^{\gamma}\,S}$$

and

$$\begin{aligned}\langle W^{-1}\rangle_S &\approx \nu^{-1}\int_{0}^{\ln S+\gamma}\frac{\mathrm{e}^{-x}}{\mathcal{N}}\exp[\beta(\sigma x + E_{\min})]\mathrm{d}x\\ &= W^{-1}(\langle E\rangle)\,\mathrm{e}^{-\beta\sigma}\,\frac{1}{\mathcal{N}}\,\frac{1}{1-\beta\sigma}\left(1 - \frac{1}{(\mathrm{e}^{\gamma}\,S)^{1-\beta\sigma}}\right)\\ &= W^{-1}(\langle E\rangle)\frac{\mathrm{e}^{-\beta\sigma}}{1-\beta\sigma}\cdot\frac{\mathrm{e}^{\gamma}\,S - (\mathrm{e}^{\gamma}\,S)^{\beta\sigma}}{\mathrm{e}^{\gamma}\,S - 1},\end{aligned}$$

where the last fraction is the finite-S correction to the expression that was formerly obtained only for $\beta\sigma < 1$. Since $S \gg 1$, this fraction can be further approximated by $\left[1 - (\mathrm{e}^{\gamma}\,S)^{\beta\sigma-1}\right]$. For very large temperatures, the correction goes to unity as it should, while for the problematic low temperatures, the combined correction factors caused by disorder and by finite S now yield $\langle W^{-1}\rangle_S \approx W^{-1}(\langle E\rangle)\frac{(\mathrm{e}^{\gamma-1}\,S)^{\beta\sigma}}{\beta\sigma}$ for $\beta\sigma \gg 1$, which is large but finite.

5.4 Simulations

Having established a set of "effective parameters" (including finite-size corrections), we shall now briefly examine whether the "effective parameters" approach can describe reasonably well the outcome of KMC simulations. In all of the following, rates are determined as in Section 3.9, and we use the standard olivine parameter set of Katz *et al.* [34] as our *average* energies. The general simulation method has been described in Chapter 4.

We compare full-grain KMC simulations of 10^6 impinging hydrogen atoms onto a dust grain in the stationary state to the above theory: We keep the (quadratic) grain size fixed at $S = 4 \times 10^4$ with a square lattice, and also fix the temperature $T = 12\,\mathrm{K}$, corresponding to a ratio $a/W \approx 1295.519$. Without any disorder, the encounter probability $p_{\mathrm{rw}} \approx 0.011$ implies an efficiency of only $\eta_{\mathrm{ME}} \sim 5 \times 10^{-5}$ under such conditions. With this setup, we first examine GAUSSian disorder of strengths $\sigma_{E_W}/\langle E_W \rangle = 0.05$, 0.1, 0.2 and 0.3; the results are shown in Figure 5.1. For each plot, the horizontal axis shows the spatial average $\overline{W^{-1}}$ of a given disorder realization, and we used $8 \ldots 10$ arbitrary realizations in each setting. For all those values as found in simulations for a certain quenched disorder realization, we also give the ME result. It is obvious that for a single realization, the ME prediction typically (except for very weak disorder) clearly overestimates the efficiency. Therefore, comparison with the result for the full disorder-averaged parameter $\langle f/W \rangle$ is moot: It has to overestimate the average of simulations as well. In a completely analogous

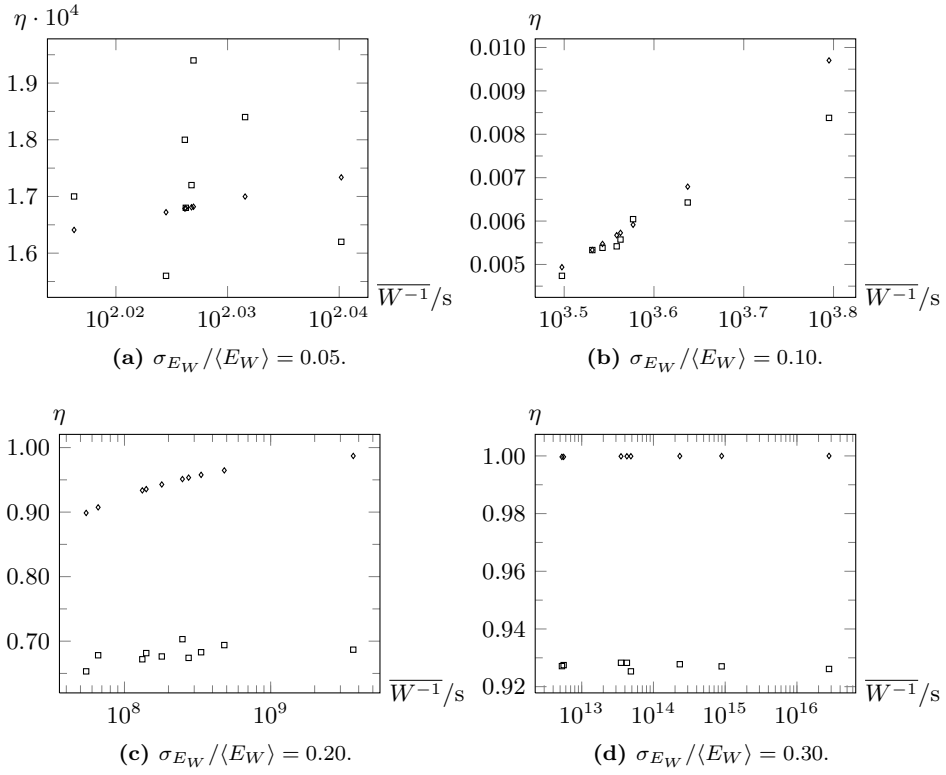

(a) $\sigma_{E_W}/\langle E_W \rangle = 0.05$. **(b)** $\sigma_{E_W}/\langle E_W \rangle = 0.10$.

(c) $\sigma_{E_W}/\langle E_W \rangle = 0.20$. **(d)** $\sigma_{E_W}/\langle E_W \rangle = 0.30$.

Figure 5.1: Recombination efficiency for GAUSSian disorder of increasing strengths $\sigma_{E_W}/\langle E_W \rangle$. Squares show the KMC result, diamonds the corresponding ME prediction for the flux / coverage parameter as evaluated for the single realization.

way, Figure 5.2 shows the result for exponential disorder in the binding energies. Here we consider strengths $\sigma_{E_W}/\langle E_W \rangle = 0.05$, 0.06, 0.08, 0.10 only, since the effect of exponential disorder is, not surprisingly (cf. Section 5.3.2), even more pronounced. For both types of disorder, broader distributions lead to averages

$\overline{f/W}$ so large that numerical evaluation of η_{ME} overflows, and just before this happens, we already have $1 - \eta_{\mathrm{ME}} < 10^{-3}$.

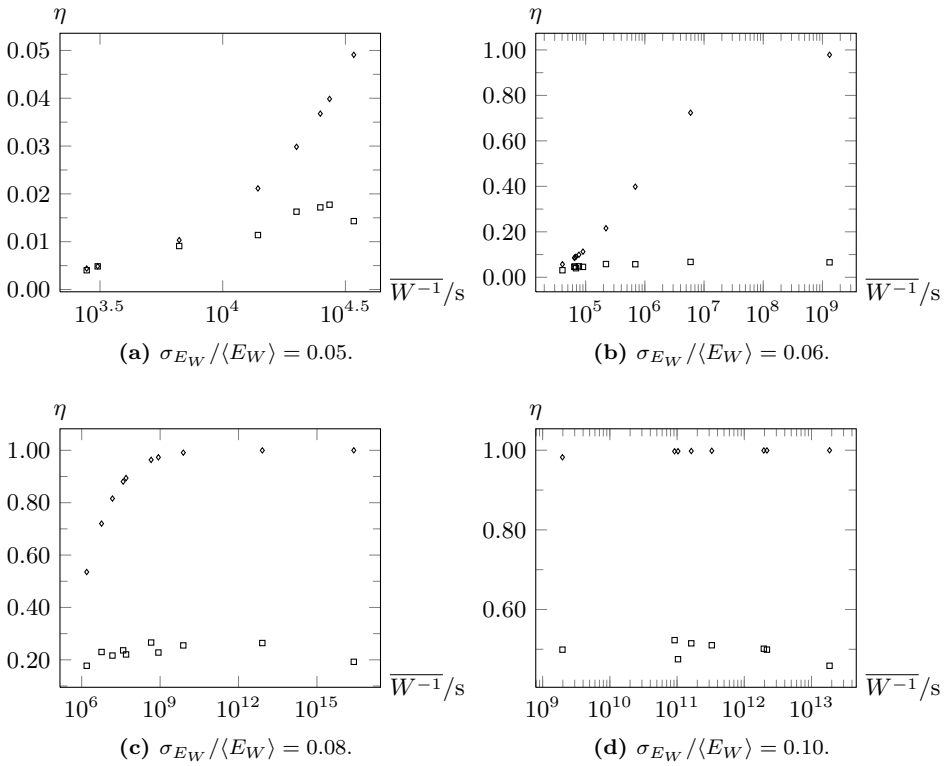

(a) $\sigma_{E_W}/\langle E_W \rangle = 0.05$. **(b)** $\sigma_{E_W}/\langle E_W \rangle = 0.06$. **(c)** $\sigma_{E_W}/\langle E_W \rangle = 0.08$. **(d)** $\sigma_{E_W}/\langle E_W \rangle = 0.10$.

Figure 5.2: Recombination efficiency as in Figure 5.1 for exponential disorder of increasing strengths $\sigma_{E_W}/\langle E_W \rangle$.

All simulations show that already for moderate disorder (below a width of $0.1\langle E_W \rangle$), the recombination efficiency increases dramatically, due to a likewise increased coverage. This corroborates the paradigm that disorder in local transition rates has such a strong effect that it may easily shift the temperature window of efficient recombination so that it complies with observed hydrogen abundances.

Unfortunately, effective rates completely fail to describe this situation, and do so on a very basic level. For the ME efficiency evaluated at a full disorder average of the parameter f/W, a discrepancy to the average of MC simulations' η values would not be too surprising. Even when the result for $\langle f/W \rangle$ is corrected for the finiteness of S, it averages over all realizations of disorder *before* η_{ME} is evaluated — for a strongly non-linear dependence as that of the efficiency on the flux parameter, the outcome can obviously be vastly different from the average of η_{ME} as evaluated for a given disorder realization (corresponding to averaging η_{MC} values).

However, even for a given quenched disorder realization, η_{ME} for the corresponding $\overline{f/W}$ value still differs significantly from the simulation result η_{MC} of this realization. There are three possible explanations, which may also apply

simultaneously. First, we have not yet examined systematically how well the master equation actually describes the full system, cf. Section 3.9. The correlations between adatoms that the ME approach neglects might become relevant at least when the mean adatom number is no longer small. Since disorder greatly increases this adatom number, it may also render these many-particle effects more important. Second, the ME framework does not and cannot account for LH rejection, in contrast to our simulations. The relative importance of this factor increases with the coverage, and hence with decreasing temperature or with increasing disorder. We believe this is not crucial for the comparison in general, as we tried to make sure that the coverage does not become too large even for the strong disorder examples above. However, it may well be partly responsible for the discrepancy seen in the strongest disorder plots in Figure 5.1, though surely not in the last plot of Figure 5.2. The third factor is, in a way, the most subtle one, but probably also the most important: One can see that by no means does η_{MC} depend in a simple manner on $\overline{W^{-1}}$ of the quenched disorder realization; in fact, in several plots it seems as if it hardly depends on it at all! This can be understood by remembering that the finite-grain average $\overline{W^{-1}}$ may be dominated by one or two very deep wells, while there could also be quite a few moderately deep wells, which are far more helpful to recombination. One very deep well will mostly be occupied, and once another atom falls into this trap, we count one recombination event. However, if it is loosely surrounded by 10 moderately deep wells, these may frequently be occupied and (by their sheer number) much more often emptied again in a recombination event. We see that rare events in the guise of deep wells dominate the system's behavior, but definitely not in a simple way.

We finally comment briefly on comparable KMC simulations of Chang *et al.* [23]. They choose activation *energies* for hopping and desorption to be related by a constant factor (as opposed to the rates). Hence the *relative* standard deviation of the distributions of both activation energies coincide, $\tilde{\sigma}_{E_a} = \sigma_{E_a}/\langle E_a\rangle = \sigma_{E_W}/\langle E_W\rangle = \tilde{\sigma}_W$, and the *absolute* σ_{E_W} is larger than σ_{E_a} by a factor of $\langle E_W\rangle/\langle E_a\rangle$. In our case, however, binding energies are only shifted w.r.t. diffusion barriers, their absolute standard deviations thus coincide. (Note that the disorder averages $\langle E_a\rangle$ and $\langle E_W\rangle$ agree between both approaches, and that we neglect the distinction between spatial and disorder average for this argument.)

We compared data points with the same *absolute* standard deviation σ_{E_a} of the *hopping* activation energy. Our (unsystematic) findings seemed to agree reasonably well with theirs (*ibid.*, Figure 3) as long as disorder is weak ($\sigma_{E_a} < 0.06\cdot\langle E_a\rangle \approx 0.045\langle E_W\rangle$), but show increasingly larger η the stronger the disorder. At a first glance, this seems contradictory: For given σ_{E_a}, Chang *et al.* [23] employ a *larger* binding energy standard deviation σ_{E_W} than we do; judging from Section 5.3.2, this should increase the average coverage and thus the efficiency, while we see just the opposite!

We offer an explanation based on the effect of the second parameter. $W/a = \exp[-\beta(\langle E_W\rangle - \langle E_a\rangle)] = \text{const.}$ in our case (independent of site and disorder). Compared to this, W/a as in Chang *et al.* [23] picks up an additional (site-dependent) factor such that

$$\begin{aligned}\frac{(W/a)_{\mathrm{Chang}}}{W/a} &= \exp\left[-\beta(E_a - \langle E_a\rangle)\left(\frac{E_W - \langle E_W\rangle}{E_a - \langle E_a\rangle} - 1\right)\right] \\ &= \exp[-\beta(E_a - \langle E_a\rangle)(\langle E_W\rangle/\langle E_a\rangle - 1)].\end{aligned}$$

We calculate the disorder average over this additional factor in terms of σ_{E_a} (which coincides in our comparison): For GAUSSian disorder, this yields

$$\left\langle \frac{W}{a} \right\rangle_{\text{Chang}} = \frac{W}{a} \cdot \exp\left(\frac{1}{2} \tilde{\beta}^2 \sigma_{E_a}^2 \right),$$

whereas for exponential disorder we obtain

$$\left\langle \frac{W}{a} \right\rangle_{\text{Chang}} = \frac{W}{a} \cdot \frac{\mathrm{e}^{\tilde{\beta}\sigma_{E_a}}}{1 + \tilde{\beta}\sigma_{E_a}},$$

with $\tilde{\beta} = \beta(\langle E_W \rangle / \langle E_a \rangle - 1)$. In both cases (with $\langle E_W \rangle / \langle E_a \rangle - 1 \lesssim 1$), the correction factor is $1 + \mathcal{O}(\beta\sigma)^2$ for small $\beta\sigma$, but it becomes significant for $\beta\sigma \geq 1$. Now since the mortality of the random walker at a given site is $W/(a+W) \approx W/a$, this increased average means that the adatoms have *on average* a higher mortality per step (or lower encounter probability) than in our treatment. This result is based on two factors: First, the activation energy scaling lowers the difference $E_W - E_a$ for energies below their average and increases it above. Second, due to the falling exponential shape of $\exp[-\beta(E_W - E_a)]$, the effect of a change in energy differences $E_W - E_a$ below the average value dominates that of the change above. The thus increased per-step mortality can overcompensate the larger coverage, so that the efficiency is diminished.

5.5 Summary

While all results point into the "right" direction (namely that disorder substantially increases the efficiency), we lack any reasonable quantitative theory: The effective-parameter ME approach fails for all but the weak-disorder case, which we deem practically irrelevant.

One problem is that the efficiency typically depends on the given quenched disorder realization, and an average over the outcomes is only loosely related to the result of an average on the parameter level because of the profound non-linearity of η_{ME}. More fundamentally, however, even the single disorder realization is typically ill-described by the (zero-dimensional) master equation framework. This appears to be an effect of the intricate way in which the dominant processes on the grain depend on the *full* distribution of binding energies in the given quenched realization, and possibly even on their spatial correlations. This calls for entirely different approaches than the zero-dimensional master equation used so far.

Coming back to an earlier point, we note that for independent distributions of W and a, using effective rates would imply to perform separate averages. This is an additional grave approximation that is insensible to even consider at this point.

An interesting approach to deal with disorder (in the case $W/a = \text{const.}$) maps the complicated energy landscape onto few types of binding sites. For such a system, one might consider coupled rate equations as in the numerical treatment of Cuppen and Herbst [24], which may at least be solved for certain reasonable simplifying assumptions. As pointed out *ibid.*, it is an irony that stochastic methods like the ME framework were introduced to properly deal with astrophysically relevant grain sizes and low coverages, yet the disorder in

energies increases the coverage again: Therefore, rate equations may not only be the only feasible means to study the system analytically, but they may also be the correct limiting equations in a stricter sense.

Chapter 6

Island Edge Nucleation

The study of this problem was motivated by its similarity to the hydrogen recombination analysis. In fact, it is a one-dimensional analogon of the dust grain nucleation problem in a certain sense (made explicit in Section 6.2.1); hence one may regard it as an "offspring problem" of the former. Moreover, a question of high mathematical semblance, viz. homogeneous second-layer nucleation, had already successfully been treated analytically, cf. Section 6.3.1. Together this let the study of island edge nucleation appear as a promising enterprise.

6.1 Introduction

Homoepitaxial crystal growth of platinum, especially of the Pt/Pt(111) system, has been extensively studied experimentally [2, also for a general review of the relevant system properties]. As an important example of thin film growth, it is of high general technological relevance, but also of particular interest because of the catalytic properties of platinum.

To fully understand its properties, one eventually has to explain its features on the basis of fundamental microscopic processes. The common method is to use kinetic Monte Carlo (KMC) simulations, and for an overview of these techniques as well as many technical details, we refer the reader to Gödecke [61]. Of course, every aspect of this complex problem that can be understood analytically is very welcome. Here we wish to analyze one particular feature to be introduced shortly.

Consider a Pt(111) surface onto which Pt atoms are deposited. They can diffuse on the surface and may attach to other adatoms, forming immobile nuclei of islands growing afterwards. This system exhibits a wide variety of island shapes (fractal, hexagonal, triangular, dendritic) and corresponding growth modes, depending on flux, surface temperature, and current island size, cf. Figure 6.1. Under the conditions used in the images, one observes a transition from fractal-like island shapes for lower temperatures to a compact growth mode leading to triangular islands around $T = 400\,\mathrm{K}$. The edges of these islands are oriented along the $\langle 1\bar{1}0\rangle$ directions. With increasing temperature this changes again to dendritic shapes, and only at much higher temperatures around 700 K one returns to compact islands, now close to hexagonal shape. The explanation lies in the changing adatom mobility on the surface. At lower T, adatoms landing

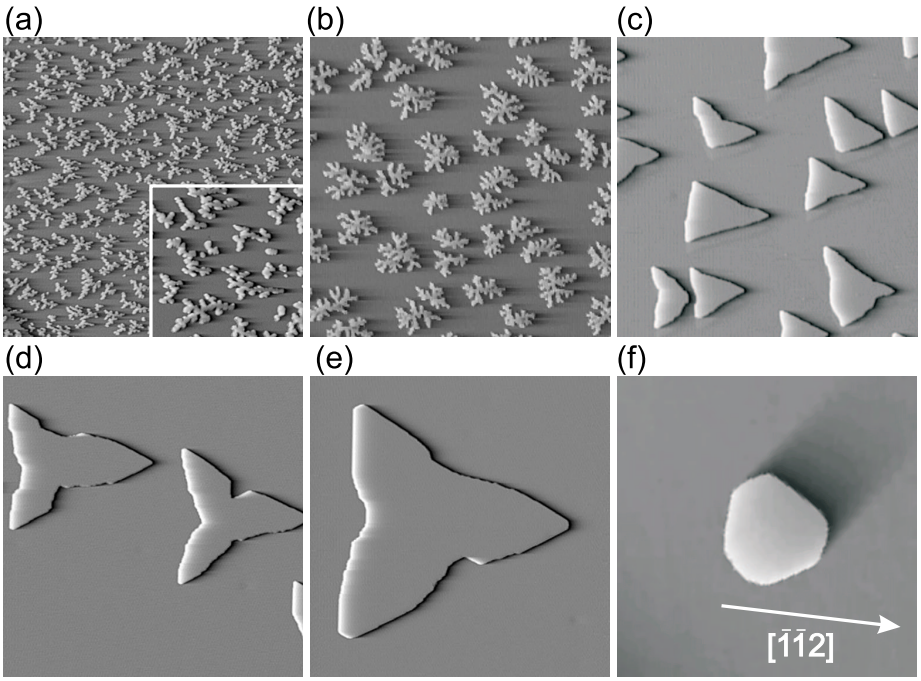

Figure 6.1: The widely varying growth shapes of Pt/Pt(111): Islands of monatomic height in STM (surface tunneling microscopy) topographs (1560 A × 1560 A). Deposition at (**a**) 200 K, (**b**) 300 K, (**c**) 400 K, (**d**) 500 K, (**e**) 600 K, (**f**) 700 K, after deposition of 0.15 ML at a rate of 7×10^{-3} ML/s in (**a**)–(**e**), and 0.08 ML at 2.7×10^{-3} ML/s in (**f**), respectively. [2], with kind permission of Joachim Krug.

on the surface between islands stick to the island edges as soon as they attach to one. Increasing the temperature, those adatoms stay mobile after attachment and diffuse along the island edges before coming to rest in energetically favorable positions (i.e., forming complete rows).

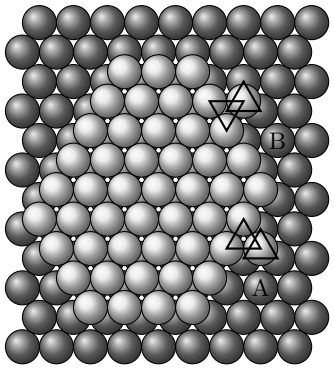

Figure 6.2: Ball-model illustration of the geometrically different A- and B-edges.

The edge orientation and the varying degree of symmetry can be explained as follows: The Pt(111) surface is an fcc(111) facet, hence one expects a six-fold symmetry. (For adatoms moving along the island edges, one need not account for intermediate hcp positions for energetic reasons.) Owed to the underlying atom layer, one can however distinguish between two types of edges, conventionally termed "A-" and "B-edges". In both cases an adatom attached to the edge has two nearest neighbors in the island layer, and three in the underlying layer. But while for A-edges, the triangle of an adatom and its island-layer nearest neighbors points into the same direction as the triangle formed by the underlying three nearest neighbors, for a B-edge, those two triangles point in opposite directions, see Figure 6.2. Edges de-

limiting an island change the edge type at the corner, once for each turn by a 30° angle.

The different geometry corresponds to a different binding energy discriminating between the two types of positions. In fact, the experiment shows that compact triangular islands are almost always delimited by B-edges exclusively, for the following reason: A-edges bind adatoms more strongly. Starting from a regular hexagonal shape with some kinks, this implies that the A-edges obtain an additional adatom influx at their corners, coming from the neighboring B-edges (Section 6.3); consequently, they grow at a faster *normal* velocity v_A than the B-edges. This means (as can be seen from a sketch) that the lengths of the A-edges shrink. As long as $v_\mathrm{A}/v_\mathrm{B} < 2$, a stationary hexagonal shape is approached, where $v_\mathrm{A}/v_\mathrm{B} = d_\mathrm{A}/d_\mathrm{B}$ and $d_\mathrm{A/B}$ are the distances to the island center. However, if $v_\mathrm{A}/v_\mathrm{B} > 2$, the A-edges eventually vanish.

This mechanism becomes irrelevant at much higher temperatures, when the difference in binding energies (and possibly in diffusion barriers) no longer outshines the thermal energy, and one can observe nearly hexagonal islands then. The overall picture is also corroborated by the observation that in the same regime, homoepitaxial growth on Ag(111) retains the full symmetry of hexagonal islands, corresponding to the fact that both step orientations have the same energies.

6.2 The Problem

Here we want to examine the particular problem of where (and possibly when) one-dimensional growth forms the *first* nucleus, i.e., where two adatoms attached to kinkless (perfectly faceted) island edges meet for the first time. This problem has not yet been understood analytically, and it is relevant for several reasons: It may provide a more detailed explanation for the different kink density on the two types of edges, starting from first principles. It also applies to other fcc(111) surfaces of transition metals [70]. Moreover as we shall see in Section 6.3, there is a regime in which formation of the first nucleus is the rate-limiting step for island growth. Finally, all further nucleation events are far more complicated and may at best be described in a continuum theory. Present kinks change the geometry *and* allow two different ways for edge atoms to be captured: By nucleating with a partner, but also by being incorporated at the kink.

6.2.1 Close Links to Hydrogen Recombination

In both cases, one considers two random walkers, and time is not essential. While the first-passage problem for hydrogen recombination arises out of the competition between meeting and desorption and we ask for the probability of one of the two possible outcomes, here the question concerns the *position* of the (eventually sure) meeting of the edge atoms. We do not treat any disorder here, but spatial homogeneity is still broken by the two types of edges. While the topology is, in a sense, the same as before (periodic boundary conditions), one-dimensionality of the island edge originally promised a reasonably simple solution.

Second-layer nucleation as described in Section 6.3.1 has a slightly different relation to the hydrogen problem. In the latter, the surface is closed and hence,

has no boundaries, but the atom can desorb from each adsorption site. In the nucleation problem, boundary conditions are partly reflecting (for a finite Ehrlich-Schwoebel (ES) barrier exacerbating inter-layer transport), so the atom may escape, but only at the boundary. In both cases, one may ask the same question, viz. with what probability does the atom nucleate / recombine?

6.3 Review of Known Results

The topic of island edge nucleation has been approached on many levels, e.g., ab initio density functional theory (DFT) calculations for the energy landscape along the island edge, molecular dynamics simulations [70], or KMC simulations as in Gödecke [61]. We will only review one string of development of the analytic kinetic theory of the process.

The conventional picture of island edge nucleation (underlying the island growth) treats edge atoms as a continuous concentration n, and takes the nucleation rate to be the RE expression $R \sim D_{\text{edge}} n^2$. The local adatom density n is obtained from the solution of a Burton-Cabrera-Frank diffusion equation. An analogous procedure used to treat second-layer nucleation, i.e., the formation of a stable nucleus *on top* of an existing island, has been demonstrated to fail for large ES barriers (effectively confining the geometry) [50]. Moreover, the analogy to the case of hydrogen recombination also suggests that fluctuations and rare events dominate nucleation, so that we have to improve upon this naïve rate equation treatment. Using the single-particle quantity n to obtain the two-particle nucleation rate ω will also be referred to as the 'mean-field' way. For the remainder of this Part, n will be a mere site index.

Concerning the ensuing island edge growth, a simple argument [2, Section 2.4.3] provides the estimate $\ell_{1\text{d}} \approx (a_0 D_{\text{edge}}/F_{1\text{d}})^{1/4}$ for the distance between kinks along the one-dimensional island edge, with D_{edge} the edge diffusion coefficient and $F_{1\text{d}}$ the one-dimensional flux[1] onto the edge. A single-adatom diffusion analysis shows [2] that this leads to a net mass transfer to the A step if $\sqrt{D_{\text{A}}/D_{\text{B}}}\exp[E_{\text{b,B}} - E_{\text{b,A}}] > 1$, where D_{A} and D_{B} label the edge diffusion coefficients and $E_{\text{b,A}}$, $E_{\text{b,B}}$ the binding energies: Differences in binding energy taken aside, faster diffusion finds kinks more quickly, which overcompensates the lower kink density, and the corresponding edge grows more quickly.

A general random walk understanding of the *first* nucleation event along an island edge is what we now focus on exclusively. As promised above, the kink density estimate provides an additional reason to consider this problem: Obviously, at low temperatures or for small islands, the typical kink distance will be much larger than the island edge length, and consequently, islands may spend a long time in a fully faceted configuration. Forming the first nucleus is then the rate-limiting step for island growth.

[1] Different from F before, $F_{1\text{d}}$ is a flux *per length*, hence of dimension $1/(LT)$.

6.3.1 Homogeneous Second-Layer Nucleation

In a series of papers Castellano and Politi [71], Politi and Castellano [72, 73] have examined the problem of second-layer-nucleation in one- and two-dimensional geometries in a truly atomistic random walk fashion. Their boundary conditions are fully or partially absorbing, but the analysis is restricted to the homogeneous case throughout.

They find [72] that the mean-field approach generally fails. For the nucleation rate, it is proven approximately equivalent to treating the particles as *non-interacting*, hence allowing for repeated meetings of a given pair of particles even after their first encounter. In fact, whenever step-edge barriers are not weak, i.e., when the geometry is effectively confined, the mean-field expression of the spatial distribution of nucleation events is *dominated* by these fictitious later nucleations. Moreover it is shown that the thus obtained nucleation rate overestimates the true nucleation rate by a factor $N_{\mathrm{all}}/N_{\mathrm{dis}}$; this is the ratio of the total number of sites (or steps) and the number of *distinct* sites a *single* random walker sees on the terrace (or the island edge, in one dimension).

The analytical theory laid out in Politi and Castellano [72, 73] is based on the following steps (we will focus on the one-dimensional case). First, the authors argue that one need only consider two-atom processes. In a discrete-space discrete-time setup, one then determines the single-particle propagator, starting from a homogeneous initial distribution $p_n(0) = p_n^{\mathrm{U}} = 1/L$ on an edge of length L, for the boundary conditions corresponding to a given ES barrier.[2] The next step considers the second atom impinging after a time τ (which is distributed exponentially with mean $\tau_{\mathrm{dep}} = 1/L$), and one aims for the probability distribution of the position of their *first meeting*. All quantities of interest are linear in the atoms' initial distributions, hence one may absorb the stochastically distributed time τ between arrivals into the single-particle distribution for the first atom, $p_n^{\mathrm{U}} \to p_n^{\mathrm{eff}} = \sum_{\tau=0}^{\infty} \frac{\mathrm{e}^{-\tau/\tau_{\mathrm{dep}}}}{\tau_{\mathrm{dep}}} p_n(\tau)$. In this way, any sought quantity can now be avaluated for two *simultaneously* present particles, but with initial distributions p_n^{eff} and p_n^{U}, respectively. Now one has to find p_n^{eff} using the time-evolution $p_n(t)$. Under mild assumptions it is shown that

$$p_n^{\mathrm{eff}} = \frac{\tau_{\mathrm{res}}}{\tau_{\mathrm{dep}} + \tau_{\mathrm{res}}} p_n^{\mathrm{S}}, \tag{6.1}$$

where p_n^{S} is the stationary one-particle distribution and τ_{res} the residence time of the single atom.

Essential for our purpose are the following further measures: It remains to calculate the probability distribution of the first encounter position of two particles deposited simultaneously with given initial distributions p_n^{eff} and p_n^{U}. For the one-dimensional setting we want to expand on, the problem of two meeting random walkers can be mapped to a single two-dimensional random walk $p_{m,n}(t)$. Initial conditions then read $p_{m,n}(t=0) = p_m^{\mathrm{eff}} p_n^{\mathrm{U}}$, and a nucleation event corresponds to the absorption at the diagonal $m = n$, i.e., $p_{n,n}(t) = 0$. The spatio-temporal distribution of nucleation events is given by the probability current to this diagonal.

[2] Throughout this Chapter, p denotes the particle propagator.

In discrete time the evolution equation reads

$$p_{m,n}(t+1) = \frac{1}{4}\left[p_{m-1,n}(t) + p_{m+1,n}(t) + p_{m,n-1}(t) + p_{m,n+1}(t)\right]$$

for $m \neq n$, with the boundary condition $p_{n,n}(t) \equiv 0$ (at all times), and starting from the initial condition $p_{m,n}(t) = \frac{1}{2}\left[p_m^{\mathrm{U}} p_n^{\mathrm{S}} + p_m^{\mathrm{S}} p_n^{\mathrm{U}}\right]$ which has been symmetrized ($p_{n,n}(t=0) = 0$). The nucleation distribution reads

$$R_n(t) = \frac{1}{4}\left[p_{n-1,n}(t) + p_{n+1,n}(t) + p_{n,n-1}(t) + p_{n,n+1}(t)\right]$$

for times $t > 0$ and $R_n(t=0) = p_n^{\mathrm{U}} p_n^{\mathrm{S}}$ using the initial distribution.

In general, the single-particle evolution is solved by a separating ansatz. This delivers spatial eigenfunctions $A_k \sin(n\phi_k) + B_k \cos(n\phi_k)$ and a temporal part $\exp\left[t \ln\cos(\phi_k)\right]$ for $k = 0 \ldots L-1$, with angles and pre-factors determined by the boundary and initial conditions.

As an example we recall the outcome for perfectly reflecting boundaries. One obtains [72] $\phi_k = k\pi/L$ and $A_k = B_k \tan(k\pi/(2L))$, such that spatial eigenfunctions read $X_k(n) = [\tan(k\pi/(2L))\sin(nk\pi/L) + \cos(nk\pi/L)]$ The initial distribution only affects the pre-factor $A_k = \frac{1}{\mathcal{N}_k}\sum_{n=1}^{L} p_n(0) X_k(n)$ with normalization $\mathcal{N}_k = \frac{L}{2}\left[1 + \tan^2(k\pi/(2L))\right](1+\delta_{k0})$. Obviously, the single-particle distribution $p_n(0) = p_n^{\mathrm{U}} = 1/L$ stays constant, while arbitrary other contributions to the initial distribution decay exponentially; they become negligible for $t \gg 2L^2/\pi^2 \sim \tau_{\mathrm{tr}}$, with τ_{tr} the single-atom traversal time of the edge.

For the two-particle case, an analogous separating ansatz delivers the general solution in terms of the one-particle eigenfunctions [73],

$$p_{m,n}(t) = \sum_{k,j=0}^{L-1} B_{k,j} \cdot \exp\left[t \ln \frac{\cos(k\pi/L) + \cos(j\pi/L)}{2}\right] X_k(m) X_j(n),$$

with coefficients $B_{k,j}$ available to satisfy boundary and initial conditions. It is now of crucial importance that both particles cannot change places without meeting first: This implies that the 'triangles' $m < n$ and $m > n$ of the distribution cannot affect each other's time evolution, they are *dynamically disconnected*. Consequently, one can apply the method of images to satisfy the "nucleation" boundary condition: Replace the initial $p_{m,n}(0)$ by

$$\tilde{p}_{m,n}(0) = \begin{cases} p_{m,n}(0) & \text{for} \quad m < n \\ 0 & \text{for} \quad m = n \\ -p_{m,n}(0) & \text{for} \quad m > n, \end{cases}$$

which clearly satisfies the condition on the diagonal. The antisymmetry renders the coefficients $B_{k,j}$ antisymmetric (due to linear independence of the eigenfunctions), and thence, it is preserved for all times. This means that the nucleation condition is automatically obeyed at all times as well, while outside the diagonal, the distribution is always the physical one or its negative, respectively. (Note that this does not work for the two-dimensional case, since then, the nucleation condition no longer separates the four-dimensional hypercube into disconnected regions.) The exact result then has coefficients

$$B_{kj} = \frac{1}{\mathcal{N}_k \mathcal{N}_j} \sum_{m<n} p_{m,n}(0)\left[X_k(m) X_j(n) - X_j(m) X_k(n)\right].$$

With this, one may finally evaluate the spatial nucleation distribution

$$P_n = \sum_t R_n(t) = p_n^{\mathrm{U}} p_n^{\mathrm{S}} + \sum_{t=0}^{\infty} \frac{1}{2} \left[\tilde{p}_{n,n+1}(t) + \tilde{p}_{n-1,n}(t) \right],$$

where $\tilde{p}$ coincides with p at the positions occurring. Politi and Castellano [73] show that to high accuracy, the distribution is approximated as

$$P_n \propto \cosh(\pi) - \cosh\left[\pi \left(\frac{2n}{L+1} - 1 \right) \right].$$

In the next Section we will explain the difficulties in extending the method of Castellano and Politi [71], Politi and Castellano [72, 73] to the situation of a periodic inhomogeneous island edge.

6.4 First Nucleation Distribution

We should state first of all that our aim was an *analytic* description of the dependence of the first nucleation distribution on the parameters (transition rates and step lengths). Obviously, one could easily simulate the system by kinetic Monte Carlo techniques [as in 61], or alternatively solve the evolution equations (see below) numerically [as in parts of 71–73]. We have not followed this road, since these approaches share one problem: Especially given the huge parameter space, one can hardly deduce the general dependence of P_n on the parameters (at least not beyond the level heuristics may provide).

6.4.1 Model Assumptions

Consider a highly simplified picture of the island edge growth processes. We start with a regular hexagonal shape, albeit with (alternating A- and B-) edges of different lengths, without any kinks present. Adsorption sites are spatially discrete positions distributed uniformly along the edges. The incoming (one-dimensional) adatom flux is assumed homogeneous, neglecting the inhomogeneity of the diffusion field around an island [61, Section 5.2]. After an adatom has attached to the edge, it only stops its edge diffusion once it has met another adatom, which is the nucleation event we are interested in. We thus assume that atoms cannot detach from the island edge, so that without a partner, its lifetime would be infinite.

In reality, the one-dimensional energy landscape for an edge atom is very complicated; for example, there is a weakly bound state at the corner position between two edges. For the effects we are interested in, we shall be content with modeling the following features: Each type of edge (synonymously, each 'zone' or step) has a uniform binding energy, given by the potential minimum at the position of the classical adsorption site. (The energy will be taken positive, so that a larger binding energy means a *weaker* binding.) The diffusion constant is homogeneous as well and governed by the uniform height of the energy barrier separating neighboring sites. At the corner where two edges meet, there is an additional barrier, see Figure 6.3. For simplicity, we consider an island with only two (instead of six) edges of lengths ℓ_{A} and ℓ_{B} (in terms of adsorption sites), so that one can imagine the edge as in the Figure, with periodic boundary conditions. We further set $L := \ell_{\mathrm{A}} + \ell_{\mathrm{B}}$.

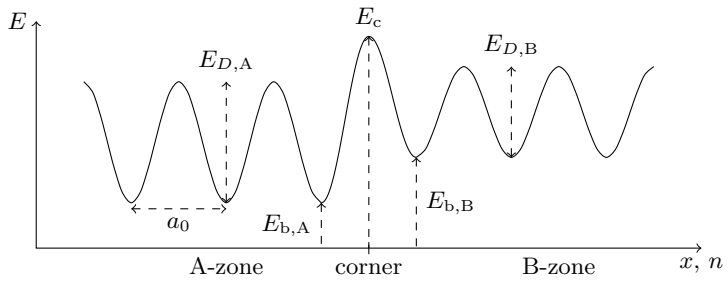

Figure 6.3: Simplified energy landscape along the island edge.

In the discrete picture, the energy landscape can be described with four hopping rates: The rates Γ_A and Γ_B for transitions between adjacent sites of one and the same edge, and the rates Γ_{AB} and Γ_{BA} for hopping from the outermost site of zone A to zone B or vice versa. We adopt the standard assumption that these rates are made up of a fixed 'attempt frequency' pre-factor ν_0 and follow an Arrhenius law, thence the connection to the characteristic energies reads:

$$\begin{aligned} \Gamma_A &= \nu_0 \exp\left(-\beta E_{D,A}\right), & \Gamma_B &= \nu_0 \exp\left(-\beta E_{D,B}\right), \\ \Gamma_{AB} &= \nu_0 \exp\left[-\beta\left(E_c - E_{b,A}\right)\right], & \Gamma_{BA} &= \nu_0 \exp\left[-\beta\left(E_c - E_{b,B}\right)\right] \\ \frac{\Gamma_{AB}}{\Gamma_{BA}} &= \exp\left[\beta\left(E_{b,A} - E_{b,B}\right)\right] =: \exp\left(-\beta \Delta E_b\right), \end{aligned} \tag{6.2}$$

where $\beta = 1/(k_B T)$ is the inverse temperature. $E_{b,A}$, $E_{b,A}$ are the binding energies for zone A and B, $E_{D,A}$, $E_{D,B}$ the diffusion barriers between adjacent sites inside zone A and B, respectively, and E_c is the corner energy barrier height. This is the simplest way to satisfy detailed balance. It has the benefit not to introduce additional parameters (governing, e.g., the lowering of transition state energies if the target position is energetically favorable) that can hardly be measured experimentally.

As in Section 6.3.1 we only treat two-atom processes. This is justified if the flux is small enough, so that the typical nucleation time is much shorter than the deposition time after which a third atom arrives (note that the validity of this assumption has been questioned for realistic experimental conditions in Gödecke [61]). For actual comparison with experimental regimes, the typical nucleation time could be calculated after we have obtained the temporal distribution of nucleation events to ensure self-consistency up to a certain maximum flux.

6.4.2 Mapping to Simultaneous Deposition

Again we start from a homogeneous initial distribution of the first edge atom, $p_n(0) = p_s^{\mathrm{U}} := 1/L$, where L is the *total length* (in terms of adsorption sites) of the edge. At a later time $t > 0$, the second atom (the 'partner') impinges on the island edge, while the first atom propagator has evolved since its own arrival. As before, all necessary information is contained in its *effective* distribution

$$p_n^{\mathrm{eff}} = \int_0^\infty \mathrm{d}t \, p_n(t) \rho_{\mathrm{dep}}(t)$$

with $\rho_{\mathrm{dep}}(t) = \exp(-t/\tau_{\mathrm{dep}})/\tau_{\mathrm{dep}}$ the time distribution between successive depositions of atoms. Time is continuous now as with inhomogeneous hopping rates, there is no longer any natural time step.

The residence time in our situation is infinite, $\tau_{\mathrm{res}} \to \infty$, since without a partner, the single adatom would live on the edge forever. Given (6.1) is valid here as well, we would obtain $p_n^{\mathrm{eff}} = p_s^{\mathrm{S}}$. We lack the one-particle-distribution necessary to prove this explicitly, but we will show it is reasonable with an order-of-magnitude estimate. We estimate the time τ_{tr} an atom needs to traverse the step edges. Along the edges themselves a random walk takes the time $\sim \ell_{\mathrm{A}}^2/\Gamma_{\mathrm{A}} + \ell_{\mathrm{B}}^2/\Gamma_{\mathrm{B}}$. Typically we assume that hopping around the corner has a slower rate, $\Gamma_{\mathrm{AB}} \ll \Gamma_{\mathrm{A}}$ and $\Gamma_{\mathrm{BA}} \ll \Gamma_{\mathrm{B}}$. This then takes a time $\sim \frac{\ell_{\mathrm{A}}}{2}\frac{\Gamma_{\mathrm{A}}+\Gamma_{\mathrm{AB}}}{\Gamma_{\mathrm{A}}\Gamma_{\mathrm{AB}}} + \frac{\ell_{\mathrm{B}}}{2}\frac{\Gamma_{\mathrm{B}}+\Gamma_{\mathrm{BA}}}{\Gamma_{\mathrm{B}}\Gamma_{\mathrm{BA}}} \sim \frac{\ell_{\mathrm{A}}}{2\Gamma_{\mathrm{AB}}} + \frac{\ell_{\mathrm{B}}}{2\Gamma_{\mathrm{BA}}}$ to 'escape' both steps. The deposition time is $\tau_{\mathrm{dep}} = 1/(F_{1\mathrm{d}}a_0 L)$ (with the probability for a deposition after a much shorter time $\tau \ll \tau_{\mathrm{dep}}$ of the order $\tau/\tau_{\mathrm{dep}} \ll 1$). If the traversal time is much smaller than the deposition time, most atoms can perform many round-trips on the island edge before their partner atom is deposited, and it is reasonable to assume they have reached their stationary distribution. The condition for this thence roughly reads

$$\max\left(\frac{\ell_{\mathrm{A}}^2}{\Gamma_{\mathrm{A}}}, \frac{\ell_{\mathrm{B}}^2}{\Gamma_{\mathrm{B}}}\right) + \max\left(\frac{\ell_{\mathrm{A}}}{2\Gamma_{\mathrm{AB}}}, \frac{\ell_{\mathrm{B}}}{2\Gamma_{\mathrm{BA}}}\right) \ll \frac{1}{F_{1\mathrm{d}}a_0 L}.$$

Interestingly, corner crossing is now one process which may limit the rate at which the stationary distribution is approached, replacing the escape via the boundaries in the original setting of Section 6.3.1. Correspondingly, for $\ell \sim \ell_{\mathrm{A}} \sim \ell_{\mathrm{B}}$, $\Gamma \sim \Gamma_{\mathrm{A}} \sim \Gamma_{\mathrm{B}}$, and $\Gamma_{\mathrm{c}} \sim \Gamma_{\mathrm{AB}} \sim \Gamma_{\mathrm{BA}}$, the left hand side reads $\frac{\ell}{\Gamma}\left(\ell + \frac{\Gamma}{\Gamma_{\mathrm{c}}}\right)$, which appears analogous to the residence time expression $(\beta L + \alpha\ell_{\mathrm{ES}})L/\Gamma$ [50, 71] upon reasonable identification of the Ehrlich-Schwoebel length ℓ_{ES} with $\frac{\Gamma}{\Gamma_{\mathrm{c}}}$. Provided the flux is small enough, this condition will always be satisfied.

6.4.3 One-Particle Distribution

Since hopping rates are no longer uniform, the evolution equations are now differential instead of difference equations in time. For the single particle, the Markovian one-step process with nearest-neighbor transitions is governed by

$$\frac{\mathrm{d}p_n(t)}{\mathrm{d}t} = g_{n-1}p_{n-1}(t) + r_{n+1}p_{n+1}(t) - (g_n + r_n)p_n(t), \tag{6.3}$$

where r_n labels the transition probability (per unit time) *from* site n to the left $n-1$, and g_n from site n to the right $n+1$. The island edge is periodic, such that $n = 0$ equals $n = L$, $n = 1$ equals $n = L+1$ etc. While sometimes periodicity is helpful in finding a solution, it turned out here that it is a fundamental problem.

In Appendix A.10 we review in more detail one standard procedure to solve this equation. Separating the time dependence $\propto \exp(-\lambda t)$, for the spatial part an eigenvalue problem (for $-\lambda$) remains to be solved. Zone-wise solutions are easily found to be linear combinations of $z^{\pm n}$ with $z = z_{\mathrm{A}}$, $z_{\mathrm{B}} \in \mathbb{C}$ depending on the zone, and they are related to the eigenvalue λ by

$$2 - \frac{\lambda}{\Gamma_{\mathrm{A}}} = z_{\mathrm{A}} + \frac{1}{z_{\mathrm{A}}}, \qquad 2 - \frac{\lambda}{\Gamma_{\mathrm{B}}} = z_{\mathrm{B}} + \frac{1}{z_{\mathrm{B}}}.$$

The eigenvalue problem is thus reduced to the matching of these two partial solutions at the corners. One obtains a homogeneous 4×4 system for the (complex) coefficients in the partial solutions, given essentially by the simple matrix

$$\begin{pmatrix} \gamma_\mathrm{A} z_\mathrm{A} & \gamma_\mathrm{A} z_\mathrm{A}^{-1} & z_\mathrm{B}^{\ell_\mathrm{B}}(1-\gamma_\mathrm{B}-z_\mathrm{B}) & z_\mathrm{B}^{-\ell_\mathrm{B}}(1-\gamma_\mathrm{B}-z_\mathrm{B}^{-1}) \\ \gamma_\mathrm{A} z_\mathrm{A}^{\ell_\mathrm{A}} & \gamma_\mathrm{A} z_\mathrm{A}^{-\ell_\mathrm{A}} & z_\mathrm{B}(1-\gamma_\mathrm{B}-z_\mathrm{B}^{-1}) & z_\mathrm{B}^{-1}(1-\gamma_\mathrm{B}-z_\mathrm{B}) \\ z_\mathrm{A}^{\ell_\mathrm{A}}(1-\gamma_\mathrm{A}-z_\mathrm{A}) & z_\mathrm{A}^{-\ell_\mathrm{A}}(1-\gamma_\mathrm{A}-z_\mathrm{A}^{-1}) & \gamma_\mathrm{B} z_\mathrm{B} & \gamma_\mathrm{B} z_\mathrm{B}^{-1} \\ z_\mathrm{A}(1-\gamma_\mathrm{A}-z_\mathrm{A}^{-1}) & z_\mathrm{A}^{-1}(1-\gamma_\mathrm{A}-z_\mathrm{A}) & \gamma_\mathrm{B} z_\mathrm{B}^{\ell_\mathrm{B}} & \gamma_\mathrm{B} z_\mathrm{B}^{-\ell_\mathrm{B}} \end{pmatrix} \tag{6.4}$$

with $\gamma_\mathrm{A} := \Gamma_\mathrm{AB}/\Gamma_\mathrm{A}$ and $\gamma_\mathrm{B} := \Gamma_\mathrm{BA}/\Gamma_\mathrm{B}$.

Solving the system non-trivially will only be possible for certain values of λ, rendering the simple matrix singular, or letting its determinant vanish. Then one can express all four coefficients in terms of only one, leaving us with one global pre-factor for the normal mode, which can be fixed by an orthonormality condition.

The general difficulty stems from the fact that either, one easily eliminates λ, thus retaining two parameters z_A and z_B which do not have a simple relation with each other, or one substitutes the explicit roots z in terms of λ, which greatly complicates matters.

Comments. With computer algebra, one quickly obtains the determinant of (6.4), and we checked that it is rightly invariant under switching the zones (i.e., simultaneous $z_\mathrm{A} \leftrightarrow z_\mathrm{B}$, $\ell_\mathrm{A} \leftrightarrow \ell_\mathrm{B}$, $\gamma_\mathrm{A} \leftrightarrow \gamma_\mathrm{B}$) as well as under the simultaneous inversion of z_A and z_B.

Furthermore, one correctly recovers the results for the homogeneous edge: Setting $z_\mathrm{A} = z_\mathrm{B} =: z$ and $\gamma_\mathrm{A} = \gamma_\mathrm{B} = 1$ yields

$$\det = z^{-2-L}(1-z^2)^2(1-z^L)^2.$$

In this case, the exact roots are given by $z = \mathrm{e}^{2\pi i \cdot k/L}$ with $k = 0 \ldots \lfloor L/2 \rfloor$, and for L odd, $z = -1$ additionally (other solutions are inverses, hence yielding the same eigenvalue $-\lambda$), which makes for $\lfloor \frac{L+1}{2} \rfloor + 1$ independent solutions. (There are no real solutions $z < -1$ in this situation.)

More generally, the determinant for equal $\Gamma_\mathrm{A} = \Gamma_\mathrm{B}$, hence $z_\mathrm{A} = z_\mathrm{B} =: z$, reads

$$\begin{aligned} \det = z^{-2-L}(1-z)^2 \big\{ &[1-(1-\gamma_\mathrm{A}-\gamma_\mathrm{B})z]^2 - z^{2\ell_\mathrm{A}}\left[(1-\gamma_\mathrm{A})-(1-\gamma_\mathrm{B})z\right]^2 \\ &- z^{2\ell_\mathrm{B}}\left[(1-\gamma_\mathrm{B})-(1-\gamma_\mathrm{A})z\right]^2 - 2\gamma_\mathrm{A}\gamma_\mathrm{B} z^L(1+z)^2 + z^{2L}\left[(1-\gamma_\mathrm{A}-\gamma_\mathrm{B})-z\right]^2 \big\}, \end{aligned}$$

which assuming lengths to be equal, $\ell_\mathrm{A} = \ell_\mathrm{B}$, further simplifies to

$$\det = z^{-2-L}(1-z)^2(1-z^L)\left\{[1-(1-\gamma_\mathrm{A}-\gamma_\mathrm{B})z]^2 - z^L\left[(1-\gamma_\mathrm{A}-\gamma_\mathrm{B})-z\right]^2\right\}.$$

While little can be said about zeros of the former, one can read off the last result that all solutions of the 'fully homogeneous' result are still zeros (except for $z = -1$ for odd L), and that one may find additional solutions in those of $(1-cz)^2 = z^{L+2}(1-c/z)^2$, where $c := 1-\gamma_\mathrm{A}-\gamma_\mathrm{B}$.

Since finding the eigenvalues in closed form (let alone the coefficients) fails for any generality, we stop our examinations here for obvious reasons. It will also become clear that the two-particle case brings about an even more fundamental problem. However, in the Appendix Section A.10.3 we nevertheless review some further efforts to analytically understand the single-particle distribution, which show the kind of problems one faces even in an approximate treatment.

6.4.4 Two-Particle Problem

As before, the joint two-particle 1d-random walk (with walker positions m, n) can be mapped onto a single two-dimensional random walker (at coordinate (m, n)). The symmetrized initial condition of the propagator (there is no need to distinguish the two particles) reads $p_{m,n}(t=0) = \frac{1}{2}\left[p_m^{\mathrm{U}} p_n^{\mathrm{S}} + p_m^{\mathrm{S}} p_n^{\mathrm{U}}\right](1-\delta_{mn})$ using the effective distribution derived above. The nucleation event translates to the absorbing diagonal $p_{n,n}(t) = 0$ at all times, and for $m \neq n$, the time evolution reads

$$\begin{aligned}\frac{\mathrm{d}p_{m,n}(t)}{\mathrm{d}t} &= g_{m-1}p_{m-1,n}(t) + r_{m+1}p_{m+1,n}(t) - (g_m + r_m)p_{m,n}(t) \\ &\quad + g_{n-1}p_{m,n-1}(t) + r_{n+1}p_{m,n+1}(t) - (g_n + r_n)p_{m,n}(t).\end{aligned}$$

Suppose this equation would hold for *all* m, n, including the diagonal. Then, analogous to the solution in Section 6.3.1, one obtains

$$p_{m,n}(t) = \sum_{k,j=0}^{L-1} B_{k,j} \cdot \exp(-(\lambda_k + \lambda_j)t)\psi_m^{(k)}\psi_n^{(j)},$$

where $\boldsymbol{\psi}^{(k)}$ is the *one*-particle normal mode for the eigenvalue $-\lambda_k$ of the system. The symmetry of the initial condition implies a symmetric $B_{k,j}$ by linear independence of the modes, so it is also preserved under time evolution. The spatio-temporal distribution of nucleation events $R_n(t)$ is now given by

$$R_n(t>0) = g_{n-1}p_{n-1,n}(t) + r_{n+1}p_{n+1,n}(t) + g_{n-1}p_{n,n-1}(t) + r_{n+1}p_{n,n+1}(t)$$

and $R_n(t=0) = p_n^{\mathrm{S}} p_n^{\mathrm{U}}$.

For the line segment topology of Section 6.3.1, the absorbing diagonal separated the 2d-lattice into two dynamically disconnected regions, hence allowing use of the image method to solve the full problem: This trick incorporated the changed equation for $m = n$, yet one could still build upon the known single-particle solutions. For our case (ring topology), periodicity breaks this method already in the one-dimensional setting: The walkers can interchange positions without meeting, or equivalently, the regions $m < n$ and $m > n$ are dynamically connected, such that the true distribution $p_{m,n}(t)$ can nowhere be replaced by an auxiliary one. As in Politi and Castellano [73] for the two-dimensional problem, we do not see a way to overcome this analytically.

We finally note that the problem on the homogeneous island edge is trivial: Since then, the uniform, the stationary, and hence the effective single-particle distribution all coincide, and the system is translationally invariant due to periodicity, the nucleation probability is uniformly distributed over the island edge.

6.5 Summary

Analysis of the first nucleation distribution at an inhomogeneous island edge arose from the similarity of this problem to the hydrogen recombination scenario. Moreover, there are KMC simulations, which provide interesting results to be checked, and the analytical and numerical work of Castellano and Politi [71], Politi and Castellano [72, 73] that uses analytical methods which seemed applicable to the new situation. It turned out however that, first, the analytical single-particle solution of the master equation is already out of reach once the island edge is inhomogeneous in the moderate sense described in Section 6.4.1 (owed to inhomogeneity and periodicity). Second, periodicity of the island edge does not allow the use of the image method to employ these one-particle solutions. Since our aim was set to study certain effects analytically, we had to stop investigations at this point.

Obviously, there are many other approaches to learn about this interesting system, of which we mention a few.

We tried to analyze a continuum diffusion approximation, first for the single-particle case. For this, one has to rescale hopping rates and edge lengths, which are sent to infinity. This introduces several new difficulties: First, for position-dependent binding energies and diffusion barriers, the form of the appropriate diffusion equation is subtle and may produce paradoxical effects [74–76]. Second, the corner plays a special role, where the concentration becomes discontinuous, while the current should stay continuous. It is non-trivial to model the corner hopping rates Γ_{AB} and Γ_{BA} in a continuum framework [77].

Since timescales for changing the edge are expected significantly larger than those for hopping inside one zone, one could try to separate those scales, and expand the problem in the number of 'edge changes'. Inside one zone, known results for the nucleation probability and distribution in the case of a partially absorbing boundary could be used. However, such results have, once again, been obtained only with rough approximations or numerically in Politi and Castellano [72, 73]. Consequently, one might at best improve upon our heuristic understanding.

Therefore it seems that at the moment, this simple yet intriguing system can be understood heuristically fairly well, but analytical results are rare, and one ultimately has to resort to KMC simulations again.

Chapter 7

Outlook

7.1 An Open Field

Concerning hydrogen recombination in the homogeneous system, further work should first assess how exactly the master equation describes the system: What is the quantitative effect of the neglect of all spatial correlations between random walkers on the lattice?

Moreover, as we have stated before, an improved quantitative analysis has to incorporate the complex surface structure of interstellar dust grains. Most notably this implies disorder in the rates, i.e., the replacement of a single binding energy and diffusion barrier by energy distributions. However, we have also seen that the given master equation framework does not seem appropriate for this hard task.

There are several approaches to this problem: As mentioned in Section 5.5, one idea is the mapping of a full disordered grain to an effective coarse-grained model of the 'relevant' strong-binding sites. Such a model could be treated with the ME approach for homogeneous grains. Relatedly, one could also set up coupled rate equations for several types of binding sites [24], which might, at least in certain regimes, be an efficient way to capture the essentials of the system.

Another approach is annealing of the disorder, such that activation energies or rates are not drawn from a distribution once and for all for each adsorption site, but are rather drawn anew on each step of a walker. This leads to a CTRW reaction-diffusion model with a (global) non-exponential waiting time PDF (WTD), and including desorption and a confined geometry. While we still deem this a hard analytical problem, the huge literature on the CTRW [standard references to start from are 25, 54, 59, 78–80] has one hoping that it can be solved at least partially. Similarly, the corresponding system might be analyzable with an appropriate fractional dynamics equation [for a review see, e.g., 81].

Geometric aspects. Somewhat complementary, but equally interesting, one can focus on geometric aspects such as the connectivity graph of adsorption sites. The effect of the porosity of the dust grains has been studied [30, for a simple heuristic model]. Conceptually related, one might also investigate the influence of geometric disorder in the sense of a complex (random, or possibly

fractal) graph of adsorption sites, and typically, first-passage problems have not been addressed in this context [3, 11]. Some exceptions are Klafter *et al.* [82], Goldhirsch and Gefen [83], Noskowicz and Goldhirsch [84] and follow-ups as well as Haynes and Roberts [85].

It should be understood that treating (rate as well as geometric) disorder is highly important for a variety of other applications as well, owed to the fact that the underlying diffusion-reaction system is of a very general nature.

7.2 Connections to Other Work

We finally want to highlight a few connections to problems to which similarities and differences might be best appreciated in retrospect.

Rosenstock. First consider the work of Rosenstock, exemplarily Rosenstock [86, 87]. It concerns a simple cubic lattice walk (in one, two, or $d \geq 3$ dimensions) among static absorbing traps of given concentration, and addresses the following problems: What is the probability of return to the origin before the walker is absorbed by a trap? If the walk has a certain probability to emit spontaneously in each step (to desorb or die in our terminology), what is the probability that this happens before the walk is absorbed? What is the mean time until the (immortal) walker is trapped? Especially the second problem is closely related to our analysis of the encounter probability. Indeed, it furnishes two regimes depending on the ratio of trap concentration (corresponding to $1/S$ for our case) and emission probability $(1-\xi)$, when both are small (so the random walk length is $\gg 1$).

The crucial difference in Rosenstock's work (compared to ours) is that space is not confined, and that the traps occur "geometrically annealed": They are modeled as a certain absorption probability per step (corresponding to reaction in our case), and not a spatially fixed configuration as in our case. The then-novel two-dimensional result of Rosenstock [86] expressed in our language is as follows: For few traps compared to the emission probability (our large grains / lattices), the leading-order probability of absorption by a trap (our recombination) is $\pi a/(SW) \cdot 1/\ln(a/W)$, only differing in numerical prefactors from our result. For many traps (our small grains), one would obtain $1 - SW/(\pi a)\,[\ln(S/\pi) + \ln\ln(S/\pi) + \text{const.} + \mathcal{O}(1/\ln(\pi/S))]$, which (apart from the overall functional form) features a double-logarithm and more logarithmic corrections compared to our result: This is to be expected, as the boundedness of our system then implies correlations of the meeting probability per step that are not present in the infinite 'stochastic absorption' case.

Trapping and trap annihilation. Other typical problems in this realm are the survival probability of particles diffusing among truly static perfect traps (the 'trapping problem'), with the famous Donsker-Varadhan asymptotics [88], and the converse problem called 'target annihilation', in which the traps move and the target is static (or equivalently, the 'trap' species no longer survives an encounter but is eliminated by the particle) [89, e.g.]. The analysis has recently been extended to traps and particles both moving [90, 91, and references therein], and possibly with super- or subdiffusive behavior [92–95, e.g.]. Throughout, there is no simple connection to our situation. As part of the analysis of a

rather elaborate model of diffusion-limited reactions, Bénichou *et al.* [96] also highlights the meaning and the possible failure of the Rosenstock approximation (to 'anneal' trap positions) in both the target and the trapping problem.

We also mention Ziff [97], where the flux of (non-interacting) particles to a trap is calculated for all times; the particles start out homogeneously distributed and either perform RAYLEIGH flights around an absorbing sphere or hop on a lattice around an absorbing site. The author also considers the effect of the spatial dimension and subtleties to care for in simulations of the system. Interest in the subject has not waned over the years [98]. Note that infinity of space renders all these problems fundamentally different from the systems analyzed in this Part of the thesis.

MFPTs in a confined geometry. Mentioned before in Section 3.4, the works Condamin *et al.* [99], and references therein consider first-passage questions in confined geometries. They examine mean first-passage times (MFPT) and *splitting probabilities*, i.e., the probability to end in a specific one of several absorbing states [6]. This yields explicit results without knowledge of the full propagator required in earlier work [100]. Those results can be applied to diffusion-limited reactions [99], and they were extended to the sub-diffusive case and arbitrary fractal graphs by means of a general scaling ansatz [101]. We have not found a straightforward application to our problems: First, desorption cannot be implemented in a natural way in this approach, and second, the confining geometry either destroys the scaling ansatz for the latter citation, or it turns out that for our two-dimensional situation its influence cannot be reasonably approximated.

7.2.1 One-dimensional Systems

Though our original problem exemplifies the difficulties of spatial dimension two, similar one-dimensional models are of great appeal: They may serve as toy models to explore general effects (mostly of disorder) not strongly dependent on the dimension, and they are also applicable to a large variety of physical situations — consider, e.g., Chapter 6, or protein-on-DNA search problems [43, 44]. At the same time, they are substantially easier to handle analytically.

Random random walks. There is a huge literature on random walks and first-passage probabilities for the 'random-force', 'random random walk' or 'Sinai' model in one dimension; some illustrative references are Bouchaud *et al.* [102, 103], Comtet and Dean [104], Chave and Guitter [105]. Their common feature is that the potential landscape is a random walk (continuous in the energies) itself. Later, a Real Space Renormalization Group (RSRG) technique was devised, in which the smallest barriers below some cutoff (set by the time-scale of interest) are successively removed. This approach allows one to study first-passage and reaction-diffusion properties as well [10, 106, 107], and can be applied to a broad class of energy landscapes [108].

It is however based on the property that the spatial *variation* of binding energies follows a stochastic process (rendering the landscape self-similar), as opposed to the energies themselves being i.i.d. random variables. This means that the differences in binding energy (at potential minima) diverge with diverging

spatial distance; one finds deeper and deeper wells on a larger length scale, making the energy distribution ever broader upon renormalization. In contrast to this, the random-trap model, e.g., does not have this property and shows normal diffusive behavior (as do other bounded potentials). The method cannot work properly here, since a very deep potential well quickly becomes the typical energy scale, and renormalization no longer increases barriers.

MFPT on quenched-disorder chain. For a one-dimensional chain (with one reflecting and one absorbing end), Murthy and Kehr [109] finds an explicit expression for the mean first-passage time in terms of the individual probabilities for hopping left or right (i.e., not yet averaged over disorder). This made concrete the findings of Noskowicz and Goldhirsch [110]. Following a quick development [111, 112], the full distribution of this quantity as induced by disorder is considered in Kehr and Murthy [113], Noskowicz and Goldhirsch [114] and references therein. Giacometti and Murthy [115] include the possibility for spontaneous desorption for an otherwise restricted class of hopping rates, and the effects of non-conservation of probability are examined. For the original generality of hopping rates, but in the extended model including desorption and on a semi-infinite chain, Sire [116] computes exactly the full escape probability distribution (caused by disorder). Again without desorption, but on a one-dimensional chain which may have two absorbing boundaries, the MFPT and the mean residence time are also known exactly, and their behavior has been analyzed for a wide variety of disorder models [117, 118].

An important step forward is the generalization of Murthy and Kehr [109] to the case including desorption, or to a ring topology, or possibly only to alternative boundary conditions. Changing the topology renders the problem hard because typically, results for these systems are obtained with techniques (such as recursion relations) which rely heavily on the essential uniqueness of the path between initial and final site. Including desorption as a site-dependent probability one would want to know the first-passage probability to a target site and the (conditional) mean first-passage time. Note that for the assumptions of Chapter 5, i.e., isotropic ('ultra-local') rates and $W/a = \text{const.}$, the argument of Section 5.3.1 means that this two-particle problem with periodic boundaries is easily solved (in terms of steps of the walk, when disorder becomes irrelevant). Here the interest is rather in a result for arbitrary disorder or truly site-dependent probabilities, when the timescale cannot be eliminated.

FPT of CTRW. Recently, the problem of the full first-passage time (FPT) distribution has, in principle, been solved for the CTRW on a chain with nearest-neighbor transitions and irreversible trapping (i.e., desorption) [119, 120]. The model includes a site-dependent bias, site- and direction-dependent hopping WTDs, and a site-dependent trapping probability and WTD: This no longer corresponds to the situation obtained by an annealing of disorder, but is in fact a much more general model than in Murthy and Kehr [109]. Moreover, the authors claim their results can also be applied to a ring topology. Complementary information on the probability of certain paths is available as well [121, 122]. These results are intriguing, but of an abstract nature, viz. given in Laplace space by rather involved summation procedures. This might make it difficult (for realistic models of disorder) to obtain information as concrete as in, e.g.,

Murthy and Kehr [109]. We have not studied this work in more detail yet.

Many-particle systems. All of these 1d-approaches as well as all the efforts concerned with first-passage information consider one-particle quantities exclusively, as opposed to the full problem including *stochastic* deposition and desorption. The many-particle features that, as we have seen, depend strongly on the average number of particles in the system, are thence inaccessible in those frameworks. Of the huge literature on interacting particle systems (contact processes, branching-annihilating RWs, heterogeneous annihilation etc.) we mention but two interesting approaches that might deserve further attention in our context (although they do not include particle deposition and desorption).

First, Schütz and Mussawisade [123] maps multi-particle annihilation on a 1d-disordered chain onto a *single-particle* first-passage problem in a *dual* landscape. Second, the relation between stochastic systems and the quantum-mechanical formalism has been exploited to employ a real-space renormalization group approach (different from the RSRG described above) for *interacting* particles [124]. In this way, one obtains information (like the particle density) about the final fate of the system as well as critical exponents. However, this technique seems hardly suited to examine finite-time properties.

Part II

Disordered Step Growth

Chapter 8

Introduction

In epitaxial crystal growth at low enough temperatures, the crystal surface exhibits atomic *steps*, thermodynamically stable one-dimensional defects which separate *terraces* at different heights between them. Along these objects, atoms are incorporated into the lattice, causing the steps to move. A wide field of study considers vicinal, i.e., stepped surfaces (a more detailed introduction to vicinal surfaces can be found in Section 10.1, where specific material systems are considered). It is often assumed that the merging of steps as well as island nucleation on the terraces are irrelevant; one may then adopt a coarse-grained point of view that treats steps (as opposed to atoms) as the fundamental objects that undergo motion.

The time evolution of such a system depends on parameters such as the impingement flux, the diffusion constant and desorption rate of atoms, and certain kinetic coefficients that govern the attachment of atoms to the step and the possibility to cross a step to the neighboring terrace. Additional influences are step curvature (via the *stiffness of the step*), its proneness to thermal *roughening*, and the interaction of steps via entropic (steric) and elastic (via bulk strain) repulsion, and genuinely electrostatic dipole and possibly electronic interactions.

As such, this system may already show *step bunching*, i.e., the morphological instability that drives an initially equi-separated step train to separate into large terraces and regions with bunches of steps. This instability can arise from attractive step-step interactions, but also from an asymmetry in the attachment rates to down- and up-steps, breaking their equivalence: It has long been known that the *normal* Ehrlich-Schwoebel (ES) effect [39] ($k_+ > k_-$), i.e., the preferential attachment of adatoms to ascending steps from below, stabilizes growing step trains (while the inverse ES effect leads to bunching) [125]. This can be understood by noting that larger terraces entail faster incorporation into the ascending step, which moves faster than its neighbors and thus equalizes the step spacing.

As additional influences are considered, the ways to instability thrive. Electromigration caused by external electric fields can de-stabilize step trains. Also, impurities in the crystal may pin steps and hence lead to step bunching. It has been noted, however, that impurities can evoke step instabilities also via a different mechanism, namely by their *codeposition* and inclusion in the flat terrace, which implies disorder in the local transition rates [126]. Exclusively this last mechanism will be considered herein.

A concise primer on the fascinating field of step dynamics and their (possible) instability is given in Krug [127], while a more general introduction to far-from-equilibrium crystal growth can be found, e.g., in Michely and Krug [2].

8.1 Physical Situation and Mapping

Thermal excitations and non-equilibrium kink nucleation at step edges are responsible for the *roughness* of a step. The corresponding step instability mode is that of *meandering* (wavy) steps. Both factors will be neglected herein, i.e., we deal with ideal straight steps, and with the instability mode of bunching only. It then suggests itself to map the whole essentially two-dimensional surface structure onto a one-dimensional model of step positions, where the terraces between adjacent steps become intervals on which atoms may diffuse.

Note that this implies that disorder in the transition rates on the terrace is effectively one-dimensional as well, hence an impurity in this model corresponds to a straight line impurity on the terrace. It depends on the kinetic regime and the nature of the disorder (hence on the kind of effect the impurity has) whether this is a gross over-simplification or qualitatively reasonable. For example, in the random-trap model considered below, we do not expect the two-dimensional analogue to show qualitative differences from our results, as the trapping of an atom in a potential well cannot be avoided in any case. In contrast, for the random-barrier model, we expect a substantial discrepancy: While a barrier in one dimension inevitably has to be overcome to move forward, there are typically many ways to circumvent it in the two-dimensional case.

For the reduced problem on a vicinal surface, we then disregard step mergers and on-terrace nucleation, as well as desorption. This amounts to treating a kinetic regime in which there is always only one atom on the terrace, and is a valid picture when the diffusion time to reach a step edge is much smaller than the deposition time of an atom, and hence, whenever the flux is small or the temperature high (to enhance diffusion).

The essential question in this highly simplified situation is with what probability an atom deposited on a certain position on the terrace reaches either the descending or the ascending step edge. As it arrives at one or the other, we also neglect step permeability, such that the atom that surmounts a given energy barrier at the boundary is always counted as being incorporated (absorbed) in the step edge. Knowing the splitting probability (i.e., where the atom attaches), one can (in principle) easily calculate the resulting step velocity, and hence identify possible (de-)stabilizing effects.

So far, there was no mention of the role of co-deposited impurities. It has been found [126] that there are situations when these "foreign" atoms, making up a small fraction of all deposited particles, are incorporated into the crystal bulk immediately upon impinging on a terrace, by changing places with an underlying "pure" atom. Obviously, one then has to account for the local change in the potential landscape, such that local binding strength is affected and a possible bias for diffusing atoms may be implied. This means that the energy landscape will become *disordered*.

On the level of the single moving atom (always of the "main species"), this introduces disorder to the local hopping rates, which will render an appropriate model much more interesting. What is more is that the strength / frequency

of the disorder will be *position-dependent*. The steps move, and only on the currently exposed parts of the crystal, viz. the terraces between steps, impurities are incorporated and generate disorder. This implies that the longer a certain part of a terrace has been exposed to the impingement flux, the higher will be the concentration of impurities in that part. Clearly, close to the ascending step, the terrace has been exposed to the impurity flux for the longest time, while close to a descending step, parts have only recently be created, and thus have hardly been exposed to the in-flux. In the approximation of a constant speed v of steps, the total exposure time of a certain part of the terrace increases linearly with its distance from the descending step. Consequently, the impurity concentration profile $\theta(x)$ on the terrace (averaged over stochastic deposition or adopting a spatially coarse-grained picture) also increases linearly, cf. Figure 8.1. The value of the maximum concentration (at the ascending step) follows from a simple argument: Imagine the crystal being built solely by the deposition flux and moving steps. As the position close to the ascending step vanishes into the bulk on movement of the adjacent step, the concentration of impurities there has to equal that in the bulk then, and this has to equal the ratio in the impingement flux.

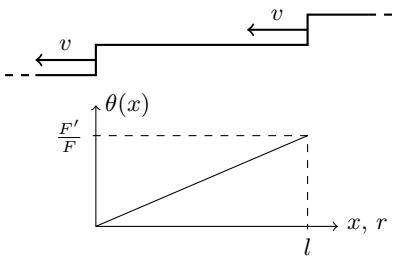

Figure 8.1: Schematic view of a moving step train and the average impurity concentration $\theta(x)$ on a terrace of length l. F and F' are the overall and the impurity impingement flux (per length), respectively.

The disorder as suggested by the physical situation is thus characterized by changed local transition probabilities wherever there is an impurity, and the probability for this to happen is linearly increasing with the distance to the descending step.

8.2 Relation to Previous Problems

From an analytical point of view, the most obvious difference to the other problems discussed in this thesis is that this model includes arbitrary disorder, but can still be solved exactly (in principle). The reasons are as follows: We have a one-dimensional system with absorbing ends; this is the easiest possible topology, and (somewhat ironically and owed to the first-passage nature) especially easier than the periodic boundary of Chapter 6. There is no mortality / desorption with the implied competition to absorption, and we are only interested in splitting probabilities, not in mean first-passage times [cf. 109]. As a result, the disorder is characterized essentially by one degree of freedom per lattice site, such that on a one-dimensional chain, an appropriate recursion equation can easily be solved explicitly.

The series of papers Condamin *et al.* [56], Condamin and Bénichou [57], Condamin *et al.* [58] shows a natural generalization to find the splitting probabilities in the higher-dimensional case in terms of pseudo-Green functions. However, to the best of our knowledge, the inclusion of quenched disorder (as is essential to our model) is not feasible in the framework described *ibid.*

8.3 Outline

In the next Chapter, we will first introduce the model and solve it exactly in the general case. We then motivate several possible choices of disorder and boundary conditions. We compare to the continuum model results of Krug [128], which we can recover exactly in the proper continuum limit with effective parameters. Careful analysis will clarify the choice of "natural" boundary conditions and how they translate between the discrete and the continuum model.

Besides obtaining nice analytical results and clarifying certain aspects of a complex experimental situation, we mention that our results may be of interest to Monte Carlo simulations. The lack of tests of the appropriateness of the one-dimensional modeling notwithstanding, the possibility to decide with a reasonably simple analytical expression at which step a single deposited atom will end up may provide an enormous speedup for such numerical analysis, actually taking the bulk of the simulation time out of the equation.

Chapter 9

A Simple Model and Results

9.1 Model and General Solution

Under the conditions described above (Section 8.1) we are naturally led to describe the atom as a one-dimensional discrete-time discrete-space random walk on an interval (the terrace) with absorbing ends (corresponding to inclusion of the atom in the step), the situation depicted in Figure 9.1.

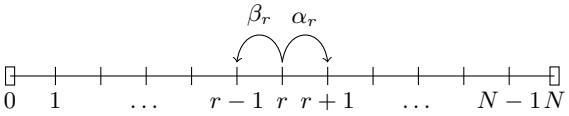

Figure 9.1: The random walk model for a single atom on a single terrace. The probability to step to the left (right) is given by β_r ($\alpha_r = 1 - \beta_r$) and fixed for each site by the realization of disorder.

Here, α_r and β_r denote the probabilities to jump *from* site r to its right or its left neighbor, respectively. It should be understood that all relations for those probabilities etc. always hold for $r = 1, \ldots, N-1$ unless stated otherwise. We will no longer care for the timescales at all, which is why the *probabilities* suffice, and because there is no desorption, they add up to unity: $\alpha_r + \beta_r = 1$. We assume our step edges to be perfectly absorbing, clearly, $\alpha_0 = 0 = \beta_N$ then. This is not a restriction on the attachment process, as we can envisage the states 0 and N to correspond to fully incorporated atoms, whereas 1 and $N-1$ would describe states of an atom 'at the step edge', and only incorporated with a certain probability β_1 or α_{N-1}, respectively. Note that, for physical reasons as well as in order for the mathematics to work smoothly, we assume that α_r and β_r are strictly positive for $r = 1, \ldots, N-1$. Therefore, any random walk will eventually end up at 0 or N.

Let us further note that step permeability could be included in a more general model using our results. No matter how the detailed processes proceed, we can definitely cater for them with an appropriate extra energy barrier at the

boundary. An atom surmounting this barrier would then be split up into a probability for both processes, i.e., into a certain part for attachment to the step (contributing to step velocity) and the complement for permeating the step (showing up as an additional influx of atoms at the step edge states $N = 1$, $N - 1$).

Our goal is now to determine the probability of a deposited atom to end up being incorporated at the left or the right step edge, in a given realization of hopping rate disorder. The answer to the above absorbing random walk problem is well-known in the literature, e.g., the nice monograph of Chung [129]; the probabilities for a walker, deposited at site j, to end up at the right at N, or at the left at 0, read

$$P_{j\rightarrow} = \frac{\sum_{r=0}^{j-1} \rho_r}{\sum_{r=0}^{N-1} \rho_r}, \qquad P_{j\leftarrow} = \frac{\sum_{r=j}^{N-1} \rho_r}{\sum_{r=0}^{N-1} \rho_r}, \tag{9.1}$$

respectively, where $\rho_r = \frac{\beta_1 \ldots \beta_r}{\alpha_1 \ldots \alpha_r}$ (with $\rho_0 := 1$).

9.2 Disorder Models

Let us briefly skim through possible implementations of disorder in the bulk. For given N, there is a surjective many-to-one correspondence of one-dimensional energy landscapes to sets of α_r (or β_r), and we will typically start from particularly simple models for the landscape. As elsewhere in this thesis, hopping rates shall always be of Boltzmann form, depending only on the difference between the current adsorption site binding energy and the transition state energy to overcome in the direction of the jump. For the time being, we will not assume anything special to happen at the boundaries, as we will later show that boundary conditions are easily implemented.

We may first rewrite the completely general result in a simpler form using the transition state energies $E_{r\rightarrow r+1}$ between site r and its right neighbor. We generally define the local change of (normalized) transition state energies as $\Delta\epsilon_r = \beta[E_{r\rightarrow r+1} - E_{r-1\rightarrow r}]$, where $\beta = \frac{1}{k_\mathrm{B}T}$. Then throughout, we have $\beta_r/\alpha_r = \exp(\Delta\epsilon_r)$. Obviously, this yields $\rho_r = \prod_{i=1}^{r} \exp(\Delta\epsilon_i) = \exp\left(\sum_{i=1}^{r} \Delta\epsilon_i\right) = \exp\left[\beta(E_{r\rightarrow r+1} - E_{0\rightarrow 1})\right]$ for $0 \leq r \leq N-1$, so that we obtain the still general result

$$P_{j\rightarrow} = \frac{\sum_{r=0}^{j-1} \exp\left(\beta E_{r\rightarrow r+1}\right)}{\sum_{r=0}^{N-1} \exp\left(\beta E_{r\rightarrow r+1}\right)}. \tag{9.2}$$

The energies can be expressed relative to an arbitrary offset, corresponding to canceling an exponential factor in all terms. It is obvious that with the above choice of hopping rates, the binding energies of adsorption states cannot matter at all. On a general note, properties such as independence, identity, and the symmetry of the disorder distribution when mirrored at the midpoint of the interval, are in general *not* equivalent irrespective of whether they are formulated with $\{\alpha_r\}$ or $\{E_{r\rightarrow r+1}\}$! For example, from the above we get $\alpha_r = \exp[\beta(E_{r\rightarrow r+1} - E_{r-1\rightarrow r})]$, such that a (non-identical) distribution of the $E_{r\rightarrow r+1}$ which is shifted by a constant offset per site would still render the α_r distributed identically. We now discuss a few special cases.

Homogeneous case. Without any local bias, we have $\alpha_r = \beta_r$ and $\rho_r \equiv 1$, whence $P_{j\to} = j/N$.

Constant local bias. This model still has no disorder, but a local bias, e.g., determined by linearly increasing transition state energies. This renders β_r/α_r a constant, say c. Consequently, $\rho_r = c^r$, and simplifying the geometric sums in (9.1), one obtains the standard result $P_{j\to} = \frac{1-c^j}{1-c^N}$.

Random traps. Here, adsorption sites correspond to wells of random depth, whereas all transition states between the wells have the same energy. The term usually also implies the choice of hopping rates described above, so that still, $\alpha_r = \beta_r = 1/2$. Therefore, $P_{j\to}$ coincides with that of the fully homogeneous case.

Random barriers. Since we have seen that random binding depths do not matter we can set them constant. Instead, we now vary the transition barriers between the sites.

Let us simplify the situation by considering binary disorder, i.e., either $E_{r\to r+1} = E$, or $E_{r\to r+1} = E + \Delta E$. For brevity, we introduce the following notation: $\|i, j\|$ will denote the number of ΔE-barriers *between* the two sites i and j. Then (9.2) is reduced to mere counting of extra barriers, and canceling a factor $\exp(\beta E)$ (or choosing E as our energy zero level) yields

$$P_{j\to} = \frac{j + (\exp(\beta\Delta E) - 1) \cdot \|0, j\|}{N + (\exp(\beta\Delta E) - 1) \cdot \|0, N\|}.$$

We will examine an interesting limit: Suppose there are few barriers, but they are so high that any atom deposited between two of them basically equilibrates in a 'cell' enclosed by those high walls before it finally escapes to the left or right. The appropriate condition for this situation is given as follows: It takes $\sim N_c^2$ steps to diffuse in a cell of width $N_c \gg 1$. With almost perfectly reflecting walls, the probability to be at an endpoint is $\sim 2/N_c$, and there, the probability to escape is $e^{-\beta\Delta E}$. Hence the number of steps needed to escape is the inverse of the average escape probability 'per step', or $\sim (N_c/2)\, e^{\beta\Delta E}$. We assume the escape takes much longer than diffusion in the cell, i.e., $e^{\beta\Delta E} \gg N_c$. Using that the number of barriers between 0 and j will be $\sim j/N_c$, only the second summands in the fraction matter, so that

$$P_{j\to} \approx \frac{\|0, j\|}{\|0, N\|}.$$

This merely says that in such a situation we can adopt a coarse-grained view of the random walk in terms of hopping between adjacent cells instead of sites. Then $\|0, j\|$ is the index of the initial cell and $\|0, N\|$ the total number of cells (counting from 0), and this result could also be written down immediately applying the homogeneous result to the walk on cells.

"I.i.d.-disorder". Let the transition state energies $E_r \equiv E_{r\to r+1}$ $(0 \le r \le N-1)$ be i.i.d. random variables — this is not relevant for the original model, but maybe of general interest: We now have a stochastic energy barrier distribution

independent of the site. Let angles denote the disorder average, then it is easy to see that $\langle P_{j\rightarrow}\rangle = \langle P_{N-j\leftarrow}\rangle$: Mirror the whole setting, and since the mirrored disorder realizations are the same as the original ones, the averages are as well. Therefore, spatial averages of the (disorder-averaged) "left-going" and the "right-going" probabilities are equal, $\frac{1}{N-1}\sum_{j=1}^{N-1}\langle P_{j\rightarrow}\rangle = \frac{1}{N-1}\sum_{j=1}^{N-1}\langle P_{j\leftarrow}\rangle$. Due to probability conservation ($P_{j\rightarrow} + P_{j\leftarrow} = 1$ for each realization), the right hand side is $1 - \frac{1}{N-1}\sum_{j=1}^{N-1}\langle P_{j\rightarrow}\rangle$, and thence,

$$\frac{1}{N-1}\sum_{j=1}^{N-1}\langle P_{j\rightarrow}\rangle = 1/2.$$

Since both averages are linear, their order is irrelevant. Note that the argument only relies on the "mirror symmetry" of the energy distribution of the different sites, so it would also hold for non-identical and even non-independent distributions of the energy barriers (or the α_r) with this property. The i.i.d.-case merely is the simplest non-trivial example.

For truly *independently and identically* distributed variables E_k we can say something about $\langle P_{j\rightarrow}\rangle$ itself. Obviously, the disorder average

$$\left\langle \frac{\mathrm{e}^{\beta E_k}}{\sum_{r=0}^{N-1}\mathrm{e}^{\beta E_r}} \right\rangle$$

cannot depend on k; it is the same for all indices in the numerator. But then it follows that $\langle P_{j\rightarrow}\rangle \propto j$. As this quantity's spatial average has to yield $1/2$ we arrive at

$$\langle P_{j\rightarrow}\rangle = \frac{j}{N}$$

for arbitrarily i.i.d. random variables E_k; the i.i.d.-disorder-average recovers the result as the homogeneous case.

These examples should provide a good idea of the behavior of $P_{j\rightarrow}$. We will shortly return to the random-trap and random-barrier cases, applied to a realistic situation that further specifies both the disorder as well as boundary conditions.

9.3 Boundary Conditions

We now introduce boundary conditions that specialize a non-bulk behavior at sites 1 and $N-1$. As described before, states 0 and N are the fully absorbing states where the atom has been incorporated, whereas states 1 and $N-1$ correspond to sites 'at the edge', where there is only a certain rate to incorporate atoms into the terrace. Those rates[1] are called $k_\pm$ (where the plus sign refers to the ascending edge we place at $N-1$) and can here be expressed in terms of a certain transition energy barrier to the absorbing states again: Let $\Delta E_\pm$ denote *additional* barriers at the respective step edges w.r.t. a pure homogeneous surface in between, then we would obtain $\beta_1/\alpha_1 = \exp(-\beta\Delta E_-)$, and $\beta_{N-1}/\alpha_{N-1} = \exp(\beta\Delta E_+)$. (The explicit relation between $k_\pm$ and our parameters will be derived for more specific assumptions below.)

[1] Using our conventions, their dimension actually is $[k_\pm] = L/T$.

Example: random traps or homogeneous case. Boundary conditions render this model interesting again, and can here be examined in great simplicity. Apart from the above expressions at edge sites, for $2 \leq r \leq N-2$, we still have $\beta_r/\alpha_r = 1$. Directly using (9.2) with the pure surface transition state energy as the offset yields

$$P_{j\rightarrow} = \frac{\exp(\beta\Delta E_-) + (j-1)}{\exp(\beta\Delta E_-) + (N-2) + \exp(\beta\Delta E_+)}. \tag{9.3}$$

In the interesting case of both $\beta\Delta E_\pm \gg 1$, the effect of the starting site becomes marginal compared to the competition between the attachment rates $k_\pm$. In the other extreme of $\beta\Delta E_\pm \ll 1$, the exponentials approach unity and we correctly regain the homogeneous result.

With the proper choice of the zero energy level, it should be fairly obvious how to implement any type of boundary condition (given via $\Delta E_\pm$) into any type of bulk model.

9.4 Comparison with a Diffusion Model

We can now compare results of the discrete model to those obtained in earlier work in a continuum diffusion picture [128].[2] First, we treat the random-barrier model (with binary disorder).

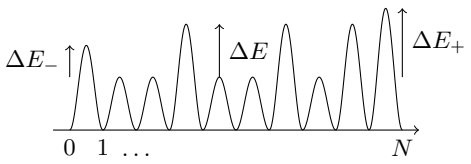

Figure 9.2: Energy landscape in the random-barrier model with binary disorder and additional step edge attachment barriers.

Random barriers (binary). In our setting the exact probability to end up at the ascending (right) edge, starting from site j, reads

$$P_{j\rightarrow} = \frac{\mathrm{e}^{\beta\Delta E_-} + (j-1) + (\mathrm{e}^{\beta\Delta E} - 1)\,\|1,j\|}{\mathrm{e}^{\beta\Delta E_-} + (N-2) + (\mathrm{e}^{\beta\Delta E} - 1)\,\|1,N-1\| + \mathrm{e}^{\beta\Delta E_+}}.$$

The physically given probability to have an impurity at position k, i.e., an increased diffusion barrier from adsorption site k to site $k-1$, reads kp, linearly increasing with the distance to the descending step (as the exposure time to the impurity flux grows linearly). Right now, p is some constant subject only to $(N-1)p \leq 1$. In the continuum limit, the number of sites will eventually become arbitrarily large, and it is therefore justified to replace $\|1,j\|$ by its disorder average or expectation value, reading $\langle\|1,j\|\rangle = \sum_{k=1}^{j-1} kp = pj(j-1)/2$, such

[2] Vollmer *et al.* [130] have performed kinetic Monte Carlo simulations of the two-dimensional system beyond quasi-stationary mean-field approximations and compared them to Krug [128].

that

$$\langle P_{j\to}\rangle = \frac{\mathrm{e}^{\beta\Delta E_-} + (j-1) + (\mathrm{e}^{\beta\Delta E}-1)p\frac{j(j-1)}{2}}{\mathrm{e}^{\beta\Delta E_-} + (N-2) + (\mathrm{e}^{\beta\Delta E}-1)p\frac{(N-1)(N-2)}{2} + \mathrm{e}^{\beta\Delta E_+}}.$$

This early change to expectation values corresponds to fixing a certain diffusion constant profile $D(x)$ in the continuum picture, see below. Averaging over initial sites $j = 1, \ldots, N-1$ and using $\sum_{j=1}^{N} k^2 = N(N+1)(2N+1)/6$ we find

$$\begin{aligned} P_\to :=& \frac{1}{N-1}\sum_{j=1}^{N-1}\langle P_{j\to}\rangle \\ =& \frac{\mathrm{e}^{\beta\Delta E_-} + \frac{N-2}{2} + (\mathrm{e}^{\beta\Delta E}-1)p\frac{N(N-2)}{6}}{\mathrm{e}^{\beta\Delta E_-} + (N-2) + (\mathrm{e}^{\beta\Delta E}-1)p\frac{(N-1)(N-2)}{2} + \mathrm{e}^{\beta\Delta E_+}} \\ =& \frac{1}{2}\frac{1 + \frac{N-2}{2}\,\mathrm{e}^{-\beta\Delta E_-}\left[1 + (\mathrm{e}^{\beta\Delta E}-1)p\frac{N}{3}\right]}{\frac{1}{2}(1+\mathrm{e}^{\beta(\Delta E_+ - \Delta E_-)}) + \frac{N-2}{2}\,\mathrm{e}^{-\beta\Delta E_-}\left[1 + (\mathrm{e}^{\beta\Delta E}-1)p\frac{N-1}{2}\right]}. \end{aligned} \tag{9.4}$$

The continuum limit is defined by $N \to \infty$ and the lattice spacing $a_0 \to 0$, with the terrace width $l = (N-c)a_0$ constant. Here c is an arbitrary constant much smaller than the typical N and independent of it, which becomes irrelevant in this limit.

We now have to establish a connection to the two special cases of step edge attachment rates discussed in Krug [128]: Type I is the impurity-independent choice $k_\pm = k$, and type II chooses rates proportional to the local adatom mobility, in continuous terms expressed as $k_-/D(0) = k_+/D(l) = \lambda^{-1}$. Note that both choices are designed to become symmetric in the absence of any impurities. The translation of these continuum picture conditions to our setting requires some thought. We first do this purely formally, and afterwards decide whether they are reasonable choices.

Type-I boundary conditions are explicitly formulated as $\lambda_0 = D_0/k_+ = D_0/k_-$, with D_0 the diffusion constant on a pure surface. Thus in terms of the *directed* hopping rate on the pure surface, Γ_0, we have $D_0 = a_0^2\Gamma_0$. In the discrete picture *and with constant binding energies*, rates can be expressed with $\Delta E_\pm$ such that the ratio $\Gamma_0/k_\pm = a_0^{-1}\exp(\beta\Delta E_\pm)$, where for type-I b.c.s, $\Delta E_+ = \Delta E_-$. Therefore, $\lambda_0 = a_0\exp(\beta\Delta E_\pm)$.

Second we adopt the definition $b = \phi(\mathrm{e}^{\beta\Delta E}-1)/l$, where $\phi = F'/F \ll 1$ is the impurity flux concentration. The physical model tells us that the impurity concentration on the terrace increases linearly up to ϕ at the ascending step, corresponding to the barrier probability $(N-1)p$ in the discrete picture (Section 8.1), whence $p = \phi/(N-1)$. This implies that $(\mathrm{e}^{\beta\Delta E}-1)p/a_0 = bl/(a_0(N-1))$.

We insert factors a_0 into $P_\to$ to get

$$P_\to = \frac{1}{2}\frac{1 + \frac{a_0(N-2)}{2}\frac{\mathrm{e}^{-\beta\Delta E_-}}{a_0}\left[1 + \frac{(\mathrm{e}^{\beta\Delta E}-1)p}{a_0}\frac{a_0 N}{3}\right]}{\frac{1}{2}(1+\mathrm{e}^{\beta(\Delta E_+ - \Delta E_-)}) + \frac{a_0(N-2)}{2}\frac{\mathrm{e}^{-\beta\Delta E_-}}{a_0}\left[1 + \frac{(\mathrm{e}^{\beta\Delta E}-1)p}{a_0}\frac{a_0(N-1)}{2}\right]}.$$

In the above limit and using the derived relations and $\Delta E_+ = \Delta E_-$ we obtain

$$P_\to \to \frac{1}{2}\frac{1 + \frac{l}{2\lambda_0} + \frac{bl^2}{6\lambda_0}}{1 + \frac{l}{2\lambda_0} + \frac{bl^2}{4\lambda_0}},$$

which is precisely the result for $j_+/(Fl) = 1 - j_-/(Fl)$ found in Krug [128], Eq. 12.[3]

Type-II boundary conditions are defined as $k_-/D(0) = k_+/D(l) = \lambda^{-1}$, where the diffusion constant used in Krug [128] reads $D(x) = \frac{D_0}{1+bx}$. Substituting $k_\pm$ for the respective energy differences we can write $\lambda = a_0\,\mathrm{e}^{+\beta\Delta E_-} = \frac{1}{1+bl} a_0\,\mathrm{e}^{+\beta\Delta E_+}$, which also implies $\mathrm{e}^{\beta(\Delta E_+ - \Delta E_-)} = 1 + bl$. In analogy to the above, we can perform the continuum limit to obtain

$$P_\rightarrow \to \frac{1}{2}\frac{1 + \frac{l}{2\lambda} + \frac{bl^2}{6\lambda}}{1 + \frac{bl}{2} + \frac{l}{2\lambda} + \frac{bl^2}{4\lambda}},$$

which differs from the type-I result only by one term in the denominator. Again, this perfectly coincides with $j_+/(Fl) = 1 - j_-/(Fl)$ as derived from Krug [128], Eq. 14, provided we identify λ_0 with λ.

We lastly describe an interesting limit: With the discrete result (9.4) consider high impurity barriers such that $\mathrm{e}^{\beta\Delta E}\, Np \gg 1$. Take absolute attachment rates (type-I), so that $\Delta E_- = \Delta E_+$, and let them be positive and small enough such that $N\,\mathrm{e}^{-\beta\Delta E_\pm} \sim 1$ or larger (boundary conditions do not dominate the results). Then we obtain $P_\rightarrow \approx 1/3$: The increasing concentration of barriers approaching the ascending step makes it only half as likely to end up there as it is to reach the descending step.

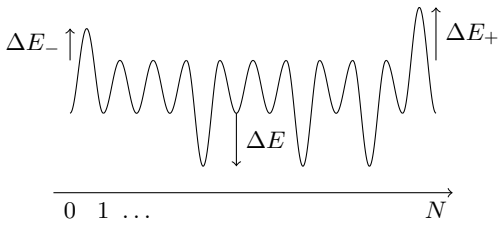

Figure 9.3: Energy landscape in the random-trap model with additional step edge attachment barriers.

Random traps (binary). While the general result for the (binary disorder) random-trap case has already been shown to be (9.3), its connection to the boundary conditions as described in the continuum model is slightly more subtle. Following the steps of the random-barrier treatment, one merely has to leave out the summands containing $(\mathrm{e}^{\beta\Delta E} - 1)$, or may even formally and sensibly set $\Delta E = 0$ (in the present notation), whence we obtain

$$P_\rightarrow = \frac{1}{2}\frac{1 + \frac{a_0(N-2)}{2}\frac{\mathrm{e}^{-\beta\Delta E_-}}{a_0}}{\frac{1}{2}(1 + \mathrm{e}^{\beta(\Delta E_+ - \Delta E_-)}) + \frac{a_0(N-2)}{2}\frac{\mathrm{e}^{-\beta\Delta E_-}}{a_0}}.$$

Note that this is not equivalent to setting $b = 0$ in the above results, since there, b can also arise in one type of boundary conditions. It may however be obtained alternatively as the spatial average of (9.3) after inserting and canceling

[3] $j_\pm$ are the particle current densities to the ascending and the descending step, respectively, and are of dimension $[j_\pm] = 1/(L^{d-1}T) = 1/T$ for a $d = 1$-dimensional system — recall that F and F' are fluxes per *length*, of dimension $1/(LT)$.

appropriate factors. We emphasize this to highlight that here, *no* disorder average (hence no approximation) is involved at this stage (in contrast to the random-barrier case), as the random trap result is independent of bulk disorder.

Next, let ΔE denote the impurity-induced binding energy difference of the model (positive for increased binding strength), and then set $b = \phi(\mathrm{e}^{\beta\Delta E} - 1)/l$ as before. Here, impurities induce a chemical potential gradient $\mu_{\mathrm{eff}}(x) = -\beta^{-1}\ln(1+bx)$ [128], where $-\mu_{\mathrm{eff}}$ expresses (arbitrary additive constant aside) the disorder-averaged continuous effective binding energy (increasing for increased binding strength), analogously to the effective diffusion coefficient in the above. However, for a surface symmetric in the absence of impurities, such a gradient can only occur together with an effective diffusion coefficient, which still reads $D(x) = D_0/(1+bx)$. This is due to the change of the *diffusion barrier* associated with a random-trap impurity, as mentioned in Krug [128]. Note that here, this term refers to the barrier as seen by the atom sitting in an adsorption site, whereas so far we exclusively used transition state energies w.r.t. a global zero level. The two effects precisely cancel on the terrace, which is obvious in the discrete picture.

This time, we begin with type-II boundary conditions $k_-/D(0) = k_+/D(l) = \lambda^{-1}$. Accounting for both the additional boundary barrier but also the effective chemical potential implies

$$\frac{D_0}{k_-} = a_0 \exp(\beta(\Delta E_- - \mu_{\mathrm{eff}}(0))), \qquad \frac{D_0}{k_+} = a_0 \exp(\beta(\Delta E_+ - \mu_{\mathrm{eff}}(l))),$$

because compared to the pure surface diffusion D_0, both the additional transition state energies as well as the increased binding by traps expressed in $-\mu_{\mathrm{eff}}$ suppress attachment. Hence, $\lambda = \frac{D_0}{k_-} = a_0 \exp(\beta\Delta E_-) = \frac{D_0}{(1+bl)k_+} = a_0 \exp(\beta\Delta E_+)\frac{1+bl}{1+bl}$, so that $\Delta E_- = \Delta E_+$, and $P_\rightarrow \to 1/2$. Here, the two competing effects also cancel at the boundary and one recovers the pure surface result as in Krug [128].

It is only in this last step that the effective diffusion constant and chemical potential of the continuum model enter, and once again, we are forced to include this separate averaging out of effects to properly establish the connection between the continuum and random walk points of view. This cancellation can be argued heuristically: Thinking continuously we have a larger impurity concentration close to the ascending step, which (in the random-trap model) renders diffusion slower there. Type II boundary conditions as originally specified clearly aim at balancing this effect by proportionally slower attachment to the edge as well. In terms of the underlying energy landscape viewed discretely, this balance is simply achieved by the same extra diffusion barrier for the transitions to both absorbing states, so $\Delta E_- = \Delta E_+$.

On the other hand, type-I boundary conditions $\lambda = D_0/k_- = D_0/k_+$ now imply $\exp(\beta(\Delta E_+ - \Delta E_-)) = 1/(1+bl)$, and this yields

$$P_\rightarrow = \frac{1}{2}\frac{1+\frac{l}{2\lambda}}{\frac{1}{2}\left(1+\frac{1}{1+bl}\right)+\frac{l}{2\lambda}} = \frac{1}{2}\left(1+\frac{bl/2}{1+\frac{bl}{2}+\frac{l}{2\lambda}+\frac{bl^2}{2\lambda}}\right).$$

Again, this agrees with the qualitative statement made in Krug [128]: For $\Delta E > 0$, $0 < bl < \infty$, and $P_\rightarrow > 1/2$, attachment to the ascending (+) step is preferred, whereas for $\Delta E < 0$, $-\phi < bl < 0$, and $P_\rightarrow < 1/2$ means that attachment to the descending (−) step is preferred.

Altogether, we have shown that the exact one-dimensional random walk result precisely and effortlessly reproduces the outcome of the continuum diffusion model. The fact that one has to use expectation values for the effect of the impurity distribution is no shortcoming, but corresponds to inevitably using a fixed diffusion constant profile and effective chemical potential in the continuum approach.

On boundary conditions. We conclude with some general statements on the relation between boundary conditions in the diffusion and the discrete model. In a way, the two types of boundary conditions change their roles when switching from the random-barrier to the random-trap model: While type-I boundary conditions ("absolute attachment rates") in the random-barrier model translate to impurity-independent (equal) $\Delta E_{\pm}$ barriers in the discrete setting, they imply impurity-dependent barriers for the random-trap model; and while type-II boundary conditions refer to an impurity-dependent boundary energy barrier for the random-barrier model, they translate into absolute (impurity-independent) and equal boundary barrier heights for the random-trap case.

The symmetry of the pure surface attachment *rates* in the absence of impurities (as postulated in the continuum model) is a subtle property: Assuming the boundary transition barriers (in our model) to be *independent* of the impurities, it is *only* satisfied if $\Delta E_- = \Delta E_+$ for the extra barriers w.r.t. the pure surface (constant) binding or transition state energy. This corresponds to type-I conditions in the random-barrier, and type-II conditions in the random-trap model. The proper way to look at the other choices is that for varying $b \propto \phi$ the step edge barriers change accordingly, and then we always recover the above condition and symmetry for the pure surface limit $b \to 0$.

On the other hand, coming from the discrete / microscopic point of view, there is (if we include special boundary effects at all) only one distinguished choice for the additional barriers at the edges, and that is $\Delta E_- = \Delta E_+$. The respective other choice (depending on the disorder models discussed above) amounts to some fine-tuning of the boundary energy barriers in dependence on the disorder-"averaged" energy landscape properties at the boundaries, as expressed by $D(x)$ and possibly by $\mu_{\text{eff}}(x)$. Thinking of the random-trap model specifically, there is a well-known possibility that a deeper trough can also "drag down" the transition state energies to its neighbors. It would be inconsistent, however, not to implement such an effect on the terrace, but exclusively at the step edges.

9.5 Outlook

Ultimately, one would like to find explicit expressions for spatial- and / or disorder-averaged splitting probabilities. This is easy only for certain types of disorder. Unfortunately, the kind of disorder which is suggested by the physical situation is a most difficult one, since transition state energies are no longer i.i.d. random variables then. For the statistics of such random variables there are very few general results to the best of our knowledge.

We tried several familiar statistical physics techniques, but failed to cast the searched expectation values into an amenable form. In the present form, we inserted expectation values of the (disorder-dependent) number of barriers

between two given sites into the splitting probabilities, corresponding to the continuum models which employ a fixed profile of the diffusion coefficient and the chemical potential. One might be content with improving this approximation by the next order: We expect a normal distribution for the number of enclosed barriers in the limit of a broad interval, and with this distribution it might be possible to integrate for the expectation values of the splitting probabilities.

More generally considering further research, we refer back to the one-dimensional machinery for first-passage problems that we reviewed in Section 7.2.1. The system provides an interesting testbed to compare KMC findings with analytical results obtained in the spirit of 'annealing the disorder'. This seems especially worthwhile w.r.t. the work of Flomenbom and Klafter [119], Flomenbom *et al.* [120]: Here we have a physically relevant example of truly site-dependent bias and waiting time distributions (obtained by site-wise averaging over the physically suggested impurity probability), not to mention the possibility to include desorption.

Part III

Isozones and Surface Reconstructions

Chapter 10

Introducing the Problem

We have stressed the ubiquity and importance of diffusion already in the introduction of this thesis. Paradoxically however, at least for surface diffusion it has been very difficult to gain reliable knowledge of the relevant parameters (attempt rates and activation energies). Such data can be obtained indirectly from experiments counting the island density [2], but this method is rendered practically useless as soon as diffusion properties become anisotropic. As is reviewed in Wall [131], there is work analyzing an influence of anisotropies on the island density distribution [132] observable with surface tunneling microscopy (STM), which needs extreme anisotropies (at least $200:1$) to function. There are microscopic studies like field ion microscopy [133], STM-adatom-tracing [134] and video-STM [135] that are restricted to slow diffusion (i.e., low temperatures) and small length scales. Finally, there are several studies of diffusion anisotropy on mesoscopic scales ($\sim 100\,\mathrm{nm}$), but they typically use scanning probe methods to examine only the difference between before- and after-states of a spreading experiment [136–140, among many others]. Yet precisely dynamic large-scale collective effects are held responsible for ordering and formation of nanostructures on surfaces (see Roos *et al.* [141] exemplarily).

It is an exciting recent development in this field that diffusion properties can now be envisaged *in situ* with *real-time* observations (i.e., producing images at video rate) on *mesoscopic* length scales and at high temperatures. The technique used to achieve this is photoemission electron microscopy (PEEM) [9]. We describe the system and experiments in the next Sections, while more detailed reviews and illustrations can be found in Wall [131].

10.1 The Physical System

While the method has been shown to be applicable also to many other epitaxial growth systems (Meyer zu Heringdorf, Roos, private communication), we focus on the epitaxial behavior of silver (Ag) on silicon (Si) surfaces exclusively.

Pure Si surfaces. A Si surface can already exhibit *surface reconstructions* without any adatom overlayer structure. For example, the Si(001) surface (i.e., the twofold-symmetric surface perpendicular to the [001] crystal direction of the Si fcc lattice) has a lot of dangling bonds if one simply truncates the bulk

structure by a cut. As a consequence, the topmost Si atoms of the substrate may form dimers by bonding to lower the free surface energy, and the resulting surface structure is called the (2×1) reconstruction of the Si(001) surface. Moreover, the dimer bonds can become asymmetric (the bond axis is angled w.r.t. the bulk), and this asymmetry is consistent inside a dimer row (i.e., in the bond direction), but may change between adjacent dimer rows, leading to various possible meta-symmetries.

Another important instance is the (7×7) reconstruction of the Si(111) surface, which has a huge unit cell, but still, it is the energetically favorable configuration up to temperatures of 850°C.

Vicinal surfaces are miscut against the main symmetry axes of the crystal, and are of great practical importance. To be more precise, they have high Miller indices, but typically, one rather specifies the miscut angle w.r.t. a certain lattice direction, as it is determined more easily. Specifically for silicon surfaces, the vicinality results in single and / or double steps occurring. As we mentioned above, dimer rows form in a certain direction, hence steps also have to be discriminated by their relative orientation to those rows. One finds an intricate dependence between the step edge orientation, the step height and the miscut angle [142, 143]. The orientation of the dimer rows alternates between layers of the crystal, such that it changes crossing a single step.

Ag on Si surfaces. Silver on silicon surfaces is a model system of surface diffusion, owed to the large diffusion lengths and the absence of any alloy formation that allows for total cleaning of any remnant silver after an experiment. In the presence of Ag adatoms, Si shows a number of surface reconstructions depending on temperature, Ag coverage and Si surface orientation and (possible) vicinality. Islands of Ag adatoms only form once a "wetting" monolayer of silver has been deposited underneath, and in this wetting layer the surface reconstructions occur.

On the Si(001) surface, the (3×2) reconstruction is omnipresent; it starts to form for lowest Ag coverages and becomes complete for 2/3 monolayers (ML) [144]. Excess Ag adatoms do not disturb this layer, but rather diffuse on top, affecting the surface roughness. Once roughly a full monolayer is deposited, Ag island formation is observed.

On the Si(111) surface, there exists a well-known $(\sqrt{3} \times \sqrt{3}) - R30°$ reconstruction for temperatures between 350°C and 600°C. Necessary Ag coverages for saturation range between 2/3 and 1 ML, a fact that Raynerd *et al.* [145] explains by measuring and deriving from a model a temperature-dependent critical coverage. A structural model (that predicts a 1 ML critical coverage) has been analyzed by Ding *et al.* [146], and STM measurements in Wan *et al.* [147] agree with it. Moreover, there exists a (3×1) surface reconstruction the structure of which has long been subject to debates. The critical coverage here is 1/3 ML of silver adatoms, and the reconstruction is only observed in a narrow range of high temperatures [147].

10.2 Experimental Techniques (PEEM, LEED)

Surface electron microscopy, i.e., the use of electrons to produce images of crystal surfaces, is a technique that started out already in the early 1930s. By now,

this field has branched into a plethora of experimental methods to examine a multitude of surface properties and processes, employing vastly differing approaches. As recounted in the review Bauer [148], the techniques that are of direct relevance to us were developed starting in the sixties of the last century, owed to the advent of ultra high vacuum (UHV) technology that precludes the influence of contaminations. One method to obtain information on metal surface structures is low energy electron diffraction (LEED), in which an electron beam upon interaction with the surface produces diffraction patterns that can be analyzed. To arrive at an unambiguous interpretation, however, still requires independently obtained information on the microstructure of the surface. This lead to low energy electron (reflection) microscopy (LEEM), in which electrons are elastically scattered at the sample, thus producing a direct image of the surface. A prototype for this technique was first successfully tested in 1962 [149, and references therein], but it took a rather long time for the method to be ready for everyday use. By ingenious experimental refinements one can select which feature of the surface to measure, e.g., the reconstruction periodicity or the local geometric surface structure.

Another method to obtain direct images of the surface structure is photo emission electron microscopy (PEEM). Here, the sample is illuminated by (typically UV energy) photons, and by the photoelectric effect, electrons are emitted and then accelerated by a high voltage supplied to the probe. The image contrast arises from the spatially varying density of states of the surface electrons as well as due to different ionization voltages of the various materials (also dependent on the surface orientation and the reconstruction).

All of these techniques are true *imaging* methods, in that they simultaneously deliver all pixels of the image to be obtained. On the contrary, scanning methods obtain information on different parts of the surface by sequentially sampling different points of a grid. It is evident that true imaging is mandatory if one finally strives for a real-time observation of surface processes (i.e., at video rate), as is fundamental to our problem.

The device used in the experiments of Roos *et al.* [9], Wall [131] works in a UHV. Electrons (or photons for PEEM) of $\sim 15\,\mathrm{keV}$ are emitted from an electron cannon, guided by a system of deflectors, condensers and lenses, and decelerated by an electric field to hit the probe at low energies. The reflected (or emitted) electrons then travel back and are accelerated again by the same electric field. This beam is separated from the ingoing one by a magnetic field (in the so-called *sector*), and is focused onto a multichannel plate (essentially an electron multiplier) and then to a CCD (charge-coupled device) camera, see Figure 10.1 for a schematic. By its very nature, this apparatus can be employed for all three imaging methods mentioned above. Specifically, a LEED image is obtained by projecting (via setting the focal length of projector lenses) not the real-space image, but rather a diffraction image. We finally mention the important μLEED technique, in which only a μm size portion of the sample is imaged via LEED. This provides detailed "microdiffraction" information on the local surface structure, especially the nature of the reconstruction.

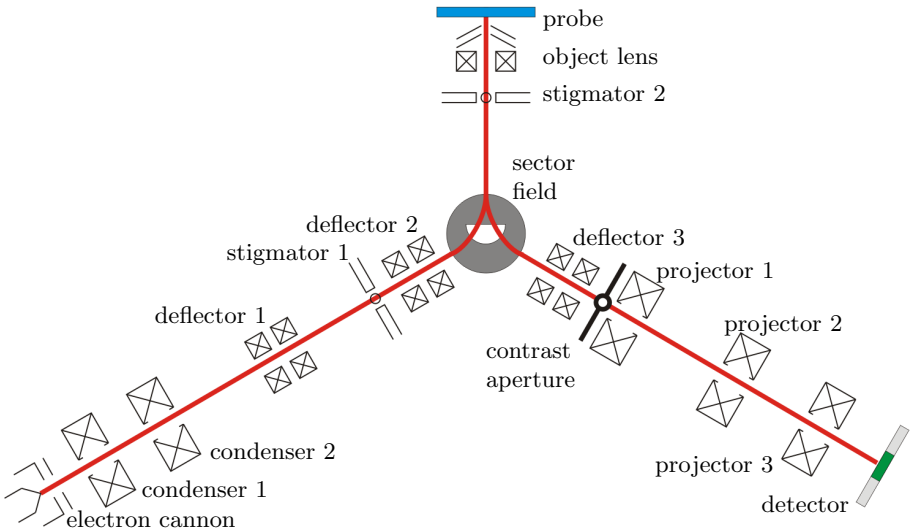

Figure 10.1: Schematic view of the IBM LEEM I, used in the experiments we refer to. (Original image: workgroup Horn-von Hoegen, University Duisburg-Essen.)

10.3 Observations

The experiments to which we refer are conducted in the PEEM imaging mode, with detailed surface reconstruction information verified by μLEED. Samples are prepared as well-oriented or vicinal (miscut by 4° in the [110] direction) Si(001) surfaces, cleaned by degassing and flash-annealing. Ag is then evaporated thermally and surface growth and desorption are monitored *in situ*.

As described before, Ag first forms the (3×2) reconstruction, and finally, Ag islands with well-defined facets form on top of the reconstruction layer. The sample is held at ≈ 650°C after the deposition process.

In the following desorption stages, one first observes that the surface breaks into bright and dark zones. Islands are seen very bright in the center of large bright zones (henceforth succinctly called "isozones" for reasons explained shortly) surrounded by dark areas. Quickly, the bright zone extension assumes a 'steady-state' value that decreases only very slowly. Simultaneously, the island radius shrinks, and once the island vanishes, the bright zone rapidly disappears as well. Figure 10.2 shows snapshots of the whole process. The typical time evolution of

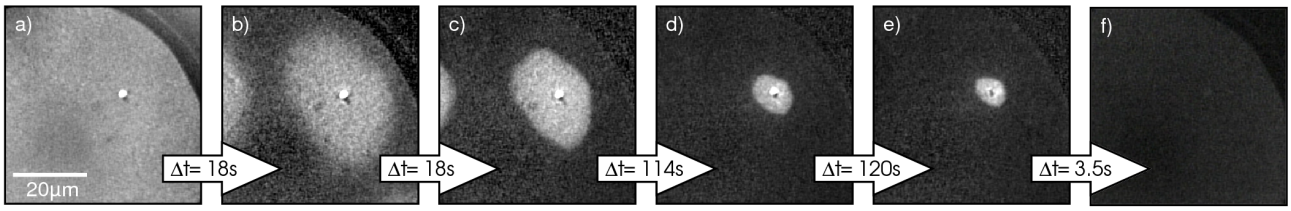

Figure 10.2: The processes of isozone formation, decay to the steady state, and final desorption stages as seen in PEEM images of Ag on a flat Si(001) surface [9].

island and isozone radius over time is seen in Figure 10.3: First, there is a fast initial relaxation to the, second, steady-state regime, and finally the quick decay of the bright zone after the island has vanished. Desorption sets the overall

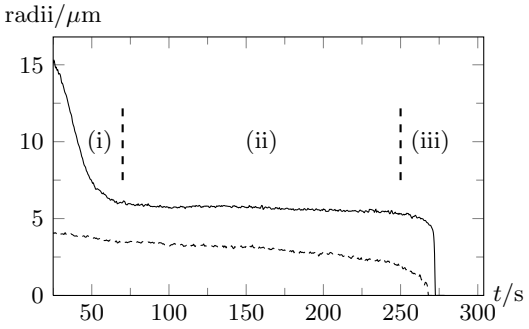

Figure 10.3: The radii of island (dashed, *values doubled* for visibility) and isozone (solid) in the time evolution depicted in Figure 10.2 [9].

timescale of the experiment. For temperatures below 640°C, no bright zones form at all, and above 690°C desorption is so fast they have no time to form. In between, the higher the temperature, the shorter the duration of the steady-state regime (ii) in Figure 10.3.

One can interpret this scenario in terms of microscopic features and processes on the surface [9]: The decaying central Ag island constantly feeds a current of Ag atoms into the surrounding areas. Around the island, where the Ag coverage is highest, it lies above the critical coverage needed to form the (3×2) reconstruction (always assumed to be 2/3 ML here), while further outside, the coverage has dropped below that value, and the surface is in the standard (2×1) reconstruction of a flat pure Si(001) surface. In both areas, one expects a dilute lattice gas of Ag atoms formed by the (excess) coverage.

In fact, μLEED pictures (Figure 10.4) show the diffraction patterns associated with the aforementioned reconstructions, and they confirm that the reconstruction precisely corresponds to the observed PEEM image contrast (via differing photoemission yields). This means that the image brightness directly depicts the surface reconstruction. Since the coverage decides on the reconstruction seen at a certain point and varies continuously over the area around one island, the boundaries between bright and dark zones are isocoverage lines of the corresponding critical reconstruction coverage: This is the reason we call the bright zones "isozones". The shape of the isozone is a direct foot-

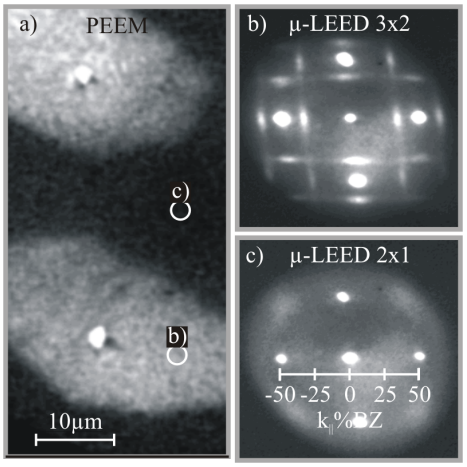

Figure 10.4: μLEED diffraction images found for the bright and the dark areas, respectively [131].

print of the diffusion field which is responsible for the surface reconstruction, a relation which is explained in more detail when we describe a theoretical model, cf. Sections 11.1ff.

Later, similar experiments were conducted on a flat (as well as a vicinal 1° miscut) Si(111) surface [131]; in Section 10.1 we briefly described the relevant reconstructions of the pure surface and Ag/Si(111). A striking observation was that for this system, one does not only see a bright zone surrounding the island, but in fact one bright zone, a surrounding small black region, and a moderately dark outside area. Along the same line of thought as above, analysis with μLEED images showed that these regions indeed are isozones again. This time they correspond (innermost to outermost zone) to the $\sqrt{3} \times \sqrt{3}$, the 3×1, and the 7×7 reconstruction (at high temperatures around 820°C, thus partially contradicting the phase diagram set up in Wan *et al.* [147]). This "double-zone" observation motivated us to generalize our model (Section 11.1) to the case of multiple isozones.

Our contribution to the analysis consists in an extension and a detailed analysis of a simple steady-state model for the isozone experiments proposed in Krug [150]. We also set up and evaluate models for both the relaxation process leading to this steady state as well as the free decay after the central island has vanished.

10.4 Relation to the Work Presented Herein

It is not hard to see that, on a theoretical level, the present task has only fairly general connections to the previous parts of this thesis. While we still deal with diffusion and its role in surface processes, the differences are as follows:

- We are interested in the *collective* diffusion of a large number of particles, as opposed to the one- to few-particle problems tackled earlier.
- There is simply no first-passage question involved.
- Most of the time, we will examine the steady state of the system. This we also did to find the encounter probability in Part I, but there we were concerned with an auxiliary quantity. The full problem was not stationary at all, although we finally removed the time-dependence by (what effectively amounts to) time-averaging (cf. Section 3.8).
- Boundary conditions in the full problem were static, e.g., the periodic boundaries of Section 3.3, whereas here, boundaries (of the isozones) are moving in principle. This leads to completely different questions, such as the necessity of a stability analysis of solutions.
- The geometry of the system does *not* play a crucial role now; more precisely, we deal with an effectively infinite system, while confinement to a limited space was essential before (due to the first-passage type of problems).

The interest arose out of the experimentally intriguing situation that quickly proved to be amenable to analytical modeling. The fact that one treats two-dimensional diffusion also provides some mathematical connections we could exploit, cf. the disc model to calculate the encounter probability in Section 3.2.4.

Chapter 11

Analytical Results

11.1 Model and Assumptions

While this model was originally conceived for the situation of a single isozone, we found it can easily be generalized to an arbitrary number of zones N, as motivated by the "double-zone" experiments. Some results will, however, only be proven rigorously for the single-zone case.

We consider a rotationally invariant setup and employ polar coordinates with the radial coordinate r, cf. Figure 11.1. The total Ag coverage is labeled $\theta(r)$, continuous throughout. Centered around the origin sits the feeding island, and its radius will be denoted by R_0. Surrounding the island are (possibly several) isozones with radii R_1, R_2 etc. from in- to outside.

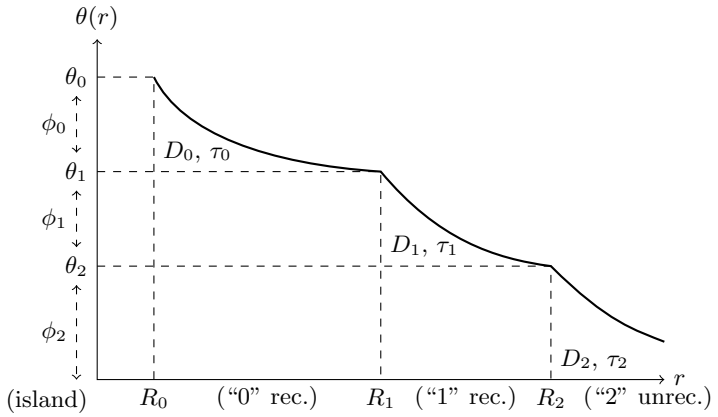

Figure 11.1: Model of the total Ag coverage versus radial coordinate for $N = 2$.

All specified radii are associated with certain critical concentrations θ_i that govern the surface reconstruction, such that $\theta(r = R_i) = \theta_i$. From now on we assume $\theta(r)$ monotonically decreasing and $\theta_1 > \theta_2 > \ldots$, so that $\theta_i > \theta(r) > \theta_{i+1}$ exactly if $R_i < r < R_{i+1}$, which we will henceforth call region or zone "i". In each of these regions, the excess coverage is defined as $\phi(r) = \theta(r) - \theta_{i+1}$, obviously discontinuous. In terms of the excess coverages, the zone radii conditions

are thence given as $\phi(R_i+) = \phi_i$ (with $\phi_i = \theta_i - \theta_{i+1}$) and $\phi(R_i-) = 0$ for $i = 0, 1, \ldots N$, and $\phi(r \to \infty) \to 0$. The last condition may also be read as a vanishing ϕ at a virtual outer boundary R_{N+1}, where $R_{N+1} \to \infty$ eventually. In this sense, all separate regions have equal boundary conditions, and we will see that we can eventually recover the proper profile in zone N from a delayed limit $R_{N+1} \to \infty$. The innermost boundary condition is a given excess coverage ϕ_0 provided by the island at its edge R_0.

Within the described setting, we assume only the excess coverage in each region i to be mobile by diffusion with coefficient D_i and to desorb on a characteristic time-scale τ_i, defining a diffusion length $\ell_i = \sqrt{D_i \tau_i}$. Hence in the steady state, the excess coverage satisfies a stationary diffusion equation throughout, and with $\nabla^2 f(r) = r^{-1}\partial(r\partial f/\partial r)/\partial r = (\partial^2/\partial r^2 + r^{-1}\partial/\partial r) f(r)$ it reads

$$\left(\frac{\partial}{\partial \tilde{r}^2} + \frac{1}{\tilde{r}}\frac{\partial}{\partial \tilde{r}} - 1\right)\phi = \frac{\partial \phi}{\partial \tilde{t}} \equiv 0$$

in rescaled coordinates $\tilde{r} = r/\ell_i$, $\tilde{t} = t/\tau_i$.

In the following we use standard units for all quantities, i.e., r, ℓ_i etc. are lengths, $[D] = L^2/T$, $[j] = 1/(LT)$, and $[\theta] = [\phi] = L^{-2}$. Sheer numbers for the latter coverages should be understood as meaning monolayers, hence in units of $1\,\mathrm{ML} = \Omega^{-1} = a_0^{-2}$, where a_0 is the lattice spacing and Ω the adatom area.

11.2 Zone Radii and Steady State

The solution for zone i is obtained as (cf. Appendix B.1)

$$\phi(r) = \phi_i \frac{H_i(r)}{H_i(R_i)} \tag{11.1}$$

with

$$H_i(r) = I_0\left(\frac{R_{i+1}}{\ell_i}\right) K_0\left(\frac{r}{\ell_i}\right) - I_0\left(\frac{r}{\ell_i}\right) K_0\left(\frac{R_{i+1}}{\ell_i}\right).$$

For the outermost region "N" and $R_{N+1} \to \infty$, the factor $K_0(R_{N+1}/\ell_N) \to 0$ lets the second term in H_N vanish, so that in ϕ, the I_0 terms in the first summands cancel; this correctly yields $\phi = \phi_N K_0(r/\ell_N)/K_0(R_N/\ell_N)$ as one would also obtain from the original boundary conditions.

This is the solution for prescribed radii R_i, however, for those to be the stationary-state radii, the diffusion current across the zone boundaries has to be continuous. The (radial component of the) particle current density reads $j = -D\nabla\theta \cdot \mathbf{e}_r = -D\partial\theta/\partial r$, such that (cf. Appendix B.1) in zone i (i.e., for $R_i < r < R_{i+1}$) one has

$$j(r) = \frac{D_i \phi_i}{\ell_i} \frac{I_0\left(\frac{R_{i+1}}{\ell_i}\right) K_1\left(\frac{r}{\ell_i}\right) + I_1\left(\frac{r}{\ell_i}\right) K_0\left(\frac{R_{i+1}}{\ell_i}\right)}{H_i(R_i)},$$

and particularly,

$$j(R_{i+1}-) = \frac{D_i \phi_i}{\ell_i} \frac{\ell_i/R_{i+1}}{H_i(R_i)} = \frac{D_i \phi_i}{R_{i+1} H_i(R_i)}.$$

The requirement of continuity at R_i, $j(R_i-) = j(R_i+)$, thus becomes

$$\Delta_i := \frac{D_{i-1}\phi_{i-1}}{D_i\phi_i} = \frac{R_i}{\ell_i}\frac{H_{i-1}(R_{i-1})}{H_i(R_i)}\times \\ \times\left[I_0\left(\frac{R_{i+1}}{\ell_i}\right)K_1\left(\frac{R_i}{\ell_i}\right)+I_1\left(\frac{R_i}{\ell_i}\right)K_0\left(\frac{R_{i+1}}{\ell_i}\right)\right]. \quad (11.2)$$

Again, by sending $R_{N+1}\to\infty$ at the outermost boundary $i=N$, the K_0 terms in the second summand of $H_N(R_N)$ as well as in the expression in brackets vanish and the remaining I_0 factors of these expressions cancel. Thence we get

$$\frac{[\dots]}{H_N(R_N)}\to\frac{K_1}{K_0}\left(\frac{R_N}{\ell_N}\right),$$

leading to the same result as a calculation which treats the outermost zone separately,

$$\Delta_N = \frac{R_N}{\ell_N}\frac{K_1}{K_0}\left(\frac{R_N}{\ell_N}\right)H_{N-1}(R_{N-1}). \quad (11.3)$$

11.3 Solvability and Stability

A solution of Equations (11.2) and (11.3), i.e., a set of radii for given parameters, is the steady-state solution of the problem. It is not clear, however, that such a solution always exists, let alone that it is stable. We found it highly involved to (analytically) address these questions for the general multi-zone case, but it is rather easy to prove that in the single-zone case $N=1$, there *always* exists a unique solution, and that this solution is stable. Because of the far-reaching analogy between the different N cases, and failing to see any substantial specialty of $N=1$, we assume there is a unique and stable solution for any N then as well.

For $N=1$ the stationarity condition reads[1]

$$\Delta_1 = \frac{R}{\ell_1}\frac{K_1}{K_0}\left(\frac{R}{\ell_1}\right)H_0(R_0). \quad (11.4)$$

Since I_0 is monotonically increasing and K_0 monotonically decreasing, $H_0(R_0)$ *as a function of* R increases monotonically (vanishing for $R=R_0$ and diverging for $R\to\infty$). The same is true for $zK_1(z)/K_0(z)$ $(z\geq 0)$:

$$z\frac{\mathrm{d}}{\mathrm{d}z}K_\nu(z)+\nu K_\nu(z) = -zK_{\nu-1}(z)$$

[51, 8.486 12.] for $\nu=1$ shows that its derivative reads $\frac{\mathrm{d}}{\mathrm{d}z}(zK_1(z)/K_0(z)) = z[(K_1/K_0)^2-1]>0$, where the sign can, e.g., be read off [51, 8.432 1.]

$$K_\nu(z) = \int_0^\infty \exp(-z\cosh x)\cosh\nu x\,\mathrm{d}x.$$

[1] Here as well as in Sections 11.5f., the (variable) isozone radius will be denoted $R\equiv R_1$, and R^* will label the stationary solution.

The limits of $zK_1(z)/K_0(z)$ are easily obtained from the exact and asymptotic series of Appendix B.1, it approaches zero as $z \to 0+$, and diverges $\sim z$ for $z \to \infty$. Hence altogether, the right-hand-side of the stationarity condition is strictly monotonic increasing from zero at $R = R_0$ to infinity for $R \to \infty$. By the intermediate value theorem there exists a unique solution $R = R^*$ then for arbitrary values $\Delta_1 > 0$ of the left-hand-side, $R^* \to R_0$ corresponding to $\Delta_1 \to 0+$.

Now we will prove that this unique solution is stable. The solution for $R = R^*$ is stationary since it has a continuous diffusion current at the zone boundary. In the general solution with zone radius at an arbitrary R this radius evolves with time according to

$$\frac{\mathrm{d}R}{\mathrm{d}t} = \Omega \left(j(R-) - j(R+) \right),$$

where Ω denotes the area occupied by a single Ag atom in the reconstructed zone. Stability thence means that

$$\left. \frac{\mathrm{d}}{\mathrm{d}R} \right|_{R=R^*} \frac{\mathrm{d}R}{\mathrm{d}t} < 0,$$

so that an infinitesimal perturbation of R^* would quickly relax. Using expressions of the previous Section we find (recall $\theta_1 = \phi_1$ for $N = 1$)

$$\frac{\mathrm{d}R}{\mathrm{d}t} = \frac{\Omega D_1 \theta_1}{\ell_1} \left[\frac{\Delta_1}{H_0(R_0)\frac{R}{\ell_1}} - \frac{K_1}{K_0}\left(\frac{R}{\ell_1}\right) \right] = \frac{-\Omega D_1 \theta_1}{\ell_1} \frac{H_0(R_0)\frac{R}{\ell_1}\frac{K_1}{K_0}\left(\frac{R}{\ell_1}\right) - \Delta_1}{H_0(R_0)\frac{R}{\ell_1}}. \tag{11.5}$$

Evaluating the derivative at $R = R^*$ with the product rule, one half vanishes due to (11.4), and the other yields

$$\left. \frac{\mathrm{d}}{\mathrm{d}R} \right|_{R=R^*} \frac{\mathrm{d}R}{\mathrm{d}t} = \frac{-\Omega D_1 \theta_1}{\ell_1} \frac{\left. \frac{\mathrm{d}}{\mathrm{d}R} \right|_{R=R^*} \left[H_0(R_0)\frac{R}{\ell_1}\frac{K_1}{K_0}\left(\frac{R}{\ell_1}\right) - \Delta_1 \right]}{H_0(R_0)\frac{R^*}{\ell_1}} < 0, \tag{11.6}$$

as the numerator derivative has been shown positive in the proof of existence.

11.4 Approximate Solution

We shall now see that, given relatively mild assumptions, one can derive simple power law behaviors of the steady-state zone radii R_i.

We assume that diffusion dominates the situation in the sense that for given i (i.e., if we want to obtain R_i) R_i, $R_{i+1} \ll \ell_i$ and R_{i-1}, $R_i \ll \ell_{i-1}$, so that all arguments appearing in the stationarity condition for R_i are small. First of all, this is a reasonable deduction from experimental facts: Once the island has disappeared, the extended isozone rapidly vanishes. This suggests that in fact, individual diffusing excess atoms necessarily have enough time to travel to the zone boundaries from the island (referring to the single-zone case) before they desorb. Second, this assumption is fully reconcilable with activation energies found experimentally and / or theoretically. In particular, such results imply that for the single-zone case, $\ell_0 \leq \ell_1$, the diffusion length in the unreconstructed area is larger than in the reconstructed one. Finally, we deem the assumption

valid judging, in hindsight, by the good agreement of its predictions with the experiment and other available data.

Note that here, we actually have to treat separately the outermost zone radius R_N, since obviously, $R_{N+1} \ll \ell_N$ is no longer satisfied if we finally send $R_{N+1} \to \infty$. This is easily accounted for by using the special form of stationarity condition for this radius; however, we emphasize that the failure to fulfill this requirement is the basic reason that *this* diffusion length will still appear in our result, whereas all others will not play any role.

With judicious use of the expressions for $I_{0,1}$ and $K_{0,1}$ (cf. Appendix B.1) we deduce that for all arguments small (in the sense defined above) we have

$$\begin{aligned} z\frac{K_1}{K_0}(z) &= z\frac{\frac{1}{z}+\mathcal{O}(z\ln z, z)}{-\ln\frac{z}{2}-\gamma+\mathcal{O}(z^2, z^2\ln z)} = \frac{1+\mathcal{O}(z^2)\mathcal{O}((\ln z)^{+1,0,-1})}{\ln(1/z)-\gamma+\ln 2}, \\ \tilde{H}(x,y) &:= I_0(x)K_0(y) - I_0(y)K_0(x) = \ln\frac{x}{y}\left[1+\mathcal{O}(x^2,y^2)\right]+\mathcal{O}(x^2,y^2), \\ \Rightarrow \frac{\partial\tilde{H}}{\partial y} &= -\frac{1}{y}\left[1+\mathcal{O}(x^2,y^2)\right]+\ln\frac{x}{y}\mathcal{O}(y), \\ \frac{\partial\tilde{H}}{\partial x} &= \frac{1}{x}\left[1+\mathcal{O}(x^2,y^2)\right]+\ln\frac{x}{y}\mathcal{O}(x). \end{aligned} \tag{11.7}$$

Using these relations in the continuity conditions (11.2) and neglecting all higher-order terms we obtain

$$\Delta_i \approx \frac{\ln(R_i/R_{i-1})}{\ln(R_{i+1}/R_i)},$$

while for the special case of the outermost boundary we get

$$\Delta_N \approx \frac{\ln(R_N/R_{N-1})}{\ln(\ell_N/R_N)+\ln 2-\gamma}.$$

This translates into the following approximate power-law dependencies (also neglecting $\ln 2-\gamma \approx .115932 \ll 1$ compared to the logarithm)

$$\begin{aligned} \frac{R_i}{R_{i+1}} &\approx \left(\frac{R_{i-1}}{R_{i+1}}\right)^{(1+\Delta_i)^{-1}} \\ \text{and}\quad \frac{R_N}{\ell_N} &\approx \left(\frac{R_{N-1}}{\ell_N}\right)^{(1+\Delta_N)^{-1}}. \end{aligned} \tag{11.8}$$

It is immediately obvious that all these steps may easily be applied to an arbitrary number of zones. We find it a striking feature that in the outermost region, the diffusion length substitutes for the "zone radius" $R_{i+1} \to \infty$ as the limiting length scale. On the other hand, the universal form of the relationship for any of the inner zone boundaries shows that, given our assumptions on the length scales, the adatom-supplying "island" boundary at R_0 is not a special boundary condition at all: In fact, for all zones the next inner region works in precisely the same way as a supplying island as well.

Comparison with experiments. Let us first collect several results on activation energies for the specific system of Ag on a Si(001) surface. The density

functional theory (DFT) calculation Kong *et al.* [151] for the unreconstructed surface finds $E_{\tau_1} = 3.1\,\mathrm{eV}$ and $E_{D_1} = 0.5\,\mathrm{eV}$. A nucleation study Hanbücken *et al.* [152] yields $E_{D_0} = 0.7\,\mathrm{eV}$ and $E_{\tau_0} \geq 2.1\,\mathrm{eV}$.

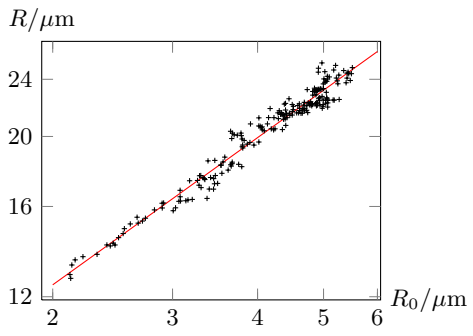

Figure 11.2: Experimentally found isozone radii vs. island radii as of Roos *et al.* [9] in a double-logarithmic plot.

Experimentally, island and isozone radii may be obtained directly from PEEM observations [9]. They are found to conform nicely to the power-law behavior (11.8) predicted by our model, as shown in Figure 11.2. Using this relation (for the single-isozone steady-state case) to fit the data, one can deduce Δ_1 as well as ℓ_1. Such an analysis has been performed [9] and yields $E_{\tau_1} - E_{D_1} \approx 2.3\,\mathrm{eV}$ (assuming coinciding attempt frequencies for hopping and desorption in one region) and $D_0/D_1 \approx 4/(9\phi_0)$ (using $\theta_1 = 2/3\,\mathrm{ML}$). The former result is consistent with the DFT-based $E_{\tau_1} - E_{D_1} \approx 2.6\,\mathrm{eV}$. From the latter one finds (for the plausible value $\phi_0 = 1\,\mathrm{ML}$) that $E_{D_0} - E_{D_1} \approx 0.1\,\mathrm{eV}$. Using the DFT estimate for E_{D_1} results in $E_{D_0} \approx 0.6\,\mathrm{eV}$, which agrees reasonably well with the nucleation study outcome.

This is the right time to assess the validity of our assumptions $R_1 \ll \ell_0, \ell_1$. The experimental data taken at $T = 919\,\mathrm{K}$ ($\approx 0.080\,\mathrm{eV}$ with $k_\mathrm{B} = 8.6173 \times 10^{-5}\,\mathrm{eV/K}$) shows that $R_1 < 30\,\mu\mathrm{m}$, such that one should have, say, $\ell_0 \geq 100\,\mu\mathrm{m}$. With equal attempt frequencies of hopping and desorption we have $\ell_0 = a_0/2 \exp\left[\beta\left(E_{\tau_0} - E_{D_0}\right)/2\right]$, and with a lattice spacing of $a_0 = 7\,\text{Å}$ this would imply $E_{\tau_0} - E_{D_0} > 2\,\mathrm{eV}$, consistent with the lower bound from nucleation given above. Moreover, the previously available data clearly suggests that the diffusion length in the unreconstructed region is much larger still. Obviously, the simple model can consistently account for all observed steady-state features of the complex Ag on Si(001) system, and the isozones are indeed a proper footprint of the diffusion field.

We finally mention the "double-zone" experiments of Wall [131]: Since the observation of this feature requires still higher temperatures (around 820° C) than for Ag/Si(001), the desorption is rather quick even in the 'quasi-stationary' phase (ii) of Figure 10.3. Moreover, islands are no longer compact. Higher contrast in the PEEM image reduces radii data scatter on the other hand, and the results of a fit to the power-law dependence (11.8) still seem to agree with data available otherwise.

11.5 Relaxation Time to Steady State

For the single-zone situation, we have shown there always exists a unique and stable solution to our model, i.e., an isozone radius R^* for given critical coverages, island radius and island edge concentration as well as kinetic parameters (diffusion coefficients and desorption times). Experimentally, one observes a relaxation of the diffusion zone radius to this steady-state value, and hence we strive for

predictions for the corresponding relaxation time.

From the stability analysis of Section 11.3 we know $\mathrm{d}R/\mathrm{d}t$ in terms of R, (11.5). Expanding this first-order differential equation about the stationary solution, i.e., in terms of $R - R^*$, one obtains a relation of the form

$$\frac{\mathrm{d}(R-R^*)}{\mathrm{d}t} = -\frac{1}{t_\mathrm{r}}(R-R^*) + \mathcal{O}\left((R-R^*)^2\right),$$

and the zeroth order vanishes due to R^* stationarity. Such an equation has the (leading-order) solution $R - R^* \propto \exp(-t/t_\mathrm{r})$, thence t_r is (to the order of the expansion) the searched relaxation time. From the expansion we have

$$t_\mathrm{r}^{-1} = -\left.\frac{\mathrm{d}}{\mathrm{d}R}\right|_{R=R^*} \frac{\mathrm{d}R}{\mathrm{d}t} = \frac{\Omega\theta_1}{\tau_1}\frac{1}{H_0(R_0)\frac{R}{\ell_1}} \cdot \ell_1 \frac{\mathrm{d}}{\mathrm{d}R}\left[H_0(R_0)\frac{R}{\ell_1}\frac{K_1}{K_0}\left(\frac{R}{\ell_1}\right)\right]\Bigg|_{R=R^*},$$

and we employed (11.6) in the evaluation. Rewriting this using an earlier result for $\mathrm{d}[zK_1/K_0]/\mathrm{d}z$ and stationarity (11.4) yields

$$\begin{aligned} t_\mathrm{r}^{-1} &= \frac{\Omega\theta_1}{\tau_1}\frac{1}{H_0(R_0)\frac{R^*}{\ell_1}}\left\{H_0(R_0)\frac{R^*}{\ell_1}\left[\left(\frac{K_1}{K_0}\right)^2\left(\frac{R^*}{\ell_1}\right) - 1\right]\right. \\ &\quad \left. + \ell_1 \left.\frac{\mathrm{d}H_0(R_0)}{\mathrm{d}R}\right|_{R=R^*} \frac{R^*}{\ell_1}\frac{K_1}{K_0}\left(\frac{R^*}{\ell_1}\right)\right\} \\ &= \frac{\Omega\theta_1}{\tau_1}\left[\left(\frac{K_1}{K_0}\right)^2\left(\frac{R^*}{\ell_1}\right)\left(1 + \frac{R^*}{\Delta_1}\left.\frac{\mathrm{d}H_0(R_0)}{\mathrm{d}R}\right|_{R=R^*}\right) - 1\right]. \end{aligned} \tag{11.9}$$

We could not improve upon this result by more explicit evaluation of the H_0 derivative. $\Omega\theta_1 < 1$ is the critical coverage for reconstruction given as a fraction of the monolayer coverage Ω^{-1}. Note that all quantities in the pre-factor also affect R^*.

11.5.1 Standard Approximation

We argued earlier in favor of the "dominating diffusion" assumption, cf. Section 11.4. For the single-zone case this means $R_0 \leq R \ll \ell_0, \ell_1$, whence we may use the approximations (11.7) in (11.9) (neglecting $\mathcal{O}(1)$ terms in the brackets) to find

$$t_\mathrm{r} \approx \frac{\tau_1}{\Omega\theta_1}\frac{\Delta_1}{1+\Delta_1}\left(\frac{R^*}{\ell_1}\right)^2\left[\ln\left(\frac{\ell_1}{R^*}\right)\right]^2.$$

The essential scaling here reads $t_\mathrm{r} \propto {R^*}^2/D_1$. Using the approximate result for R^*, we can eliminate the isozone radius,

$$t_\mathrm{r} \approx \frac{\tau_1}{\Omega\theta_1}\frac{\Delta_1}{(1+\Delta_1)^3}\left(\frac{R_0}{\ell_1}\right)^{2/(1+\Delta_1)}\left[\ln\left(\frac{\ell_1}{R_0}\right)\right]^2. \tag{11.10}$$

Further specialization to uniform diffusion and desorption merely allows for the substitution $\Delta_1 = \phi_0/\phi_1$. More interesting in view of experimental data is the case $\Delta_1 \ll 1$, which implies a nearly linear relation between R and R_0, such that $t_\mathrm{r} \propto {R_0}^2/D_1$.

11.5.2 Temperature Dependence

We finally examine the temperature dependence of the relaxation time in our standard approximation (11.10).

For low temperatures, $\beta(E_{D_0} - E_{D_1}) \gg 1$, $\Delta_1 \ll 1$, and expansion to leading order in Δ_1 yields

$$t_\mathrm{r} \approx \frac{\tau_1 \Delta_1}{\Omega\theta_1} \left(\frac{R_0}{\ell_1}\right)^2 \left[\ln\left(\frac{\ell_1}{R_0}\right)\right]^2 = \frac{\Delta_1}{\Omega\theta_1} \frac{R_0^2}{D_1} \left[\ln\left(\frac{\ell_1}{R_0}\right)\right]^2 .$$

Inserting thermally activated behavior, for $T \to 0$ the logarithm essentially contributes a factor $\beta^2(E_{\tau_1} - E_{D_1})^2/4$ which only adds to the exponential divergence of $\Delta_1/D_1 \propto D_0/D_1^2 \propto \exp[-\beta(E_{D_0} - 2E_{D_1})]$; we reasonably assume that $E_{D_0} - 2E_{D_1} < 0$, and consequently $t_\mathrm{r} \to \infty$ for $T \to 0$ with this activation energy.

For high temperatures $\beta(E_{D_0} - E_{D_1}) \ll 1$ we have $\Delta_1 \approx \phi_0/\theta_1 \sim 1$ instead. Obviously, for $T \to \infty$, the relaxation time decreases to a finite limit, viz.

$$t_\mathrm{r} \approx \frac{\tau_1}{\Omega\theta_1} \frac{\phi_0/\theta_1}{(1+\phi_0/\theta_1)^3} \left[\ln\left(\frac{\ell_1}{R_0}\right)\right]^2 \left(\frac{R_0}{\ell_1}\right)^{2/(1+\phi_0/\theta_1)} ,$$

where $\ell_1 \to a_0/2\sqrt{\nu_{D_1}/\nu_{\tau_1}}$ is the limit of the diffusion length for attempt frequencies ν_{D_1} and ν_{τ_1} of hopping and desorption, respectively. While one can easily insert the temperature dependencies and properly expand in the small parameter $\beta(E_{D_0} - E_{D_1}) \ll 1$, the result is awkward and not particularly enlightening.

Experimental results. There have been efforts to determine the temperature dependence of the relaxation time in the Duisburg group of F. J. Meyer zu Heringdorf. At present, there are no data sets to reasonably compare our results with, mostly owed to the narrow temperature range exhibiting a steady state at all.

11.6 Free Isozone Decay: A Toy Model

As mentioned above, the end of the steady-state scenario is marked by a quickly vanishing central island, triggering a rapid decay of the remaining isozone. To enhance our understanding of the overall situation, as well as to use one more observed process to gather information about involved activation energies and such, we propose a simple model for this decay as well.

We re-consider the circular single-isozone setup. Obviously, we now need a *time-dependent* description of the situation. However, the diffusion equation with structurally different zones, in which diffusion and desorption coefficients can differ, and only the excess coverage is mobile, is a highly involved Stefan problem [153]. Therefore we shall be content to treat a single equation with uniform D, τ, and for the *total* coverage $\theta(\mathbf{r}, t)$ mobile and desorbing, which then reads

$$D\nabla^2\theta - \frac{\theta}{\tau} = \frac{\partial\theta}{\partial t},$$

with the diffusion length $\ell = \sqrt{D\tau}$.

We use an ansatz starting from free desorption: $\theta = \exp(-t/\tau)\tilde{\theta}(\mathbf{r}, t)$. For the resulting standard equation $D\nabla^2\tilde{\theta} = \partial\tilde{\theta}/\partial t$ (without any desorption term), the solution in two dimensions (bounded at all times $t > 0$) writes [154, pp.251ff.]

$$\tilde{\theta}(\mathbf{r}, t) = \frac{1}{4\pi D t} \int \mathrm{d}^3\mathbf{r}' \theta(\mathbf{r}', t = 0) \exp\left[-\frac{|\mathbf{r} - \mathbf{r}'|^2}{4Dt}\right]$$

with $\theta(\mathbf{r}, t = 0)$ the initial coverage. The searched isocoverage line is given by $\theta(\mathbf{r}(t), t) = \theta_1$, and restricting ourselves to rotational symmetry the isozone radius is determined by $\theta(R(t), t) = \theta_1$.

Delta peak model. We prescribe an initial delta profile $\theta(\mathbf{r}, t = 0) = C\delta(\mathbf{r})$, where $C > 0$ is the initial number of adatoms. Obviously, the solution has $R(t = 0) = 0$ and growing at first, but we may simply start at an appropriate later time $t_0 > 0$. One obtains the well-known GAUSSian for $t \geq t_0$,

$$\theta(r, t) = \frac{C}{4\pi D t} \exp\left[-\left(\frac{r^2}{4Dt} + \frac{t}{\tau}\right)\right]. \tag{11.11}$$

This will be our (analytically tractable) approximation of an initial profile; we will later comment on its applicability. For clarity, the parameters C and t_0 can be expressed in terms of the initial *peak concentration* $\theta_0 = \theta(r = 0, t = t_0)$ (the notation purposely suggests to use the former island edge concentration here), and the initial isocoverage radius $R(t = t_0)$, where $\theta(R(t_0), t_0) = \theta_1$. Those definitions imply

$$\theta(r, t = t_0) = \theta_0 \, \mathrm{e}^{-\left(\frac{\sqrt{\ln \theta_0/\theta_1}}{R(t_0)} r\right)^2},$$

and comparison (for all r) then yields

$$\frac{1}{4Dt_0} = \frac{\ln \theta_0/\theta_1}{R^2(t_0)}, \qquad \frac{C\,\mathrm{e}^{-t_0/\tau}}{4\pi D t_0} = \theta_0, \tag{11.12}$$

such that

$$\frac{C}{\theta_1} = \frac{\theta_0}{\theta_1} \pi \frac{R^2(t_0)}{\ln \theta_0/\theta_1} \exp\left(\frac{R^2(t_0)}{4\ell^2 \ln \theta_0/\theta_1}\right).$$

$R(t)$ **analysis.** From the original form (11.11) we find the isocoverage line radius

$$R(t) = \sqrt{-4Dt\left(\ln \frac{4\pi D t \theta_1}{C} + \frac{t}{\tau}\right)},$$

with the following behavior: $R(t = 0) = 0$, and as long as $4\pi D t\theta_1/C \ll 1$, $R(t) \approx \sqrt{4Dt \ln(4\pi D t\theta_1/C)^{-1}}$ first grows by diffusive spreading (with negligible desorption). At the time when $(4\pi D t\theta_1/C)^{-1} = \exp(1 + 2t/\tau)$, the radius $R(t)$ reaches a maximum. After the following decline, $R(t)$ becomes zero again at the time t^* given by

$$\frac{C}{4\pi D t^* \theta_1} = \mathrm{e}^{t^*/\tau}, \tag{11.13}$$

which is the time when the isozone has vanished.

A few notes on orders of magnitude of the different terms are appropriate. At the initial time t_0, the isozone is covered with at least the critical coverage θ_1, so that $\theta_1 \cdot \pi R^2(t_0) < C$. We now assume that desorption is weak compared to dominating diffusion, in the sense $C \ll \theta_1 \ell^2$ (where $\theta_1 \sim 1\,\mathrm{ML}$) — this also implies $R^2(t_0) \ll \ell^2$, like we generally assumed in the more involved models and was found experimentally. Moreover, we then have $t/\tau \ll 4\pi D t \theta_1 / C < 1$ throughout, the latter inequality as at that time, the radicand in $R(t)$ is already negative: The whole vanishing of the isozone takes place long before the desorption timescale τ is reached. Diffusion dominates the process, and the zone vanishes by spreading out the coverage over the plane, not by desorption.

Under these assumptions, $4\pi D t \theta_1 / C \ll 1$ in the phase of growing $R(t)$ implies $t/\tau \lll 1$, which is obviously no longer true at the maximum of $R(t)$. Now let t be large enough such that $\ln(4\pi D t \theta_1 / C)^{-1} < 1 + 2t/\tau$, when $R(t)$ is declining again. Assume for a moment we turn off desorption by $\tau \to \infty$, so that we reach $R(t) = 0$ slightly later, when $4\pi D t \theta_1 / C = 1$. Set $4\pi D t \theta_1 / C = 1 - \epsilon$ for the late stage close to the vanishing of the isozone. To leading order in ϵ one obtains $R(t) \approx \sqrt{C\epsilon/(\pi\theta_1)} = \sqrt{\frac{1-4\pi D t \theta_1/C}{\pi \theta_1 / C}}$, which still reproduces the exact time at which the isozone vanishes.

For weak (instead of no) desorption we have $t/\tau \ll 4\pi D t \theta_1 / C =: 1 - \epsilon$, where $\epsilon \to 0$ can no longer be reached, but still $\epsilon \ll 1$. The $R(t)$ solution then approximates to

$$R(t) = \sqrt{\frac{1-\epsilon}{\pi\theta_1/C}\left(\epsilon + \mathcal{O}(\epsilon^2) - \frac{1-\epsilon}{4\pi\theta_1\ell^2/C}\right)},$$

and to leading order in both ϵ and $(\theta_1 \ell^2/C)^{-1}$ this yields

$$R(t) \approx \sqrt{\frac{C}{\pi\theta_1}}\sqrt{\epsilon - (4\pi\theta_1\ell^2/C)^{-1}} = \sqrt{\frac{C}{\pi\theta_1}}\sqrt{1 - 4\pi D t \theta_1/C - (4\pi\theta_1\ell^2/C)^{-1}}.$$

This has the same functional form as the $R(t)$ dependence obtained from another simple model: Decay of a hemisphere island without desorption by outflow through its (shrinking) circular boundary touching the surface [131]. It appears as if the dominating diffusion lets the isozone spread through its boundary in a similar way. The time at which the isozone vanishes is read off as

$$t^* \approx \frac{1 - (4\pi\theta_1\ell^2/C)^{-1}}{4\pi D \theta_1 / C},$$

corresponding to $\epsilon \approx (4\pi\theta_1\ell^2/C)^{-1} \ll 1$.

Finally, we have seen earlier that $R(t)$ might first grow at the initial time t_0 if the maximal R occurs only later, a situation *not* seen in the experiment. The condition for $R(t)$ monotonically decreasing right from the start $t = t_0$ is that $\ln(4\pi D t \theta_1/C) + 1 + 2t/\tau > 0$ at $t = t_0$. Equivalently we have (with (11.12))

$$\ln\left(\frac{\theta_1}{\theta_0}\,\mathrm{e}^{-t_0/\tau}\right) + 1 + 2t_0/\tau > 0$$

which is satisfied if and only if $1 + t_0/\tau > \ln\frac{\theta_0}{\theta_1}$, or (neglecting weak desorption) if and only if the initial coverage contrast is not larger than e. For the typical experimental situation, $\theta_0/\theta_1 \approx 3/2$, which is on the proper side of the inequality.

Central result. It remains to evaluate the time $\Delta t := t^* - t_0$ passing from our starting point with a certain initial distribution until the zone finally vanishes, and to express it in physical parameters. Though possible, it makes for a rather intransparent derivation to employ the approximate results obtained so far. Instead we use that by (11.12) we have

$$\frac{\theta_0}{\theta_1} = \frac{C}{4\pi\theta_1 D t_0}\,\mathrm{e}^{-t_0/\tau},$$

while t^* is implicitly given by (11.13), hence

$$\frac{\theta_0}{\theta_1} = \frac{t^*}{t_0}\exp\left(\frac{t^*-t_0}{\tau}\right) = \left(\frac{\Delta t}{\tau}\frac{\tau}{t_0}+1\right)\mathrm{e}^{\Delta t/\tau}\,.$$

We expand the exponential as we have seen that $\Delta t/\tau \ll 1$ for realistic conditions, thus obtaining

$$\frac{\theta_0}{\theta_1} - 1 = \frac{\Delta t}{\tau}\left[\left(\frac{\tau}{t_0}+1\right) + \frac{\Delta t}{\tau}\left(\frac{\tau}{t_0}+\frac{1}{2}\right) + \dots\right].$$

In the first term, the desorption timescale drops out, hence we still include the second one as our first correction. Solving this truncated equation yields

$$\frac{\Delta t}{t_0} = \left(\frac{\theta_0}{\theta_1}-1\right)\left(1 - \frac{\theta_0}{\theta_1}\frac{t_0}{\tau} + \mathcal{O}(t_0/\tau)^2\right)$$

or, upon inserting $t_0 = \frac{R^2(t_0)}{4D\ln\theta_0/\theta_1}$,

$$\Delta t = \frac{R^2(t_0)}{D}\frac{\theta_0/\theta_1 - 1}{4\ln\theta_0/\theta_1}\left(1 - \frac{\theta_0}{\theta_1}\frac{R^2(t_0)}{4\ell^2\ln\theta_0/\theta_1} + \mathcal{O}(t_0/\tau)^2\right). \tag{11.14}$$

This is the most important and experimentally relevant result of this model. The leading order dependence reads $\Delta t \sim \frac{R^2(t_0)}{D}$. This is to be expected for dominating diffusion, because that is the time for diffusive motion of a length $R(t_0)$ over which the coverage falls off from its maximum to the critical coverage — we now have additionally found the pre-factor (of $\mathcal{O}(1)$ since $\ln\theta_0/\theta_1 \lesssim 1 \sim \theta_0/\theta_1$) and correction terms. The first correction in parentheses is small due to the weak desorption assumption $R(t_0) \ll \ell$. In the limit of no desorption, $\ell \to \infty$ and this would vanish completely.

Beyond the Gaussian. The time-dependent coverage for an arbitrary initial distribution $\theta(\mathbf{r}, t=0)$ is an integral that can only be evaluated for special cases. However, for a radially symmetric function the angular part can be integrated out: Without any restriction let the $\varphi = 0$ ray of plane polar coordinates coincide with the direction $\mathbf{r}$ in which to evaluate the integral. Hence $|\mathbf{r}-\mathbf{r}'|^2 = r^2 - 2rr'\cos\varphi + r'^2$, and

$$\theta(\mathbf{r},t) = \frac{\mathrm{e}^{-t/\tau}}{4\pi Dt}\int_0^\infty \mathrm{d}r'\, r' \exp\left(-\frac{r^2+r'^2}{4Dt}\right)\theta(r', t=0)\int_0^{2\pi}\mathrm{d}\varphi\,\exp\left(\frac{2rr'\cos\varphi}{4Dt}\right),$$

and using $\int_0^\pi \exp(z\cos x)\mathrm{d}x = \pi I_0(z)$ [51, 3.339] we obtain

$$\theta(\mathbf{r},t) = \frac{\exp\left(-\frac{t}{\tau}+\frac{r^2}{4Dt}\right)}{2Dt}\int_0^\infty \mathrm{d}r'\, r' \exp\left(-\frac{r'^2}{4Dt}\right)\theta(r', t=0) I_0\left(\frac{2rr'}{4Dt}\right).$$

One might want to insert a stationary profile obtained from the full model introduced in Roos *et al.* [9], where coefficients could differ in the different zones, and only excess coverage w.r.t. the critical coverage is mobile in the inside zone. However, such a procedure is complicated and unlikely to be fruitful: Even when evaluated with uniform coefficients all over the surface, the models have obvious structural differences. Furthermore, one cannot simply extend the solution (11.1) (a combination of modified BESSEL functions) to the origin: Certain terms diverge in this limit, since the solution of the diffusion equation *without* an inner boundary is the GAUSSian, not a BESSEL function. Moreover, as we now expect diffusion to be the main driving force behind the isozone decay, it is natural to assume that all smooth distributions rapidly approach a shape similar to the GAUSSian found in our delta peak example. Hence, we cannot expect to improve upon our current results in this direction, and thus abstain from introducing unnecessary complications.

11.7 Final Remarks

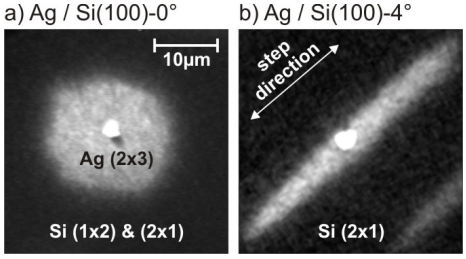

Figure 11.3: Comparison of the isozone shapes for a flat surface as opposed to a vicinal one. (Image kindly provided by Frank Meyer zu Heringdorf.)

Anisotropic diffusion. We first show an interesting implication of the isozone concept for the interpretation of observations. As mentioned before, isozone experiments have been performed also on vicinal Si(001) and Si(111) surfaces, miscut by various angles. This leads to a surface morphology incorporating step edges at regular intervals. Diffusion *along* the edges as well as *across* the edges may be much easier or harder than on the terraces between steps, and it could also be anisotropic on the terrace itself (based on the orientation of dimer rows, e.g., cf. Section 10.1). If the diffusion is effectively anisotropic, this can drastically affect the isozone shape [9, 131]: Even on well-oriented surfaces, local perturbations lead to an aspect ratio of island and isozone that varies stochastically over the surface; for vicinal surfaces, the effect becomes systematic. A rescaling of the fundamental diffusion equation of the analytical model shows that the isozone aspect ratio directly reflects the ratio of diffusion lengths, or the square root of the effective diffusion coefficients, in the two directions.

In this way, without any detailed knowledge of all the diffusion barriers, one may immediately deduce from a PEEM picture as shown in Figure 11.3 the dominant direction of adatom diffusion. Such information cannot be easily obtained from a study of island densities and the shapes of the compact islands themselves; in fact, both have been found to be virtually independent of the vicinality of the Ag/Si(001) system in Roos *et al.* [9].

Typically, diffusion across step edges is severely hindered. Since an isozone usually spans a lot of these steps, small changes in the diffusion activation energies suffice to evoke a highly anisotropic isozone shape (elongated parallel to the step edges). It can even lead to isozone shapes that are no longer elliptical,

but where the smaller diameter is effectively reduced to the island radius. Clearly, this situation can no longer be described by our simple model.

Outlook. A more general comparison between theory and experiments is hampered by the fact that the steady-state situation only arises in a narrow temperature range, cf. Section 10.3. It is therefore difficult to make meaningful statements about, e.g., the temperature dependence of the exponent in the zone-radii power law (11.8).

Progress in this direction may include determining the dependence of the relaxation time on the island radius as of (11.10) (although this involves a larger uncertainty since desorption sets the timescale, depending on activation energy *and* attempt frequency), and testing the prediction (11.14) for the isozone decay time after the island has disappeared.

The images of Figures 10.2 and 11.3 as well as the data shown in Figures 10.3 and 11.2 were kindly provided by Frank Meyer zu Heringdorf. The schematic drawing in Figure 10.1 was friendly enough made available to me by Dirk Wall, courtesy of the workgroup of Michael Horn-von Hoegen, University of Duisburg-Essen. We also thank Dirk Wall for the image in Figure 10.4.

Chapter 12

Conclusions

Part I: Hydrogen Recombination on Interstellar Dust Grains. Starting with a master equation analysis, we have shown that it is possible to rigorously define the true sweeping rate for such diffusion-mediated reactions on a closed surface, namely in terms of the two-particle *encounter probability*. This quantity has been calculated using both a continuum diffusion model as well as a random walk on a periodic lattice. We have compared both approaches and find that the RW result only converges logarithmically slow to the continuum limit, a consequence of the critical dimension two of diffusion. The generalization of the RW model to a distorted lattice has been thoroughly analyzed. Even in the quadratic case, the confining geometry plays a crucial role, and with the rectangular lattice we have a toy model to study this influence: Distortion can strongly decrease the encounter probability by several mechanisms, with a crossover to effectively one-dimensional behavior. These quantitative findings have been explained in depth. On the other hand, the effect of the lattice type is marginal. All these results have been validated by kinetic Monte Carlo simulations of the continuous-time equivalent of the random walk model.

As for the sweeping rate one wants to evaluate, we find it is reduced compared to its conventional approximation due to back-diffusion, most pronounced for *large grains*. Consequently, the recombination efficiency as predicted by the ME framework is decreased in this regime, and we have analyzed the implications under typical astrophysical conditions, finding that the temperature window of efficient recombination is hardly shifted.

As far as the homogeneous situation is concerned, we have thus described a fully analytic theory for the encounter probability that precisely agrees with simulations, including the aspects of global grain geometry and lattice type. The full recombination problem is thence solved inasmuch as the zero-dimensional master equation suffices. We expect these results to remain relevant for much more general reaction networks and grain types, since the explanation of the relevant effects remains sensible as well.

For the case of disordered transition rates, we have identified the simplest reasonable kind of disorder, and examined the influence on the encounter probability, sweeping rate, and recombination efficiency if one sticks to the zero-dimensional ME approach with a set of *effective* parameters. We have also considered how these parameters can account for the finite number of adsorption sites on the grain. Not too surprisingly however, it has turned out in KMC simulations that

for all but very weak disorder, the simplistic idea of effective parameters does not work well. This outcome is explained by the dependence of the recombination process on the full distribution of binding energy depths in a given realization. Finally, we have shown how the choice of disorder model can subtly affect the outcome of KMC simulations by comparing to previous work in the field.

Lastly, we have also examined the offspring problem of (inhomogeneous) island edge nucleation. Unfortunately, an analytical treatment beyond most restrictive assumptions seems out of reach.

Part II: Disordered Step Growth. For the problem of step growth in the presence of codeposited impurities, we have analyzed a simple one-dimensional model of the adatom on the terrace between two step edges. It has an explicit quenched-disorder expression for the probability to attach to the ascending or the descending step, respectively. This general result can already be useful in greatly speeding up Monte Carlo simulations of the system or of possible extensions to more complex models. We have applied it to several models of disorder which may strongly or not at all affect the outcome, and examined interesting limiting cases. The relation to continuum models that were used before has been established, and we have clarified the nature and importance of boundary conditions in this setting.

These results can be but one small piece in the puzzle of morphological step (in)stability, and as mentioned in Section 8.1 the one-dimensionality of our toy model obviously can have grave consequences. However, it is our impression that the experimental findings as well as the interpretation of simulations have not produced any consensus yet as to which factors are truly governing the phenomena observed for a particular physical system. Depending on the details of impurity effects we thence believe that our work is helpful in a better understanding of the physics of step growth.

Part III: Isozones and Surface Reconstructions. We have given a simple analytical theory for several of the observed Ag isozone phenomena on silicon surfaces as observed with the exciting PEEM approach. Based on the steady-state solution of simple diffusion equations with moving boundaries, we have derived a simple power-law dependence of the isozone radii in terms of the supplying island, which has been generalized to the multi-zone case also observed. It agrees with the experimentally measured dependence to the extent that results are fully compatible with activation energies obtained from various other experimental and analytical methods. The theory thus enhances our understanding of the fundamental processes that lead to the observed phenomena.

For the initial relaxation to the steady state, we have shown how to obtain the characteristic time-scale and analyzed its behavior in several regimes. Finally, we have thoroughly investigated a toy model of the isozone decay once the island has vanished, identifying reasonable assumptions on parameters. This eventually yields a simple expression for the time it takes for the isozone to vanish. These results are still to be tested in experiments.

The bigger picture. In the three Parts of this thesis, the emphasis clearly lies on different aspects.

The model system for hydrogen recombination is long-known and naturally suggests itself, yet even for the homogeneous case we have seen that there were blind spots (such as the sweeping rate definition) concerning fundamental questions (the importance of back-diffusion and the influence of the geometry to name only two). Addressing these questions, we feel we have essentially contributed to the theory, such that the zero-dimensional approach for the homogeneous (standard-lattice) system may be considered complete. Obviously this does not hold true for the disordered system, where work has just begun it seems.

For disordered step growth on the other hand, the focus was rather on the application of easily obtained results for the simple 1d-model to concrete physical conditions. This has established relations to other treatments of the same (physical) model, and served to clarify conceptual issues on the role of boundary conditions.

Still different, the work on isozones is basically a proof that we have the proper notion of the interplay of surface reconstructions and adatom diffusion and desorption. After all, predictions derived from the intuitive model could be tested (and verified) in experiments. Without these steps that provide an understanding of what we see, the value of the PEEM observations would be very limited.

However, these differences in emphasis should not create the impression that the Parts of this thesis are separate and unrelated to each other. Quite the opposite, the connections are manifold, and they show on the conceptual or mathematical level as well as in the form of identical physical mechanisms or similar material systems. In addition to our explanation in Chapter 1, this has also been stressed in the introductions to the various Parts (also cf. Section 6) — we have hopefully convinced the reader of our feeling that this is indeed *one* big field of study.

As should have become clear in the individual Parts, we have only touched tiny research areas of this huge field summarized by the title *Diffusion, Nucleation and Recombination in Confined Geometries*. Apart from a plethora of open questions in this general context, there is still a lot to do simply naturally continuing some trains of thoughts we presented herein. We hope to pursue some of these lines a bit further in the future.

Part IV

Appendices

Appendix A

Related to Part I

A.1 Lattice Geometry

Assuming $S \gg 1$, curvature effects do not play any role for the single atomic 'tile', and we cover the surface area $4\pi R^2$ by simply dividing it into such tiles, each of the area that a single atom occupies. This tile area depends on the distance of (the centers of) nearest-neighbor sites, $2r$, and the lattice type. From elementary trigonometry one deduces that, for a hexagonal lattice (which by common terminology refers to a 'honeycomb' lattice formed by the adsorption sites, with coordination number 3), it is given by $3\sqrt{3}r^2$, for a square lattice it is obviously $4r^2$, and a triangular lattice (i.e., one with coordination number 6) has a tile area of $2\sqrt{3}r^2$. Therefore, $S = g(2R/r)^2$ with a factor $g = \pi/(3\sqrt{3})$ for the hexagonal, $\pi/4$ for the square, and $\pi/(2\sqrt{3})$ for the triangular lattice, which is smaller than but of the order of unity in all three cases.

A.2 Expansion of p_{diff}

Erdélyi [155], 3.9.1 (13)ff. provides asymptotic expansions of Legendre functions near their singularity. It was not clear from the outset that their order sufficed, so we extended them with the aid of computer algebra, and en route found a misprint (not accounted for in the errata) in equation (15) *ibid.*, which erroneously lacks a factor of 2 preceding Euler's constant, cf. (A.1)f. below.

After rewriting (3.13) as

$$p_{\mathrm{diff}} = \left\{ \frac{1-z^2}{2\nu(\nu+1)} \frac{\mathrm{d}}{\mathrm{d}z} \left[\ln P_\nu(z)\right] + \frac{1+z}{2} \right\}_{z=-\cos(r/R)} ,$$

we use `Mathematica` to expand the encounter probability to first order in $(1+z)$ about 0, keeping ν (hence the regime) fixed. Then we manually apply various transformations (valid for arbitrary complex ν) to cast the result into a reasonable form by getting rid of all Γ and most ψ functions, viz. $\Gamma(1\mp\nu) = \pm\pi/\left[\sin(\nu\pi)\Gamma(\pm\nu)\right]$, $\psi(\pm\nu) = \psi(1\pm\nu) \mp 1/\nu$, and $\psi(1\mp\nu) = \psi(\pm\nu) \pm \pi\cot(\nu\pi)$.

We may identify $u = (1+z)/2$, and with

$$X := \ln u^{-1} - 2\gamma - 2\psi(\nu+1) - \pi\cot(\nu\pi) \tag{A.1}$$

(the square brackets in (3.14)) we obtain

$$p_{\text{diff}} \approx \frac{1}{-\nu(\nu+1)X} + \frac{1+2\nu(\nu+1)+2\nu(\nu+1)X}{-\nu(\nu+1)X^2} \cdot u$$

as the expansion of the encounter probability up to linear order in $u \approx [r/(2R)]^2$. The zeroth order term corresponds to equation (3.14) and describes a non-trivial behavior that is examined in the main text. It remains to explain why the next order is not needed in either of the two regimes discussed in Section 3.2.3. Again, we consider the $\ln u^{-1}$ term as being of the order of unity (cf. Footnote 5).

For large grains, terms of $\mathcal{O}(u)$ need not be included: X is then of $\mathcal{O}(1)$ (shown in the main text), while $-\nu(\nu+1) = (R/\ell_D)^2 \gg 1$. Even the largest contribution of the second term thence has an additional factor of $-\nu(\nu+1)u \approx [r/(2\ell_D)]^2 \ll 1$ compared to the first summand.

The small-grain regime is more subtle, since ν and u may generally be of comparable order now. Expanding about $\nu \to 0-$, we get $\psi(1+\nu) = -\gamma + \mathcal{O}(\nu)$ so that $X = \ln u^{-1} - 1/\nu + \mathcal{O}(\nu)$. Hence $-\nu X = 1 - \nu \ln u^{-1} + \mathcal{O}(\nu^2)$ and $(\nu+1)X = -1/\nu + \ln u^{-1} - 1 + \mathcal{O}(\nu) = -1/\nu[1 - \nu(\ln u^{-1} - 1) + \mathcal{O}(\nu^2)]$. The $\mathcal{O}(u^0)$ term thus reads $1 + \nu(\ln u^{-1} - 1) + \mathcal{O}(\nu^2)$. Similarly evaluating the $\mathcal{O}(u^1)$ terms yields the pre-factor $\nu[1 - \nu + \mathcal{O}(\nu^2)]$: Since there is no contribution of $\mathcal{O}(\nu^0 u^1)$ present, this is but a higher order correction to the first summand. Note further that the direct impingement term u included in (3.13) is of precisely that order, and thence must have gone to cancel a corresponding term of the expression (3.12). Altogether we have shown that equation (3.14) of the main text contains all terms necessary to consistently perform the subsequent approximations.

A.3 Asymptotics of p_{disc}

The disc model of Krug [40] is described by the stationary diffusion equation

$$D\nabla^2 n + \tilde{f} - Wn = 0,$$

where n is the moving adatom concentration, $\tilde{f}$ the impingement flux per unit *area* and D and W diffusion constant and desorption rate, respectively. Boundary conditions are given in terms of the radial coordinate r by $\partial n/\partial r = 0$ at the outer reflecting boundary $r = L$, and $n(r = l) = 0$ at the absorbing target area boundary.[1] Due to rotational symmetry, ∇^2 simplifies to $\partial^2/\partial r^2 + r^{-1}\partial/\partial r$, and one finds the exact solution

$$n(r) = \frac{\tilde{f}}{W}\left[1 - \frac{I_0(kr)K_1(kL) + I_1(kL)K_0(kr)}{I_0(kl)K_1(kL) + I_1(kL)K_0(kl)}\right],$$

where $k := \sqrt{W/D} =: 1/\ell_D$. For this and the following, Appendix B.1 provides some mathematical reference.

The translation to the discrete model parameters is achieved by $D = al^2$ as before, and completed by the relation $S = g \cdot L^2/l^2$, also completely analogous to the spherical case, and the reasoning and values of the lattice factor g precisely apply as given in Appendix A.1. With this we have $kl = \sqrt{W/a}$ and $kL = \sqrt{W/a}L/l$. We assume again that $\sqrt{W/a} \ll 1$ and $S \gg 1$, or correspondingly that l is the smallest of the three lengths l, ℓ_D and L.

[1] Notation herein differs from that of the spherical model (Section 3.2 of the main text).

The encounter probability for this setting (including the direct impingement onto the target area) is then given by

$$\begin{aligned} p_{\mathrm{disc}} &= \frac{2\pi l D\, \partial n/\partial r|_{r=l}}{\tilde{f}\pi L^2} + \frac{l^2}{L^2} \\ &= 2\frac{al^3}{WL^2} k \frac{I_1(kL)K_1(kl) - I_1(kl)K_1(kL)}{I_0(kl)K_1(kL) + I_1(kL)K_0(kl)} + \frac{l^2}{L^2} \\ &= 2\sqrt{\frac{a}{W}}\frac{l^2}{L^2}\frac{I_1(kL)K_1(kl) - I_1(kl)K_1(kL)}{I_0(kl)K_1(kL) + I_1(kL)K_0(kl)} + \frac{l^2}{L^2}. \end{aligned}$$

For the asymptotics we assume l is the smallest length. In the numerator we note that $kl \ll 1$, $K_1(kl) \sim 1/(kl)$ decreases and $I_1(kl) \sim kl$ (much smaller) increases monotonically. Even if $kL \ll 1$ to compensate, we have $I_1(kL) \sim kL$ and $K_1(kL) \sim 1/(kL)$, such that the second term can always be neglected. In the denominator, leading-order terms of I_0 and K_0 suffice and canceling $I_1(kL)$ one obtains (treating logarithms of large quantities as being large as well)

$$p_{\mathrm{disc}} \approx \frac{4ga}{SW}\left[\ln(4a/W) + 2K_1/I_1\left(\sqrt{SW/ga}\right)\right]^{-1},$$

as given in Krug [40] apart from logarithmic differences and the assumption $g = 1$; the ensuing asymptotics for the two regimes are given *ibid.*

A more detailed analysis shows that, using $kl \ll 1$, one first has for $p = p_{\mathrm{disc}} - g/S$ (thus excluding the direct impingement)

$$p = \frac{2ga}{SW}\frac{I_1(kL)\left[1 + \frac{(kl)^2}{2}\left(\ln\frac{kl}{2} + \gamma - \frac{1}{2}\right) + \mathcal{O}(kl)^4\right] - K_1(kL)\left[\frac{(kl)^2}{2} + \mathcal{O}(kl)^4\right]}{K_1(kL)\left[1 + \left(\frac{kl}{2}\right)^2 + \mathcal{O}(kl)^4\right] + I_1(kL)\left[\ln\frac{2}{kl} - \gamma + \mathcal{O}(kl)^2\right]}.$$

In the small-disc regime, $kL \ll 1$ still, whence

$$p = \frac{2ga}{SW}\frac{\frac{kL}{2}\left[1 + \frac{1}{2}\left(\frac{kL}{2}\right)^2 - \frac{l^2}{L^2} + \mathcal{O}\left((kL)^4, (kl)^2, (kL)^2(l/L)^2\right)\right]}{\frac{1}{kL}\left[1 + \frac{(kL)^2}{2}\left(\ln\frac{kL}{2} + \gamma - \frac{1}{2}\right) + \frac{(kL)^2}{2}\left(\ln\frac{2}{kl} - \gamma\right) + \mathcal{O}\left((kL)^4, (kl)^2\right)\right]},$$

and upon translation one obtains

$$p_{\mathrm{disc}} \approx 1 - \frac{SW}{4ga}\left(\ln\frac{S}{g} - \frac{3}{2}\right),$$

neglecting terms with additional powers of S and / or W/a. Note that (as for the spherical case), the direct impingement contribution cancels a corresponding term in the mere flux expression. For the large-disc regime we have $kL \gg 1$, such that the (exponentially!) small K_1 terms can immediately be neglected. Canceling the I_1 factors we get

$$p_{\mathrm{disc}} = \frac{2ga}{SW}\frac{1}{\ln\frac{2}{kl} - \gamma}\left(1 + \mathcal{O}(kl)^2\right) \approx \frac{4ga}{SW}\frac{1}{\ln\frac{4a}{W} - 2\gamma},$$

and here, the direct impingement is irrelevant as it is smaller by the order W/a.

A.4 Derivation of p_{rw}

We closely follow and mimic the notation of Hughes [55] without citing individual known results. The techniques used here have been devised quite some time ago,

see, e.g., Montroll and Weiss [54] with the exact same formula as (A.5), and we basically put together all the necessary pieces in an appropriate form to treat a physically motivated problem.

We consider a finite homogeneous lattice with $S = \prod_{j=1}^{d} L_j$ sites in total and with periodic boundary conditions, or a d-dimensional torus with extensions L_j in the jth direction. (Although most references herein consider lattices with equal lengths in all directions, the generalization is usually straightforward.) We place two discrete-time random walkers, onto random sites of this lattice, independently and homogeneously distributed. They do not interact except when they meet. The walkers are assumed mortal (corresponding to desorption) with a constant and equal survival probability ξ per step. Our question is: "What is the probability that these two walkers meet before one of them dies?"

This problem can be mapped to that of a single walker which starts from a random site s_0, with the same survival probability per step, the question being with what probability it eventually reaches a certain fixed site s^* on the lattice without dying prematurely (all sites are labeled by a variable s whose structure is irrelevant right now).

As dying and moving of the walker are independent, one has

$$\begin{aligned}
&\Pr\{\text{Mortal walker reaches site } s^* \text{ for the first time on the } k\text{th step}\} \\
&= \Pr\{\text{Mortal walker has completed at least } k \text{ steps}\} \times \\
&\quad \times \Pr\{\text{Immortal walker reaches } s^* \text{ for the first time on the } k\text{th step}\} \\
&= \xi^k \cdot F_k(s^*|s_0),
\end{aligned}$$

where $F_k(s|s_0)$ is the probability (of an immortal random walker) of arriving at site s *for the first time* on the kth step, given that the walk started at site s_0. Note that we first adopt the convention that $F_0(s|s_0) = 0$, and therefore do not count a walker already starting at s_0. We do not care for the time when this first passage of s^* occurs, but are only interested in the quantity

$$F(s^*|s_0;\xi) := \sum_{k=0}^{\infty} \xi^k F_k(s^*|s_0),$$

which happens to be the *generating function* of $F_k(s^*|s_0)$. One can convince oneself that, by the definition of F_k as the *first*-passage probability, every encounter is counted precisely once, so $F(s^*|s_0;\xi)$ is the probability of a mortal random walker with survival rate ξ, starting from s_0, to reach s^* before dying.

For the remainder we only have to be concerned with immortal (usual) random walkers. Then for *any* random walk we have [e.g. 55, Eq. 3.27]

$$F(s|s_0;\xi) = \frac{P(s|s_0;\xi) - \delta_{s,s_0}}{P(s|s;\xi)}, \tag{A.2}$$

where $P(s|s_0;\xi)$ is the generating function of $P_k(s|s_0)$, the probability that the random walker, starting at site s_0, is at site s on the kth step (its propagator), with the convention that $P_0(s|s_0) = \delta_{s,s_0}$.

For the first-passage probability we now want to count a walker that starts at the target site as "reaching it for the first time" on the 0th step, not counting later returns. Denoting the corresponding probability by $\tilde{F}_k(s|s_0)$, it is related

to the original one by

$$\tilde{F}_k(s|s_0) = \delta_{s,s_0}\delta_{k,0} + (1-\delta_{s,s_0})F_k(s|s_0).$$

For the generating functions this means that

$$\tilde{F}(s|s_0;\xi) = \delta_{s,s_0} + (1-\delta_{s,s_0})F(s|s_0;\xi),$$

and inserting (A.2) yields

$$\tilde{F}(s|s_0;\xi) = \frac{P(s|s_0;\xi)}{P(s|s;\xi)}. \tag{A.3}$$

We can already write down a very general answer to our problem. We actually want the average $S^{-1}\sum_{s_0\in\Omega}\tilde{F}(s|s_0)$ of the revised first-passage probability (A.3) over all starting sites s_0 of our finite periodic lattice Ω, which gives us the encounter probability of the original two random walkers:

$$p_{\mathrm{rw}} = \frac{\sum_{s_0\in\Omega}P(s|s_0;\xi)}{SP(s|s;\xi)}. \tag{A.4}$$

The dependence on the target site s will vanish in passing to a homogeneous setting.

For further evaluation, we need to obtain $P(s|s_0;\xi)$. For the time being, let this denote the generating function of the random walk propagator on an *infinite* lattice. Moreover, as our walk is homogeneous or translationally invariant, we may use a single vector $\mathbf{l}$ pointing from the starting site s_0 to the final site s as our variable. Such 'lattice vectors' have d components, all of which take arbitrary integer values that can be thought of as components of a 'spatial vector' with respect to the d fundamental vectors of the lattice. It is well-known that [e.g. 55, section 3.3.1]

$$P(\mathbf{l};\xi) = \frac{1}{(2\pi)^d}\int\limits_{[-\pi,\pi]^d}\mathrm{d}^d k\,\frac{\exp(-i\mathbf{lk})}{1-\xi\lambda(\mathbf{k})},$$

with the integration domain the first Brillouin zone. $\lambda(\mathbf{k})$ is the *structure function* of the walk,

$$\lambda(\mathbf{k}) = \sum_{\mathbf{l}}\exp(i\mathbf{lk})q(\mathbf{l}),$$

the sum running over all lattice vectors, and $q(\mathbf{l})$ being the probability of a step translating by $\mathbf{l}$. Since $\sum_{\mathbf{l}}q(\mathbf{l})=1$, $|\lambda(\mathbf{k})|\leq 1$.

The transition to a truly finite periodic lattice is achieved by

$$P_n^*(\mathbf{l}) = \sum_{\mathbf{m}}P_n(\mathbf{l}+\mathbf{Lm}),$$

where we attach a star to the respective residence probabilities, and $\mathbf{L} = \mathrm{diag}(L_1,\ldots,L_d)$. The sum runs over all translation vectors of the (infinite) lattice, and this implies a completely analogous relation for the generating functions. Obviously, $P_n^*(\mathbf{l}+\mathbf{Lm}) = P_n^*(\mathbf{l})$ for an arbitrary $\mathbf{m}$ in the infinite lattice. From now on the vector $\mathbf{l}$ is understood to lie in the subset Ω of the infinite lattice that stands for the finite periodic lattice (we use the same symbol

for both the finite sets of sites and of associated translation vectors). It can be shown that consequently we have[2]

$$P^*(\mathbf{l};\xi) = \frac{1}{S}\sum_{\mathbf{m}\in\Omega}\frac{\exp[-2\pi i\mathbf{l}(\mathbf{L}^{-1}\mathbf{m})]}{1-\xi\lambda(2\pi\mathbf{L}^{-1}\mathbf{m})}. \tag{A.5}$$

The sum over the finite lattice Ω is explicitly a multiple sum over the components of the vector $\mathbf{m}$, each ranging between $m_j = 0 \dots L_j - 1$.

After we rewrite (A.4) for the homogeneous walk and substitute the appropriate starred probabilities, we obtain

$$p_{\mathrm{rw}} = \frac{\sum_{\mathbf{l}\in\Omega} P^*(\mathbf{l};\xi)}{SP^*(\mathbf{0};\xi)}. \tag{A.6}$$

The numerator of this expression is nothing but the ξ transform of $\sum_{\mathbf{l}\in\Omega} P_n^*(\mathbf{l})$, but this is unity due to conservation of the immortal walker, so that

$$\sum_{\mathbf{l}\in\Omega} P^*(\mathbf{l};\xi) = \frac{1}{1-\xi}.$$

Again using (A.5) for the denominator of (A.6) yields a general expression for the encounter probability on a homogeneous regular finite periodic lattice, namely (3.19) of the main text.

One often wants to consider a different convention that does *not* allow both walkers to start at the same site. To this end, one simply has to exclude the lattice distance $\mathbf{0}$ (talking about translationally invariant walks) from the average (A.4), the result of which is given in the main text as well. We note this is *not* equivalent to simply employing the original first-passage probability F instead of $\tilde{F}$, which would allow this situation, but not appreciate it as an encounter, and would simply lead to ξp_{rw} instead of p_{rw}.

A.5 Evaluation of One Sum

We restrict ourselves to a still fairly large class of walks, namely those with structure functions

$$\lambda(\mathbf{k}) = 2q_0[\cos k_1 + \cos k_2] + 2(q_1+q_2)\cos k_1 \cos k_2 + 2(q_2-q_1)\sin k_1 \sin k_2.$$

This corresponds to walks with transition probabilities q_0 to take a step into either lattice unit direction, and q_1 and q_2 the probabilities to step into direction $(1,1)$ or $(-1,-1)$, and $(1,-1)$ or $(-1,1)$, respectively, subject to the normalization $4q_0 + 2(q_1+q_2) = 1$. Clearly, this includes the aforementioned cases of the main text: The isotropic square lattice 'type (a)' is represented by $q_0 = 1/4$ and $q_1 = q_2 = 0$, the isotropic triangular lattice walk 'type (b)' has $q_0 = q_2 = 1/6$, $q_1 = 0$.

For this class of walks, one summation can be explicitly evaluated [42]. The result can be generalized to the $L_1 \neq L_2$ case by some easy accounting work and

[2] The underlying identity $\sum_{\mathbf{m}} \exp[-i(\mathbf{Lm})\mathbf{k}]/(2\pi)^d = \sum_{\mathbf{m}} \delta(\mathbf{k} - 2\pi\mathbf{L}^{-1}\mathbf{m})/(\prod_j L_j)$ works component-wise. In a way, this is a more general expression than that for the infinite lattice, which can be recovered by sending $L_j \to \infty$.

then reads

$$P^*(\mathbf{0};\xi) = \frac{1}{L_1}\sum_{m_1=0}^{L_1-1}[1-2q_0\xi\cos(2\pi m_1/L_1)]^{-1} \times [1-\rho_{m_1}^2]^{-1/2}\frac{1-x_{m_1}^{2L_2}}{1-2x_{m_1}^{L_2}\cos L_2\phi_{m_1}+x_{m_1}^{2L_2}}, \tag{A.7}$$

corresponding to Eq. B1 *ibid.* Here, $0 < x_{m_1} = [1-(1-\rho_{m_1}^2)^{1/2}]/\rho_{m_1} < 1$, and with

$$w_1 = \frac{2\xi[q_0+(q_1+q_2)\cos(2\pi m_1/L_1)]}{1-2\xi q_0\cos(2\pi m_1/L_1)}, \qquad w_2 = \frac{2\xi(q_1-q_2)\sin(2\pi m_1/L_1)}{1-2\xi q_0\cos(2\pi m_1/L_1)},$$

$0 < \rho_{m_1} < 1$ and ϕ_{m_1} are given by $w_1 + iw_2 = \rho_{m_1}\,\mathrm{e}^{i\phi_{m_1}}$. In general, this yields

$$\begin{aligned}\rho_{m_1}^2 &= w_1^2 + w_2^2 \\ &= \frac{(2\xi)^2\left[q_0^2+q_1^2+q_2^2+2q_1q_2\cos\frac{4\pi m_1}{L_1}+2q_0(q_1+q_2)\cos\frac{2\pi m_1}{L_1}\right]}{[1-2\xi q_0\cos(2\pi m_1/L_1)]^2},\end{aligned}$$

and

$$\tan\phi_{m_1} = \frac{(q_1-q_2)\sin\frac{2\pi m_1}{L_1}}{q_0+(q_1+q_2)\cos\frac{2\pi m_1}{L_1}}$$

(whenever well-defined).

For case (a) one obtains $\rho_{m_1} = [2/\xi - \cos(2\pi m_1/L_1)]^{-1}$ and $\phi_{m_1} = 0$, such that

$$P^*(\mathbf{0};\xi) = \frac{1}{L_1}\sum_{m_1=0}^{L_1-1}\frac{2/\xi}{\sqrt{\rho_{m_1}^{-2}-1}}\times\frac{1+x_{m_1}^{L_2}}{1-x_{m_1}^{L_2}}.$$

For type (b) one has

$$\rho_{m_1} = \frac{\sqrt{2}\sqrt{1+\cos(2\pi m_1/L_1)}}{3/\xi-\cos(2\pi m_1/L_1)} = \frac{2|\cos(\pi m_1/L_1)|}{3/\xi-\cos(2\pi m_1/L_1)}$$

and

$$\tan\phi_{m_1} = -\frac{\sin(2\pi m_1/L_1)}{[1+\cos(2\pi m_1/L_1)]} = -\tan(\pi m_1/L_1)$$

(whenever well-defined), which yields $\phi_{m_1} = -\pi(m_1/L_1 - \lfloor 2m_1/L_1\rfloor)$. The peculiar form of the angle is necessary to assure $|\phi_{m_1}| \le \pi/2$ corresponding to $w_1 \ge 0$, and while the chosen expression may result in a wrong sign of $\sin\phi_{m_1}$, only the unaffected $\cos(L_2\phi_{m_1})$ is used in the remainder. Hence we obtain

$$P^*(\mathbf{0};\xi) = \frac{1}{L_1}\sum_{m_1=0}^{L_1-1}\frac{3/\xi}{2|\cos(\pi m_1/L_1)|}\frac{1}{\sqrt{\rho_{m_1}^{-2}-1}}\frac{1-x_{m_1}^{2L_2}}{1-2x_{m_1}^{L_2}\cos(L_2\phi_{m_1})+x_{m_1}^{2L_2}},$$

and throughout, $x_{m_1}(\rho_{m_1})$ as given above.

The attentive reader may object that, in case (b), there is actually one term for which both $w_1 = 0 = w_2$ and thus ρ_{m_1} vanishes (see our valid explicit result for the latter), namely for even L_1 and $m_1 = L_1/2$. Hence, x_{m_1}, ϕ_{m_1} and the last expression for $P^*(\mathbf{0};\xi)$ are ill-defined then. From the definition of x_{m_1} one can see that for $\rho_{m_1} \to 0+$, $x_{m_1} \approx \rho_{m_1}/2 \to 0+$ as well, and the second line of (A.7)

(corresponding to the evaluated 'inner sum' in the derivation of Montroll [42]) converges to unity, which is the correct value of the original quantity. Our last expression complies with this via canceling singularities — we chose the simplest form of the result, which has to be slightly altered for numerical evaluation.

A.6 Large-Lattice Approximation

Sending $L_{1,2} \to \infty$ in $P^*(\mathbf{0};\xi)$ of (3.19) one obtains a double integral, which after two linear substitutions becomes

$$\frac{p_{\mathrm{rw}}^{-1}}{(1-\xi)S} = P(\mathbf{0};\xi) = \frac{1}{(2\pi)^2} \int\limits_{[0,2\pi]^2} \frac{\mathrm{d}k_1\,\mathrm{d}k_2}{1-\xi\lambda(\mathbf{k})}.$$

λ periodicity allows a shift of the patch of integration to the first Brillouin zone. As is shown in the Appendices of Hughes [55], in terms of the complete elliptic integral of the first kind,

$$K(k) = \int\limits_0^1 \frac{\mathrm{d}x}{\sqrt{(1-x^2)(1-k^2x^2)}}, \quad \text{with} \quad |k|<1,$$

one can derive that $P(\mathbf{0};\xi) = \frac{2}{\pi}K(\xi)$ for the square, and

$$P(\mathbf{0};\xi) = \frac{6}{\pi\xi\sqrt{(c_-+1)(c_+-1)}} \times K\left(\sqrt{\frac{2(c_+-c_-)}{(c_-+1)(c_+-1)}}\right)$$

for the triangular lattice, where $c_\pm = 3/\xi + 1 \pm \sqrt{3+6/\xi}$. One then employs the expansion of the elliptic integral for $k \lesssim 1$ (which is also the case for the triangular lattice if ξ itself is close to unity), viz.

$$K(k) = \sum_{n=0}^{\infty} \left[\frac{\left(\frac{1}{2}\right)_n}{n!}\right]^2 (1-k^2)^n \left[-(1/2)\ln(1-k^2) + \psi(n+1) - \psi(n+1/2)\right],$$

here $(z)_n = \Gamma(z+n)/\Gamma(z)$ is the Pochhammer symbol, equal to $z(z+1)\ldots(z+n-1)$ for positive integer n. Using these expressions in the exact results for $P(\mathbf{0};\xi)$, one obtains

$$P(\mathbf{0};\xi) = [1+\mathcal{O}(1-\xi)] \times \begin{cases} \frac{1}{\pi}\ln[8/(1-\xi)] & \text{square lattice,} \\ \frac{\sqrt{3}}{2\pi}\ln[12/(1-\xi)] & \text{triangular lattice.} \end{cases}$$

This yields the expressions for p_{rw} presented in the main text.

A.7 Generalization of the p_{rw} Asymptotics

We follow the derivation of Montroll [42], and refer to the corresponding equations *ibid.* for the interested reader. Our starting point is (B1) therein, corresponding to our (3.19), and proceeding as in Appendix A.5 to evaluate the sum over m_2 for certain structure functions, we consider the expression (A.7) for $P^*(\mathbf{0};\xi)$.

For $m_1 = 0$ ($w_2 = \phi_{m_1=0} = 0$) one has (B8) $\rho_{m_1} = 2\xi(q_0+q_1+q_2)/(1-2q_0\xi) = \xi(1-2q_0)/(1-2q_0\xi)$. Hence the corresponding term in P^* is (B9, corrected)

$$\frac{1}{L_1}\frac{1+x^{L_2}}{1-x^{L_2}}\left[(1-2q_0\xi)^2-\rho^2(1-2q_0\xi)^2\right]^{-1/2} = \dots$$
$$= \frac{1}{L_1}\frac{1+x^{L_2}}{1-x^{L_2}}\alpha^{-1}\left\{2\left[1-2q_0\right]\left[1-\beta^2(1-4q_0)\right]\right\}^{-1/2},$$

where $\alpha = (1-\xi)^{1/2}$ and $\beta = \alpha\left[2(1-2q_0)\right]^{-1/2}$. Here, $x_{m_1=0}$ yields the unchanged β expansion (B11),

$$x = 1-2\beta+2\beta^2+(4q_0-3)\beta^3+\mathcal{O}(\beta^4),$$

whence (B12) reads

$$x^{L_2} = 1-2L_2\beta+2L_2^2\beta^2-\frac{4}{3}L_2\beta^3\left(L_2^2-3q_0+\frac{5}{4}\right)+\mathcal{O}(\beta^4),$$

and the $m_1 = 0$ term (B13) finally becomes

$$\frac{1}{L_1L_2(1-\xi)}+\frac{L_2^2-1}{6L_1L_2(1-2q_0)}+\mathcal{O}(1-\xi)^{1/2}.$$

We define

$$r = \frac{2[(q_0+2q_1)(q_0+2q_2)]^{1/2}}{1-2q_0},$$
$$\eta = \frac{q_0(1-2q_0)}{(q_0+2q_1)(q_0+2q_2)}-1 = \frac{4q_0}{(1-2q_0)r^2}-1,$$

which take the values $r = 1 = \eta$ for the square lattice case (a), and $r = \sqrt{3}/2$, $\eta = 1/3$ for the triangular lattice case (b). For $m_1 \neq 0$ one obtains the unchanged relation (B14),

$$\left(1-2q_0\xi\cos(2\pi m_1/L_1)\right)\left(1-\rho_{m_1}^2\right)^{1/2}$$
$$= \left\{4\left[(q_0+2q_1)(q_0+2q_2)\right]^{1/2}\left[1+\eta\sin^2(\pi m_1/L_1)\right]^{1/2}\sin(\pi m_1/L_1)\right\}\times$$
$$\times\left(1+\mathcal{O}(1-\xi)\right).$$

Combining several results yields expression (B15),

$$P^*(\mathbf{0};\xi) = \frac{1}{L_1L_2(1-\xi)}+\frac{1}{2(1-2q_0)}\left\{\frac{L_2^2-1}{3L_1L_2}+\frac{S_1+S_2+S_3}{r}\right\}+\mathcal{O}(1-\xi)^{1/2},$$

where all contributions from $m_1 \neq 0$ occur in the split sums (B16, corrected)

$$S_1 = \frac{1}{L_1}\sum_{m_1=1}^{L_1-1}\frac{1}{\sin(\pi m_1/L_1)},$$
$$S_2 = \frac{1}{L_1}\sum_{m_1=1}^{L_1-1}\frac{\left[1+\eta\sin^2(\pi m_1/L_1)\right]^{-1/2}-1}{\sin(\pi m_1/L_1)},$$
$$S_3 = \frac{1}{L_1}\sum_{m_1=1}^{L_1-1}\frac{\left[1+\eta\sin^2(\pi m_1/L_1)\right]^{-1/2}}{\sin(\pi m_1/L_1)}\left\{\frac{2x_{m_1}^{L_2}(\cos L_2\phi_{m_1}-x_{m_1}^{L_2})}{1-2x_{m_1}^{L_2}\cos L_2\phi_{m_1}+x_{m_1}^{2L_2}}\right\}.$$

The evaluation of S_1 and S_2 is essentially a clever application of the Euler-MacLaurin summation formula, detailed in Montroll [42]. The results read (B22), (B24),

$$S_1 = \frac{2}{\pi}\left\{\ln L_1 + [\gamma + \ln(2/\pi)] - \frac{\pi^2}{72L_1^2} + \frac{7\pi^4}{43200L_1^2} + \dots\right\},$$
$$S_2 = -\frac{1}{\pi}\ln(1+\eta) + \frac{\eta\pi}{12L_1^2} + \frac{\eta\pi^3}{720L_1^2}(1+9\eta/2) + \dots.$$

So far, the assumptions on which all approximations have been based are: $1-\xi$ (and consequently, α and β) is so small that $\beta L_2 \sim L_2/\ell \ll 1$ (for the $x_{m_1}^{L_2}$ expansion to be valid), L_1 is large enough such that the Euler-MacLaurin formulas are applicable, and $L_1 L_2(1-\xi) \sim S/\ell^2 \ll 1$ for the overall expansion of P^* to make sense.

The most laborious part of the derivation is to find the S_3 asymptotics. First, we have (B26)

$$x_{m_1} = 1 - 2r\sin(\pi m_1/L_1) + 2r^2\sin^2(\pi m_1/L_1) - \frac{\sin^3(\pi m_1/L_1)}{r}\left[\frac{4q_0(1-2r^2)}{1-2q_0} + r^2(4r^2-1)\right].$$

From that one finds for small x (B28),

$$x_{m_1}^{L_2} \sim \mathrm{e}^{-2\pi r m_1(L_2/L_1)} \times \times\left[1 + \frac{1}{L_1^2}\frac{L_2}{L_1}\frac{4\pi^3 m_1^3}{3r}\frac{2r^2-1}{1-2q_0}(3q_0 - r^2 + 2r^2 q_0) + \mathcal{O}(L_1^{-4})\right].$$

This step holds provided L_2/L_1 is not too small (which will be an evident restriction looking at the result for S_3), and more importantly, that $L_2/L_1^3 \ll 1$ for the above equation to be a proper expansion.

One now specializes to the two cases detailed above. For (a) one finds that $\phi_{m_1} \equiv 0$, while in case (b), $\phi_{m_1} = -\pi(m_1/L_1 - \lfloor 2m_1/(L_1)\rfloor)$, the peculiar form of the angle necessary to assure $|\phi_{m_1}| \le \pi/2$ corresponding to $w_1 \ge 0$[3] . This yields

$$\frac{2x_{m_1}^{L_2}(\cos L_2\phi_{m_1} - x_{m_1}^{L_2})}{1 - 2x_{m_1}^{L_2}\cos L_2\phi_{m_1} + x_{m_1}^{2L_2}} = \frac{2x_{m_1}^{L_2}}{1 - x_{m_1}^{L_2}}$$

for case (a). While for $L_2 = L_1$ as in Montroll [42], lengths cancel in $\cos L_2\phi_{m_1}$, whence this becomes $(-1)^{\min(m_1, L_1-m_1)}$ for case (b), this no longer holds for arbitrary lengths, and we could not find a reasonably simple way around this complication. Thence we focus on the square lattice case (a) in the remainder of this Section, which consists in brute-force expansions in the inverse lattice lengths. Symmetry considerations for S_3 still apply, and it can be shown that x_{m_1} vanishes exponentially for fixed m_1/L_1 and $L_1 \to \infty$. Therefore the small-x

[3] This form with the 'conditional offset' by π also changes the sign of $\sin\phi_{m_1}$, which could be preserved by the choice $\phi_{m_1} = -\pi(1 - m_1/L_1)$ *whenever* $m_1 \ge L_1/2$. The difference is irrelevant in the following as it amounts to a conditional change of sign of ϕ_{m_1} and we only consider $\cos L_2\phi_{m_1}$.

expansion for $x_{m_1}^{L_2}$ can be used in the sum and one obtains first that

$$\frac{2x_{m_1}^{L_2}}{1-x_{m_1}^{L_2}} = 2\left(\frac{\mathrm{e}^{-2\pi(L_2/L_1)m_1}}{1-\mathrm{e}^{-2\pi(L_2/L_1)m_1}}\right) \times \left[1+\frac{L_2}{L_1}\frac{4\pi^3 m_1^3/3}{L_1^2(1-\mathrm{e}^{-2\pi(L_2/L_1)m_1})}\left(\frac{5q_0-1}{1-2q_0}\right)+\mathcal{O}(L_1^{-4})\right],$$

$$[\sin(\pi m_1/L_1)]^{-1}\left[1+\eta^2\sin^2(\pi m_1/L_1)\right]^{-1/2} = \frac{L_1}{\pi m_1}\left[1-\frac{\pi^2 m_1^2}{3L_1^2}+\mathcal{O}(L_1^{-4})\right],$$

and from that (B30),

$$\begin{aligned} S_3 &= \frac{4}{\pi}\sum_{m_1=0}^{\lfloor m/2\rfloor}\frac{1}{m_1}\left(\frac{\mathrm{e}^{-2\pi(L_2/L_1)m_1}}{1-\mathrm{e}^{-2\pi(L_2/L_1)m_1}}\right) \\ &\quad\times\left\{1-\frac{\pi^2 m_1^2}{3L_1^2}\left[1-\frac{4\pi(L_2/L_1)m_1}{1-\mathrm{e}^{-2\pi(L_2/L_1)m_1}}\left(\frac{5q_0-1}{1-2q_0}\right)\right]+\mathcal{O}(L_1^{-4})\right\} \\ &= \frac{4}{\pi}\left[\mathrm{e}^{-2\pi\mu}+\frac{3}{2}\mathrm{e}^{-4\pi\mu}+\frac{4}{3}\mathrm{e}^{-6\pi\mu}+\dots\right]-\frac{4\pi\,\mathrm{e}^{-2\pi\mu}}{3L_1^2} \\ &\quad\times\left\{\left[1+3\,\mathrm{e}^{-2\pi\mu}+4\,\mathrm{e}^{-4\pi\mu}+\dots\right]\right. \\ &\quad\left.-4\pi\frac{5q_0-1}{1-2q_0}\frac{L_2}{L_1}\left[1+6\,\mathrm{e}^{-2\pi\mu}+12\,\mathrm{e}^{-4\pi\mu}+\dots\right]\right\}+\mathcal{O}(L_1^{-4}), \end{aligned}$$

where denominators have been expanded as geometric series, and we use the aspect ratio $\mu = L_2/L_1$.

A.8 Asymptotics of the Truly One-Dimensional Result

The one-dimensional symmetric random walk with structure function $\lambda \equiv \cos$ on a lattice of $S \equiv L$ sites has

$$P^*(0;\xi) = \frac{1}{L}\sum_{m=0}^{L-1}\frac{1}{1-\xi\cos(2\pi m/L)}.$$

Using the identity of Appendix A in Montroll [42] (with $w_1 = \xi$, $w_2 = 0$, so that $\rho_{m_1} = \xi$ and $\phi_{m_1} \equiv 0$, and $x_{m_1} = [1-(1-\xi^2)^{1/2}]/\xi$) then yields

$$P^*(0;\xi) = \frac{1}{\sqrt{1-\xi^2}}\frac{1+x_{m_1}^L}{1-x_{m_1}^L} = \frac{1}{\sqrt{1-\xi^2}}\frac{\xi^L+[1-(1-\xi^2)^{1/2}]^L}{\xi^L-[1-(1-\xi^2)^{1/2}]^L}.$$

For comparison with the asymptotic two-dimensional behavior, we determine the asymptotics of the 1d-expression for a 'small' lattice, i.e., for $L \ll \ell = \sqrt{\xi/(1-\xi)}$. Let $\alpha = \sqrt{1-\xi^2} \ll 1$, which is *not* exactly the α of Montroll [42]. However, $L/\ell \approx L\sqrt{1-\xi} = L\sqrt{1-\sqrt{1-\alpha^2}} \approx L\alpha/\sqrt{2}$, and since this is to be $\ll 1$, we still have $L\alpha \ll 1$ in the following. With $1-\xi = 1-\sqrt{1-\alpha^2}$ and

$p_{\mathrm{rw}}^{-1} = L(1-\xi)P^*(0;\xi)$ we then obtain after minor manipulations

$$p_{\mathrm{rw,\,1d}}^{-1} = \frac{L[1-(1-\alpha^2)^{1/2}]}{\alpha} \frac{1+\left(\frac{1-\alpha}{1+\alpha}\right)^{L/2}}{1-\left(\frac{1-\alpha}{1+\alpha}\right)^{L/2}}. \tag{A.8}$$

Straight-forward expansion in $L\alpha \ll 1$ yields

$$p_{\mathrm{rw,\,1d}}^{-1} = 1 + \frac{(L\alpha)^2}{12} + \mathcal{O}(L\alpha)^3, \tag{A.9}$$

where we omitted all terms of relative order α. This is sufficient for the sought scaling limit $L \to \infty$, $\alpha \to 0$ while $L\alpha \simeq$ const., and it is additionally justified by a `Mathematica` check of our calculations, which shows that the only interesting α orders left out in the result are terms of $\mathcal{O}(\alpha^2)$ and thus much smaller than $(L\alpha)^2 = L^2(1-\xi^2) \approx 2(L/\ell)^2$.

Obviously, the most striking difference compared to the 2d case is the absence of logarithmic terms, which are a characteristic sign of the marginal dimension two.

Let us also give the large-lattice asymptotics, i.e., for the case $L\alpha \gg 1$. Starting from the still exact (A.8), we use $(1-\alpha)/(1+\alpha) = 1-2\alpha+\mathcal{O}(\alpha^2)$. For $L\alpha \gg 1$, this raised to the $L/2$ power is much smaller than unity, the correct expansion thus reading $\exp(-L\alpha)(1+\mathcal{O}(L\alpha^2))$, where we assume that terms of the latter relative order can be omitted as being much smaller than unity — this is an example that may be refined as necessary. One thus obtains the large-lattice result

$$p_{\mathrm{rw,\,1d}} = \frac{2}{L\alpha}\left(1-2\,\mathrm{e}^{-L\alpha}+\mathcal{O}(\mathrm{e}^{-L\alpha}\,L\alpha^2,\,\mathrm{e}^{-2L\alpha})\right) \approx \sqrt{2}\frac{\ell}{L}\left(1-2\,\mathrm{e}^{-\sqrt{2}L/\ell}\right).$$

Note that in this regime, the ratio of lengths no longer appears squared. In one dimension and for large lattices, the essential question for the encounter probability is whether the walker is deposited in the range ℓ from the target, and the probability for this to happen is the length ratio raised to the lattice dimension. The crucial difference to the two-dimensional case is that the 1d random walk explores a dense region instead of a sponge-like structure.

Lastly, corresponding asymptotics for the extremely distorted version of the originally two-dimensional random walk are obtained by a mere rescaling $\ell \to \ell/\sqrt{2}$, as can be seen from Section 3.4.3.

A.9 Analysis of Master Equation Results

A.9.1 Mean Particle Number

Obviously, $\langle N\rangle \le F/W$: There can be at most as many atoms on the grain as when there is no recombination, but only impingement and desorption. This can also be seen from (3.27): Inserting the series representation [51, 8.445] for I_ν gives (ν, $z \in \mathbb{R}_+$)

$$f_\nu(z) := \frac{I_\nu(z)}{I_{\nu-1}(z)} = \frac{\sum_{k=0}^{\infty} \frac{(z/2)}{\nu+k}\frac{(z/2)^{2k}}{k!\Gamma(\nu+k)}}{\sum_{k'=0}^{\infty}\frac{(z/2)^{2k'}}{k'!\Gamma(\nu+k')}} < \frac{z}{2\nu}.$$

Identifying $z = 2\sqrt{2F/A}$ and $\nu = W/A$ in (3.27) shows $\langle N\rangle < (z/4)z/(2\nu) = z^2/(8\nu) = F/W$. This limit is realized by a vanishing meeting rate $A \to 0$, making ν and z approach ∞ simultaneously. ν then dominates in $1/(\nu + k)$, so that $f_\nu(z)$ and $\langle N\rangle$ approach their maximum. (While not rigorously proved, this result is obvious by common sense.)

Hence $F/W \ll 1$ is a *sufficient* condition for $\langle N\rangle \ll 1$. The converse cannot simply be based on physical intuition: Even when $F/W \ll 1$ is not satisfied, diffusion and recombination, i.e., an A large enough, could strongly deplete the grain to still achieve $\langle N\rangle \ll 1$. However, while a large meeting rate heavily decreases $\langle N\rangle$ compared to F/W, there is a lower bound (for fixed F/W) completely independent of W/A: We start with z and ν as above, and set $c = 2F/W$, so that $z/2 = \sqrt{c\nu}$. Then

$$\langle N\rangle = \frac{c\nu}{2}\frac{\sum_{k=0}^{\infty}\frac{(c\nu)^k}{k!\Gamma(\nu+k+1)}}{\sum_{k'=0}^{\infty}\frac{(c\nu)^{k'}}{k'!\Gamma(\nu+k')}} = \frac{c\nu}{2}\frac{\sum_{k=0}^{\infty}\frac{(c\nu)^k}{k!\Gamma(\nu+k+1)}}{\frac{1}{\Gamma(\nu)}+\sum_{k'=0}^{\infty}\frac{(c\nu)^{k'+1}}{(k'+1)!\Gamma(\nu+k'+1)}},$$

where we split off the first term in the denominator and performed an index shift. The first estimate uses $c\nu/(k'+1) \le c\nu$ in the denominator sum, whence

$$\begin{aligned}\langle N\rangle &\ge \frac{c\nu}{2}\frac{\sum_{k=0}^{\infty}\frac{(c\nu)^k}{k!\Gamma(\nu+k+1)}}{\frac{1}{\Gamma(\nu)}+c\nu\sum_{k'=0}^{\infty}\frac{(c\nu)^{k'}}{k'!\Gamma(\nu+k'+1)}}\\ &= \frac{c}{2}\left[\left(\nu\Gamma(\nu)\sum_{k=0}^{\infty}\frac{(c\nu)^k}{k!\Gamma(\nu+k+1)}\right)^{-1}+c\right]^{-1}.\end{aligned}$$

The second estimate is to neglect all but the zeroth term of the sum to get rid of any ν-dependence. This means that $\nu\Gamma(\nu)\sum_{k=0}^{\infty}\cdots \ge \nu\Gamma(\nu)/\Gamma(\nu+1) = 1$. So we finally have

$$\langle N\rangle \ge \frac{c}{2}\frac{1}{1+c} = \frac{F}{W}\frac{1}{1+2F/W} = \frac{1}{2+W/F}.$$

Both estimates involved become equalities for $\nu = 0$ (canceling terms in the second sum properly is subtle and crucial): The bound is the limit as $W/A \to 0$.

The mean particle number thus obeys

$$\frac{1}{2+W/F} \le \langle N\rangle \le \frac{F}{W},$$

where (for fixed F/W) the lower bound is realized by a diverging meeting rate, and the upper bound for vanishing A, with $\langle N\rangle$ growing monotonically (as a function of W/A, F/W fixed) in between. (Proof omitted, since, e.g., by considering the situation of fixed F *and* W, this result is physically obvious.) Keeping W/A fixed and increasing F/W, $\langle N\rangle$ grows monotonically as well (as becomes clear from a similar reasoning).

The maximum relative error of approximating $\langle N\rangle$ by one of its bounds is given by

$$\frac{\Delta\langle N\rangle}{\langle N\rangle} \le \frac{\frac{F}{W}-\frac{1}{2+W/F}}{\frac{1}{2+W/F}} = \frac{2F}{W}.$$

This means that for small flux $F/W \ll 1$, the approximation $\langle N\rangle \approx F/W$ only bears a small (relative) error. Phrasing this differently, a large A can *only* be effective (in achieving $\langle N\rangle \ll F/W$) for F/W not much smaller than 1, i.e., when there would be a considerable number of atoms on the grain in the absence of diffusion and recombination; this is rather intuitive. If $\langle N\rangle \ll 1$, the lower bound also shows that inevitably $F/W \ll 1$, implying $\langle N\rangle \approx F/W$ again. We have thus established that $\langle N\rangle \ll 1$ if and only if $F/W \ll 1$, and then the approximation $\langle N\rangle \approx F/W$ is valid with small relative error. (Of course, the converse of the last implication does not hold, since without diffusion, we *always* have $\langle N\rangle = F/W$ independent of the value of F/W.)

A.9.2 Recombination Efficiency

We start from a simple connection between particle number and efficiency: Gradshteyn and Ryzhik [51], 8.486 1. states $zI_{\nu-1}(z) - zI_{\nu+1}(z) = 2\nu I_\nu(z)$. With the above identifications in (3.27), (3.28) we easily read off $(2\nu/z = \sqrt{F/(2A)}/(F/W)$, and again, $\eta \equiv \eta_{\mathrm{ME}}$ in this Section)

$$\eta = 1 - \frac{\langle N\rangle}{F/W},$$

which has a clear interpretation: The fraction of atoms participating in recombination events is exactly the relative deficit of $\langle N\rangle$ to the 'diffusionless' particle number F/W. Moreover, one can see that $\langle N\rangle \ll F/W$ always goes hand in hand with $\eta \to 1$, efficient recombination, whereas $\langle N\rangle \lessapprox F/W$ yields $\eta \ll 1$. From the above, the latter case of small efficiency is also entailed by a small impingement flux $F/W \ll 1$ or, equivalently, by a small mean particle number $\langle N\rangle \ll 1$.

Using the bounds obtained for $\langle N\rangle$ yields $0 \le \eta \le 1/(1 + W/(2F))$, with η as a function of W/A for fixed F/W monotonically decreasing in between. The lower bound *can* only be useless, because (owed to the derivation) it does not depend on W/A, and for a vanishing meeting rate obviously $\eta = 0$. The upper bound of the efficiency however is realized for infinitely fast diffusion.

We now derive a lower bound on η that still depends on W/A, and an analogous upper bound will also prove useful. In analogy to the $\langle N\rangle$ expression we have

$$\eta = \frac{I_{\nu+1}(z)}{I_{\nu-1}(z)} = \frac{\sum_{k=0}^{\infty} \frac{(z/2)^2}{(\nu+k)(\nu+k+1)} \frac{(z/2)^{2k}}{k!\Gamma(\nu+k)}}{\sum_{k'=0}^{\infty} \frac{(z/2)^{2k'}}{k'!\Gamma(\nu+k')}} < \frac{(z/2)^2}{\nu(\nu+1)},$$

hence $\eta < (2F/W)/(W/A + 1)$. A lower bound will also be obtained along the same line of thought as before: Now separating the first *two* terms of the nominator sum (to reach the same expression for both sums) and shifting its index results in

$$\eta = c\nu \frac{\sum_{k=0}^{\infty} \frac{(c\nu)^k}{k!\Gamma(\nu+k+2)}}{\frac{1}{\Gamma(\nu)} + \frac{c\nu}{\Gamma(\nu+1)} + \sum_{k'=0}^{\infty} \frac{(c\nu)^{k'+2}}{(k'+2)!\Gamma(\nu+k'+2)}}.$$

Estimating $(c\nu)^2/[(k'+1)(k'+2)] \le (c\nu)^2/2$ and canceling the sums and ν yields

$$\eta \ge c\left[\left(\nu\Gamma(\nu)\sum(\dots)\right)^{-1} + c\left(\Gamma(\nu+1)\sum(\dots)\right)^{-1} + \frac{c^2\nu}{2}\right]^{-1},$$

where $\sum(\dots)$ is the original denominator expression of which we retain the zeroth term $1/\Gamma(\nu+2)$ only. Both inner parentheses then equal $\geq 1/(\nu+1)$, so that

$$\begin{aligned}\eta &\geq \frac{c}{(\nu+1)(1+c)+c^2\nu/2} > \frac{c}{\nu+1}\frac{1}{1+c+c^2/2} \\ &= \frac{2F}{W}\frac{1}{W/A+1}\frac{1}{1+2F/W+(2F/W)^2/2}.\end{aligned}$$

The last estimate enables us to cancel the W/A dependence when evaluating below the relative error of the approximation. Note that one could again obtain an upper bound independent of W/A from these considerations, namely $\eta < 2F/W$, which is larger than the one derived from the bound on $\langle N\rangle$.

Together, the restrictions on η read

$$\frac{2F}{W}\frac{1}{W/A+1}\frac{1}{1+2F/W+(2F/W)^2/2} \leq \eta \leq \frac{2F}{W}\frac{1}{W/A+1}.$$

The maximum relative error of approximating η by these bounds is given by

$$\frac{\Delta\eta}{\eta} \leq \frac{2F}{W}+\frac{1}{2}\left(\frac{2F}{W}\right)^2,$$

which implies that $\langle N\rangle \ll 1$ (whence $\langle N\rangle \lessapprox F/W \ll 1$) renders $\eta \lessapprox \frac{2F/W}{W/A+1} \ll 1$ valid.

A.10 Island Edge: One-Particle Eigen-Problem

We briefly review the standard method to solve an equation like (6.3) [156]. This master equation is an L-dimensional system of linear homogeneous ordinary first-order differential equations. Written in matrix form it reads $\mathrm{d}\mathbf{p}/\mathrm{d}t = \mathbf{M}\mathbf{p}$ for the 'vector' $\mathbf{p}(t)$ with components $p_n(t)$, and $\mathbf{M}$ the real square matrix

$$\mathbf{M} = \begin{pmatrix}
-\Gamma_{\mathrm{A}\uparrow} & \Gamma_{\mathrm{A}} & & & & & & & & \Gamma_{\mathrm{BA}} \\
\Gamma_{\mathrm{A}} & -2\Gamma_{\mathrm{A}} & \Gamma_{\mathrm{A}} & & & & & & & \\
& \ddots & \ddots & \ddots & & & & & & \\
& & \Gamma_{\mathrm{A}} & -2\Gamma_{\mathrm{A}} & \Gamma_{\mathrm{A}} & & & & & \\
& & & \Gamma_{\mathrm{A}} & -\Gamma_{\mathrm{A}\uparrow} & \Gamma_{\mathrm{BA}} & & & & \\
& & & & \Gamma_{\mathrm{AB}} & -\Gamma_{\mathrm{B}\uparrow} & \Gamma_{\mathrm{B}} & & & \\
& & & & & \Gamma_{\mathrm{B}} & -2\Gamma_{\mathrm{B}} & \Gamma_{\mathrm{B}} & & \\
& & & & & & \ddots & \ddots & \ddots & \\
& & & & & & & \Gamma_{\mathrm{B}} & -2\Gamma_{\mathrm{B}} & \Gamma_{\mathrm{B}} \\
\Gamma_{\mathrm{AB}} & & & & & & & & \Gamma_{\mathrm{B}} & -\Gamma_{\mathrm{B}\uparrow}
\end{pmatrix}$$

where $\Gamma_{\mathrm{A}\uparrow} = \Gamma_{\mathrm{AB}} + \Gamma_{\mathrm{A}}$ and $\Gamma_{\mathrm{B}\uparrow} = \Gamma_{\mathrm{BA}} + \Gamma_{\mathrm{B}}$. Each column adds up to zero, since what is at one site has to go *some*where for probability to be conserved. The exponential ansatz $p_n(t) = \exp(-\lambda t)\psi_n$ leads to an eigenvalue problem for the 'vector' $\boldsymbol{\psi}$, namely $\mathbf{M}\boldsymbol{\psi} = -\lambda\boldsymbol{\psi}$. If the matrix $\mathbf{M}$ can be diagonalized, this problem can be solved to give L linearly independent eigenvectors (for possibly degenerate $\leq L$ different eigenvalues), hence a basis of solution space. We will now show that this is the case.

$\mathbf{M}$ is *not* symmetric due to the situation at the corners, hence it is not obvious it can be diagonalized. It admits a unique and positive stationary state (corresponding to a non-degenerate eigenvalue $\lambda = 0$), since $\mathbf{M}$ cannot be decomposed into dynamically disconnected parts (each two sites are connected by a chain of non-zero transition probabilities). One can easily check that

$$p_n^{\mathrm{S}} = \begin{cases} \left[\ell_{\mathrm{A}} + \ell_{\mathrm{B}} \frac{\Gamma_{\mathrm{AB}}}{\Gamma_{\mathrm{BA}}}\right]^{-1} & (n = 1 \dots \ell_{\mathrm{A}}), \\ \left[\ell_{\mathrm{A}} \frac{\Gamma_{\mathrm{BA}}}{\Gamma_{\mathrm{AB}}} + \ell_{\mathrm{B}}\right]^{-1} = \frac{\Gamma_{\mathrm{AB}}}{\Gamma_{\mathrm{BA}}}\, p_n^{\mathrm{S}}\big|_{\mathrm{A}} & (n = \ell_{\mathrm{A}} + 1 \dots L = \ell_{\mathrm{A}} + \ell_{\mathrm{B}}), \end{cases}$$

is in the kernel of $\mathbf{M}$. Because of (6.2), this obeys the Boltzmann distribution (which in turn suffices, together with normalization, to derive it).

We prove by symmetrization that $\mathbf{M}$ can be diagonalized: Treating p_n^{S} as a non-singular diagonal matrix, powers work component-wise. Consider $\tilde{\mathbf{M}} = \left(\mathbf{p}^{\mathrm{S}}\right)^{-1/2} \mathbf{M} \left(\mathbf{p}^{\mathrm{S}}\right)^{1/2}$ with elements $\tilde{M}_{mn} = [p_m^{\mathrm{S}}]^{-1/2} M_{mn} [p_n^{\mathrm{S}}]^{1/2}$, i.e., a mere change of basis. Suppose this can be diagonalized, then for an eigenvector $\tilde{\boldsymbol{\psi}}$ with eigenvalue $-\tilde{\lambda}$, $\tilde{\mathbf{M}}\tilde{\boldsymbol{\psi}} = -\tilde{\lambda}\tilde{\boldsymbol{\psi}}$ implies $\sum_n M_{mn} [p_n^{\mathrm{S}}]^{1/2} \tilde{\psi}_n = -\tilde{\lambda} [p_m^{\mathrm{S}}]^{1/2} \tilde{\psi}_m$, hence $\boldsymbol{\psi} = \left(\mathbf{p}^{\mathrm{S}}\right)^{1/2} \tilde{\boldsymbol{\psi}}$ is an eigenvector of $\mathbf{M}$ with the same eigenvalue. Starting with the existing basis of eigenvectors of $\tilde{\mathbf{M}}$ the newly constructed eigenvectors is again a basis (by the properties of a similarity transformation). Therefore, $\mathbf{M}$ can be diagonalized as well choosing the eigenvectors $\boldsymbol{\psi}$ as our basis.

Since the stationary solution only takes one of two different values depending on the zone, the 'diagonal blocks' in $\mathbf{M}$ (transitions inside one zone) remain unchanged. The almost empty other two blocks acquire additional factors $(p^{\mathrm{S}}\big|_{\mathrm{A}} \,/\, p^{\mathrm{S}}\big|_{\mathrm{B}})^{\pm 1/2} = (\Gamma_{\mathrm{BA}}/\Gamma_{\mathrm{AB}})^{\pm 1/2}$, changing their every entry to $\sqrt{\Gamma_{\mathrm{AB}}\Gamma_{\mathrm{BA}}}$: $\tilde{\mathbf{M}}$ *is* symmetric, and real symmetric matrices are (even orthonormally) diagonalizable. From the above lemma, $\mathbf{M}$ can then be diagonalized as well.[4]

A.10.1 Finding the 'Normal Modes'

In principle the eigenvalues can be obtained by solving $\det(\mathbf{M} + \lambda \mathbb{1}_L) = 0$, but although the matrix is only sparsely populated, we failed to find a sufficiently simple recursion relation to calculate this determinant. It would finally lead to a polynomial of high degree in λ, which we will find in a different way.

For given λ, we first find the general solution of the eigen-equation *restricted to one zone*, i.e., without boundary conditions. The equation can be written as

$$\left(2 - \frac{\lambda}{\Gamma_{\mathrm{A}}}\right) \psi_n = \psi_{n-1} + \psi_{n+1} \qquad \text{for} \quad n = 2 \dots \ell_{\mathrm{A}} - 1, \tag{A.10}$$

in zone A, and the standard ansatz to solve this difference equation with constant coefficients is $\psi_n \propto z^n$ with $z \in \mathbb{C}$ (any complex solution ψ_n conveys two real solutions by its real and imaginary part). The resulting equation

$$2 - \frac{\lambda}{\Gamma_{\mathrm{A}}} = z + \frac{1}{z} \tag{A.11}$$

[4] We only used positivity of the stationary distribution in the above reasoning, but it can be shown [156] that this specific choice proves diagonalizability of $\mathbf{M}$ whenever the physical system obeys 'detailed balance', i.e., for the stationary solution and *each* pair of states m and n, transitions balance: $M_{m,n} p_n^{\mathrm{S}} = M_{n,m} p_m^{\mathrm{S}}$. In our case the solution makes this explicit, it is intuitive from a microscopic point of view, and lastly it generally applies to a broad class of systems the present one belongs to.

has two solutions $z_{1,2}$ satisfying $z_1 z_2 = 1$. By (A.11), their sum is real, so that either, $z_1 \in \mathbb{R}$ with modulus $|z_1| > 1$ and its inverse z_2, or $z_1 = \mathrm{e}^{iq}$, $z_2 = \mathrm{e}^{-iq}$ with a real angle $0 \leq q \leq \pi$ (including the case $z_1 = z_2 = -1$, and $z_1 = z_2 = 1$ which corresponds to the stationary mode $\lambda = 0$). Detailed balance also implies that the non-zero eigenvalues of M are negative, $\lambda \geq 0$; this is to be expected as our system should always approach the stationary solution. Therefore the left hand side of (A.11) is smaller than 2, and real solutions $z > 1$ can be excluded. For the 'oscillating'[5] $z \in S^1$ solutions, we have $\lambda = 2\Gamma_\mathrm{A}(1 - \cos q) = 4\Gamma_\mathrm{A} \sin^2(q/2) \in [0, 4\Gamma_\mathrm{A}]$, while for the remaining real solutions, $\lambda > 4\Gamma_\mathrm{A}$. Figure A.1 visualizes these possibilities and the correspondence to the eigenvalue $-\lambda$. In either case, the (still complex) general solution reads $\psi_n = C^+_\mathrm{A} z^n_\mathrm{A} + C^-_\mathrm{A} z^{-n}_\mathrm{A}$ with complex coefficients and z_A one of the above solutions. Note that, to obey (A.10) for all appropriate values of n, this form must hold for all n *occurring* in the equation, i.e., for the whole zone $n = 1 \ldots \ell_\mathrm{A}$.

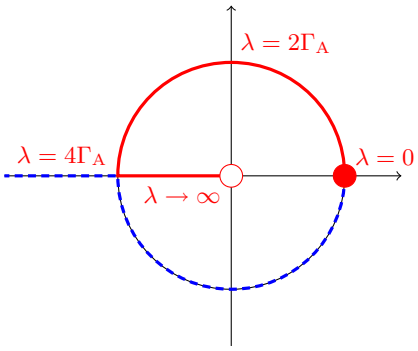

Figure A.1: Structure of possible solutions z; one drawn red, the inverse drawn blue (and dashed), with some corresponding values λ indicated.

The exact same procedure can be carried out for zone B. Since we examine a restriction of the *same* eigenfunction, λ is already fixed. But now Γ_B appears in the place of Γ_A, so the solutions z_B of (A.11) and the angle q_B are first taken independent, and $C^\pm_\mathrm{B}$ are independent coefficients anyway. Therefore an eigenfunction for the eigenvalue $-\lambda$ is of the following form (better, the real part of)

$$\psi_n = \begin{cases} C^+_\mathrm{A} z^n_\mathrm{A} + C^-_\mathrm{A} z^{-n}_\mathrm{A} & \text{for } n \in \mathrm{A}\,, \\ C^+_\mathrm{B} z^n_\mathrm{B} + C^-_\mathrm{B} z^{-n}_\mathrm{B} & \text{for } n \in \mathrm{B}\,, \end{cases} \tag{A.12}$$

where z_A and z_B are given uniquely by $\lambda > 0$: Fixing the z-ranges (without any loss of generality), we either have $z_\mathrm{A} > -1$ for $\lambda > 4\Gamma_\mathrm{A}$, while $z_\mathrm{A} = \mathrm{e}^{iq_\mathrm{A}}$ $(0 \leq q_\mathrm{A} \leq \pi)$ corresponds to $\lambda = 4\Gamma_\mathrm{A} \sin^2(q_\mathrm{A}/2) \leq 4\Gamma_\mathrm{A}$ (and analogously for zone B). The general form of the latter solutions (per zone), i.e., the sinusoidal function of the argument qn, can easily be guessed as it was in Castellano and Politi [71].

A.10.2 Matching Conditions

We stress that in our context, periodicity does *not* impose typical restrictions on the wave vectors q_A and q_B when $z = \mathrm{e}^{iq}$, as the solution has an expression that differs between the two zones.

The two parts of (A.12) have to match using the equations for the corner sites. Note that this possibly glues together solutions of different type (oscillatory vs. real z) in the two regions. The yet unused equations of (6.3) for the corner

[5] We will stick to that term although it might be a misnomer: $z < -1$-solutions also oscillate in a way.

sites ($n = L,\ 1,\ \ell_\mathrm{A},\ \ell_\mathrm{A}+1$) read

$$\begin{aligned}
(\Gamma_{\mathrm{B}\uparrow} - \lambda)\psi_L &= \Gamma_\mathrm{B}\psi_{L-1} + \Gamma_\mathrm{AB}\psi_1 \\
(\Gamma_{\mathrm{A}\uparrow} - \lambda)\psi_1 &= \Gamma_\mathrm{BA}\psi_L + \Gamma_\mathrm{A}\psi_2 \\
(\Gamma_{\mathrm{A}\uparrow} - \lambda)\psi_{\ell_\mathrm{A}} &= \Gamma_\mathrm{A}\psi_{\ell_\mathrm{A}-1} + \Gamma_\mathrm{BA}\psi_{\ell_\mathrm{A}+1} \\
(\Gamma_{\mathrm{B}\uparrow} - \lambda)\psi_{\ell_\mathrm{A}+1} &= \Gamma_\mathrm{AB}\psi_{\ell_\mathrm{A}} + \Gamma_\mathrm{B}\psi_{\ell_\mathrm{A}+2},
\end{aligned}$$

and inserting (A.12) yields

$$\begin{aligned}
&(\Gamma_{\mathrm{B}\uparrow} - \lambda)(C_\mathrm{B}^+ z_\mathrm{B}^L + C_\mathrm{B}^- z_\mathrm{B}^{-L}) \\
&\qquad = \Gamma_\mathrm{B}(C_\mathrm{B}^+ z_\mathrm{B}^{L-1} + C_\mathrm{B}^- z_\mathrm{B}^{-L+1}) + \Gamma_\mathrm{AB}(C_\mathrm{A}^+ z_\mathrm{A} + C_\mathrm{A}^- z_\mathrm{A}^{-1}) \\
&(\Gamma_{\mathrm{A}\uparrow} - \lambda)(C_\mathrm{A}^+ z_\mathrm{A} + C_\mathrm{A}^- z_\mathrm{A}^{-1}) = \Gamma_\mathrm{BA}(C_\mathrm{B}^+ z_\mathrm{B}^L + C_\mathrm{B}^- z_\mathrm{B}^{-L}) + \Gamma_\mathrm{A}(C_\mathrm{A}^+ z_\mathrm{A}^2 + C_\mathrm{A}^- z_\mathrm{A}^{-2}) \\
&(\Gamma_{\mathrm{A}\uparrow} - \lambda)(C_\mathrm{A}^+ z_\mathrm{A}^{\ell_\mathrm{A}} + C_\mathrm{A}^- z_\mathrm{A}^{-\ell_\mathrm{A}}) \\
&\qquad = \Gamma_\mathrm{A}(C_\mathrm{A}^+ z_\mathrm{A}^{\ell_\mathrm{A}-1} + C_\mathrm{A}^- z_\mathrm{A}^{-\ell_\mathrm{A}+1}) + \Gamma_\mathrm{BA}(C_\mathrm{B}^+ z_\mathrm{B}^{\ell_\mathrm{A}+1} + C_\mathrm{B}^- z_\mathrm{B}^{-\ell_\mathrm{A}-1}) \\
&(\Gamma_{\mathrm{B}\uparrow} - \lambda)(C_\mathrm{B}^+ z_\mathrm{B}^{\ell_\mathrm{A}+1} + C_\mathrm{B}^- z_\mathrm{B}^{-\ell_\mathrm{A}-1}) \\
&\qquad = \Gamma_\mathrm{AB}(C_\mathrm{A}^+ z_\mathrm{A}^{\ell_\mathrm{A}} + C_\mathrm{A}^- z_\mathrm{A}^{-\ell_\mathrm{A}}) + \Gamma_\mathrm{B}(C_\mathrm{B}^+ z_\mathrm{B}^{\ell_\mathrm{A}+2} + C_\mathrm{B}^- z_\mathrm{B}^{-\ell_\mathrm{A}-2}).
\end{aligned} \tag{A.13}$$

We use $\lambda + \Gamma_\mathrm{A} z_\mathrm{A}^{\pm 1} - \Gamma_{\mathrm{A}\uparrow} = \Gamma_\mathrm{A}(1 - z_\mathrm{A}^{\mp 1}) - \Gamma_\mathrm{AB}$ (and the $\mathrm{A} \leftrightarrow \mathrm{B}$ equivalent) and $L = \ell_\mathrm{A} + \ell_\mathrm{B}$, and then absorb Γ_A in $C_\mathrm{A}^\pm$ and $\Gamma_\mathrm{B} z_\mathrm{B}^{\pm\ell_\mathrm{A}}$ in $C_\mathrm{B}^\pm$ (all without changing the notation). Thus we obtain the simple matrix (6.4) of this system (with rows re-arranged), shown in the main text.

A.10.3 The Most Interesting Normal Modes

Typically, one can learn about the long-time asymptotic behavior of a stochastic system more easily than about its full time-dependent behavior. Here this means to examine the small eigenvalue modes: λ is the decay rate of a mode, hence modes with smallest λ are most stable and dominate the late-time behavior of the approach to the stationary distribution (corresponding to $\lambda = 0$). Smallness is defined by the diffusion rates; we assume hopping rates inside each zone to clearly differ from their 'corner-crossing' values, though not by much more than an order of magnitude, in which case we end up in limiting regimes corresponding to much simpler models.

Determinant in the oscillatory regime. Clearly, the most stable normal modes will be of the 'oscillating' type (Section A.10.1) on the whole edge, and both wave numbers $q_\mathrm{A},\ q_\mathrm{B} \ll 1$. The latter will additionally be of the same order of magnitude, as this should also hold for the rates $\Gamma_\mathrm{A},\ \Gamma_\mathrm{B}$. To obtain the spectrum of small eigenvalues, we use the known form of $z_\mathrm{A},\ z_\mathrm{B}$ in (A.13), and can pass to the real part of ψ_n, thence substituting $C^+ z^n + C^- z^{-n}$ with $\tilde{C}^+ \cos(qn) + \tilde{C}^- \sin(qn)$ with newly defined real coefficients $\tilde{C}^+ = \mathrm{Re}(C^+ + C^-)$ and $\tilde{C}^- = \mathrm{Im}(C^- - C^+)$. Using computer algebra again, and after re-ordering

terms in a lengthy expression to make the symmetry explicit, we obtain

$$\begin{aligned}\frac{\det}{2\Gamma_\mathrm{A}^2\Gamma_\mathrm{B}^2} &= (2-\gamma_\mathrm{B}-\gamma_\mathrm{A})\Big[\gamma_\mathrm{B}\sin(\ell_\mathrm{A}q_\mathrm{A})\cos(\ell_\mathrm{B}q_\mathrm{B})\sin q_\mathrm{B}[1-\cos q_\mathrm{A}]\\ &\qquad +\gamma_\mathrm{A}\sin(\ell_\mathrm{B}q_\mathrm{B})\cos(\ell_\mathrm{A}q_\mathrm{A})\sin q_\mathrm{A}[1-\cos q_\mathrm{B}]\Big]\\ &\quad +\gamma_\mathrm{A}\gamma_\mathrm{B}\sin q_\mathrm{A}\sin q_\mathrm{B}\,[1-\cos(\ell_\mathrm{A}q_\mathrm{A})\cos(\ell_\mathrm{B}q_\mathrm{B})]\\ &\quad +\sin(\ell_\mathrm{A}q_\mathrm{A})\sin(\ell_\mathrm{B}q_\mathrm{B})\big\{[1-\cos q_\mathrm{A}]\,\gamma_\mathrm{B}^2+[1-\cos q_\mathrm{B}]\,\gamma_\mathrm{A}^2\\ &\qquad -[1-\cos q_\mathrm{A}]\,[1-\cos q_\mathrm{B}]\times\\ &\qquad\quad \times\big[[2(1-\gamma_\mathrm{A})(1-\gamma_\mathrm{B})-\gamma_\mathrm{A}\gamma_\mathrm{B}]+\gamma_\mathrm{A}^2+\gamma_B^2\big]\big\}.\end{aligned}$$

The arguments of trigonometric functions are reduced to q_A, q_B, $\ell_\mathrm{A}q_\mathrm{A}$, and $\ell_\mathrm{B}q_\mathrm{B}$ here. Again we checked proper recovery of the homogeneous expression, which yields $2\sin^2 q\sin^2[qL/2]$, with the exact same solutions as before in terms of q.

One can rewrite the multiple angle functions using Chebyshev polynomials of the first and second kind, T_n and U_n, respectively [51, 8.940 with $x\to\cos q$],

$$\sin(nq)=\sin q\,U_{n-1}(\cos q),\quad\text{and}\quad\cos(nq)=T_n(\cos q).$$

For non-trivial zeros of the determinant consider X as defined by $\det = -\sin q_\mathrm{A}\sin q_\mathrm{B}\cdot X$; this solely depends on the wave numbers via $\cos q_\mathrm{A,B} = 1-\lambda/(2\Gamma_\mathrm{A,B})$, so we can rewrite it as a polynomial in λ at the price of re-introducing all rate parameters:

$$\begin{aligned}X &= \lambda(\Gamma_\mathrm{A}\Gamma_\mathrm{BA}-2\Gamma_\mathrm{A}\Gamma_\mathrm{B}+\Gamma_\mathrm{B}\Gamma_\mathrm{AB})\times\\ &\quad\Big[\Gamma_\mathrm{BA}U_{\ell_\mathrm{A}-1}\left(1-\frac{\lambda}{2\Gamma_\mathrm{A}}\right)T_{\ell_\mathrm{B}}\left(1-\frac{\lambda}{2\Gamma_\mathrm{B}}\right)\\ &\quad+\Gamma_\mathrm{AB}U_{\ell_\mathrm{B}-1}\left(1-\frac{\lambda}{2\Gamma_\mathrm{B}}\right)T_{\ell_\mathrm{A}}\left(1-\frac{\lambda}{2\Gamma_\mathrm{A}}\right)\Big]\\ &\quad+2\Gamma_\mathrm{A}\Gamma_\mathrm{B}\Gamma_\mathrm{AB}\Gamma_\mathrm{BA}\left[T_{\ell_\mathrm{A}}\left(1-\frac{\lambda}{2\Gamma_\mathrm{A}}\right)T_{\ell_\mathrm{B}}\left(1-\frac{\lambda}{2\Gamma_\mathrm{B}}\right)-1\right]\\ &\quad+U_{\ell_\mathrm{A}-1}\left(1-\frac{\lambda}{2\Gamma_\mathrm{A}}\right)U_{\ell_\mathrm{B}-1}\left(1-\frac{\lambda}{2\Gamma_\mathrm{B}}\right)\Big\{-\lambda\Gamma_\mathrm{A}\Gamma_\mathrm{BA}^2-\lambda\Gamma_\mathrm{B}\Gamma_\mathrm{AB}^2\\ &\qquad+\frac{\lambda^2}{2}\left[[2(\Gamma_\mathrm{A}-\Gamma_\mathrm{AB})(\Gamma_\mathrm{B}-\Gamma_\mathrm{BA})-\Gamma_\mathrm{AB}\Gamma_\mathrm{BA}]+\frac{\Gamma_\mathrm{A}}{\Gamma_\mathrm{B}}\Gamma_\mathrm{BA}^2+\frac{\Gamma_\mathrm{B}}{\Gamma_\mathrm{A}}\Gamma_\mathrm{AB}^2\right]\Big\}.\end{aligned}\tag{A.14}$$

Approximation of the determinant. Finally, one can approximate (A.14) for small λ. This is difficult for the following reasons. One can show that

$$\begin{aligned}T_\ell\left(1-\frac{\lambda}{2\Gamma}\right)&=\sum_{m=0}^{\ell}\frac{\ell}{\ell+m}\binom{\ell+m}{2m}\left(\frac{-\lambda}{\Gamma}\right)^m=1-\frac{\ell^2}{2}\left(\frac{\lambda}{\Gamma}\right)+\mathcal{O}(\lambda^3),\\ U_{\ell-1}\left(1-\frac{\lambda}{2\Gamma}\right)&=\sum_{m=0}^{\ell-1}\binom{\ell+m}{2m+1}\left(\frac{-\lambda}{\Gamma}\right)^m=\ell\left[1-\frac{\ell^2-1}{6}\left(\frac{\lambda}{\Gamma}\right)+\mathcal{O}(\lambda^3)\right].\end{aligned}$$

For the lowest eigenvalues one expects $\lambda/\Gamma\sim L^{-2}$, the basic reason being that the decay time of an 'excitation' mode of a ring of length L is set (in the 'worst'

case, i.e., for the most stable mode) by the traversal time $\sim L^2$ of a single random walker. Hence *all* terms in the above expressions are of $\mathcal{O}(1)$ for T_ℓ and of $\mathcal{O}(\ell)$ for $U_{\ell-1}$, suppressed only by the denominator factorial, as higher orders only acquire additional factors of the order $\ell^2\lambda/\Gamma \sim 1$. Terminating a λ/Γ expansion is thence inconsistent: The Chebyshev polynomials (expanded about unity) are *very* poorly approximated by the first few terms (e.g., one needs the first *seven* terms of $U_{30}(1-\lambda/(2\Gamma))$ to approximate its *smallest* zero reasonably well).

Closer inspection of X instead suggests to neglect terms which are (taking into account powers of the lengths as well as powers of λ) suppressed by negative powers of a length, leaving the Chebyshev polynomials untouched. The whole second summand is of $\mathcal{O}(1)$, as are the terms of the form '$UU\lambda \sim \ell^2\lambda$' in the last summand. All other terms are suppressed by inverse powers of lengths, e.g., the first term is of $\mathcal{O}(\ell_\mathrm{A}\lambda/\Gamma) < \mathcal{O}(L\lambda/\Gamma) \lesssim \mathcal{O}(L^{-1})$. This approximation relies on the idea that once the edge lengths become too small, the basis of the model (a highly simplified energy landscape), becomes obsolete anyway. For large edge lengths, we consequently have

$$\begin{aligned} X \approx 2\Gamma_\mathrm{A}\Gamma_\mathrm{B}\Gamma_\mathrm{AB}\Gamma_\mathrm{BA} \Bigg[& T_{\ell_\mathrm{A}}\left(1-\frac{\lambda}{2\Gamma_\mathrm{A}}\right) T_{\ell_\mathrm{B}}\left(1-\frac{\lambda}{2\Gamma_\mathrm{B}}\right) - 1 \Bigg] \\ & - \lambda U_{\ell_\mathrm{A}-1}\left(1-\frac{\lambda}{2\Gamma_\mathrm{A}}\right) U_{\ell_\mathrm{B}-1}\left(1-\frac{\lambda}{2\Gamma_\mathrm{B}}\right) \left(\Gamma_\mathrm{A}\Gamma_\mathrm{BA}^2 + \Gamma_\mathrm{B}\Gamma_\mathrm{AB}^2\right). \end{aligned} \tag{A.15}$$

Plotting this approximation in comparison with the exact (A.14) shows that X is approximated quite well up to the first zero, provided only a large enough *total* length ($L > 50$). The larger L, the better the approximation also for the next zeros, though it soon breaks down anyway. Moreover, (A.15) still shows a highly irregular oscillatory behavior that sensitively depends on all parameters. We did not see any way for analytical progress here, and even a numerical solution seemed rather involved.

Comment on equal rates. Interestingly, in this approximation (in contrast to the exact result), there is no difference between setting all rates equal to a single Γ, or setting the 'intra-zone' rates to one rate Γ and the 'inter-zone' rates to another rate Γ_c. From the energy landscape of Figure 6.3, the only difference to the homogeneous case is then the corner barrier separating the two identical landscape parts, and the lowest eigenvalues of the problem are approximately insensitive to this barrier. This is reasonable if we obey the earlier assumption that the corner hopping rate must not differ extremely from Γ, such that the majority of hopping processes still occurs inside one zone. For rates specified like this ($\Gamma_\mathrm{A} = \Gamma_\mathrm{B}$ and $\Gamma_\mathrm{AB} = \Gamma_\mathrm{BA}$), the zeros of the approximation (A.15) are still unavailable exactly, but with the additional $\ell_\mathrm{A} = \ell_\mathrm{B}$, one again re-covers the result for the completely homogeneous edge.

Appendix B

General Auxiliary Material

B.1 Properties of Modified Bessel Functions

The ordinary differential equation of second order

$$\left[\frac{\mathrm{d}^2}{\mathrm{d}z^2}+\frac{1-2\alpha}{z}\frac{\mathrm{d}}{\mathrm{d}z}+\left(\beta^2+\frac{\alpha^2-\nu^2}{z^2}\right)\right]f=0$$

has solutions $f(z)=z^\alpha Z_\nu(\beta z)$, where $Z=J, N, H^{(1)}, H^{(2)}$ [51, 8.491 8.]. Modified Bessel functions occur upon transforming to imaginary argument, such that the solution to $(\mathrm{d}^2/\mathrm{d}z^2+z^{-1}\mathrm{d}/\mathrm{d}z-1)f=0$ reads $f(z)=AI_0(z)+BK_0(z)$, where I_0 and K_0 are modified Bessel functions [51, 8.494 with $\nu=0$]. In the case $\arg(z)\in(-\pi,\pi/2]$, Gradshteyn and Ryzhik [51], 8.406f. defines

$$I_\nu(z)=\mathrm{e}^{-i\pi\nu/2}\,J_\nu(\mathrm{e}^{i\pi/2}\,z),\qquad K_\nu(z)=i\pi/2\;\mathrm{e}^{i\pi\nu/2}\,H_\nu^{(1)}(\mathrm{e}^{i\pi/2}\,z),$$

furnishing series representations [51, 8.445f.]

$$\begin{aligned}I_\nu(z)&=\sum_{k=0}^{\infty}\frac{(z/2)^{\nu+2k}}{k!\Gamma(\nu+k+1)},\\ K_n(z)&=\frac{1}{2}\sum_{k=0}^{n-1}(-)^k\frac{(n-k-1)!}{k!(z/2)^{n-2k}}\\ &\quad+(-)^{n+1}\sum_{k=0}^{\infty}\frac{(z/2)^{2k+n}}{k!(k+n)!}\left[\ln\frac{z}{2}-\frac{1}{2}\psi(k+1)-\frac{1}{2}\psi(n+k+1)\right]\end{aligned}$$

with $n\in\mathbb{N}_0$. For $z\to\infty$, Gradshteyn and Ryzhik [51], 8.451 5.f. provide the asymptotic expansions

$$\begin{aligned}I_\nu(z)&\sim\frac{\mathrm{e}^z}{\sqrt{2\pi z}}\left[\sum_{k=0}^{\infty}\frac{(-1)^k}{(2z)^k}\frac{\Gamma(\nu+k+1/2)}{k!\Gamma(\nu-k+1/2)}\right]+\;\propto\mathrm{e}^{-z}\to\infty,\\ K_\nu(z)&\sim\sqrt{\frac{\pi}{2z}}\,\mathrm{e}^{-z}\left[\sum_{k=0}^{n-1}\frac{1}{(2z)^k}\frac{\Gamma(\nu+k+1/2)}{k!\Gamma(\nu-k+1/2)}+\mathrm{remainder}(n)\right]\to 0.\end{aligned}$$

For $z \ll 1$ one uses the exact series to get [51, 8.447 1.–3., 8.446 for $n = 1$]

$$
\begin{aligned}
I_0(z) &= \sum_{k=0}^{\infty} \frac{(z/2)^{2k}}{k!^2} = 1 + \left(\frac{z}{2}\right)^2 + \mathcal{O}(z^4), \\
I_1(z) &= \sum_{k=0}^{\infty} \frac{(z/2)^{2k+1}}{k!(k+1)!} = \frac{z}{2} + \frac{1}{2}\left(\frac{z}{2}\right)^3 + \mathcal{O}(z^5), \\
K_0(z) &= -I_0(z) \ln\frac{z}{2} + \sum_{k=0}^{\infty} \frac{(z/2)^{2k}}{k!^2} \psi(k+1) \\
&= -\ln\frac{z}{2} - \gamma + \left(\frac{z}{2}\right)^2 \left(-\ln\frac{z}{2} + 1 - \gamma\right) + \mathcal{O}(z^4), \\
K_1(z) &= \frac{1}{z} + I_1(z) \ln\frac{z}{2} - \sum_{k=0}^{\infty} \frac{(z/2)^{2k+1}}{k!(k+1)!} \left(\psi(k+1) + \frac{1}{2(k+1)}\right) \\
&= \frac{1}{z} + \frac{z}{2}\left(\ln\frac{z}{2} + \gamma - \frac{1}{2}\right) + \mathcal{O}(z^3),
\end{aligned}
$$

where we employed $\psi(k+1) = -\gamma + \sum_{n=1}^{k} n^{-1}$.

We note a few further properties of modified Bessel functions that are used in the main text. First, $\mathrm{d}I_0(z)/\mathrm{d}z = I_1(z)$ and $\mathrm{d}K_0(z)/\mathrm{d}z = -K_1(z)$ [51, 8.486 9. & 18.]. Also, one has $I_\nu(z)K_{\nu+1}(z) + I_{\nu+1}(z)K_\nu(z) = 1/z$ [51, 8.477 2.]. Lastly, with $\Gamma(5/2) = 3\sqrt{\pi}/4$, $\Gamma(1/2) = \sqrt{\pi}$, $\Gamma(3/2) = \sqrt{\pi}/2$ and $\Gamma(-1/2) = -2\sqrt{\pi}$, we find that

$$
\frac{K_1(z)}{K_0(z)} \sim 1 + \frac{1}{2z} + \mathcal{O}(z^{-2}) \quad \text{as} \quad z \to \infty.
$$

List of Frequently Used Symbols

The following list is not exhaustive; in particular, quantities which only occur in the Appendices are not listed. Notation in the different Parts is generally unrelated; collisions within one Part were hard to avoid, and should always be unambiguous from the context.

Part I: Hydrogen Recombination on Interstellar Dust	
A	sweeping rate
a	hopping rate
S	# adsorption sites on grain / lattice
F	total impingement flux (surface-integrated)
W	desorption rate
N, $P(N)$, $\langle N \rangle$	# adatoms, its PDF, its time / ensemble average
R_{ME}, R_{RE}	reaction rate in given framework
p	encounter probability (subscripts for model)
$\tilde{p}$	encounter probability, without 'on-top' contribution
g	lattice type factor
D	diffusion coefficient
r	target area radius
R	grain radius
ℓ_D	diffusion length (dimension of a length)
$n(\mathbf{x}), n(\theta)$	diffusion model adatom probability
L_i	lattice dimensions (L for 1d case)
μ	lattice aspect ratio
ξ	survival probability per step
$\lambda(\mathbf{k})$	structure function
ℓ	random walk "length" (dimensionless, steps)
q_i	transition probabilities for RW
$P^*(\mathbf{l}; \xi)$	RW generating fn. on periodic lattice
Ω	lattice (vectors)
$S_3^{(0),(1)}$	sum contributions [54]
N_{dis}	# distinct sites visited by RW
η	recombination efficiency (subscripts for framework)
f	impingement flux per site
a_s, W_s, p_s	hopping rate, desorption rate, occ. probability at site s
ρ	PDF (subscripts denote shape or quantity)
σ, $\tilde{\sigma}$	standard deviation; relative s. d.
F_{1d}	1d-flux per length
D_{edge}, D_{A}, D_{B}	general and specific edge diffusion coefficients
$E_{\mathrm{b,A}}$, $E_{D,\mathrm{A}}$	binding energy, diffusion barrier (zone A)
$p_n(t)$, $p_{m,n}(t)$	1d / 2d-particle propagator
p_n^{U}, p_n^{S}, p_n^{eff}	special distributions (uniform, stationary, effective)
τ_{dep}, τ_{tr}, τ_{res}	time scales of deposition, traversal, residence
ℓ_{A}, ℓ_{B}, L	island edge zone lengths, total length (dimensionless)
$R_n(t)$	nucleation probability at site n, time t
P_n	spatial nucleation distribution
Γ_{A}, Γ_{AB}, γ_{A}	intra-zone, corner, and rescaled corner rates (zone A)
λ, z_{A}, q_{A}	eigenvalue, complex parameter, wave number (zone A)

Part II: Disordered Step Growth	
$k_\pm$	step edge attachment rates (dimension L/T)
v	step velocity
F, F'	total / impurity flux (dimension $1/(LT)$)
l	terrace length
$\theta(x)$	average impurity concentration profile
α_r, β_r	stepping probabilities
N	# sites on terrace
$P_{j\rightarrow/\leftarrow}$	right / left side attachment probability starting from j
$P_{\rightarrow/\leftarrow}$	$P_{j\rightarrow/\leftarrow}$ averaged over starting position and disorder
$E_r \equiv E_{r\rightarrow r+1}$	transition state energies
ΔE, $\Delta E_\pm$	additional trap / barrier height, step edge barriers
$\|i,j\|$	# extra barriers between i and j (random-barrier model)
$D(x)$, $\mu(x)$	effective diffusion coefficient and chemical potential
ϕ	impurity concentration in influx
p	impurity concentration gradient (on terrace)
λ, λ_0	kinetic lengths

Part III: Isozones and Surface Reconstructions	
N	# isozones
r	radial coordinate
R_0, R, R_i, R^*	isozone / island radii
$\theta(r)$	total coverage
θ_i	critical (or supplied) coverage
$\phi(r)$	excess coverage
ϕ_i	critical (or supplied) excess coverage
D_i, τ_i	diffusion coefficient, desorption time in zone i
ℓ_i	diffusion length in zone i
Ω	adatom area
Δ_i	dimensionless constant for stationary profile
j	radial component of current
t_r	relaxation time to steady state
D, τ	diffusion coefficient and desorption time in decay model
t_0, t^*, Δt	decay start and end time, vanishing time

General Notation:	
t	time variable
T	temperature (subscripts specify)
$\beta = 1/(k_\mathrm{B}T)$	inverse temperature, k_B the Boltzmann constant
E_W, E_a, E_{D_i}, E_{τ_i}	activation energies for subscripted quantity
E_s, E_r	relevant activation energy at a site (with disorder)
ν	attempt frequency (subscripts: activated quantity)
a_0	lattice constant
d	number of dimensions
$\underline{\langle \dots \rangle}$	disorder average
$\overline{\dots}$	spatial average

List of Abbreviations

This is a list of abbreviations used herein, roughly in order of appearance.

RE	rate equation
(K)MC	(kinetic) Monte Carlo
ME	master equation
TPD	temperature-programmed desorption
UHV	ultra-high vacuum
(CT)RW	(continuous-time) random walk
LH	Langmuir-Hinshelwood (rejection mechanism)
PDF	probability distribution function
WTD	waiting time distribution
DFT	density functional theory
RSRG	real-space renormalization group
(M)FPT	(mean) first-passage time
ES	Ehrlich-Schwoebel (inter-layer transport barriers)
i.i.d.	independent identically distributed (random variables)
STM	surface tunneling microscopy
PEEM	photoemission electron microscopy
(μ)LEED	(μm size) low energy electron diffraction
LEEM	low energy electron microscopy
ML	mono-layer, coverage unit

Bibliography

[1] Albert Einstein. Über die von der molekularkinetischen Theorie der Wärme geforderte Bewegung von in ruhenden Flüssigkeiten suspendierten Teilchen. *Annalen der Physik* **17** 549–560 (1905)

[2] Thomas Michely, Joachim Krug. *Islands, Mounds and Atoms. Patterns and Processes in Crystal Growth Far from Equilibrium.* Springer, Berlin (2004)

[3] J. W. Haus, K. W. Kehr. Diffusion in Regular and Disordered Lattices. *Phys. Rep.* **150** 263–406 (1987)

[4] Jean-Philippe Bouchaud, Antoine Georges. Anomalous Diffusion in Disordered Media: Statistical Mechanisms, Models and Physical Applications. *Phys. Rep.* **195** 127–293 (1990)

[5] Gianfranco Vidali, Joe Roser, Giulio Manicó, Valerio Pirronello, Hagai B. Perets, Ofer Biham. Formation of molecular hydrogen on analogues of interstellar dust grains: experiments and modeling. *J. Phys.: Conf. Ser.* **6** 36–58 (2005)

[6] Sidney Redner. *A Guide to First-Passage Processes.* Cambridge University Press (2001)

[7] Ingo Lohmar, Joachim Krug. The sweeping rate in diffusion-mediated reactions on dust grain surfaces. *Mon. Not. R. Astron. Soc.* **370**(2) 1025–1033 (2006)

[8] Ingo Lohmar, Joachim Krug. Diffusion-Limited Reactions and Mortal Random Walkers in Confined Geometries. *J. Stat. Phys.* **134**(2) 307 (2009). doi:10.1007/s10955-009-9680-x

[9] K. R. Roos, K. L. Roos, I. Lohmar, D. Wall, J. Krug, M. Horn-von Hoegen, F.-J. Meyer zu Heringdorf. Real-Time View of Mesoscopic Surface Diffusion. *Phys. Rev. Lett.* **100** 016103 (2008)

[10] Pierre Le Doussal, Cécile Monthus, Daniel S. Fisher. Random walkers in one-dimensional random environments: Exact renormalization group analysis. *Phys. Rev. E* **59**(5) 4795–4840 (1999). doi:10.1103/PhysRevE.59.4795

[11] Daniel ben Avraham, Shlomo Havlin. *Diffusion and Reactions in Fractals and Disordered Systems.* Cambridge University Press (2000)

[12] Robert J. Gould, Edwin E. Salpeter. The Interstellar Abundance of the Hydrogen Molecule. I. Basic Processes. *ApJ* **138**(2) 393–407 (1963). doi:10.1086/147654

[13] David J. Hollenbach, Michael W. Werner, Edwin E. Salpeter. Molecular Hydrogen in H_1 Regions. *ApJ* **163**(1) 165–180 (1971)

[14] David Hollenbach, E. E. Salpeter. Surface Adsorption of Light Gas Atoms. *J. Chem. Phys.* **53** 79–86 (1970)

[15] David Hollenbach, E. E. Salpeter. Surface Recombination of Hydrogen Molecules. *ApJ* **163**(1) 155–164 (1971). doi:10.1086/150754

[16] A. G. G. M. Tielens, W. Hagen. Model Calculations of the Molecular Composition of Interstellar Grain Mantles. *A&A* **114** 245–260 (1982)

[17] T. Stantcheva, P. Caselli, E. Herbst. Modified rate equations revisited. A corrected treatment for diffusive reactions on grain surfaces. *A&A* **375**(2) 673–679 (2001)

[18] S. B. Charnley. Stochastic Theory of Molecule Formation on Dust. *ApJ* **562** L99–102 (2001)

[19] N. J. B. Green, T. Toniazzo, M. J. Pilling, D. P. Ruffle, N. Bell, T. W. Hartquist. A stochastic approach to grain surface chemical kinetics. *A&A* **375** 1111–1119 (2001)

[20] Ofer Biham, Itay Furman, Valerio Pirronello, Gianfranco Vidali. Master Equation for Hydrogen Recombination on Grain Surfaces. *ApJ* **553**(2) 595–603 (2001)

[21] Ofer Biham, Azi Lipshtat. Exact results for hydrogen recombination on dust grain surfaces. *Phys. Rev. E* **66**(5) 056103 (2002). doi:10.1103/PhysRevE.66.056103

[22] Azi Lipshtat, Ofer Biham. Efficient Simulations of Gas-Grain Chemistry in Interstellar Clouds. *Phys. Rev. Lett.* **93**(17) 170601 (2004). doi:10.1103/PhysRevLett.93.170601

[23] Q. Chang, H. M. Cuppen, Eric Herbst. Continuous-time random-walk simulation of H_2 formation on interstellar grains. *A&A* **434** 599–611 (2005)

[24] H. M. Cuppen, E. Herbst. Monte Carlo simulations of H_2 formation on grains of varying surface roughness. *Mon. Not. R. Astron. Soc.* **361** 565–576 (2005)

[25] H. Scher, M. Lax. Stochastic Transport in a Disordered Solid. I. Theory. *Phys. Rev. B* **7**(10) 4491–4502 (1973). doi:10.1103/PhysRevB.7.4491

[26] H. M. Cuppen, O. Morata, Eric Herbst. Monte Carlo simulations of H_2 formation on stochastically heated grains. *Mon. Not. R. Astron. Soc.* **367**(4) 1757–1765 (2006)

[27] John S. Mathis, William Rumpl, Kenneth H. Nordsieck. The Size Distribution of Interstellar Grains. *ApJ* **217** 425–433 (1977). doi:10.1086/155591

[28] Joseph C. Weingartner, B. T. Draine. Dust Grain-Size Distributions and Extinction in the Milky Way, Large Magellanic Cloud, and Small Magellanic Cloud. *ApJ* **548**(1) 296–309 (2001)

[29] Azi Lipshtat, Ofer Biham. The effect of grain size distribution on H_2 formation rate in the interstellar medium. *Mon. Not. R. Astron. Soc.* **362**(2) 666–670 (2005)

[30] Hagai B. Perets, Ofer Biham. Molecular Hydrogen Formation on Porous Dust Grains. *Mon. Not. R. Astron. Soc.* **365**(3) 801–806 (2006). doi: 10.1111/j.1365-2966.2005.09803.x

[31] V. Pirronello, Chi Liu, Liyong Shen, Gianfranco Vidali. Laboratory Synthesis of Molecular Hydrogen on Surfaces of Astrophysical Interest. *ApJ* **475** L69–72 (1997)

[32] Valerio Pirronello, Ofer Biham, Chi Liu, Lyong Shen, Gianfranco Vidali. Efficiency of Molecular Hydrogen Formation on Silicates. *ApJ* **483** L131–134 (1997)

[33] Valerio Pirronello, Chi Liu, Joe E. Roser, Gianfranco Vidali. Measurements of molecular hydrogen formation on carbonaceous grains. *A&A* **344** 681–686 (1999)

[34] N. Katz, I. Furman, O. Biham, V. Pirronello, G. Vidali. Molecular Hydrogen Formation on Astrophysically Relevant Surfaces. *ApJ* **522** 305–312 (1999)

[35] G. Manicò, G. Ragunì, V. Pirronello, J. E. Roser, G. Vidali. Laboratory Measurements of Molecular Hydrogen Formation on Amorphous Water Ice. *ApJ* **548** L253–256 (2001)

[36] Hagai B. Perets, Ofer Biham, Giulio Manicó, Valerio Pirronello, Joe Roser, Sol Swords, Gianfranco Vidali. Molecular Hydrogen Formation on Ice under Interstellar Conditions. *ApJ* **627** 850–860 (2005)

[37] H. B. Perets, A. Lederhendler, O. Biham, G. Vidali, L. Li, S. Swords, E. Congiu, J. Roser, G. Manicò, J. R. Brucato, V. Pirronello. Molecular Hydrogen Formation on Amorphous Silicates under Interstellar Conditions. *ApJ* **661** L163–166 (2007)

[38] G. Vidali, V. Pirronello, L. Li, J. Roser, G. Manicó, E. Congiu, H. Mehl, A. Lederhendler, H. B. Perets, J. R. Brucato, O. Biham. Analysis of Molecular Hydrogen Formation on Low-Temperature Surfaces in Temperature Programmed Desorption Experiments. *J. Phys. Chem. A* **111** 12611–12619 (2007)

[39] Richard L. Schwoebel, Edward J. Shipsey. Step Motion on Crystal Surfaces. *J. Appl. Phys.* **37**(10) 3682–3686 (1966)

[40] Joachim Krug. Lonely adatoms in space. *Phys. Rev. E* **67** 065102(R) (2003)

[41] Alex A. Lushnikov, Jayesh S. Bhatt, Ian J. Ford. Stochastic approach to chemical kinetics in ultrafine aerosols. *Journal of Aerosol Science* **34** 1117–1133 (2003)

[42] E. W. Montroll. Random Walks on Lattices. III. Calculation of First-Passage Times with Application to Exciton Trapping on Photosythetic Units. *J. Math. Phys.* **10** 753 (1969)

[43] Michael Slutsky, Mehran Kardar, Leonid A. Mirny. Diffusion in correlated random potentials, with applications to DNA. *Phys. Rev. E* **69**(6) 061903 (2004). doi:10.1103/PhysRevE.69.061903

[44] Michael Slutsky, Leonid A. Mirny. Kinetics of Protein-DNA Interaction: Facilitated Target Location in Sequence-Dependent Potential. *Biophysical Journal* **87**(6) 4021–4035 (2004). doi:10.1529/biophysj.104.050765

[45] Ronny Straube, Michael J. Ward, Martin Falcke. Reaction Rate of Small Diffusing Molecules on a Cylindrical Membrane. *J. Stat. Phys.* **129**(2) 377–405 (2007)

[46] Ofer Biham, Itay Furman, N. Katz, Valerio Pirronello, Gianfranco Vidali. H_2 formation on interstellar grains in different physical regimes. *Mon. Not. R. Astron. Soc.* **296** 869–872 (1998)

[47] Ofer Biham, Joachim Krug, Azi Lipshtat, Thomas Michely. Reaction Kinetics in a Tight Spot. *Small* **1**(5) 502–504 (2005)

[48] P. Caselli, T. I. Hasegawa, Eric Herbst. A Proposed Modification of the Rate Equations for Reactions on Grain Surfaces. *ApJ* **495**(1) 309–316 (1998)

[49] R. T. Garrod. A new modified-rate approach for gas-grain chemical simulations. *A&A* **491** 239–251 (2008)

[50] Joachim Krug, Paolo Politi, Thomas Michely. Island nucleation in the presence of step-edge barriers: Theory and applications. *Phys. Rev. B* **61**(20) 14037–14046 (2000). doi:10.1103/PhysRevB.61.14037

[51] I. S. Gradshteyn, I. M. Ryzhik. *Table of Integrals, Series, and Products*. Academic Press, San Diego, sixth edn. (2000)

[52] W. Th. F. den Hollander, P. W. Kasteleyn. Random Walks with 'Spontaneous Emission' on Lattices with Periodically Distributed Imperfect Traps. *Physica A* **112** 523–543 (1982)

[53] Irving Langmuir. The Adsorption of Gases on Plane Surfaces of Glass, Mica and Platinum. *J. Am. Chem. Soc.* **40**(9) 1361–1403 (1918)

[54] Elliott W. Montroll, George H. Weiss. Random Walks on Lattices. II. *J. Math. Phys.* **6**(2) 167 (1965)

[55] Barry D. Hughes. *Random Walks and Random Environments*, vol. 1. Oxford University Press (1995)

[56] S. Condamin, O. Bénichou, M. Moreau. First-Passage Times for Random Walks in Bounded Domains. *Phys. Rev. Lett.* **95** 260601 (2005)

[57] S. Condamin, O. Bénichou. Exact expressions of mean first-passage times and splitting probabilities for random walks in bounded rectangular domains. *J. Chem. Phys.* **124** 206103 (2006)

[58] S. Condamin, O. Bénichou, M. Moreau. Random walks and Brownian motion: A method of computation for first-passage times and related quantities in confined geometries. *Phys. Rev. E* **75** 021111 (2007)

[59] Elliott W. Montroll, Harvey Scher. Random Walks on Lattices. IV. Continuous-Time Walks and Influence of Absorbing Boundaries. *J. Stat. Phys.* **9** 101–135 (1973)

[60] F. van Wijland, S. Caser, H. J. Hilhorst. Statistical properties of the set of sites visited by the two-dimensional random walk. *J. Phys. A* **30**(2) 507–531 (1997)

[61] Andreas Gödecke. *Kinetische Monte Carlo Simulationen zum Wachstum zweidimensionaler Kristalle.* Master's thesis, Rheinisch-Westfälische Technische Hochschule Aachen (2004)

[62] Michael D. Hatlee, John J. Kozak. Random walks on finite lattices with traps. *Phys. Rev. B* **21**(4) 1400–1407 (1980). doi:10.1103/PhysRevB.21.1400

[63] Dick Bedeaux, Katja Lakatos-Lindenberg, Kurt E. Shuler. On the Relation between Master Equations and Random Walks and Their Solutions. *J. Math. Phys.* **12** 2116–2123 (1971)

[64] Eric Herbst. Chemistry in the Interstellar Medium. *Annu. Rev. Phys. Chem.* **46** 27–53 (1995)

[65] V. Buch, R. Czerminski. Eigenstates of a quantum-mechanical particle on a topologically disordered surface: H(D) atom physisorbed on an amorphous ice cluster $(H_2O)_{115}$. *J. Chem. Phys.* **95**(8) 6026–6038 (1991)

[66] Holly G. Hixson, Marek J. Wojcik, Matthew S. Devlin, J. Paul Devlin. Experimental and simulated vibrational spectra of H_2 absorbed in amorphous ice: Surface structures, energetics, and relaxations. *J. Chem. Phys.* **97**(2) 753–767 (1992)

[67] S. Cazaux, A. G. G. M. Tielens. H_2 Formation on Grain Surfaces. *ApJ* **604** 222–237 (2004)

[68] L. Amiaud, J. H. Fillion, S. Baouche, F. Dulieu, A. Momeni, J. L. Lemaire. Interaction of D_2 with H_2O amorphous ice studied by temperature-programed desorption experiments. *J. Chem. Phys.* **124** 094702 (2006)

[69] L. Amiaud, F. Dulieu, J.-H. Fillion, A. Momeni, J. L. Lemaire. Interaction of atomic and molecular deuterium with a nonporous amorphous water ice surface between 8 and 30 K. *J. Chem. Phys.* **127** 144709 (2007)

[70] R. Ferrando, G. Tréglia. Anisotropy of diffusion along steps on the (111) faces of gold and silver. *Phys. Rev. B* **50**(16) 12104–12117 (1994). doi: 10.1103/PhysRevB.50.12104

[71] Claudio Castellano, Paolo Politi. Spatiotemporal Distribution of Nucleation Events during Crystal Growth. *Phys. Rev. Lett.* **87**(5) 056102 (2001). doi: 10.1103/PhysRevLett.87.056102

[72] Paolo Politi, Claudio Castellano. Process of irreversible nucleation in multilayer growth. I. Failure of the mean-field approach. *Phys. Rev. E* **66**(3) 031605 (2002). doi:10.1103/PhysRevE.66.031605

[73] Paolo Politi, Claudio Castellano. Process of irreversible nucleation in multilayer growth. II. Exact results in one and two dimensions. *Phys. Rev. E* **66**(3) 031606 (2002). doi:10.1103/PhysRevE.66.031606

[74] R. Collins, S. R. Carson, J. A. D. Matthew. Diffusion equation for one-dimensional unbiased hopping. *Am. J. Phys.* **65**(3) 230–237 (1997)

[75] W. N. Hugrass. Comment on "Diffusion equation for one-dimensional unbiased hopping" by R. Collins, S. R. Carson, and J. A. D. Matthew [A. J. Phys. 65 (3), 230–237 (1997)]. *Am. J. Phys.* **66**(9) 813–814 (1998)

[76] P. Lançon, G. Batrouni, L. Lobry, N. Ostrowsky. Drift without flux: Brownian walker with a space-dependent diffusion coefficient. *Europhys. Lett.* **54**(1) 28–34 (2001)

[77] Tong Zhao, John D. Weeks, Daniel Kandel. From discrete hopping to continuum modeling on vicinal surfaces with applications to Si(001) electromigration. *Phys. Rev. B* **71** 155326 (2005)

[78] V. M. Kenkre, E. W. Montroll, M. F. Shlesinger. Generalized Master Equations for Continuous-Time Random Walks. *J. Stat. Phys.* **9**(1) 45–50 (1973)

[79] J. Klafter, R. Silbey. Derivation of the Continuous-Time Random-Walk Equation. *Phys. Rev. Lett.* **44**(2) 55–58 (1980). doi:10.1103/PhysRevLett. 44.55

[80] Michael F. Shlesinger, Joseph Klafter, Y. M. Wong. Random Walks with Infinite Spatial and Temporal Moments. *J. Stat. Phys.* **27**(3) 499–512 (1982)

[81] Ralf Metzler, Joseph Klafter. The random walk's guide to anomalous diffusion: a fractional dynamics approach. *Phys. Rep.* **339** 1–77 (2000)

[82] J. Klafter, A. Blumen, G. Zumofen. Fractal Behavior in Trapping and Reaction: a Random Walk Study. *J. Stat. Phys.* **36**(5/6) 561–577 (1984)

[83] Isaac Goldhirsch, Yuval Gefen. Analytic method for calculating properties of random walks on networks. *Phys. Rev. A* **33**(4) 2583–2594 (1986). doi:10.1103/PhysRevA.33.2583

[84] S. H. Noskowicz, I. Goldhirsch. Distribution Functions for Random Walk Processes on networks: An Analytic Method. *J. Stat. Phys.* **48**(1/2) 255–290 (1987)

[85] C. P. Haynes, A. P. Roberts. Global first passage times on fractal lattices. *arXiv.org* (2008). ArXiv:0809.0563v1 [cond-mat.stat-mech]

[86] Herbert B. Rosenstock. Random Walks on Lattices with Traps. *J. Math. Phys.* **11**(2) 487–490 (1970)

[87] Herbert B. Rosenstock. Absorption time by a random trap distribution. *J. Math. Phys.* **21**(7) 1643–1645 (1980)

[88] M. D. Donsker, S. R. S. Varadhan. Asymptotics for the Wiener sausage. *Commun. Pure Appl. Math.* **28**(4) 525–565 (1975)

[89] A. Blumen, G. Zumofen, J. Klafter. Target annihilation by random walkers. *Phys. Rev. B* **30**(9) 5379–5382 (1984). doi:10.1103/PhysRevB.30.5379

[90] M. Moreau, G. Oshanin, O. Bénichou, M. Coppey. Pascal principle for diffusion-controlled trapping reactions. *Phys. Rev. E* **67**(4) 045104 (2003). doi:10.1103/PhysRevE.67.045104

[91] Alan J. Bray, Satya N. Majumdar, Richard A. Blythe. Formal solution of a class of reaction-diffusion models: Reduction to a single-particle problem. *Phys. Rev. E* **67**(6) 060102 (2003). doi:10.1103/PhysRevE.67.060102

[92] S. B. Yuste, Katja Lindenberg. Trapping reactions with subdiffusive traps and particles. *Proc. SPIE* **5845** 27 (2005)

[93] S. B. Yuste, Katja Lindenberg. Trapping reactions with subdiffusive traps and particles characterized by different anomalous diffusion exponents. *Phys. Rev. E* **72**(6) 061103 (2005). doi:10.1103/PhysRevE.72.061103

[94] S. B. Yuste, Katja Lindenberg. Subdiffusive target problem: Survival probability. *Phys. Rev. E* **76**(5) 051114 (2007)

[95] S. B. Yuste, G. Oshanin, K. Lindenberg, O. Bénichou, J. Klafter. Survival probability of a particle in a sea of mobile traps: A tale of tails. *arXiv.org* (2008). ArXiv:0805.2920v1 [cond-mat.stat-mech]

[96] O. Bénichou, M. Moreau, G. Oshanin. Kinetics of stochastically gated diffusion-limited reactions and geometry of random walk trajectories. *Phys. Rev. E* **61**(4) 3388–3406 (2000). doi:10.1103/PhysRevE.61.3388

[97] Robert M. Ziff. Flux to a Trap. *J. Stat. Phys.* **65**(5/6) 1217–1233 (1991)

[98] Robert M. Ziff, Satya N. Majumdar, Alain Comtet. General flux to a trap in one and three dimensions. *J. Phys. CM* **19** 065102 (2007)

[99] S. Condamin, V. Tejedor, O. Bénichou. Occupation times of random walks in confined geometries: From random trap model to diffusion-limited reactions. *Phys. Rev. E* **76** 050102(R) (2007)

[100] Jae Dong Noh, Heiko Rieger. Random Walks on Complex Networks. *Phys. Rev. Lett.* **92**(11) 118701 (2004). doi:10.1103/PhysRevLett.92.118701

[101] S. Condamin, O. Bénichou, V. Tejedor, R. Voituriez, J. Klafter. First-passage times in complex scale-invariant media. *Nature* **450** 77–80 (2007)

[102] J. P. Bouchaud, A. Comtet, A. Georges, P. Le Doussal. The Relaxation-Time Spectrum of Diffusion in a One-Dimensional Random Medium: an Exactly Solvable Case. *Europhys. Lett.* **3** 653–660 (1987)

[103] J. P. Bouchaud, A. Comtet, A. Georges, P. Le Doussal. Classical Diffusion of a Particle in a One-Dimensional Random Force Field. *Ann. Phys.* **201** 285–341 (1990)

[104] Alain Comtet, David S. Dean. Exact results on Sinais diffusion. *J. Phys. A* **31**(43) 8595–8605 (1998)

[105] J. Chave, E. Guitter. Statistical and dynamical properties of the discrete Sinai model at finite times. *J. Phys. A* **32**(3) 445–468 (1999)

[106] Daniel S. Fisher, Pierre Le Doussal, Cecile Monthus. Random Walks, Reaction-Diffusion, and Nonequilibrium Dynamics of Spin Chains in One-Dimensional Random Environments. *Phys. Rev. Lett.* **80**(16) 3539–3542 (1998). doi:10.1103/PhysRevLett.80.3539

[107] Pierre Le Doussal, Cécile Monthus. Reaction diffusion models in one dimension with disorder. *Phys. Rev. E* **60**(2) 1212–1238 (1999). doi:10.1103/PhysRevE.60.1212

[108] Pierre Le Doussal, Cécile Monthus. Exact solutions for the statistics of extrema of some random 1D landscapes, application to the equilibrium and the dynamics of the toy model. *Physica A* **317**(1–2) 140–198 (2003)

[109] K. P. N. Murthy, K. W. Kehr. Mean first-passage times of random walks on a random lattice. *Phys. Rev. A* **40**(4) 2082–2087 (1989). doi:10.1103/PhysRevA.40.2082

[110] S. H. Noskowicz, I. Goldhirsch. Average versus Typical Mean First-Passage Time in a Random Random Walk. *Phys. Rev. Lett.* **61**(5) 500–502 (1988). doi:10.1103/PhysRevLett.61.500

[111] Pierre Le Doussal. First-passage time for random walks in random environments. *Phys. Rev. Lett.* **62**(26) 3097 (1989). doi:10.1103/PhysRevLett.62.3097

[112] S. H. Noskowicz, I. Goldhirsch. Noskowicz and Goldhirsch reply. *Phys. Rev. Lett.* **62**(26) 3098 (1989). doi:10.1103/PhysRevLett.62.3098

[113] K. W. Kehr, K. P. N. Murthy. Distribution of mean first-passage times in random chains due to disorder. *Phys. Rev. A* **41**(10) 5728–5730 (1990). doi:10.1103/PhysRevA.41.5728

[114] S. H. Noskowicz, I. Goldhirsch. First-passage-time distribution in a random random walk. *Phys. Rev. A* **42**(4) 2047–2064 (1990). doi:10.1103/PhysRevA.42.2047

[115] Achille Giacometti, K. P. N. Murthy. Diffusion and trapping on a one-dimensional lattice. *Phys. Rev. E* **53**(6) 5647–5655 (1996). doi:10.1103/PhysRevE.53.5647

[116] Clément Sire. Analytical results for random walks in the presence of disorder and traps. *Phys. Rev. E* **60**(2) 1464–1474 (1999). doi:10.1103/PhysRevE.60.1464

[117] Pedro A. Pury, Manuel O. Cáceres. Survival and residence times in disordered chains with bias. *Phys. Rev. E* **66**(2) 021112 (2002). doi:10.1103/PhysRevE.66.021112

[118] Pedro A. Pury, Manuel O. Cáceres. Mean first-passage and residence times of random walks on asymmetric disordered chains. *J. Phys. A* **36** 2695–2706 (2003)

[119] Ophir Flomenbom, Joseph Klafter. Closed-Form Solutions for Continuous Time Random Walks on Finite Chains. *Phys. Rev. Lett.* **95** 098105 (2005)

[120] O. Flomenbom, J. Klafter, R. J. Silbey. Comment on "Path Summation Formulation of the Master Equation". *Phys. Rev. Lett.* **97** 178901 (2006)

[121] O. Flomenbom, R. J. Silbey. Path-probability density functions for semi-Markovian random walks. *Phys. Rev. E* **76** 041101 (2007)

[122] Ophir Flomenbom, Robert J. Silbey. Properties of the generalized master equation: Green's functions and probability density functions in the path representation. *J. Chem. Phys.* **127** 034103 (2007)

[123] G. M. Schütz, K. Mussawisade. Annihilating random walks in one-dimensional disordered media. *Phys. Rev. E* **57**(3) 2563–2567 (1998). doi:10.1103/PhysRevE.57.2563

[124] Jef Hooyberghs, Carlo Vanderzande. Real-space renormalization for reaction-diffusion systems. *J. Phys. A* **33** 907–919 (2000)

[125] Rochard L. Schwoebel. Step Motion on Crystal Surfaces. II. *J. Appl. Phys.* **40**(2) 614–618 (1969)

[126] E. T. Croke, F. Grosse, J. J. Vajo, M. F. Gyure. Substitutional C fraction and the influence of C on Si dimer diffusion in $Si_{1-y}C_y$ alloys grown on (001) and (118) Si. *Applied Phys. Lett.* **77**(9) 1310–1312 (2000)

[127] Joachim Krug. *Introduction to Step Dynamics and Step Instabilities*, vol. 149 of *International Series on Numerical Mathematics*, 69–95. Birkhäuser Verlag Basel (2005)

[128] Joachim Krug. New mechanism for impurity-induced step bunching. *Europhys. Lett.* **60** 788–794 (2002)

[129] Kai Lai Chung. *Markov Chains With Stationary Transition Probabilities*. No. 104 in Die Grundlehren der mathematischen Wissenschaften in Einzeldarstellungen. Springer-Verlag, second edn. (1967)

[130] Jürgen Vollmer, József Hegedüs, Frank Grosse, Joachim Krug. Impurity-induced step interactions: a kinetic Monte-Carlo study. *New J. Phys.* **10** 053017 (2008)

[131] Dirk Wall. *LEEM- und PEEM-Untersuchungen zur Diffusion von Silber auf Siliziumoberflächen anhand des dynamischen Gleichgewichts während der Desorption von Silberinseln – Die Isozone –*. Master's thesis, Institut für Experimentelle Physik, Universität Duisburg-Essen (2007)

[132] T. R. Linderoth, J. J. Mortensen, K. W. Jacobsen, E. Lægsgaard, I. Stensgaard, F. Besenbacher. Homoepitaxial Growth of Pt on Pt(100)-hex: Effects of Strongly Anisotropic Diffusion and Finite Island Sizes. *Phys. Rev. Lett.* **77**(1) 87–90 (1996). doi:10.1103/PhysRevLett.77.87

[133] Gert Ehrlich, F. G. Hudda. Atomic View of Surface Self-Diffusion: Tungsten on Tungsten. *J. Chem. Phys.* **44**(3) 1039–1049 (1966)

[134] B. S. Swartzentruber. Direct Measurement of Surface Diffusion Using Atom-Tracking Scanning Tunneling Microscopy. *Phys. Rev. Lett.* **76**(3) 459–462 (1996). doi:10.1103/PhysRevLett.76.459

[135] L. Kuipers, M. S. Hoogeman, J. W. M. Frenken. Step dynamics on Au(110) studied with a high-temperature, high-speed scanning tunneling microscope. *Phys. Rev. Lett.* **71**(21) 3517–3520 (1993). doi:10.1103/PhysRevLett.71.3517

[136] R. Persaud, H. Noro, M. Azim, R. H. Milne, J. A. Venables. Recent Surface Studies Using Biased Secondary Electron Imaging. *Scanning Microscopy* **8** 803 (1994)

[137] M. Hanbücken, T. Doust, O. Osasona, G. le Lay, J. A. Venables. SEM Observations of Ag Surface Diffusion at the Si(111)$\sqrt{3}$-Ag Interface. *Surface Science* **168** 133–141 (1986)

[138] R. Butz, H. Wagner. Surface Diffusion of Pd and Au on W Single Crystal Planes. II. Anisotropy of Pd surface diffusion due to the influence of substrate structure. *Surface Science* **87** 85–100 (1979)

[139] Claude A. Roulet. Diffusion en surface de l'argent sur les plans (001), (111), (110) et des surfaces vicinales du cuivre. *Surface Science* **36** 295–316 (1973)

[140] Nan-Jian Wu, Akiko Natori, Hitoshi Yasunaga. Mass transport of a Ag thin film on a stepped Si(111) surface. *Surface Science* **242** 191–194 (1991)

[141] K. R. Roos, K. L. Roos, M. Horn von Hoegen, F.-J. Meyer zu Heringdorf. High temperature self-assembly of Ag nanowires on vicinal Si(001). *J. Phys. CM* **17**(16) S1407–1414 (2005)

[142] D. J. Chadi. Stabilities of single-layer and bilayer steps on Si(001) surfaces. *Phys. Rev. Lett.* **59**(15) 1691–1694 (1987). doi:10.1103/PhysRevLett.59.1691

[143] E. Pehlke, J. Tersoff. Nature of the step-height transition on vicinal Si(001) surfaces. *Phys. Rev. Lett.* **67**(4) 465–468 (1991). doi:10.1103/PhysRevLett.67.465

[144] H. W. Yeom, I. Matsuda, K. Tono, T. Ohta. Electronic structures of the Si(001)2 × 3Ag surface. *Phys. Rev. B* **57**(7) 3949–3954 (1998). doi:10.1103/PhysRevB.57.3949

[145] G. Raynerd, M. Hardiman, J. A. Venables. Temperature-dependent coverage of the $\sqrt{3} \times \sqrt{3}R30°$ structure of Ag/Si(111). *Phys. Rev. B* **44**(24) 13803–13806 (1991)

[146] Y. G. Ding, C. T. Chan, K. M. Ho. Structure of the $\sqrt{3} \times \sqrt{3}R30°$ Ag/Si(111) Surface from First Principles Calculations. *Phys. Rev. Lett.* **67**(11) 1454–1457 (1991)

[147] K. J. Wan, X. F. Lin, J. Nogami. Surface reconstructions in the Ag/Si(111) system. *Phys. Rev. B* **47**(20) 13700–13712 (1993). doi:10.1103/PhysRevB.47.13700

[148] E. Bauer. Surface electron microscopy: the first thirty years. *Surface Science* **299/300** 102–115 (1994)

[149] E. Bauer. Low energy electron microscopy. *Rep. Prog. Phys.* **57** 895–938 (1994)

[150] Joachim Krug. A simple model for the diffusion zones of Ag on Si(001) (2005). Unpublished

[151] Ki-jeong Kong, H. W. Yeom, Doyeol Ahn, H. Yi, B. D. Yu. Ab initio study of adsorption and diffusion of Ag atoms on a Si(001) surface. *Phys. Rev. B* **67** 235328 (2003)

[152] M. Hanbücken, M. Futamoto, J. A. Venables. Nucleation, Growth and the Intermediate Layer in Ag/Si(100) and Ag/Si(111). *Surface Science* **147** 433–450 (1984)

[153] Anvarbek M. Meirmanov. *The Stefan Problem*. No. 3 in de Gruyter Expositions in Mathematics. Walter de Gruyter, Berlin, New York (1992)

[154] L. D. Landau, E. M. Lifschitz. *Lehrbuch der theoretischen Physik: Hydrodynamik*, vol. 6. Harri Deutsch, fifth edn. (1991)

[155] A. Erdélyi, ed. *Higher Transcendental Functions*, vol. 1. McGraw-Hill, New York (1953)

[156] N. G. van Kampen. *Stochastic Processes in Physics and Chemistry*. North-Holland Personal Library, Amsterdam, second edn. (1992)

Danksagung

Ich möchte mich zunächst sehr herzlich bei meinem Betreuer Joachim Krug bedanken. Er hat mir in einem interessanten Themengebiet ermöglicht, vielfältige Probleme zu bearbeiten. Dabei habe ich (so jedenfalls meine Hoffnung) vieles über die Physik und das wissenschaftliche Arbeiten gelernt, und insbesondere von seinem Gespür dafür profitiert, welche Fragen lohnend und vielversprechend zu verfolgen sind.

Weiterhin danke ich Kelly Roos, Frank Meyer zu Heringdorf und Dirk Wall für die interessante Zusammenarbeit, die zu einer Publikation geführt hat, und letzteren beiden speziell für die Erlaubnis, einige von Ihnen angefertigte Abbildungen sowie experimentelle Daten in dieser Arbeit verwenden zu dürfen. Ofer Biham hat hilfreiche Kommentare zu Artikelentwürfen gegeben, und hat in der persönlichen Diskussion viele Anregungen für weitere Untersuchungen eingebracht. Aufschlussreiche Gespräche zum Modell aus Teil II haben wir mit Thomas Kriecherbauer geführt, und Eric Herbst hat uns in Diskussionen die Sichtweise der Astrochemie auf die Oberflächenreaktionen nahegebracht. Schließlich hat Su-Chan Park mir mit seiner Erfahrung in Sachen Zufallszahlengeneratoren über eine merkliche Hürde geholfen.

Diese Arbeit wurde ab 2006 im Rahmen des Sonderforschungsbereichs TR-12, *Symmetries and Universality in Mesoscopic Systems*, durchgeführt, weshalb ich dessen Mitgliedern danken möchte, ebenso wie der Deutschen Forschungsgemeinschaft für die finanzielle Förderung.

Das Korrekturlesen haben ganz kurzfristig und sehr tatkräftig und detailliert Jasper Franke, Su-Chan Park, Gordian Prescher, Gregor Wergen und Andrea Wolff übernommen, wofür ich ausgeprochen dankbar bin. Darüber hinaus möchte ich von meinen zahlreichen BürokollegInnen im Institut aber besonders Jakob Müller-Hill und Barbara Sandhöfer hervorheben, die ganz wesentlich für eine sehr angenehme Atmosphäre verantwortlich waren.

Schließlich ist es mir eine große Freude, meinen Eltern, Carolin und meinem Bruder Arne für andauernde Unterstützung zu danken, und dafür, dass sie immer für mich da waren.

Erklärung

Ich versichere, dass ich die von mir vorgelegte Dissertation selbständig angefertigt, die benutzten Quellen und Hilfsmittel vollständig angegeben und die Stellen der Arbeit — einschließlich Tabellen, Karten und Abbildungen —, die anderen Werken im Wortlaut oder dem Sinn nach entnommen sind in jedem Einzelfall als Entlehnung kenntlich gemacht habe; dass diese Dissertation noch keiner anderen Fakultät oder Universität zur Prüfung vorgelegen hat, dass sie — abgesehen von unten angegebenen Teilpublikationen — noch nicht veröffentlicht worden ist sowie, dass ich eine solche Veröffentlichung vor Abschluss des Promotionsverfahrens nicht vornehmen werde. Die Bestimmungen der Promotionsordnung sind mir bekannt. Die von mir vorgelegte Dissertation ist von Herrn Prof. Dr. Joachim Krug betreut worden.

Ingo Lohmar

Köln, 6. Oktober 2009

Teilpublikationen

- Ingo Lohmar, Joachim Krug. The sweeping rate in diffusion-mediated reactions on dust grain surfaces. *Mon. Not. R. Astron. Soc.* **370**(2) 1025–1033 (2006)
- K. R. Roos, K. L. Roos, I. Lohmar, D. Wall, J. Krug, M. Horn-von Hoegen, F.-J. Meyer zu Heringdorf. Real-Time View of Mesoscopic Surface Diffusion. *Phys. Rev. Lett.* **100** 016103 (2008)
- Ingo Lohmar, Joachim Krug. Diffusion-Limited Reactions and Mortal Random Walkers in Confined Geometries. *J. Stat. Phys.* **134**(2) 307 (2009). doi: 10.1007/s10955-009-9680-x